To the Graduate Council:

I am submitting herewith a dissertation written by Lawretta Chineze Leaticia Ononye entitled "The Effect of Implantation Temperature and Ionizing Radiation on the Microstructure of Ion Implanted Sapphire." I have examined the final electronic copy of this dissertation for form and content and recommend that it be accepted in partial fulfillment of the requirements for the degree of Doctor of Philosophy, with a major in Materials Science and Engineering.

Carl J. McHargue

Major Professor

We have read this dissertation
And recommend its acceptance:

Raymond A. Buchanan

David C. Joy

Thomas T. Meek

Claudia J. Rawn

Acceptance for the Council:

Anne Mayhew

Vice Provost and Dean of Graduate Studies

(Original signatures are on file with official student records.)

THE EFFECT OF IMPLANTATION TEMPERATURE AND IONIZING RADIATION ON THE MICROSTRUCTURE OF ION IMPLANTED SAPPHIRE

A Dissertation

Presented for the

Doctor of Philosophy

Degree

The University of Tennesee, Knoxville

Lawretta Chineze Leaticia Ononye

December 2002

DEDICATION

This dissertation is dedicated to my dear husband and children, Dr. Ambrose H. E. Ononye, Ifechukwu and Nnaebuka.

ACKNOWLEDGMENTS

First and foremost, I give thanks to God, who blessed all my efforts in completing this Ph.D. program. My indebtedness is due to my advisor, Dr. Carl J. McHargue, for financially supporting me for this study and for his guidance, valuable suggestions, and insights regarding the ideas presented in the dissertation. My sincere gratitude is due to Dr. Lawrence F. Allard at the Oak Ridge National Laboratory, for training me on the use of the transmission electron microscope, his willingness to assist anytime when needed and for many good discussions and suggestions.

Many thanks are due to Dr. David C. Joy, Dr. Raymond A. Buchanan, Dr. Thomas T. Meek and Dr. Claudia J. Rawn for their support and accepting the responsibility to be on my committee. I am particularly grateful to Dr. David C. Joy, for numerous helps and useful suggestions.

I would also like to thank Ms. Shawn Trent, Ms. Dorothy Coffey, Dr. Doug Bloom and Dr. Harry M. Meyer III at the Materials Analysis Group, Oak Ridge National Laboratory for all their help. Ms. Shawn trained me on TEM sample preparation techniques. Ms. Coffey was instrumental for the focus ion beam (FIB) work on the samples. Dr. Bloom and Dr. Allard trained me on the use of HD-2000 STEM, while Dr. Meyer helped with the auger spectroscopy.

My appreciation is due to Dr. Joseph E. Spruiell for his help with the XRD. I am grateful to Dr. Allan Kirkpatrick, President, Epion Corp, Billerica, MA, Dr. Eduardo Alves, Mr. Jorge Rocha and Mr. C. Marguer all of ITN for their invaluable help. Dr. Kirkpatrick helped with the ion implantation; Dr. Alves and Mr. Rocha assisted with the RBS – ion-channeling measurements, while Mr. Marguer helped with the optical absorption measurements.

Many thanks are due to Dr. Jeffrey Weimer, at The University of Alabama and Joshua Williams for their assistance with the XPS. Also, my thanks go to Dr. Roberto Benson for his support, the entire faculty of the department of materials science and engineering, my colleagues and friends, for their various help and support throughout my graduate program.

This research is supported in part by U.S. Department of Energy, Division of Materials Sciences, and the Assistant Secretary of Energy and Efficiency and Renewable Energy, Office of Transportation Technologies, as part of the High Temperature Materials Laboratory User Program at the Oak Ridge National Laboratory, managed by UT-Battelle, LLC, for the U.S. Department of Energy under contract number DE-AC05-00OR22725.

Finally, I wish to express my sincere appreciation and thanks to my beloved husband, Dr. Ambrose H. E. Ononye for his understanding, moral support and encouragement even at the most difficult period throughout my Ph.D. program. I share all my achievements with him. This acknowledgment would not be complete without acknowledging my two sons, Ifechukwu and Nnaebuka, who bore, prayed and supported me morally throughout this program.

ABSTRACT

Single crystalline specimens of aluminum oxide (Al_2O_3) were irradiated with boron, nitrogen and iron ions at room temperature and 1000°C to fluences of 1×10^{17} B^+/cm^2, 3×10^{16} N^+/cm^2 and 1×10^{17} Fe^+/cm^2 respectively with 150 keV of energy. Following irradiation, the structures were examined by several experimental techniques: transmission electron microscopy (TEM), Rutherford backscattering - ion channeling (RBS-C) spectroscopy, optical absorption measurements, x-ray diffraction (XRD) technique, and x-ray photoelectron spectroscopy (XPS). The samples implanted at room temperature were then annealed for one hour at 1000°C in a reducing (Ar-4%H_2) gas and the microstructures examined.

The implantation temperature significantly influenced the microstructure of the implanted samples. The room temperature boron-implanted microstructure consists of the typical "black spot" radiation damage, which differs from the microstructural features observed at 1000°C. Cross-sectional TEM micrograph for the nitrogen-implanted at room temperature reveals a band of bubbles or voids; whereas the 1000°C N-implanted specimen exhibits a different type of "black spot" radiation damage generally ascribed to defect clusters. The microstructure of the iron-implanted sapphire at room temperature contains "black spot damage" clusters and small (1-2 nm) precipitates at depths greater than about 25 nm. The sample implanted with iron at 1000°C contains particles of iron as large as 50 nm and no evidence of "black spot" radiation damage. These iron particles were identified as α-Fe.

The microstructures for all three species implanted into sapphire at room temperature followed by annealing in Ar-4% H_2 for one hour at 1000°C were quite different from the as-implanted ones. None contained "black-spot damage" or interstitial defect clusters, but all contained evidence for small second phase particles. The annealing promoted the recombination of point defects and defect clusters and allowed the system to move toward the equilibrium phase compositions.

The lattice disorder as measured by RBS-C was greater for iron and boron implantation at room temperature than at 1000°C, but higher for nitrogen-implanted at

1000°C. The highest lattice disorder was produced by the iron implantation and is attributed to the higher density of displacements in the cascades. The optical absorption measurements indicate the presence of oxygen vacancies and defect clusters involving oxygen vacancies. The number of F-type centers was highest for boron-implanted at 1000° C.

The depth-dependent microstructures of the irradiated specimens, the energy deposited (elastic and inelastic) as a function of depth from the surface, the range of implanted species, and the defect production were modeled using the transport and range of ions in materials (TRIM) program. The results of the model showed that the ionizing component of the irradiation did not noticeably affect the microstructures. The ENSP ratios $\{(dE/dx)_e/(dE/dx)_n\}$ obtained from the TRIM simulations did not differ significantly for the three species through the range where significant displacements occurred. The range of boron-implanted into sapphire is more than that for nitrogen and iron. Iron has the shortest range. The density of vacancy (and interstitial) production is much higher for the Fe than for the B or N. The number of Al vacancies produced at all positions along the range is greater than the concentration of O vacancies.

CONTENTS

CHAPTER **Page No.**

1. INTRODUCTION……1

2. LITERATURE SURVEY……..5

2.1. An Overview of Ion Implantation..…….……5

2.1.1. *Introduction*……..5

2.1.2. *Energy Loss* ……..……...……5

2.1.3. *Ion Range and Distribution*.....……...8

2.1.4. *Channeling Effects of Ion Implantation*……...…..11

2.1.5. *Ion Implantation Damage*…….…….……...…..11

2.2. Defects in Sapphire (α-Al_2O_3)…….13

2.3. Previous Studies of Ion Implantation of Sapphire……19

2.4. The Role of Ionizing Radiation on the Microstructure of Ceramics..21

3. MATERIALS AND EXPERIMENTAL PROCEDURES …….……25

3.1. Material …….……...…….……25

3.2. Transmission Electron Microscopy …….…….…26

3.2.1. *Specimen preparation* ……...…26

3.2.2. *Microscopy* ……30

3.3. Rutherford Backscattering Spectroscopy…...……...……30

3.4. Optical Absorption…….……31

3.5. Analytical Techniques…… ……...33

3.5.1. *Nuclear Reaction Techniques* ……...…33

3.5.2. *X-ray Photoelectron Spectroscopy*...……34

3.5.3. *Auger Spectroscopy* …… .34

4. EXPERIMENTAL RESULTS……36

4.1. Boron Implanted Sapphire (α-Al_2O_3)..…….……36

4.1.1. *TRIM Calculations*……...……..36

4.1.2. *Transmission Electron Microscopy.* ..…..…….……..44

4.1.3. *Rutherford Backscattering Spectroscopy* ……...……...56
4.1.4. *Optical Absorption Measurements*……...…….……58
4.1.5. *X-Ray Diffraction* …… …….……60
4.1.6. *X-ray Photoelectron Spectroscopy* ……...……60
4.2. Nitrogen Implanted Sapphire (α-Al_2O_3)..…….……64
4.2.1. *TRIM Calculations*……...……..64
4.2.2. *Transmission Electron Microscopy* ……..…….……..64
4.2.3. *Rutherford Backscattering Spectroscopy* ……...……...76
4.2.4. *Optical Absorption Measurements*……...…….……88
4.2.5. *X-Ray Diffraction* …… …….……88
4.2.6. *X-ray Photoelectron Spectroscopy* ……...……88
4.3. Iron Implanted Sapphire (α-Al_2O_3)..……91
4.3.1. *TRIM Calculations*……...……..91
4.3.2. *Transmission Electron Microscopy* ……..…….…….100
4.3.3. *Rutherford Backscattering Spectroscopy* ...…….……119
4.3.4. *Optical Absorption Measurements*……...…125
4.3.5. *X-Ray Diffraction* ……. ……...…….……...127
5. DISCUSSION OF RESULTS……...…...……130
5.1. Role of Ionizing Energy to Displacement Energy Ratio…….……130
5.2. Deposited Damage Energy Density and Nature of Cascades……..…130
5.3. Microstructures of Samples Implanted at Room Temperature……136
5.4. Effect of Implantation Temperature……139
5.5. Post Implantation Annealing……141
6. CONCLUSIONS AND SUGGESTIONS FOR FUTURE WORK……143
6.1. Conclusions……....143
6.2. Suggestions for Future Work……145
LIST OF REFERENCES……..148
VITA..……154

LIST OF TABLES

TABLE **Page No.**

2.1: Threshold displacement energies in ceramics…..……..…12

2.2: Absorption and emission bands in sapphire……..……..…18

3.1: Ion species and implantation parameters..…….……26

3.2: The properties of sapphire (α-Al_2O_3)……27

4.1: Boron energy deposited per incident B ion as a function of depth in the target material……37

4.2: Vacancies produced per lattice ion (dpa) for a fluence of 1×10^{17} B^+/cm^2…….37

4.3: Nitrogen energy deposited per incident N ion as a function of depth in the target material……65

4.4: Vacancies produced per lattice ion (dpa) for a fluence of 3×10^{16} N^+/cm^2…….65

4.5: Iron energy deposited per incident Fe ion as a function of depth in the target material……93

4.6: Vacancies produced per lattice ion (dpa) for a fluence of 1×10^{17} Fe^+/cm^2……93

5.1: The ratio of implanted ion to Al lattice ion at the peak concentration……132

5.2: Energy transferred to "primary knock-ons" and projected ranges……...136

5.3: Summary of microstructures described in Chapter 4……...…142

LIST OF FIGURES

FIGURE **Page No.**

1.1: Optical transmission curves ……2

2.1: A schematic of ion collision with a target……6

2.2: An example of the rate of energy transfer for the two processes for a light ion entering a target……7

2.3: Schematic drawing showing (a) a two dimensional view of an ion's path in a target material, (b) a three dimensional presentation of the ion path into a solid…9

2.4: Gaussian distribution profile of concentration for an implant dose of 10^{15} ions/cm^2 over depth calculated for 500keV carbon ions implanted into silica.…10

2.5: The structure of sapphire. (a) Filling of 2/3 of the octahedral sites in the basal plane of sapphire (only one oxygen layer is shown), (b) Unit structure of Al_2O_3 showing only the planes and (c) Unit structure of Al_2O_3 showing only the cation sublattice. The A_i's (a_i's) are the hexagonal base vectors……..14

2.6: Loop density plotted as a function of the electronic to nuclear stopping power (ENSP) ratio in Al_2O_3 specimens irradiated at 650^oC with ions ranging from 1 MeV H to 3.6 MeV Fe ……..23

2.7: Loop size plotted as a function of the electronic to nuclear stopping power (ENSP) ratio in Al_2O_3 specimens irradiated at 650^oC with ions ranging from 1 MeV H to 3.6 MeV Fe……..…24

3.1: Schematic of TEM specimen preparation using FIB…….……29

3.2: A schematic diagram of a typical backscattering spectrometry system and analysis …….…….32

4.1: Boron ion trajectories……..…...38

4.2: The range of boron ion in sapphire as a function of depth……39

4.3: Collision events showing the plots of the number of vacancies produced per lattice ion (dpa)……40

4.4: Plot of electronic (ionizing) energy loses with the target depth……41

4.5: Plot of elastic (displacive) energy loses with the target depth……..…..42

4.6: Plot of energy (electronic and nuclear) loses as a function of the ion energy (the implant ion energy in this case is 150 keV)……..….43

4.7: Cross-sectioned micrograph of α Al_2O_3 specimen implanted with fluence of 1×10^{17} B/cm^2 (150 keV) at room temperature. (a) x 20K (b) x 80K (c) x 500K……..45

4.8: Cross-sectioned micrograph of α Al_2O_3 specimen implanted with fluence of 1×10^{17} B/cm^2 (150 keV) at 1000^{o}C. (a) x 20K (b) x 80K……...48

4.9: Selected area diffraction pattern of α Al_2O_3 specimen implanted with a fluence of 1×10^{17} B/cm^2 (150 keV) at room temperature. A, B, Cand D are from regions A, B, C and D respectively of Figure 4.7 (a)..….50

4.10: Selected area diffraction pattern of α Al_2O_3 specimen implanted with a fluence of 1×10^{17} B/cm^2 (150 keV) at 1000^{o}C. A, B, C and D are from regions A, B, C and D respectively of Figure 4.8(a)…..51

4.11: EDX spectrum from a cross section α Al_2O_3 specimen implanted with boron at room temperature. A and B are from regions B and D respectively of Figure 4.7(a)……..52

4.12: EDX spectrum from a cross section α Al_2O_3 specimen implanted with boron at 1000^{o}C. A and B are from regions B and D respectively of Figure 4.8 (a)……53

4.13: Cross-sectioned micrograph of α Al_2O_3 specimen implanted with a fluence of 1×10^{17} B/cm^2 (150 keV) at room temperature and annealed in Ar-4% H_2 at 1000^{o}C for 1 hour. (a) x 20K (b) x 80K…….54

4.14: RBS spectra for α–Al_2O_3 specimens implanted with boron. (a) at room temperature and (b) at 1000^{o}C...…….57

4.15: Optical absorption spectrum for α–Al_2O_3 specimen implanted with boron at room temperature and 1000^{o}C……...…….59

4.16: XRD spectrum for α–Al_2O_3 specimen implanted with boron at room temperature. ……..……61

4.17: XRD spectrum for α–Al_2O_3 specimen implanted with boron at 1000^{o}C……..62

4.18: XPS spectrum for $\alpha-Al_2O_3$ specimen implanted with boron at room temperature……63

4.19: Nitrogen ion trajectories……66

4.20: The range of nitrogen ion in sapphire as a function of depth……67

4.21: Collision events showing the plots of the number of vacancies produced per lattice ion (dpa)……....68

4.22: Plot of electronic (ionizing) energy loses with the target depth……69

4.23: Plot of elastic (displacive) energy loses with the target depth……...70

4.24: Plot of energy (electronic and nuclear) loses as a function of the nitrogen ion energy (the implant ion energy in this case is 150 keV)……..71

4.25: TEM cross-sectioned micrographs of α-Al_2O_3 specimen implanted with fluence of 3×10^{16} N/cm^2 (150 keV) at room temperature. (a) × 5K, (b) × 20K, (b) ×250K (Bright field image) and (d) ×250K (Dark field image)……..……72

4.26: Cross-sectioned micrographs of $\alpha-Al_2O_3$ specimen implanted with fluence of 3×10^{16} N/cm^2 (150 keV) at 1000^{o}C. (a) x 10K, (b) x 20K and (c) 250 K……77

4.27: Selected area diffraction pattern of $\alpha-Al_2O_3$ specimen implanted with a fluence of 3×10^{16} N/cm^2 (150 keV) at room temperature. A, B, C and D are from regions A, B, C and D respectively of Figure 4.25(b)…80

4.28: Selected area diffraction pattern of $\alpha-Al_2O_3$ specimen implanted with a fluence of 3×10^{16} N/cm^2 (150 keV) at 1000^{o}C. A and B are from regions A and B respectively of Figure 4.26 (b)……..81

4.29: EDX spectra from a cross section $\alpha-Al_2O_3$ specimen implanted with nitrogen at room temperature. A and B are from B and D regions respectively of Figure 4.25 (b)……..82

4.30: EDX spectra from a cross-section $\alpha-Al_2O_3$ specimen implanted with nitrogen at 1000^{o}C. A and B are from A and D regions respectively of Figure 4.26 (b)…….……..83

4.31: Cross-sectioned micrographs of $\alpha-Al_2O_3$ specimen implanted with a fluence of 3×10^{16} N/cm^2 (150 keV) at room temperature and annealed

in Ar-4% H_2 at 1000°C for 1 hour. (a) x 20K, (b) x 40K and (c) x 80K……...84

4.32: RBS spectrum α–Al_2O_3 specimen implanted with nitrogen. (a) At room temperature and (b) at 1000°C……...87

4.33: Optical absorption spectrum for α Al_2O_3 specimen implanted with nitrogen at room temperature and 1000°C……...…..89

4.34: XRD spectrum for α–Al_2O_3 specimen implanted with nitrogen at room temperature……90

4.35: XPS spectrum for α–Al_2O_3 specimen implanted with boron at 1000°C……...92

4.36: Iron ion trajectories……....94

4.37: The range of iron ion in sapphire as a function of depth……...95

4.38: Iron collision events showing the plots of the number of vacancies produced per lattice ion (dpa)……96

4.39: Plot of iron electronic (ionizing) energy loses with the target depth…….……97

4.40: Plot of elastic (displacement) energy loses with the target depth……..……98

4.41: Plot of energy (electronic and nuclear) loses as a function of the iron ion energy (the implant ion energy in this case is 150 keV)……..…...…….99

4.42: TEM cross-sectioned micrographs of α–Al_2O_3 specimen implanted with a fluence of 1×10^{17} Fe/cm^2 (150 keV) at room temperature. (a) × 20K, (b) ×60 K, (c) × 80K and (d) ×400K…….……101

4.43: TEM plan view micrograph of α–Al_2O_3 specimen implanted with a fluence of 1×10^{17} Fe/cm^2 (150 keV) at room temperature. (× 250K)…….…….105

4.44: Cross-sectioned micrographs of α–Al_2O_3 specimen implanted with a fluence of 1×10^{17} Fe/cm^2 (150 keV) at 1000°C. (a) x 20K, (b) x 80K, and (c) 250 K…106

4.45: TEM plan view micrographs of α–Al_2O_3 specimen implanted with a fluence of 1×10^{17} Fe/cm^2 (150 keV) at 1000°C. (a) 60 K, (c) x 80K (bright field image), (c) x 80K (dark field image), (d) (d) × 250K (bright field image) and (e) × 250K (dark field image)……..109

4.46: SAD taken from a cross-section α–Al_2O_3 specimen implanted with iron at room temperature. A, B, C and D are from regions A, B, C and D respectively of Figure 4.42(a)……..112

4.47: SAD taken from a cross-section $\alpha-Al_2O_3$ specimen implanted with iron at 1000°C. A, B, C and D are from regions A, B, C and D respectively of Figure 4.44 (a)……...……..113

4.48: SAD taken from plan view $\alpha-Al_2O_3$ specimen implanted with iron at 1000°C. (a) is taken from the matrix region and (b) from the large particle of Figure 4.45(a)……...114

4.49: EDX spectra from a cross-section $\alpha-Al_2O_3$ specimen implanted with iron at room temperature. (a), (b) and (c) are from regions A, B and D respectively of Figure 4.42 (a)……115

4.50: EDX spectra from a cross-section $\alpha-Al_2O_3$ specimen implanted with iron at 1000°C. (a), (b) and (c) are from B, C and D regions respectively of Figure 4.44(a)……..117

4.51: Cross-sectioned micrograph of $\alpha-Al_2O_3$ specimen implanted with a fluence of 1×10^{17} Fe/cm^2 (150 keV) at room temperature and annealed in Ar-4% H_2 at 1000°C for 1 hour (x 250K)…….120

4.52: Plan view micrographs of α Al_2O_3 specimen implanted with a fluence of 1×10^{17} Fe/cm^2 (150 keV) at room temperature and annealed in Ar-4% H_2 at 1000°C for 1 hour. (a) x 250K-bright field image, (b) x 250K-dark field image, (c) x 450K-bright field image and (d) x 450K-dark field image……121

4.53: RBS spectra for $\alpha-Al_2O_3$ specimen implanted with iron. (a) At room temperature, (b) at 1000°C and (c) for the beam parallel to $<02\bar{2}1>$ …..…….123

4.54: Optical absorption spectra for $\alpha-Al_2O_3$ specimen implanted with iron at room temperature and 1000°C……..…126

4.55: XRD spectra for $\alpha-Al_2O_3$ specimen implanted with iron at 1000°C. (a) Backside of the specimen (not implanted) and (b) Implanted surface……...128

5.1: TRIM simulation of 10 B ions (150 keV) bombarding sapphire. The red lines indicate the path of the B ions, the black squares show the position of the stopped B ions, the dark blue points indicate stopped Al ions; and the dark green points indicate stopped O ions. (a) ion trajectories,

(b) projection of ion paths and displaced ions onto the X-Y plane and (c) transverse projection showing the spreading of the ions and displacements ….133

5.2: TRIM simulation of 10 N ions (150 keV) bombarding sapphire. The red lines indicate the path of the N ions, the black squares show the position of the stopped N ions, the dark blue points indicate stopped Al ions; and the dark green points indicate stopped O ions. (a) ion trajectories, (b) projection of ion paths and displaced ions onto the X-Y plane and (c) transverse projection showing the spreading of the ions and displacements…...134

5.3: TRIM simulation of 5 Fe ions (150 keV) bombarding sapphire. The red lines indicate the path of the Fe ions, the black squares show the position of the stopped Fe ions, the dark blue points indicate stopped Al ions; and the dark green points indicate stopped O ions. (a) ion trajectories, (b) projection of ion paths and displaced ions onto the X-Y plane and (c) transverse projection showing the spreading of the ions and displacements…...135

CHAPTER 1

INTRODUCTION

The science of ion implantation technology is concerned with the modification of the near surface properties of a wide range of materials. The technique provides excellent control of implantation parameters such as dose range, energy of ion species and implantation temperature. Researchers [1-3] in the field have investigated the influence of ion implantation on the near surface properties of insulating materials.

Ion beam interactions with ceramics are more complex than with metals or elemental semiconductors. Ceramics consist of two or more chemical species that are distributed in an ordered manner over at least two sublattices. Upon interaction of an accelerated beam of ions having energy ranging from tens to hundreds kilo-electron-volt with a solid, the energy is transformed by two fundamental processes: the electronic excitation (ionization) and the nuclear collision (elastic) events. The rate of energy transfer for each process is a function of the mass and charge of the incoming ions, the target material and the energy. The nuclear collision displaces lattice ions and can result in damage cascades. Previous studies [4-14] on metals and ceramics have shown that ionizing radiation can influence radiation damage, often in very subtle ways. The relative importance of the two processes (elastic and electronic) is dependent on the choice of the ion mass and energy.

Sapphire (single crystal Al_2O_3) has a unique capability to transmit in a broad range of wavelength spanning from 0.25 to 5 microns wavelength (Figure 1.1) [15]. This high optical transmission from the vacuum ultra violet to the infrared spectrum coupled with its good mechanical strength leads to its application as a window material for infrared detectors such as in satellites, missiles, medical equipment, space technology, instruments and lasers.

During the “Star Wars” Program (Strategic Defense Initiative), sapphire infrared windows were a key component for the High Endoatmosphere Defense Interceptor (HEDI). The windows were required to withstand very high launch stresses and to protect the infrared sensors from damage from raindrops, dust and other debris at speeds

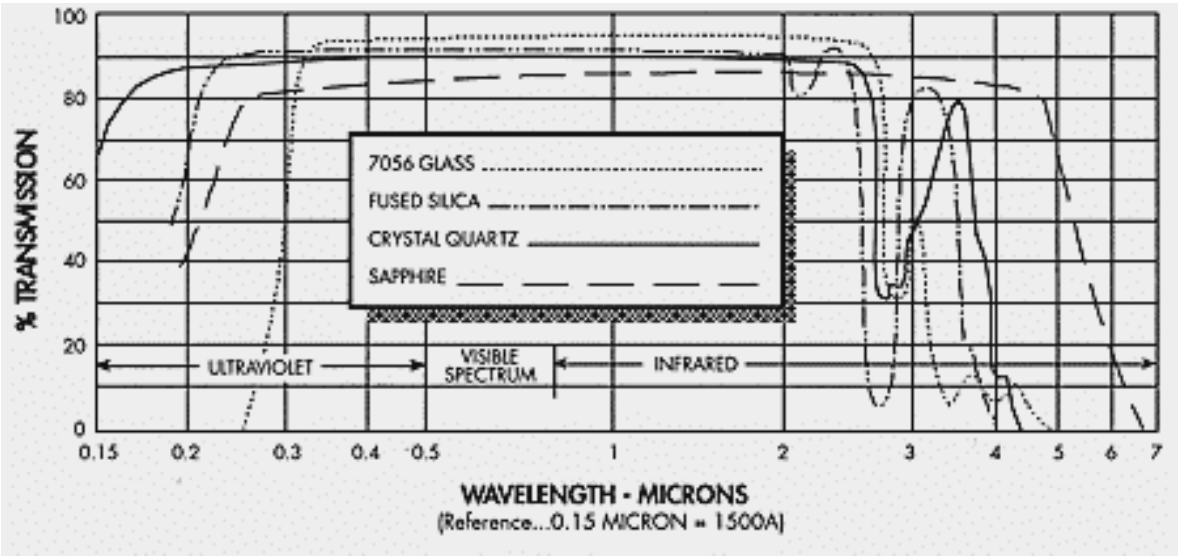


Figure 1.1: Optical transmission curves [Adapted from reference 15].

as high as Mach 15. As part of that program, McHargue and Snyder [16] demonstrated that an improved polishing technique followed by implantation of chromium greatly increased the resistance to fracture. The design stress for high reliability, i.e., probability of failure less than 0.1%, could be increased by a factor of 100 over that allowed for conventional fabrication processes. The transmission was decreased by 1% in the infrared region of interest. The increase in fracture strength was attributed to the elimination of surface flaws by the polishing and the introduction of a high residual compressive stress by the implantation. The residual compressive stress was measured to be greater than 1 GPa [17,18].

After the Gulf War, a new missile defense program was initiated. The Theater High Area Defense (THAD) system also requires a window to protect the infrared detectors in a near-earth battle space. Again, sapphire is the material of choice, but its mechanical reliability was defined as one of three critical questions in the performance of this system. The Epion Corporation, Billerica, MA, explored the effects of implantation of several ions species on the infrared transmission and mechanical properties of sapphire. It was found that implantation of B, N or Fe at both room temperature and 1000^{o}C gave improvements similar to those for Cr-implantation at room temperature [19]. This observation of significant strengthening by implantation at 1000^{o}C suggests that some factor other than residual stress is important. However, no microstructural characterization was performed as part of those studies.

In another series of studies initiated at the Oak Ridge National Laboratory and continued at University of Tennessee, it was found that implantation of many cation species into sapphire often produce unique structures consisting of nanometer size metallic particles distributed in the sapphire matrix. The size, shape and distribution of such nanoclusters could be systematically altered by post-implantation annealing [20,21].

The extremely low solubility of sapphire for impurities makes it an ideal host for exploring the use of ion implantation to prepare nanostructures. An understanding of the microstructural changes that occur during irradiation is of utmost importance for the development of models to predict the structure and properties and to extend the use of such structures in high technology areas.

In the current study, specimens of sapphire (α-Al_2O_3) were implanted with boron, nitrogen or iron at room temperature (RT) and 1000^{o}C and examined by several experimental techniques:

a. Transmission electron microscopy to characterize the microstructures;
b. Rutherford backscattering-ion channeling to measure lattice disorder in the Al-sublattice and to determine the distribution of the implanted species;
c. Optical absorption measurements to characterize the defect structure of the O-sublattice;
d. Selected area diffraction (SAD) and x-ray diffraction (XRD) to determine the crystal structure of the micro-constituents;
e. X-ray photoelectron spectroscopy (XPS) also to determine the chemical nature of the implanted species.
f. TRIM simulations to model the deposition of elastic (displacement) and inelastic (ionizing or electronic) energy as a function of depth from the surface, range of implanted species, and defect production.

The results of the experiments were analyzed with respect to the effects of:

- Implantation temperature;
- Deposited energy density;
- Ratio of ionizing energy to displacement energy in the range typical encountered during ion implantation;
- Density of implanted species and cascade overlap (related to mass of implanted species).

The major objectives of the research are to:

1. Study systematically the effects of ion implantation temperature and ionizing radiation on the microstructure of sapphire implanted with boron, nitrogen and iron.

2. Characterize the defects produced and develop an understanding of the defect mechanism responsible for the microstructural changes and/or properties at room temperature and at 1000^{o}C for the boron, nitrogen and iron implanted sapphire.

CHAPTER 2

LITERATURE SURVEY

2.1. An Overview of Ion Implantation

2.1.1. *Introduction*

When ions interact with a solid, they lose kinetic energy to the target atoms; this energy loss is complex and involves many kinds of interactions between the projectile ion, target nuclei and target electrons. The bombardment of a material surface by energetic beam of ions may cause changes in the microstructure and composition of the near surface region and in the properties of the material. This near surface influence is due to the fact that the implanted ions only penetrate a few microns deep into the material; the depth depends on the incident ion energy and ion mass for a given substrate material. As the ions hit the target material, they interact with the atoms of the material, which slow them down and perturb their trajectory. Large numbers of lattice defects are created and impurities or alloying species are introduced. A schematic of ion collision with a target is shown in Figure 2.1 [22].

2.1.2. *Energy Loss*

The two main processes of energy transfer are nuclear collision (elastic) and electronic (inelastic collision) excitation. The rate of energy transfer for each process is a function of the mass and charge of the incoming ions, the target material and the energy. When the velocity, v, of the projectile ion, is significantly lower than the Bohr velocity, v_o, of the atomic electrons of the target, elastic collisions with the target nuclei (nuclear energy loss) dominate [23]. The nuclear energy loss decreases as 1/E, as the ion velocity increases, and soon, the inelastic collisions (electronic energy loss) with the atomic electrons prevail as the main interaction [23]. The total energy loss is therefore the sum of the nuclear and electronic energy losses. Figure 2.2 [24] shows an example of the rate of energy transfer for the two processes for a light ion entering a target. The theoretical framework of energy loss originates from the works of Bohr [25], and major theoretical

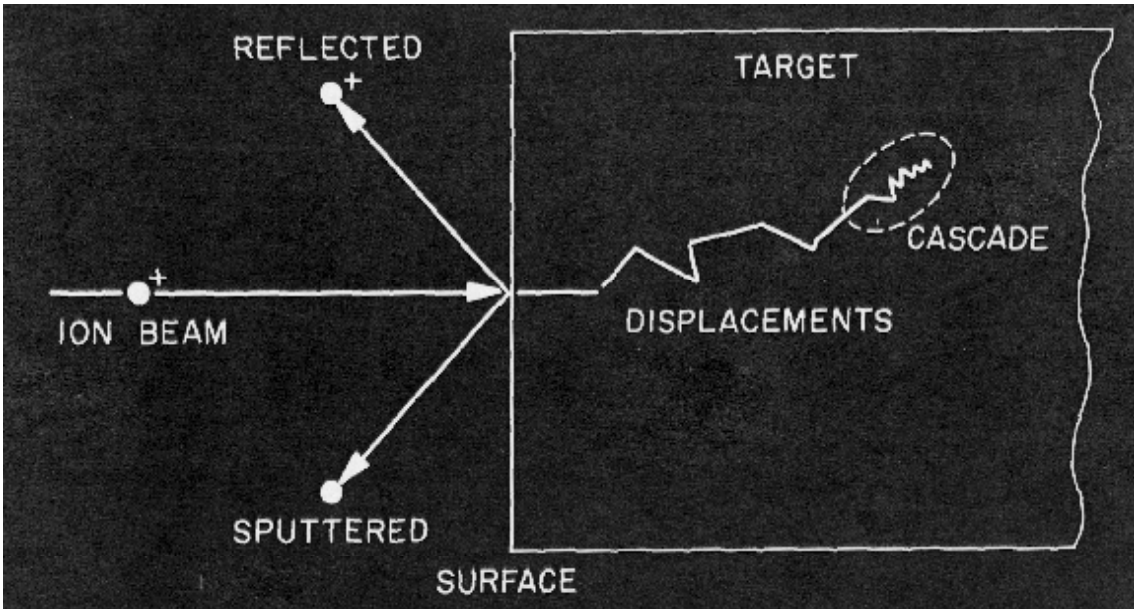


Figure 2.1: A schematic of ion collision with a target [Adapted from reference 22].

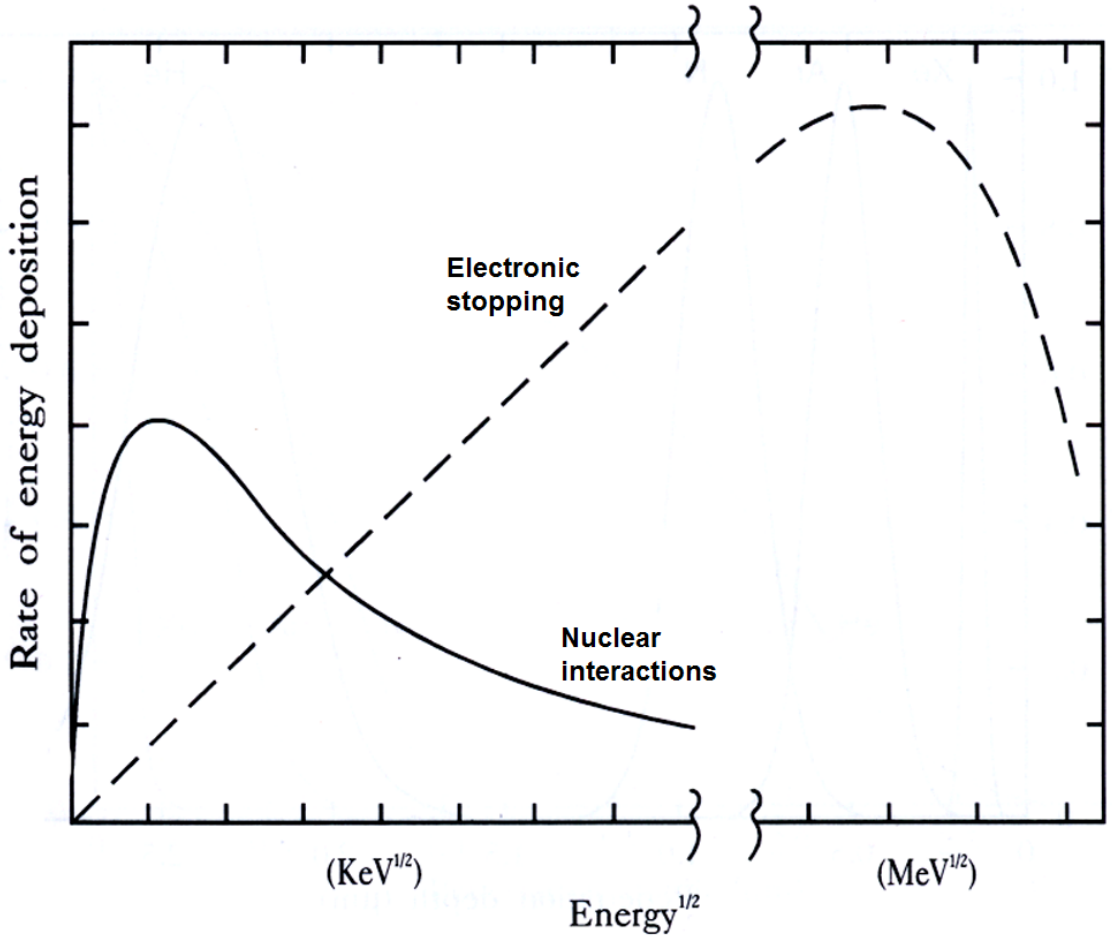


Figure 2.2: An example of the rate of energy transfer for the two processes for a light ion entering a target [24].

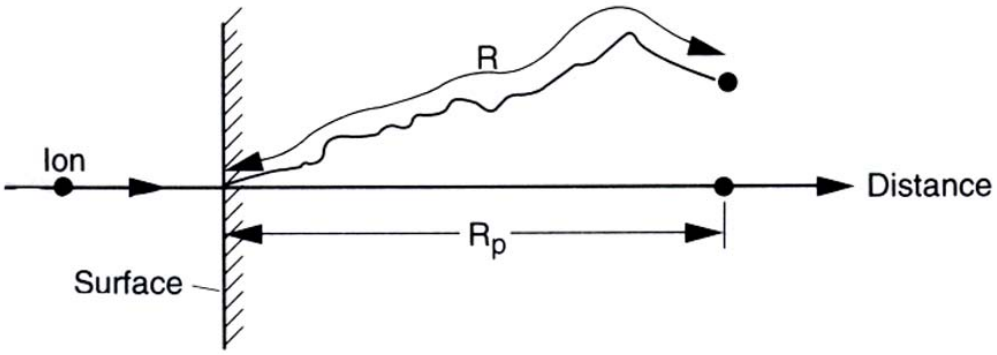
advances were accomplished by the works of Sigmund [26] and Ziegler et al [27] among others.

2.1.3. *Ion Range and Distribution*

The depth (range) distribution of the implanted ions is one of the most important considerations in the description of ion implantation into a solid. When ions are implanted into a material, they lose kinetic energy to the collided nuclei and electrons of the material, penetrate to a certain depth in the near surface region and come to rest. The ions do not travel in a straight path to its resting place due to collisions with target atoms. Shown in Figure 2.3, is a two dimensional schematic view of an ion's path in a target material [28] and a three dimensional presentation of the ion path into a solid [29]. The actual distance traveled by the ion is called the range, R. R_p is the projected range, and R_r, the radial range is the distance from the surface at the point of entrance, (000), to the point where the projectile comes to rest, (x_s, y_s, z_s). The spreading range, R_s, is the distance between the point where the projectile enters the surface and the projection of the projectile's final resting place onto the surface plane. The transverse projected range, R^t_p, is the vector connecting the radial range and the projected range. If the projectile is incident normal to the target surface, the range spreading will be equal to the transverse projected range.

In studying the range distribution of the implanted ions, two parameters are of great concern, the projected range, R_p, and the straggle in the projected range, ΔR_p. We know that the stopping of ion in a solid is a random process; hence, ions of the same type, having the same energy may not have the same range. It has been observed that the implanted ions are distributed beneath the surface of the target material in a profile that is approximately Gaussian. This is illustrated in Figure 2.4 [24]. Projected range is defined as the mean depth from the target surface at which the ion comes to a halt; while straggling is the width of the ion range distribution [23]. The range distribution calculation is viewed as a transport problem describing the motion of the ions in the solid until they come to rest. Analytical and simulation calculations approach have been developed by the efforts of Lindhard et al. [30] and Ziegler et al. [27], among others.

(a)



(b)

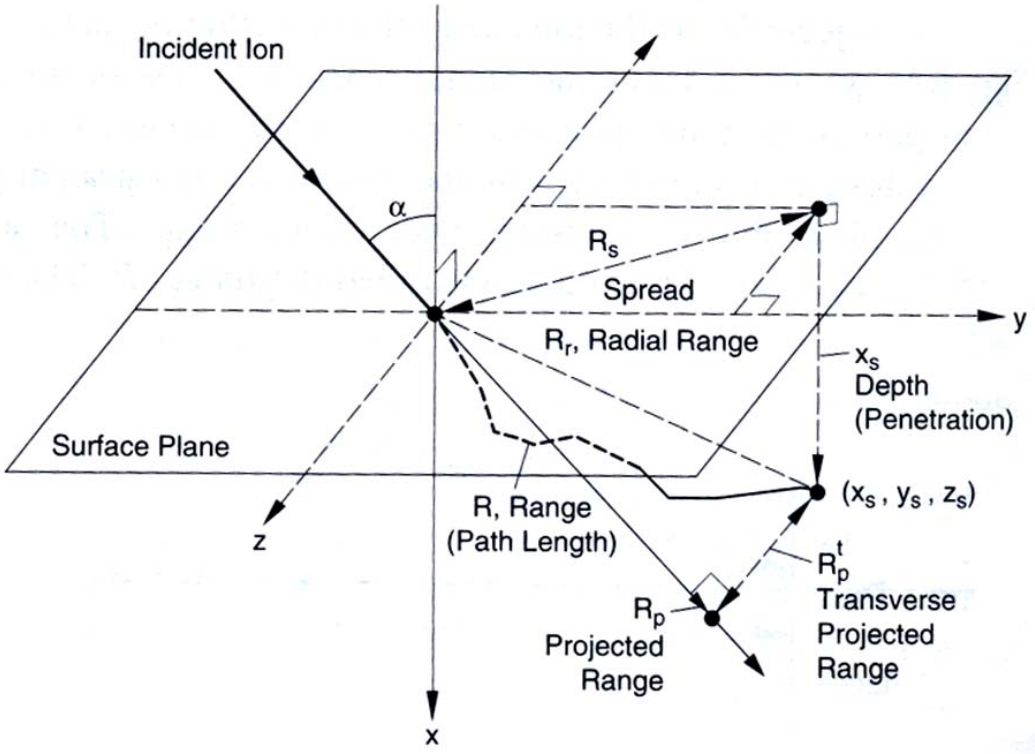


Figure 2.3: Schematic drawing showing (a) a two dimensional view of an ion's path in a target material (28), (b) a three dimensional presentation of the ion path into a solid [29].

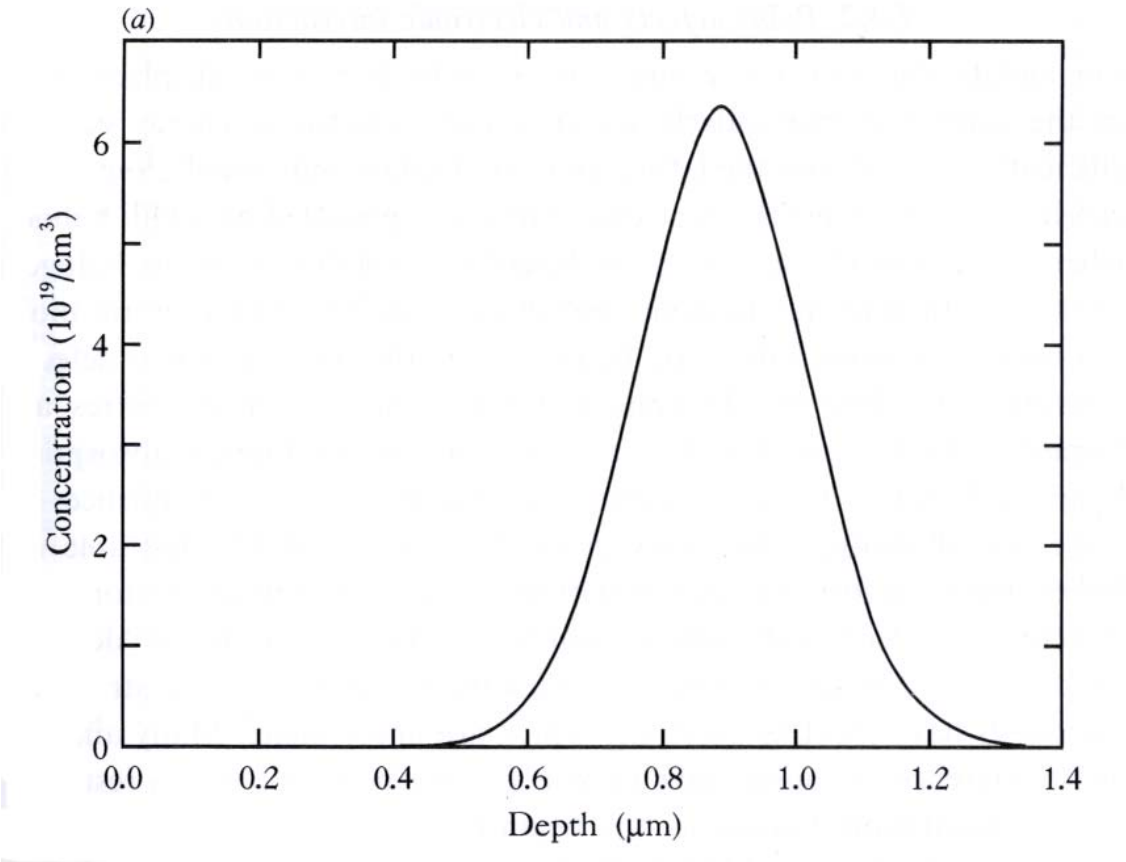


Figure 2.4: Gaussian distribution profile of concentration for an implant dose of 10^{15} ions/cm^2 over depth calculated for 500 keV carbon ions implanted into silica [24].

A powerful computer program "SRIM/TRIM" [http://www.srim.org] is now available for calculating the projected range, spatial distribution of the implanted ions, straggling, etc.

2.1.4. *Channeling Effect of Ion implantation*

Channeling or channeling effect is the influence on ion penetration due to crystal orientation. Lattice planes of crystalline structures act like channels in which the implanted ions can travel without nuclear interactions (collisions); as a result, they have lower rate of energy loss and a greater range than the non-channeled ions. This effect is often avoided. Channeling depends mostly on the critical angle of approach and hence the target orientation, substrate temperature, surface preparation, and amorphization.

There is a critical angle (typically less than 5^{o}) of the crystal axes or planes within which the incident ion must be aligned for channeling to be effective. Therefore, to minimize channeling effects during ion implantation, the ion beam is oriented approximately 7^{o} to 10^{o} from any major crystallographic axis. Also, as the substrate temperature increases, the lattice atoms acquire more energy and may be scattered out of the channels. With amorphization of the substrate, crystalline structures are destroyed leading to eradication of channels and hence, channeling effects are totally prevented. Detailed discussion on channeling effects during ion implantation can be found in the review by Simonton and Tasch [31].

2.1.5. *Ion Implantation Damage*

The bombardment of a crystal with an energetic heavy ion produces regions of lattice disorder. This region may see the formation of amorphous layers. Of importance is the range of damage in the substrate material. The damage range is not equal to the implanted ion range; in fact, the implanted ion range is greater than the damage range. However, damage defects are often detected at distances 2 to 3 times the calculated damage range. The reasons for this extended damage zone are not entirely clear. It may be the result of stresses introduced by the presence of implanted ions and the defects generated. The damage range occurs near the surface of the target, as the damage occurs not only from primary ion-atom collisions but also from the secondary collisions between

atoms of the target. Sufficient energy may be transferred from the ion to displace an atom from its lattice site. The displaced lattice atoms by the incident ions are called primary knock-on atoms (PKAs). When the PKAs displace other atoms, these other atoms are called secondary knock-on atoms, resulting in a cascade of atomic collisions leading to vacancies and interstitial atoms, hence, a heavily damaged layer may be formed. The range (depth) distribution and the total amount of disorder is a function of temperature, total ion dose, energy, ion species, and channeling effects.

Radiation damage arises from the fact that when an energetic ion or a recoiling target atom hits a lattice atom, a minimum amount of transferred kinetic energy is required to displace the lattice atom; this energy is known as the threshold displacement energy, E_d. The atom displaced leaves a vacancy and occupies an interstitial site in the lattice to form a Frenkel defect. Cluster type complex defects may be produced due to cascade complex interactions. Ceramics have multiple sublattices and E_d for each sublattice must be measured separately. Table 2.1 gives the values of the recommended threshold displacement energy [32].

Table 2.1: Threshold displacement energies in ceramics [32].

Material	**Threshold displacement energy (eV)**	
Al_2O_3	E_d (Al) ≈ 20	E_d (O) = 50
MgO	E_d (Mg) = 55	E_d (O) = 55
$MgAl_2O_4$		E_d (O) = 60
ZnO	E_d (Zn) ≈ 50	E_d (O) = 55
BeO	E_d (Be) ≈ 25	E_d (O) = 70
UO_2	E_d (U) = 40	E_d (O) = 20
SiC	E_d (Si) ≈ 40	E_d (C) = 20
Graphite	E_d (C) = 30	
Diamond	E_d (C) = 40	

2.2. Defects in Sapphire (α-Al_2O_3)

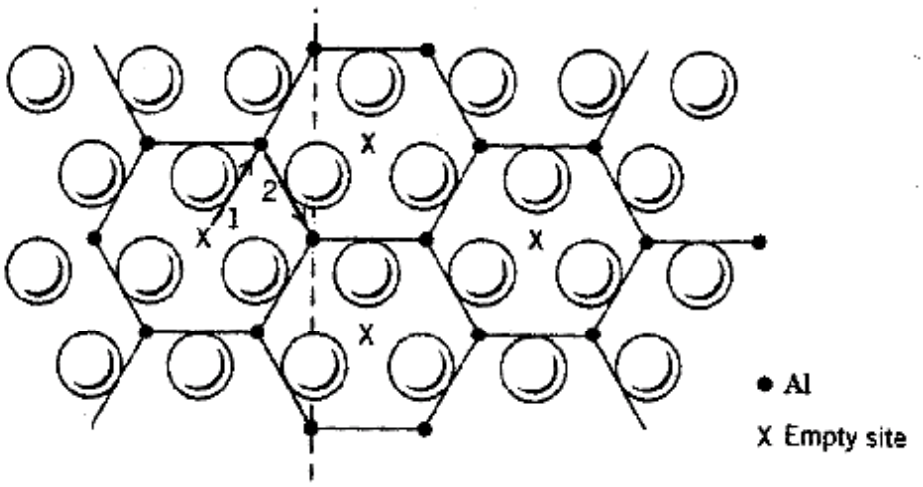
Generally, ceramics consist of two or more chemical species that are distributed in an ordered manner over at least two sublattices. When an ion is bombarded onto a target, the displaced atoms of the target during elastic collisions are not likely to come to rest at the lattice sites of the other type. Different amounts of energy are required to displace the different atom species from their lattice sites as noted in section 2.1.5. The chemical bonding types for ceramics range from ionic to covalent to metallic-like.

In this study, the ceramic of interest, sapphire (α-Al_2O_3), is rhombohedral, and belongs to the space group $R\bar{3}c$. The O^{2-} anions are approximately hexagonal close packed. The Al^{3+} cations are ordered, occupying 2/3 of the available octahedral sites due to 2:3 (cation:anion) stoichiometry of this compound. The crystal structure of sapphire and the octahedral sites between two layers of close packed oxygen ions are shown in Figure 2.5. The structure of sapphire may be described on the basis of the close packing, but there are significant deviations from the ideal close-packed structure as a result of the electrostatic interactions between the ions. The Al^{3+} ions and the vacant octahedral sites are arranged to achieve maximum separation of like charges and minimum separation of unlike charges, consistent with the necessary bonding between aluminum and oxygen, while maintaining overall electrical neutrality. The bonding is mainly ionic with some covalent character.

Many oxides may exhibit large deviation from stoichiometry, but in α-Al_2O_3, any deviation from stoichiometry is too small to be detected [33]. Therefore, while it is possible to substitute 3+ impurities for Al^{3+}, impurities cannot be added without creating charge-compensation defects. The vacant octahedral sites are structural vacancies and are ordered to maintain the electrostatic forces within the crystal.

The principal point defects experimentally observed in α-Al_2O_3 are oxygen vacancies containing trapped electrons: the F^+-center (an oxygen vacancy containing one electron) and the F-center (an oxygen vacancy containing two electrons). Oxygen divacancy centers are also observed, and there is evidence for Al^{3+} interstitial-type defects in the form of Al pairs. No evidence for aluminum vacancies exists [33].

(a)



(b)

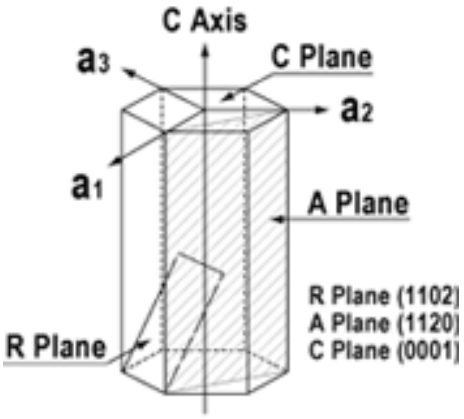


Figure 2.5: The structure of sapphire. (a) Filling of 2/3 of the octahedral sites in the basal plane of sapphire (only one oxygen layer is shown), (b) unit structure of Al_2O_3 showing only the planes and (c) unit structure of Al_2O_3 showing only the cation sublattice. The A_i's (a_i's) are the hexagonal base vectors [34].

(c)

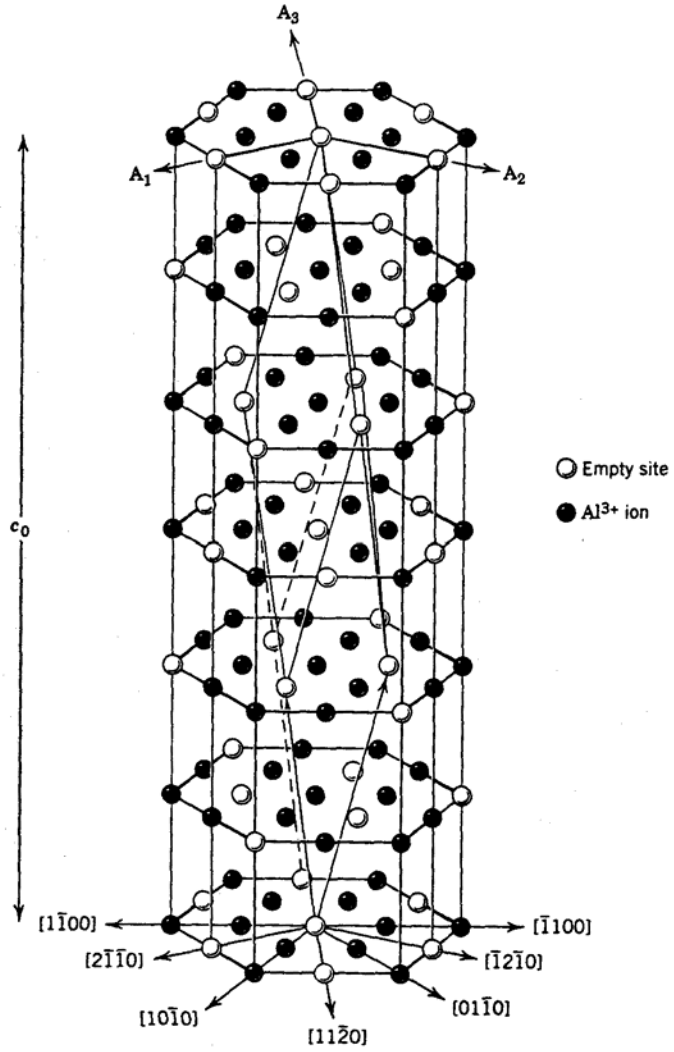


Figure 2.5 continued.

Dislocations are also observed, as are impurity-defect complexes.

Defects energies for α-Al_2O_3 doped with Mg^{2+} and Ti^{4+} have been calculated by Catlow et al. [35] using atomic potentials that are essentially ionic and exclusively two bodies. For dopants added in absence of oxygen interchange with the atmosphere, the calculations indicate that defect clustering will dominate at temperature below 1500^{o}K for tetravalent impurities (Ti^{4+}) at concentrations of 1 ppm and higher. There are two possible configurations - substitutional with cation vacancies or O^{2}-interstitial clusters. The substitutional-vacancy cluster that is electro-neutral and energetically favored consists of three Ti^{4+} substitutionals in nearest-neighbor cation sites with respect to one cation (Al^{3+}) vacancy. The predicted dopant-interstitial cluster consists of two Ti^{4+} substitutionals at nearest-neighbor sites to one O^{2-} interstitial. The effective charge of O^{2-} interstitials is neutralized by the Ti^{4+} substitutionals in adjacent sites along the c-axis. The calculated binding energies favor the substitutional-vacancy configuration.

In divalent-doped α-Al_2O_3 (Mg^{2+}), two configurations are again energetically favored - substitutional vacancy and "self compensation". Both configurations involve clustering. The vacancy mode of compensation consists of a cluster of two substitutionals occupying nearest-neighbor sites to the vacancy. The self-compensating model has the charge of a Mg^{2+} interstitial neutralized by two Mg^{2+} substitutionals lying above and below the interstitial site along the c-axis. Again, the binding energy results favor the vacancy-substitutional cluster.

Jacobs and Kotomin [36] used a procedure similar to that of Catlow et al. [35] to calculate the defect properties of corundum (α-Al_2O_3 or sapphire) doped with divalent Mg, Mn, Fe, Co, or Ni ions. These calculations also indicate that defect-impurity clusters are favored in order to retain local charge neutrality. The self-compensation model of two substitutional M^{2+} ions on cation sites normally occupied by Al^{3+} separated by an M^{2+} interstitial on the vacant octahedral site that separates the two M sites is preferred for Fe, Co, and Ni. The cluster of two M^{2+} with an O^{2-} vacancy is slightly preferred for Mg and Mn. These investigators did not calculate the binding energies of the clusters.

It is clear that both theoretical simulations confirm the importance of impurity defect clusters to maintain electrical (charge) neutrality. Strains introduced in the

corundum lattice contribute to the orientation of the clusters.

Kotomin and co-workers [37] extended the study cited above to include impurity-related centers (F_{Mg}) and intrinsic dimer centers. The impurity center observed in Mg doped α-Al_2O_3 [38] was considered as the prototype for impurity centers. There are two possible configurations: $F_{Mg} = Mg^{2+} + F^{+}$ with the Mg^{2+} substituting for Al^{3+} on a lattice site and $F^{-}_{Mg} = Mg^{2+} + F$. The first is neutral but the second has a negative charge. The calculated absorption and emission spectra for the F_{Mg} center agree with the experimental values better than those for the F^{-}_{Mg} center. The calculated values for the F_{Mg} center indicate three absorption bands {243nm (5.1eV); 234nm (5.3eV); 210nm (5.9eV)} and an emission band at 295nm (4.2eV). The experimentally observed absorption peaks appear at slightly higher wavelengths than the calculated values. The important conclusion is that impurity-defect clusters containing oxygen vacancies give rise to absorption and emission bands in the optical measurements.

Crawford [39] notes that the optical transformation of F^{+} to F centers in α-Al_2O_3 has been observed. Kotmin, Popov and Stashans [40] used semi-empirical calculations of the atomistic and electronic structure of F^{+} and F -centers in corundum to explain this photo stimulated conversion. On this basis irradiation conditions that contain a strong ionizing component should favor a higher concentration of F centers compared to F^{+} centers.

As indicated, the optical properties of sapphire are sensitive to the presence of point defects and defects complexes in the oxygen sublattice. The identity of the principal absorption and emission bands given by Evans and Stapelbroek [41] and Chen and Abraham [42] come from analyses of crystals subjected to neutron or electron irradiation and are tabulated in Table 2.2. Crawford [39] noted that there is a gap to bridge between the low fast-neutron exposures and the heavy ion-implantation damage in interpreting optical data. Not only are the damage characteristics (density of cascades and cascade overlap) different, but the presence of the implanted species must be considered.

Ren [21] measured both the optical absorption and luminescence spectra for specimens of sapphire crystals after the standard 5 day anneal at 1400 – 1500^{o}C in

Table 2.2: Absorption and emission bands in sapphire [27,28].

Defect Center	Absorption nm (eV)	Emission nm (eV)	Number of Oxygen Vacancies	Number of Trapped Electrons
F	205 (6.06)	420 (3.0)	1	2
F^+	258 (4.8) 225 (5.5) 203 (6.1)	325 (3.8)	1	1
F_2	300 (4.1)	322 (3.85)	2	4
F^+_2	355 (3.5)	379 (3.27)	2	3
F^{2+}_2	455 (2.7)	550 (2.25)	2	2

flowing oxygen and after implantation with 4×10^{16} Fe/cm^2 and 2×10^{17} Fe/cm^2 at room temperature. The luminescence measurements indicated that both F and F^+ -centers were present in the implanted samples. The ratio of the intensities of the luminescence bands suggest that the implantation damage increased the number of F^+ centers relative to the number of F centers. Ren's samples exhibited broad absorption bands in the region of about 230 to 400 nm that she attributed it to Mie scattering from metallic iron nanoclusters.

The observations of Ren for as-implanted specimens are consistent with the study by Dalal et al. [43] that found F^+ - centers to be favored at the expense of F – centers in the regions of high defect density generation by ions having massed greater than the light gases, e.g., hydrogen or helium. These investigators found that F- center production was favored for implantation of lighter ions that did not produce dense cascades along their tracks. They also observed additional absorption peaks that they attributed to clusters of defects involving the oxygen sublattice.

The simulations of TRIM give information on the production of vacancies in each sublattice; however, many vacancies recombine with an interstitial of the same kind during the "cool-down" period (< 10^{-10} sec) of the cascade. It is the surviving defects that are of interest.

Attempts to determine the surviving fraction of defects in the anion (oxygen) sublattice by comparing the number of F- and F^+ - centers present in ion implanted sapphire with the number obtained by calculations have been reported by Agnew [44] and Pell [45]. Agnew's results for implantations and measurements made at room temperature indicate surviving fractions of 0.08 to 0.17 for implantation of B, N, Ar and Kr for fluences of 1 to 5×10^{12} ions/cm^2. The low fluences were used in an attempt to avoid overlap of the paths of the displaced lattice ions. The measurements did not include surviving defects that may have formed clusters. It is important to note that the surviving fraction was higher for B than the other species.

The nature of the residual damage resulting from displacements in the Al sublattice is poorly characterized and understood. Crawford [39] noted that any enhancement of the V- type absorption band expected to be associated with cation vacancies has not been observed. Pells and co-workers [46,47,48] observed features in sapphire subjected to electron irradiation at 600^{o}C and above in the electron microscope. The features were suggested to be stoichiometric interstitial dislocation loops and Al colloidal particles. The loops were composed of aluminum and oxygen interstitial ions in the ratio of 2:3. It was proposed that the features identified as Al colloids arose from the precipitation of Al interstitials.

Hunt and Hamikian [49] reported the presence of 12 – 13 nm crystals of Al containing a slight amount of yttrium in the amorphous region of a sample of sapphire implanted with 5×10^{16} Y/cm^2 (150 keV) at room temperature. No attempt was made to ascertain the disposition of the vacancies left in the Al sublattice.

2.3. Previous Studies of Ion Implantation of Sapphire

There have been many studies of ion implantation into sapphire since 1980. Most of these studies used Rutherford backscattering-ion channeling to characterize the disorder introduced and the distribution of the implanted species as a function of distance from the free surface. For a review of many of these studies, see reference [3]. There have been few detailed microstructural studies and few studies involving temperatures

above room temperature. This section will be a limited review of studies involving the ion species and implantation conditions used in the current investigation.

Studies on implantation of very light ions have been restricted to implantation of hydrogen and helium. There appears to be no report of implantation of boron. Implantation of inert gases generally leads to formation of bubbles, blisters and exfoliation of the surface layers [50,51].

Hioki et al. [52] reported that blisters formed on the surfaces of samples implanted with 2×10^{17} N^+/cm^2 (400 keV) at room temperature. Soumoy et al. [53] detected a buried amorphous layer in sample implanted with 7×10^{15} N^+/cm^2 (50 keV) at room temperature. Cross-section TEM examination implanted with 2×10^{17} N^+/cm^2 revealed a damaged region that contained bubbles on each side of the amorphous region. Low energy electron-induced X-ray spectroscopy indicated that the nitrogen remained in the form of a gas for fluences as high as 8×10^{17} N^+/cm^2 (50 keV).

A comprehensive study of iron implanted into sapphire at room temperature and at 77 K employed RBS-C, TEM and Conversion Electron Mössbauer Spectroscopy (CEMS) techniques to characterize the defect structure and the microstructure [20,54]. An important finding of these studies was the residual charge state of the iron and the information on its associated defects. At low fluences (less than 2×10^{16} Fe/cm^2 (16 keV) at room temperature, all the iron was present as Fe^{2+}. At higher fluences, the amount of Fe^{2+} decreased and metallic iron (Fe^0) increased, reaching a relative value of 45-50% at a fluence of 1×10^{17} Fe/cm^2. At fluences greater than 7×10^{16} Fe/cm^2, some of the iron was in a Fe^{4+} state. Annealing in a reducing atmosphere reduced all the iron to the metallic state.

The TEM examination revealed the presence of 1-3 nm diameter metallic iron (body-centered cubic) particles in samples implanted to the higher fluences. Ren [21] continued the study of the formation of iron nanoclusters in samples implanted at room temperature with fluences of 4×10^{16}, 1×10^{17} and 2×10^{17} Fe/cm^2 (160 keV). She used TEM, RBS-C, optical absorption and luminescence, and nanoindentation to characterize samples. This study confirmed the presence of F- and F^+-centers and charge

compensating defects. It also gave information of the effect of annealing in a reducing atmosphere on the size, shape and distribution of the nano-particles.

2.4. The Role of Ionizing Radiation on the Microstructure of Ceramics

It has been known for many years that the intense inelastic energy deposition associated with fission tracks can produce an amorphous zone around the track in ceramic materials [55]. With the availability of very high energy accelerators, studies of implantation with "swift heavy ions" have confirmed that direct amorphization of ceramics such as sapphire and MgO, can occur at implantation energies of tens of MeV or GeV [56]. Zinkle et al. have listed the threshold value of $(dE/dx)_e$ to observe such effects in sapphire as ~ 20 keV/nm [57]. This value is much higher than encounter in usual ion implantation studies. In the current study, the maximum value for $(dE/dx)_e$ is ~ 1 keV/nm.

The effect of ionizing radiation at the lower values of $(dE/dx)_e$ on the microstructure of implanted ceramics has been generally ignored until recently. The view was held that the implantation energies were too low to produce displacements in high band gap materials. However, there have been hints that deposited ionizing energy does have subtle effects.

Researchers at Sandia National Laboratory [58-61] noted that the residual stress induced by implantation of Al_2O_3, MgO and SiO_2 saturated for conditions where the ionizing component was high but not when it was low. Likewise, subsequent radiation with light ions (high ionizing component) reduced the volume swelling (damage) caused by implantation with heavy ions.

Zinkle [14,62-64] found zones depleted in point defect clusters near free surfaces and grain boundaries of Al_2O_3, MgO, and $MgAl_2O_4$ implanted with MeV ions. The effects were most pronounced for implantation of light ions where the ratio of ionizing energy deposition to nuclear energy deposition was high. In fact, the deposited nuclear energy was so low that production of defects was confined to a zone very near the end of range. These observations led Zinkle to extend earlier studies on point defect mobility [65-70] and to propose that radiation-induced diffusion promoted the recombination of

radiation-produced point defects. The resultant lower concentration of defects suppresses dislocation loop formation. The same process promotes the growth of the loops once they are formed. The effect should be to produce fewer but larger dislocation loops or point defect clusters. Figures 2.6 and 2.7 [32] summarize Zinkle's data, which were obtained for implantation energies of 1 to 3.6 MeV and an irradiation temperature of 650^{o}C. The major effects appear at Electronic to Nuclear Stopping Power Ratios ($(dE/dx)_e/(dE/dx)_n$) greater than 1000.

The question of how radiation-induced diffusion (RID) or radiation-assisted diffusion (RAD) might affect the formation and growth of second phases has not been addressed. Such phases are often produced during implantation of Al_2O_3 because of the extremely low solubility of impurities in this material. The role of thermal effects on RID or RAD has not been studied. The study of microstructural development as a function of implantation temperature and post-implantation annealing may show if thermal diffusion and radiation-induced diffusion are competing or complementary processes.

The ratio of rates of electronic energy losses $(dE/dx)_e$ to nuclear energy loses $(dE/dx)_n$ differ by a factor of about thirty for the boron and iron ions under the implantation conditions used in this study. However, the total ionizing effect also has a contribution from the ionization caused by the displaced target ions (in this case, Al and O). The ranges of the implanted ions and thus the extent of the damage zones vary significantly for the three ions used. The energy density (both nuclear and ionizing) at each position along the ion path must be determined. This information can be obtained from the TRIM calculations. A careful analysis of the microstructure as a function of the distance from the incident surface will show if there is any correlation with ionizing energy deposited at each position. If ionization-induced diffusion is present, there should be denuded zones near the free surfaces and the size of the clusters should vary along the ion path, showing a peak near the position of maximum ionizing energy deposition.

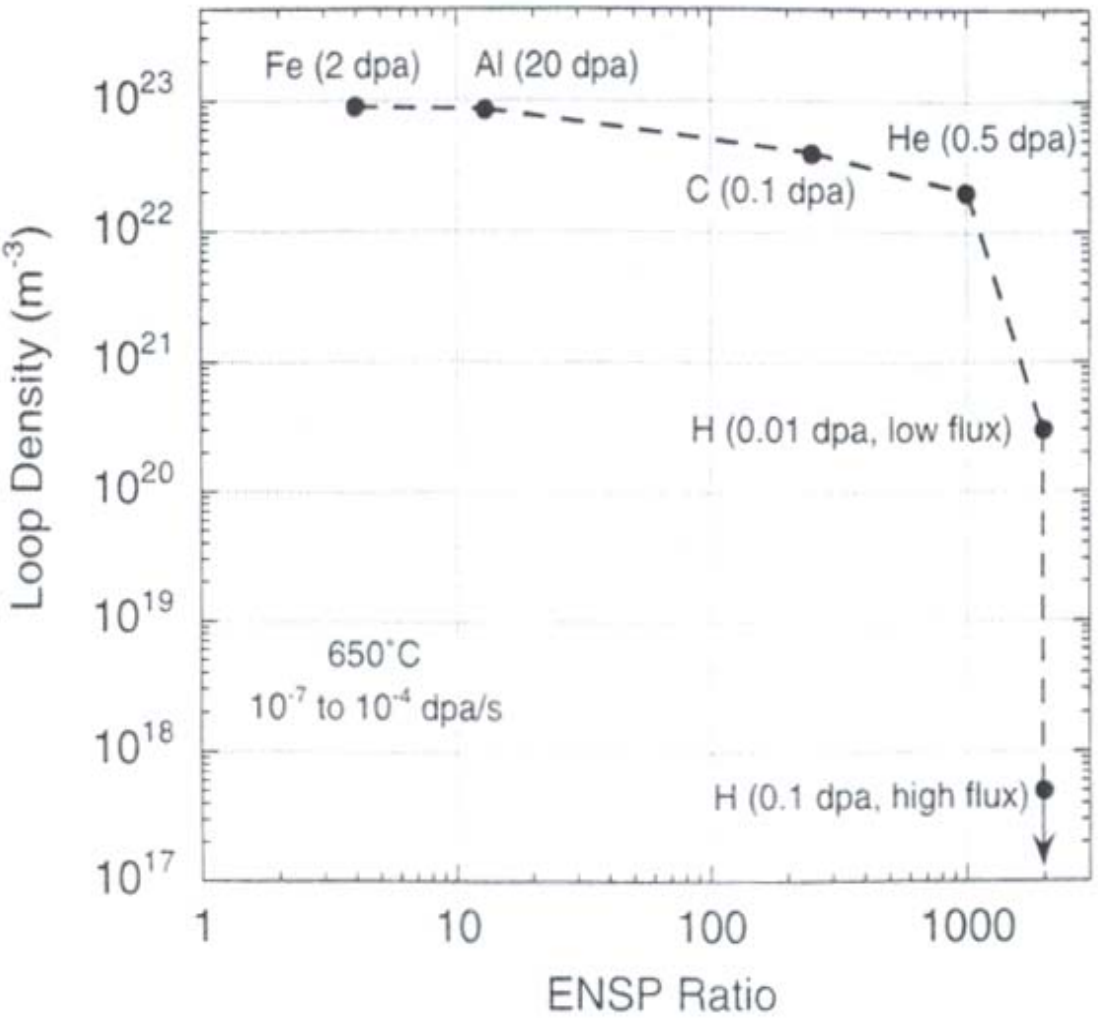


Figure 2.6: Loop density plotted as a function of the electronic to nuclear stopping power (ENSP) ratio in Al_2O_3 specimens irradiated at 650°C with ions ranging from 1 MeV H to 3.6 MeV Fe [32].

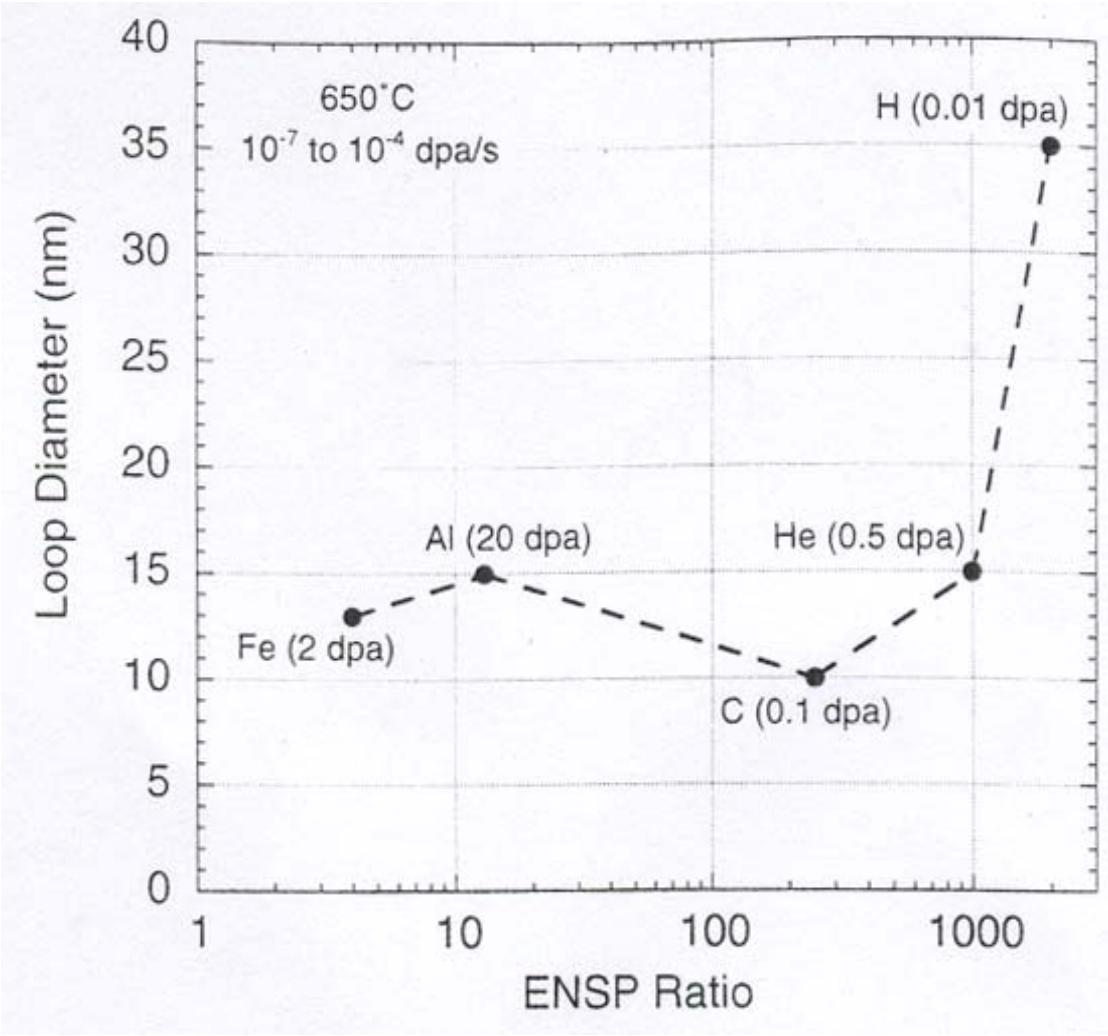


Figure 2.7: Loop size plotted as a function of the electronic to nuclear stopping power (ENSP) ratio in Al_2O_3 specimens irradiated at 650^{o}C with ions ranging from 1 MeV H to 3.6 MeV Fe [32].

CHAPTER 3

MATERIALS AND EXPERIMENTAL PROCEDURES

3.1. Material

The material being investigated is a high purity single crystal of sapphire (α-Al_2O_3) obtained from Crystal Systems Inc., Bedford, MA. It has optically polished surfaces and the <0001> (c-axis) oriented normal to the surface. Prior to ion implantation, the crystals were annealed at 1350^{o}C in flowing air for 120 hours to remove any residual polishing damage. Specimens of the crystal were implanted at room temperature and at 1000^{o}C with boron, nitrogen and iron ions having energy of 150 keV to fluences of 1×10^{17} B^+/cm^2, 3×10^{16} N^+/cm^2 and 1×10^{17} Fe^+/cm^2 respectively. The implantation conditions are tabulated in Table 3.1. The ion implantation was performed at the Epion Corporation, Billerica MA. During the implantations, the ion beam was approximately 7^o off normal to minimize channeling effects. The samples implanted at room temperature were then annealed for one hour at 1000^{o}C in a reducing (Ar-4%H_2) gas at ORNL to compare the microstructure with those of as implanted.

Sapphire is a rhombohedral single crystal anisotropic material, which exhibits different characteristic properties when measured along different axes. Out of the three major orientations, the c-axis is preferred for optical application because it is the zero birefringence orientation. A disadvantage of sapphire is that it must be produced in single crystal form because of its anisotropic structure. As noted in section 2.2, it belongs to the space group $R\bar{3}c$. The O^{2-} anions are approximately hexagonal close-packed. The Al^{3+} cations are ordered, occupying 2/3 of the available octahedral sites. The structure of sapphire may be described on the basis of the close packing, but there are significant deviations from the ideal close-packed structure as a result of the electrostatic interactions between the ions. The Al^{3+} ions and the vacant octahedral sites are arranged to achieve maximum separation of like charges and minimum separation of unlike charged, consistent with the necessary bonding between aluminum and oxygen, while maintaining overall electrical neutrality. The bonding is mainly ionic with some covalent character.

Table 3.1: Ion species and implantation parameters.

Ion species	Ion energy (keV)	Temperature	Fluence (ions/cm^2)	Target plane	Anneal for 1hr. at 1000^{o}C
B^+	150	RT	1×10^{17}	(0001)	Ar-4%H_2
B^+	150	1000^{o}C	1×10^{17}	(0001)	-
N^+	150	RT	3×10^{16}	(0001)	Ar-4%H_2
N^+	150	1000^{o}C	3×10^{16}	(0001)	-
Fe^+	150	RT	1×10^{17}	(0001)	Ar-4%H_2
Fe^+	150	1000^{o}C	1×10^{17}	(0001)	-

The properties of sapphire are given in Table 3.2.

3.2. Transmission Electron Microscopy

3.2.1. *Specimen Preparation*

Transmission electron microscopy (TEM) specimens were prepared in cross-section and back-thinned geometries. The cross-section specimens were cut using diamond saw lubricated with lapping oil to a dimension of about 1 mm × 2 mm × 800 μm (thickness), and were mechanically polished/grounded to a thickness of 50 μm or less using lapping films (30, 15 and 9 μm) and a precision grinder/polisher from Allied High Tech. Products, Inc. These specimens were then glued on metal disks (3 mm in diameter) using the Gatan G-1 epoxy (10 parts) and hardener (1 part) for focused ion beam (FIB) milling.

FIB is a new technique that has unique advantages over the conventional ion milling and requires no dimpling of the specimen. It is a site-specific thinning technique in which a pre-determined area can be sectioned and watched as it is being sectioned. It is automated and accelerates the specimen preparation process. It produces specimens

Table 3.2: The properties of sapphire (α-Al_2O_3) [15].

PHYSICAL		**THERMAL**	
Chemical formula	Al_2O_3	Thermal conductivity (60° to c-axis) at 25 °C	0.065 cal cm^{-1} s^{-1} $°C^{-1}$
Crystal structure	Hexagonal system (rhombohedral)		
Unit cell dimension	a = 4.758 Å , c = 12.991 Å	Thermal expansion coefficient (60° to c-axis) 25 - 800 °C	8.40 x 10^{-6} $°C^{-1}$
Density	3.98 g cm^{-3}		
Hardness	9 mohs, 1525-2000 Knoop		
Melting point	2040 °C	Specific heat at 25 °C	0.10 cal g^{-1}
Boiling point	2980 °C	Heat capacity at 25 °C	18.6 cal $°C^{-1}$ mol^{-1}
MECHANICAL*		**ELECTRICAL**	
Tensile strength	40,000-60,000 psi (design criterion)	Volume resistivity	10^{14} Ohm-cm
Flexural strength	70,000-130,000 psi (design criterion)	Dielectric strength	480,000 V cm^{-1}
Young's modulus	50 x 10^6 psi	Dielectric constant	
Compressive modulus	55 x 10^6 psi	E perpendicular to c-axis	9.4
Flexural modulus	52 x 10^6 psi	E parallel to c-axis	11.5
Rigidity modulus	21.5 x 10^6 psi	Dissipation factor, *tan delta*	10^{-4}
Volumetric modulus of elasticity (bulk modulus)	35 x 10^6 psi		
Poisson's ratio	0.29		

* psi = 6.9 kPa

without stress or specimen deformation because no physical force is applied during the milling process. The Hitachi FB-2000A FIB system at the Material Analysis User Center at ORNL was used to mill the cross-sectional specimens to a thickness of about 0.1 μm. Figure 3.1 shows a schematic diagram illustrating the TEM specimen preparation using FIB. The disadvantage of using FIB is the possibility of implantation of the ion used for milling and damage to the edges of the material being sectioned. This can be minimized by using smaller beam size/lower beam current and reduced voltage at the last stages of sectioning. Prior to FIB sectioning, a thick film (> 1 μm) of tungsten was deposited on the top edge of the specimen via ion-assisted deposition. This is to ensure protection of the area of interest from ion damage and implantation. The Hitachi FB-2000A is compatible with SEM stages and TEM holders; thus, once the specimen is mounted on the TEM holder for FIB, the same holder can be transferred back to the TEM/STEM for examination.

In the FB-2000A, the ion source is a Gallium Liquid Metal Ion Source (Ga-LMIS); this is actually a tungsten tip coated with molten gallium. The gallium flows from a reservoir down over the tip to form the molten gallium coating. When the reservoir is empty the life of the tip is over. During normal operation, flashing (heating of the tip and reservoir) may be needed to supply gallium to the emitting region. Flashing also removes oxide buildup and other contaminants from the gallium surface of the tip. The flashing temperature of the tip is precisely controlled by an infrared sensor located on the gun chamber. The optics system of the FB-2000A consists of electrostatic lens and deflectors. The standard electromagnetic lens cannot supply enough power to focus the ion beam due to the ions great mass. The two-stage electrostatic lens system has two basic beam modes: milling and imaging. Imaging is done with the condenser lens off to spread the beam and lower probe current, which reduces specimen damage. Milling is done with the condenser lens on. This creates a parallel beam condition which increases probe current and the system also has two basic operation modes: sputtering and deposition. The imaging detector of the system is the standard SE detector but an SI (secondary ion) detector is available as an option.

Plan view specimens were mechanically polished and dimpled from the backside

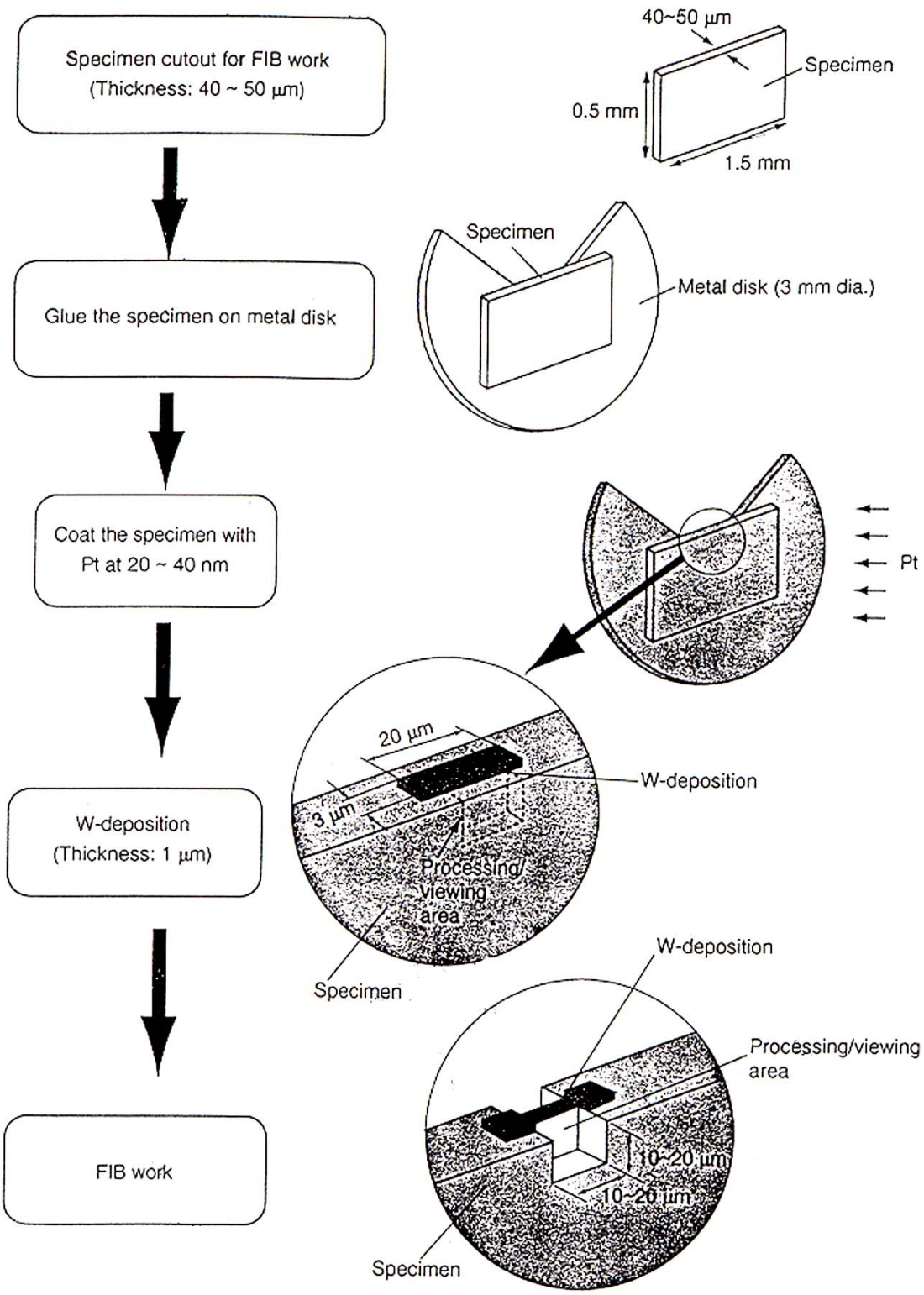


Figure 3.1: Schematic of TEM specimen preparation using FIB.

and ion milled with Gatan ion milling instrument that uses 6 keV Ar^+ ions at 15^o sputtering angle until perforation occurred.

3.2.2. *Microscopy*

Microstructural characterization and analysis were conducted on the cross sectional and back thinned TEM specimens using the Hitachi HF-2000 Field Emission Gun-Transmission Electron Microscope (FEG-TEM) operating at 200 KV and the most recent Hitachi HD-2000 Scanning Transmission Electron Microscope (STEM) also operating at 200 KV. The Instruments utilize a fine electron beam accelerated at 200 KV to irradiate a thin-film specimen. The electrons are emitted from an electron source of a single crystal tungsten tip with <310> orientation. The instruments have the advantages of having high-resolution images (HF-2000 FEG-TEM: 0.1 nm (lattice image) and 0.23nm (point to point); HD-2000 STEM: 0.24nm (lattice image)) and ultra-fine x-ray probe (about 1 nm for HF-2000 FEG-TEM and 0.2nm for the HD-2000 STEM) for energy dispersive x-ray (EDX) spectroscopy analyzer that enables compositional analysis of specimens. The HD-2000 STEM produces secondary electrons, transmitted electrons and scattered electrons used for observing and analyzing the surface and inner structure of the specimen.

3.3. Rutherford Backscattering Spectroscopy

Rutherford Backscattering (RBS)-ion channeling and random measurements were performed via a Van de Graaff generator with a 1.6 MeV He^+ beam with silicon barrier detectors placed at 140^o and 180^o in the standard IBM geometry. For the ion channeling spectra, the beam was aligned along the c-axis, while the random spectra were obtained with the sample rotated off axis. No special sample preparation is required except for the surface to be smooth. Typically, the size of the sample is about 1 cm × 1 cm × 1 mm.

The three main components of RBS instrument are a source of helium ions, an accelerator to convert them to high-energy alpha particles, and a detector to measure the energies of the backscattered ions. When charged particles of helium ions are generated in an ion source, they are accelerated by the accelerator, usually a Van de Graaff, where

their energy is then raised to several mega electron volts. The high-energy beam of alpha particles from the accelerator then passes through series of devices, which collimate or focus the beam and filter it for a selected type of particle and energy. The function of the collimator is to physically define the beam so that it has sharp edges, and to prevent beam particles, which have scattered from entering the chamber. A collimator is just a series of adjustable slits that are driven by micrometers, either manually or electrically. When analyzing solids with high-energy ions, a monoenergetic beam containing only one kind of ion is necessary. The selection of the ion species required is performed by the magnetic analyzer. The monoenergetic and collimated beam then impinges perpendicularly on the sample to be analyzed. Some of them are backscattered and are collected by the detector (surface barrier silicon detector are used), where they generate an electrical signal. This signal is amplified and processed. A multichannel analyzer (MCA) digitizes the analog input voltage signal and sorts all signals during an experiment. The MCA plots backscattering energy spectrum counts versus channel number or energy. That is, it provides the number of scattering events per unit energy interval as a function of energy of the backscattered particles. Pressures in accelerator tube and elsewhere must be kept at 10^{-6} Torr to avoid atomic interaction. Diffusion and turbomolecular pumps are used, backed up by rotary pumps. A schematic diagram of a typical backscattering spectrometry system is shown in Figure 3.2 [71].

3.4. Optical Absorption

The optical absorption was measured over the wavelength range of 200 to 800 nm using a Varian Cary 5G IR-Vis-UV (Infrared-Visible-Ultraviolet) spectrometer. The type of excitation depends on the wavelength of the light. Electrons are promoted to higher orbital by ultraviolet or visible light and vibrations are excited by infrared light. Absorption measurements can be at a single wavelength or over an extended spectral range as in this study. Ultraviolet and visible lights are energetic enough to promote outer electrons to higher energy levels, while the infrared light promotes molecular vibrations.

One of the ways to study the energy levels of the atoms, molecules, and solids is

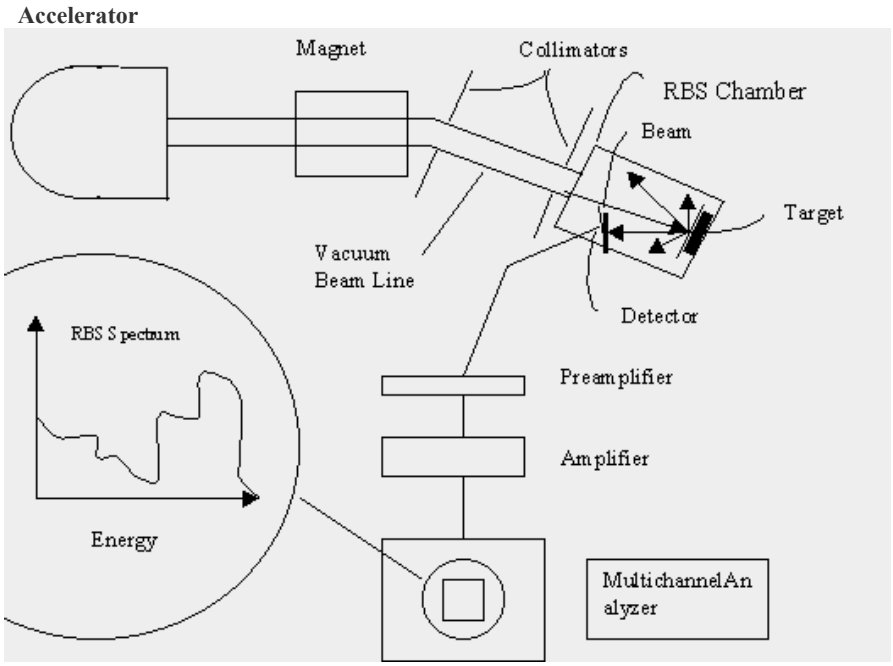


Figure 3.2: A schematic diagram of a typical backscattering spectrometry system and analysis [Adapted from reference 71].

by optical absorption spectroscopy. An absorption spectrum is the absorption of light as a function of wavelength. The absorption spectrum of an atom or molecule depends on its energy-level structure; hence, defects study using the optical methods has the advantage that each defect has a characteristic energy levels, which lie within the forbidden energy gap, and show separate optical absorption and luminescence bands [24].

Ultraviolet and visible (UV-Vis) absorption spectroscopy is the measurement of the attenuation of a beam of light after it passes through a sample or after reflection from a sample surface. The light source is usually a deuterium discharge lamp for UV measurements and a tungsten-halogen lamp for visible and near infrared (NIR) measurements. The instruments automatically swap lamps when scanning between the UV and visible regions. The detector in single-detector instruments is a photodiode, phototube, or photomultiplier tube (PMT). UV-Vis-NIR spectrometers utilize a combination of a PMT and a Peltier-cooled PbS IR detector. The light beam is redirected automatically to the appropriate detector when scanning between the visible and NIR regions. The diffraction grating and instrument parameters such as slit width can also change. Spectrometer designs and optical components are optimized to reject stray light, which is one of the limiting factors in quantitative absorbance measurements.

3.5. Analytical Techniques

Attempts to determine the concentration-depth profiles of the implanted boron and nitrogen and to identify the nature of the nanometer size precipitates were unsuccessful. The low atom masses of the implanted ions, the small sizes of the second phases, and the highly insulating properties of sapphire contributed to the difficulty of obtaining quantitative data. The techniques tried are described below.

3.5.1. *Nuclear Reaction Techniques*

Trace amounts of impurities that have lower atomic masses than the matrix are difficult to detect. The yield from the matrix is usually so high that the signal from the impurity cannot be distinguished by Rutherford backscattering spectroscopy. In the present study, the backscattered signal from boron and nitrogen are obscured by both the

aluminum and the oxygen spectra. Limited success for very light elements has been reported by the used of nuclear reactions.

The reaction $^{11}B(\alpha,\alpha)^{11}B$ has a resonance absorption for 2.65 MeV alpha-particles. Attempts to use this reaction by irradiating with 2.65 MeV ^{4}He were unsuccessful.

Attempts to use the reactions $^{14}N(p,p)^{14}N$ with 2.4 MeV protons and $^{14}N(p,p)^{14}N$ with 1.75 MeV protons were unsuccessful. The strong signal from aluminum and oxygen masked the weaker signals from nitrogen.

3.5.2. *X-ray Photoelectron Spectroscopy*

The XPS unit at the University of Tennessee was not in operation during the period of this study. A few samples were examined in a unit located at the University of Alabama-Huntsville. A Kratos XSAM 800 spectrometer was used to determine the elemental composition, chemical states and bonding on the surface for the few samples analyzed, but no useful data were obtained. It is possible that a more detailed study with optimal sample preparation could be successful. Since the maximum effects occur at some distance from the surface, carefully controlled sputter profiling might be used. Alternately, mechanical polishing to a depth corresponding to R_p or to the position of peak damage energy could be used. However, it has been found that sputtering sapphire preferentially removes oxygen, leading to detection of sub-oxides of aluminum [72].

3.5.2. *Auger Spectroscopy*

Specimens implanted with boron or nitrogen was examined in the PHI 680 Scanning Auger Microprobe unit at the High Temperature Materials Laboratory, Oak Ridge National Laboratory. The results were inconclusive. Charging of the sapphire matrix prevented the electron probe beam from being focused onto a given area. No results were obtained for the B-implanted samples nor for the N-implanted at room

temperature. An upper limit of 1.8 to 3.2 at % was tentatively assigned to the N-content of the sample implanted with nitrogen at 1000° C, but the value is highly questionable.

CHAPTER 4

EXPERIMENTAL RESULTS

4.1. Boron Implanted Sapphire (α-Al_2O_3)

4.1.1. *TRIM Calculations*

The transport and range of ions in materials (TRIM) program was used to simulate the implantation process and to model the energy deposition (elastic and inelastic) as a function of depth from the surface, the range of implanted species, and the defect production. TRIM calculation for 1×10^{17} B^+/cm^2 (150 keV) gave the R_p (range of ion) = 301.1 nm, the range straggle = 56.8 nm and the number of vacancies per ion = 417.9. The energy deposited (per ion) and vacancies produced per lattice ion are modeled with respect to position in the target as shown in Tables 4.1 and 4.2 respectively. Figure 4.1 shows the simulated boron ions trajectories in sapphire. The range of boron ion and the vacancies produced per lattice ion (dpa) are presented in Figures 4.2 and 4.3 respectively. The energy deposition (electronic and nuclear) plots as a function of target depth and ion energy are shown in Figures 4.4, 4.5, and 4.6.

The distribution of ions, defects and deposited energy shown in Figures 4.1 – 4.5 are based on 9999 incident ions per surface atom (ion). Since TRIM is a Monte Carlo calculation based on two-body interactions, the large number of incident ions is required to give satisfactory statistics to the calculated values. The areal density of ions for sapphire is 2.37×10^{15} ions/cm^2. For a fluence (dose) of 1×10^{17} B/cm^2, each surface ion is struck about 40 times. Because of lateral spreading, the ions located away from the surface will be struck by more ions as indicated in the figures. The peak concentration of B using the data from Figure 4.2 and the fluence of 1×10^{17} B/cm^2 is calculated to be approximately 0.2 B per Al ion. The data in Figures 4.3, 4.4 and 4.5 are shown per incident ion.

Table 4.1: Boron energy deposited per incident B ion as a function of depth in the target material.

Target Position, x	**Inelastic (Ionizing or Electronic) (eV/Å)**			**Elastic (Displacement) (eV/ Å)**	**Ratio (Inelastic/Elastic)**
	Ions	**Recoils**	**Total**		
Surface, x=0	51.4	1.4	52.8	3.3	16
Peak damage energy, x = 286.5nm	21.2	4.2	25.6	14.9	1.7
R_p, x = 301.1nm	18.1	4.0	22.1	14.2	1.6

Table 4.2: Vacancies produced per lattice ion (dpa) for a fluence of 1×10^{17} B^+/cm^2.

Target Position, x	**Al**	**O**
Surface, x=0	6.7	2.0
Peak damage energy, x = 286.5nm	28	10.0
R_p, x = 301.1nm	26.0	9.0

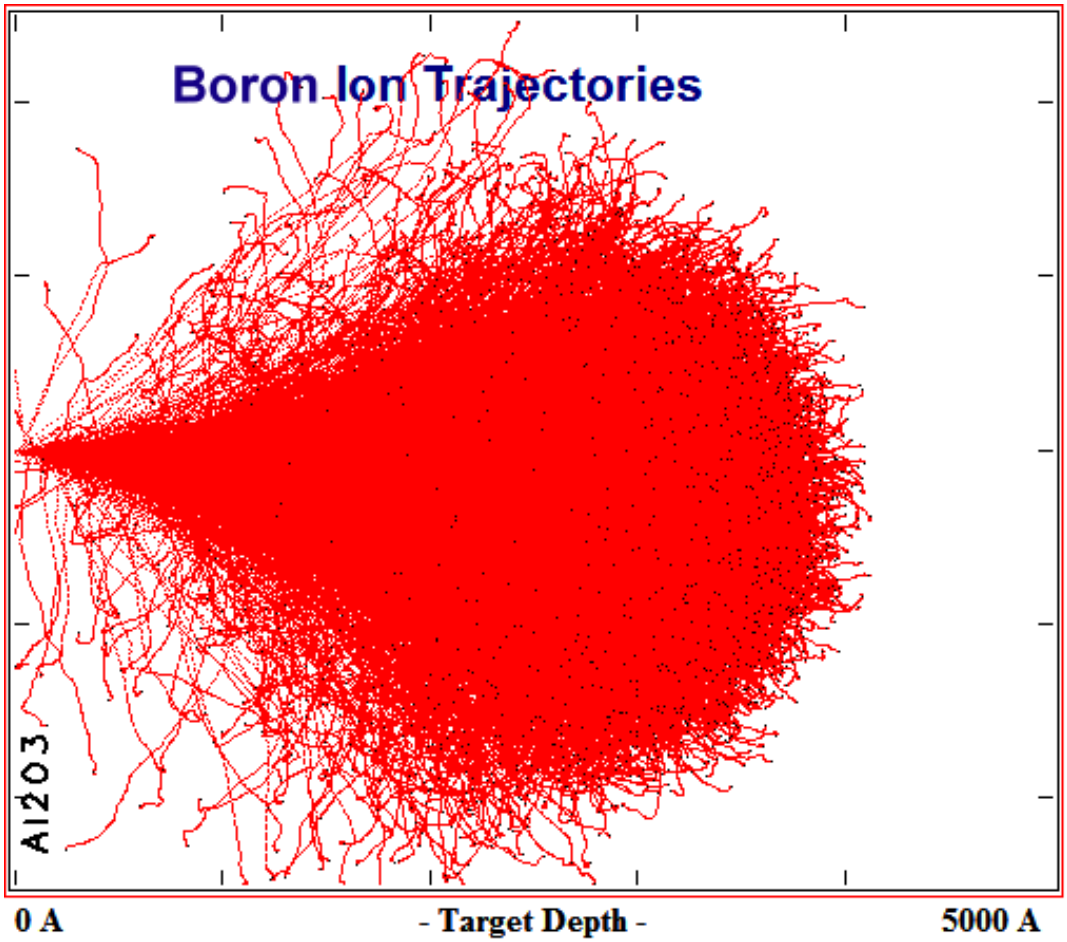


Figure 4.1: Boron ion trajectories.

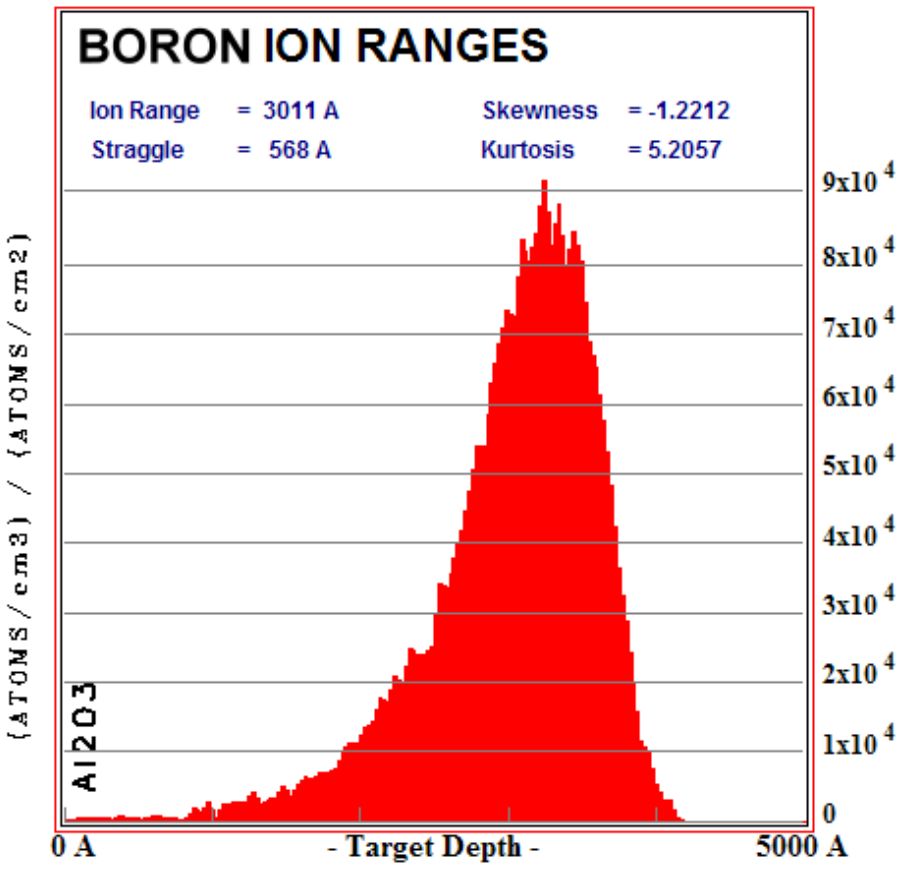


Figure 4.2: The range of boron ion in sapphire as a function of depth.

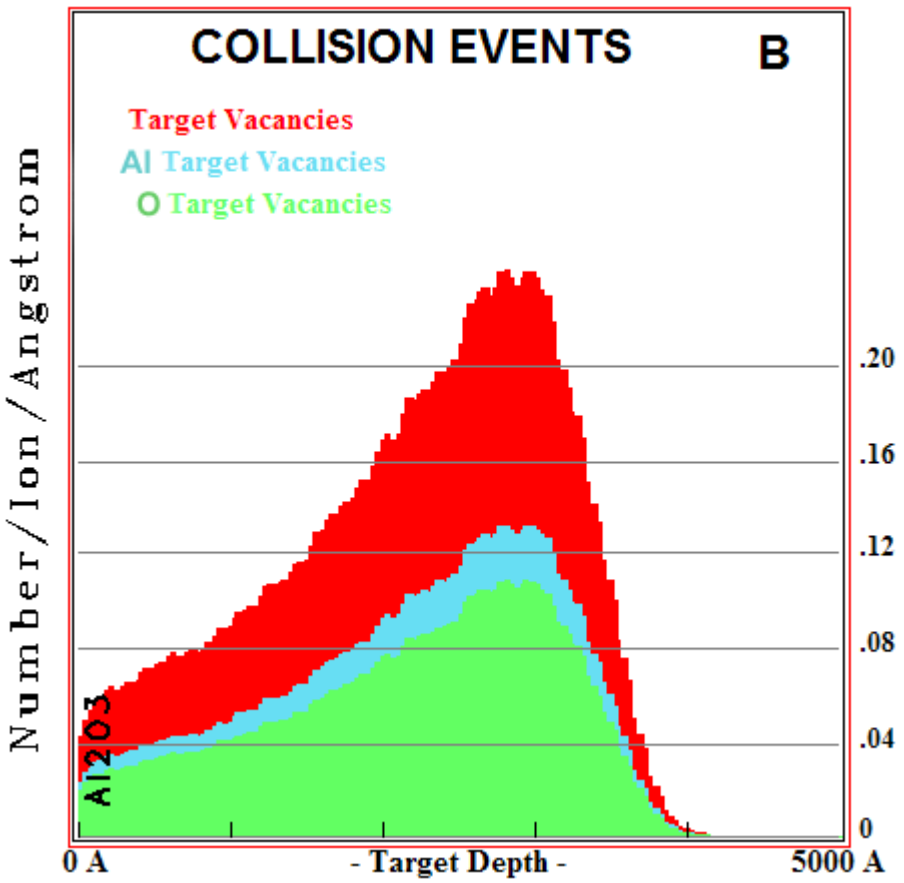


Figure 4.3: Boron collision events showing the plots of the number of vacancies produced per lattice ion (dpa).

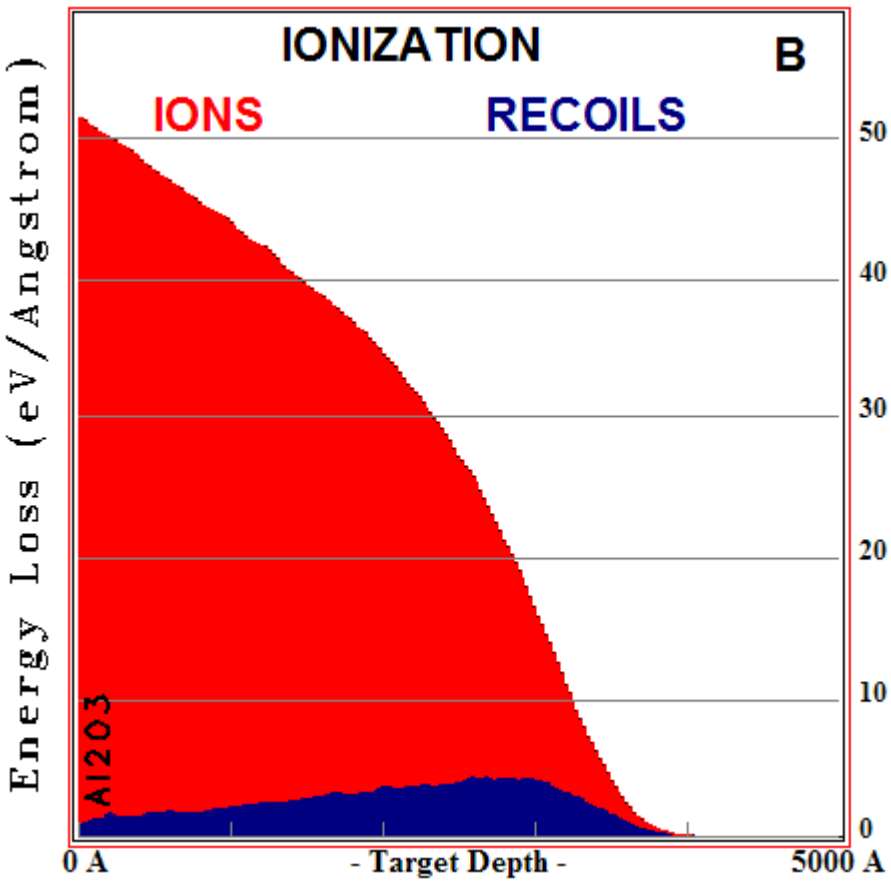


Figure 4.4: Plot of electronic (ionizing) energy loses with the target depth.

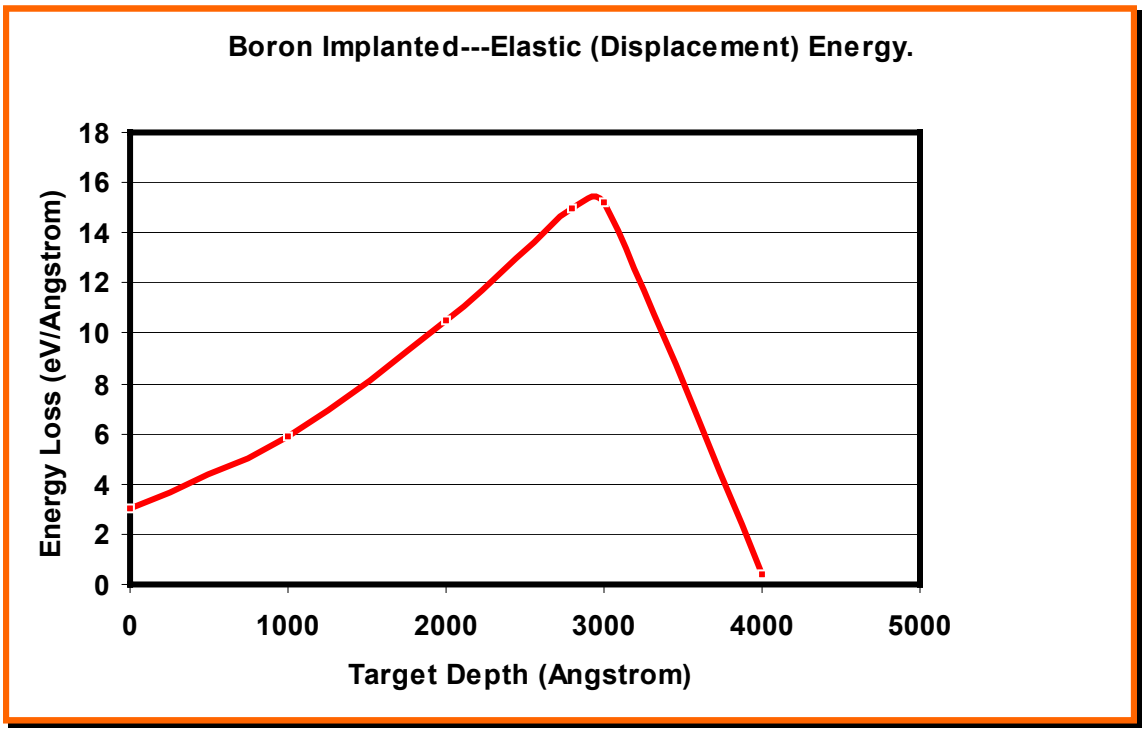


Figure 4.5: Plot of elastic (displacement) energy loses with the target depth.

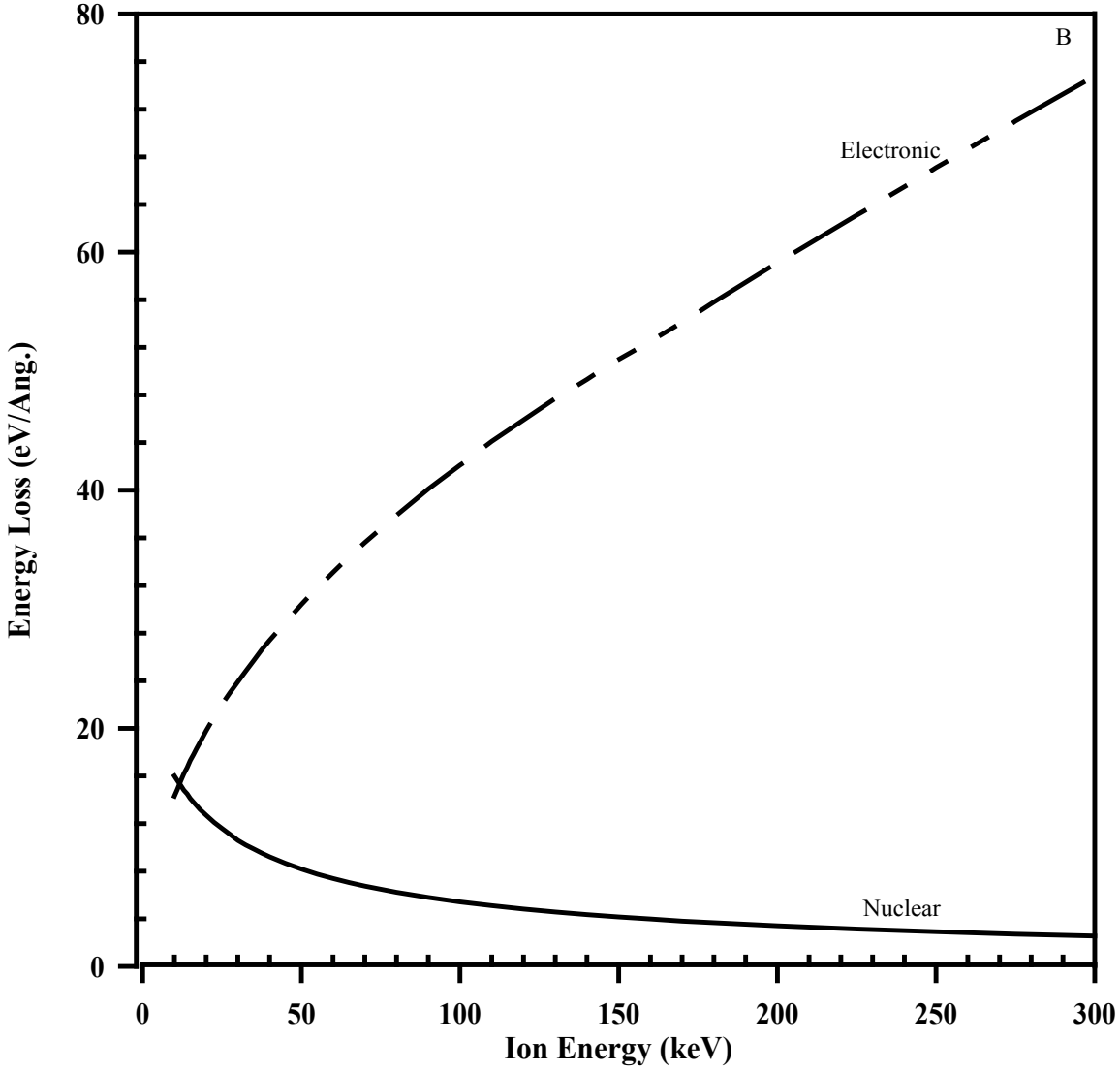


Figure 4.6: Plot of energy (electronic and nuclear) loses as a function of the boron ion energy (the implant ion energy in this case is 150 keV).

4.1.2. *Transmission Electron Microscopy*

The microstructures of boron implanted $\alpha-Al_2O_3$ at the fluence of 1×10^{17} B/cm^2 (150 keV) at room temperature (RT) and at 1000^{o}C are shown in Figures 4.7 and 4.8, respectively. These cross-sectional micrographs show the typical "black spot" damage typical of radiation damage. The exact nature of these clusters has not yet been determined. These features are generally ascribed to defect clusters, usually interstitial in nature and often bounded by dislocation loops. The "black spot" features in Figure 4.7 (c) (RT implant) appear to be elongated in a direction parallel to the surface, i.e. along the traces of (0001).

The selected area diffraction patterns of Figures 4.9 and 4.10 contained no indication of a second phase. The diffraction spots for the sample implanted at 1000^{o}C were sharper than those for the sample implanted at room temperature, reflecting the lesser amount of disorder for that specimen. Attempts to identify features in Figures 4.7 and 4.8 using x-ray diffraction, electron micro-beam diffraction and convergent beam electron techniques were unsuccessful. The implanted regions remained crystalline as evidence from the selected area diffraction patterns shown in Figures 4.9 and 4.10. The EDX pattern from the surface region (Figure 4.11 (A)) shows the presence of carbon at the surface. This carbon contamination probably occurred in the implantation chamber at Epion.

The features in the microstructure of the sample implanted at 1000^{o}C (Figure 4.8 (a) and (b)) appear to differ from the "black spots" of the room temperature implanted sample. The features are better defined and give the appearance of possibly being a second phase. They appear to lie along planes at an angle to the surface. The EDX spectra (Figure 4.12) showed only the presence of Al and O, and in the near surface region, Gallium (Ga) retained from the ion milling.

Room temperature implant followed by annealing in Ar-4% H_2 at 1000^{o}C for one hour micrographs are shown in Figure 4.13. The microstructural features reveal none of the "black spot" damage observed in the room temperature and 1000^{o}C implanted specimens. There appears to be a precipitate throughout the implanted zone with the size of the particles extending up to 6-7 nm. There is evidence that the end-of-range damage

(a)

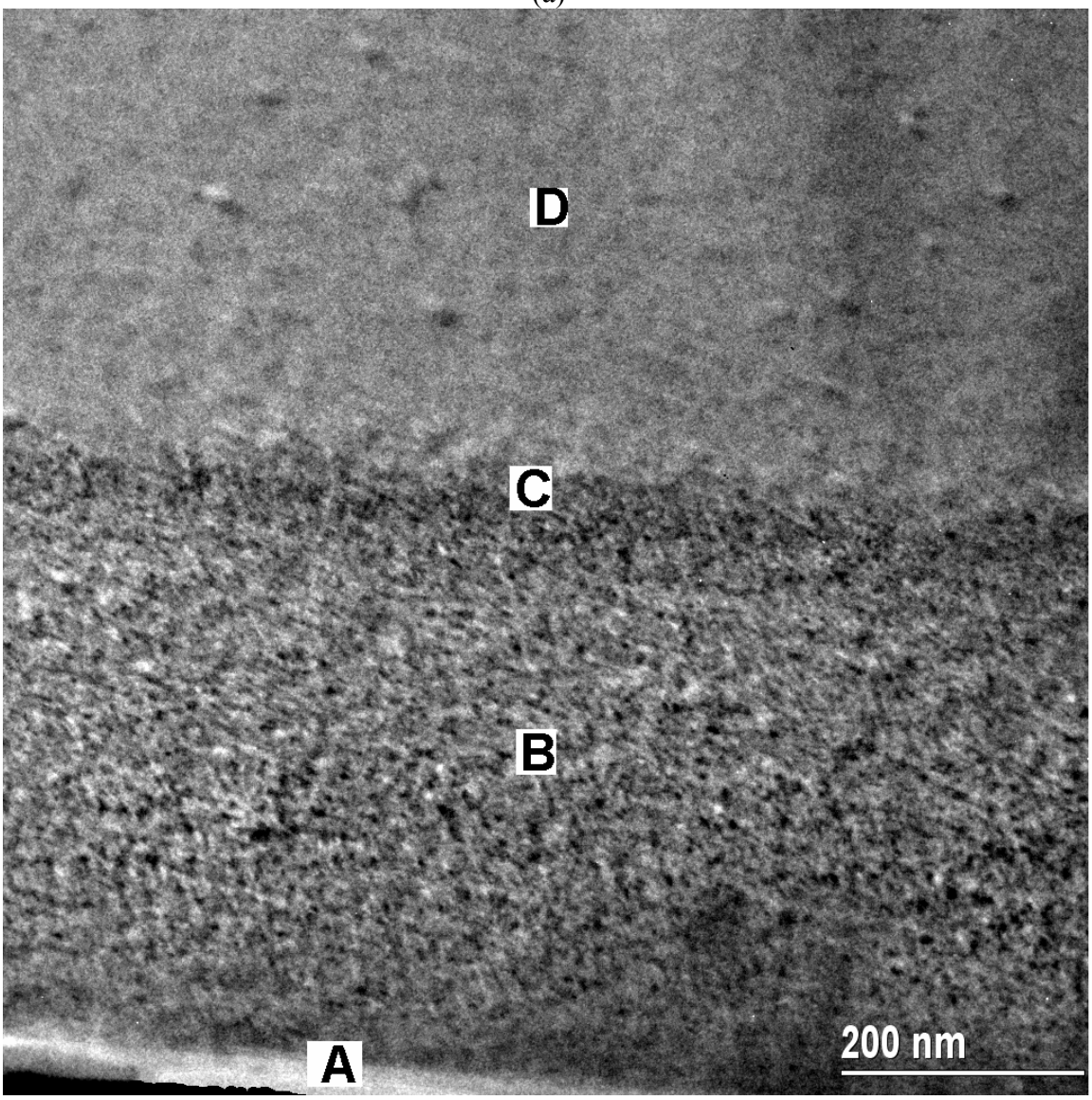


Figure 4.7: Cross-sectioned micrographs of $\alpha-Al_2O_3$ specimen implanted with fluence of 1×10^{17} B/cm^2 (150 keV) at room temperature. (a) x 20K (b) x 80K (c) x 500K.

(b)

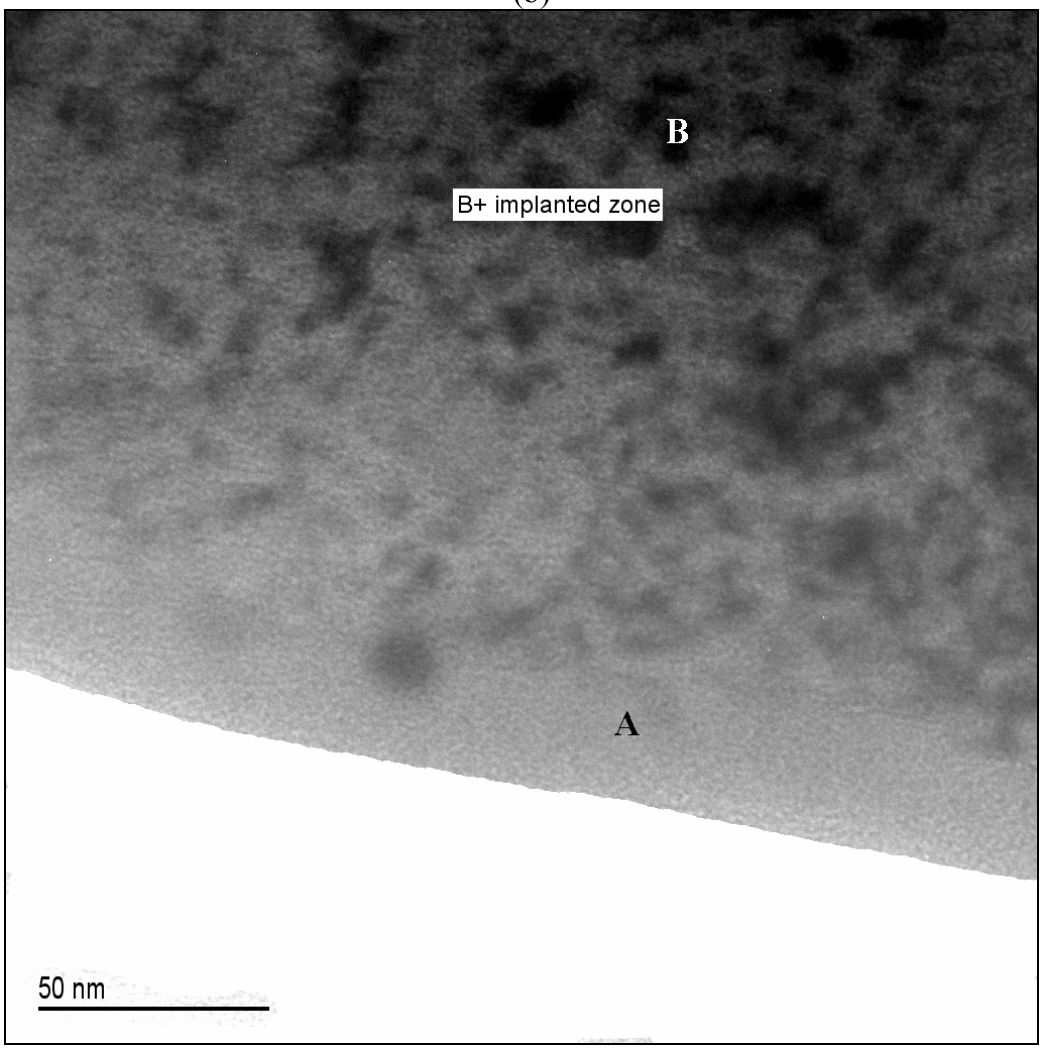


Figure 4.7 continued.

(c)

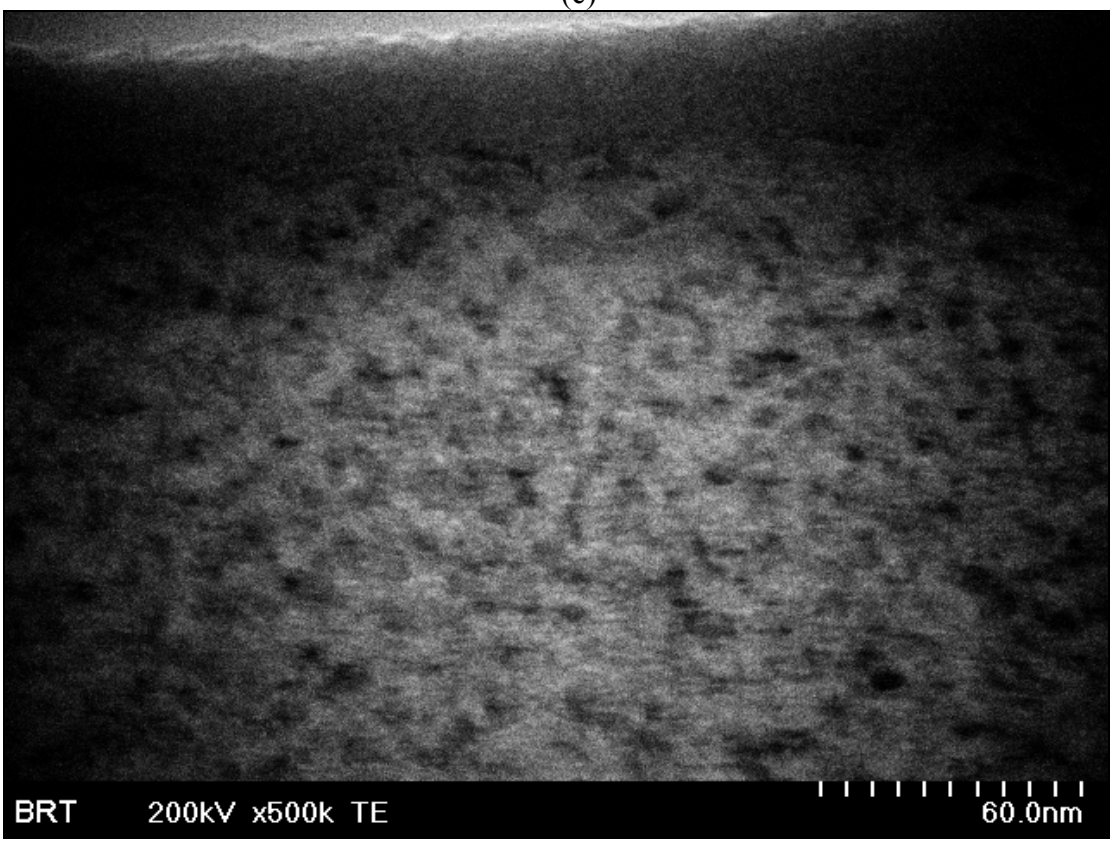


Figure 4.7 continued.

(a)

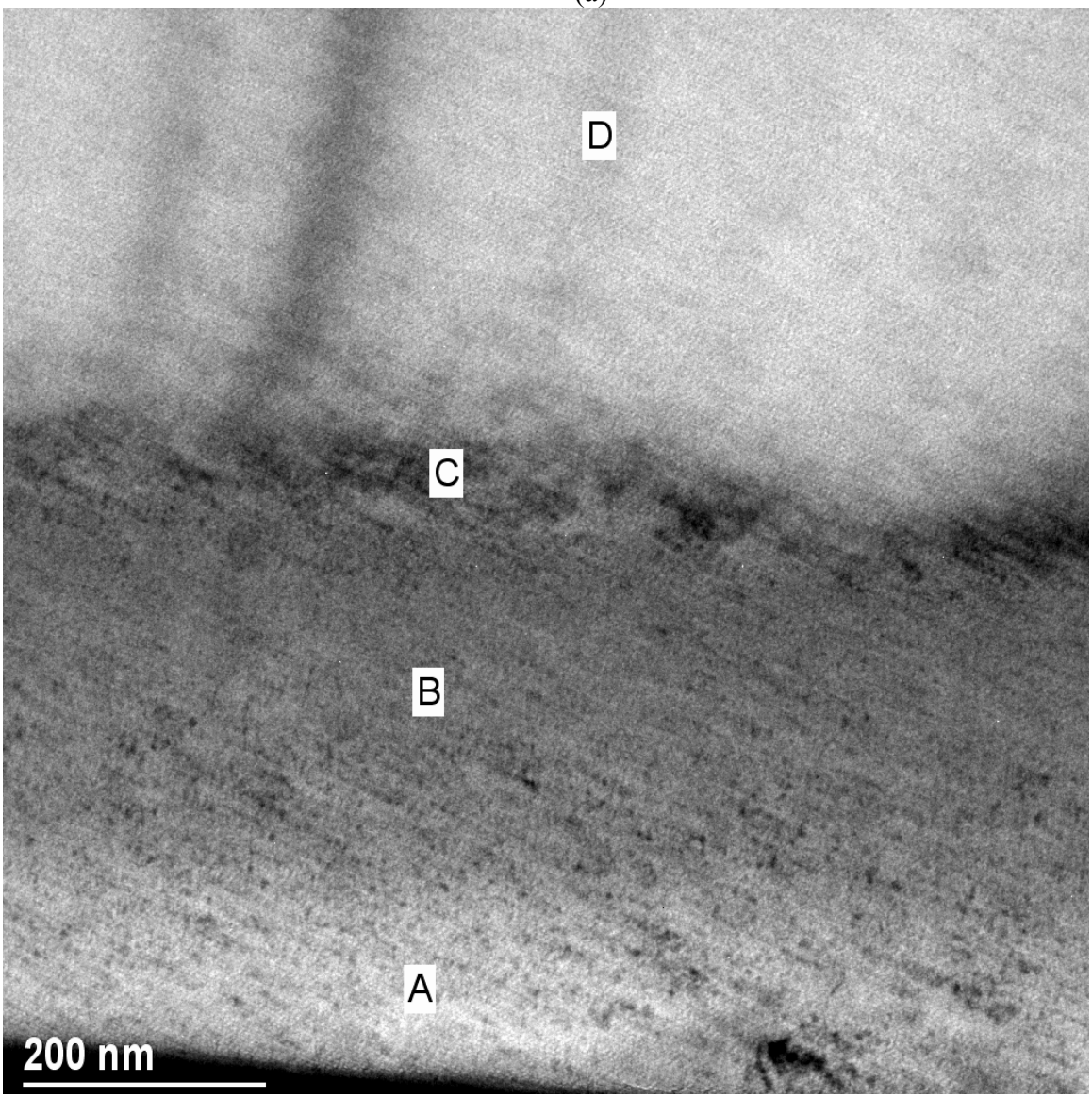


Figure 4.8: Cross-sectioned micrographs of α–Al_2O_3 specimen implanted with fluence of 1×10^{17} B/cm^2 (150 keV) at 1000^{o}C. (a) x 20K & (b) x 80K.

(b)

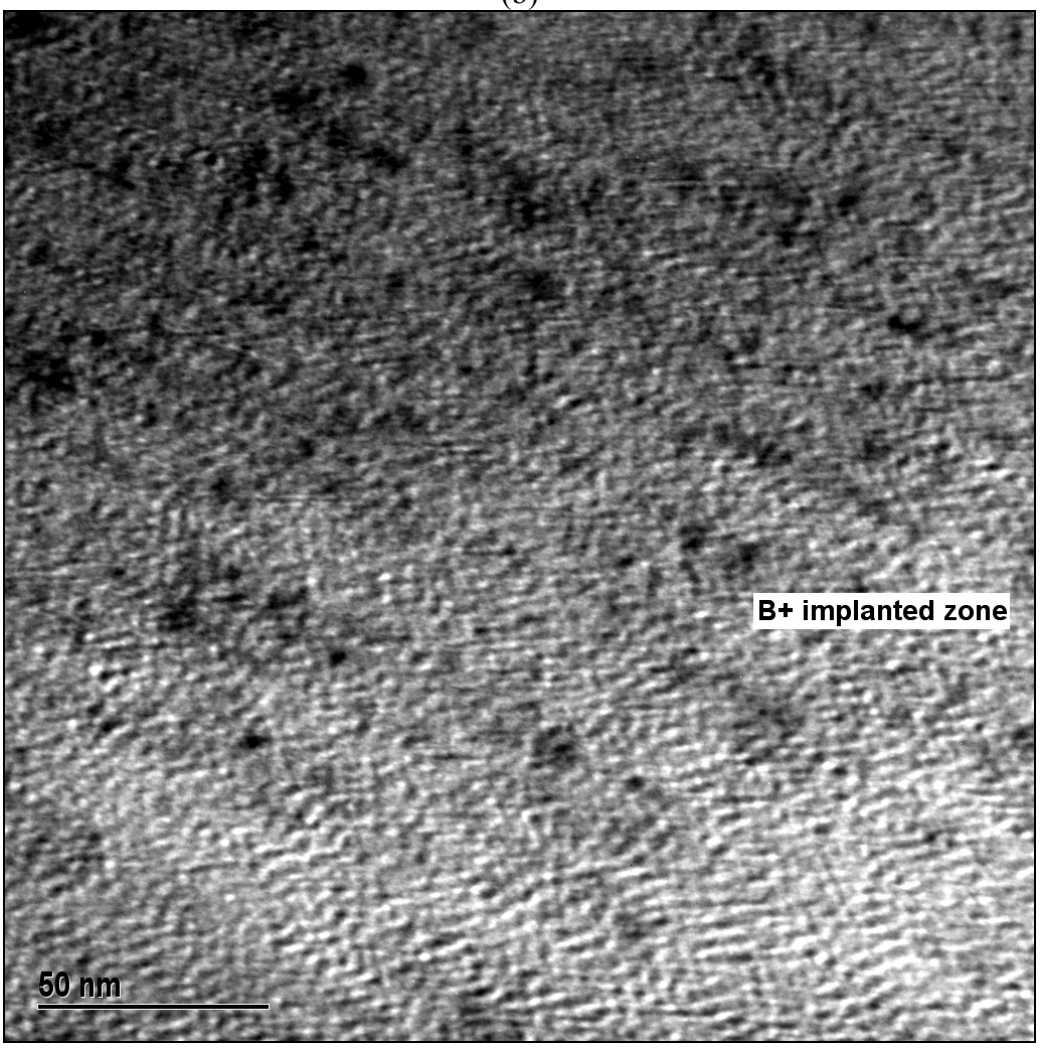


Figure 4.8 continued.

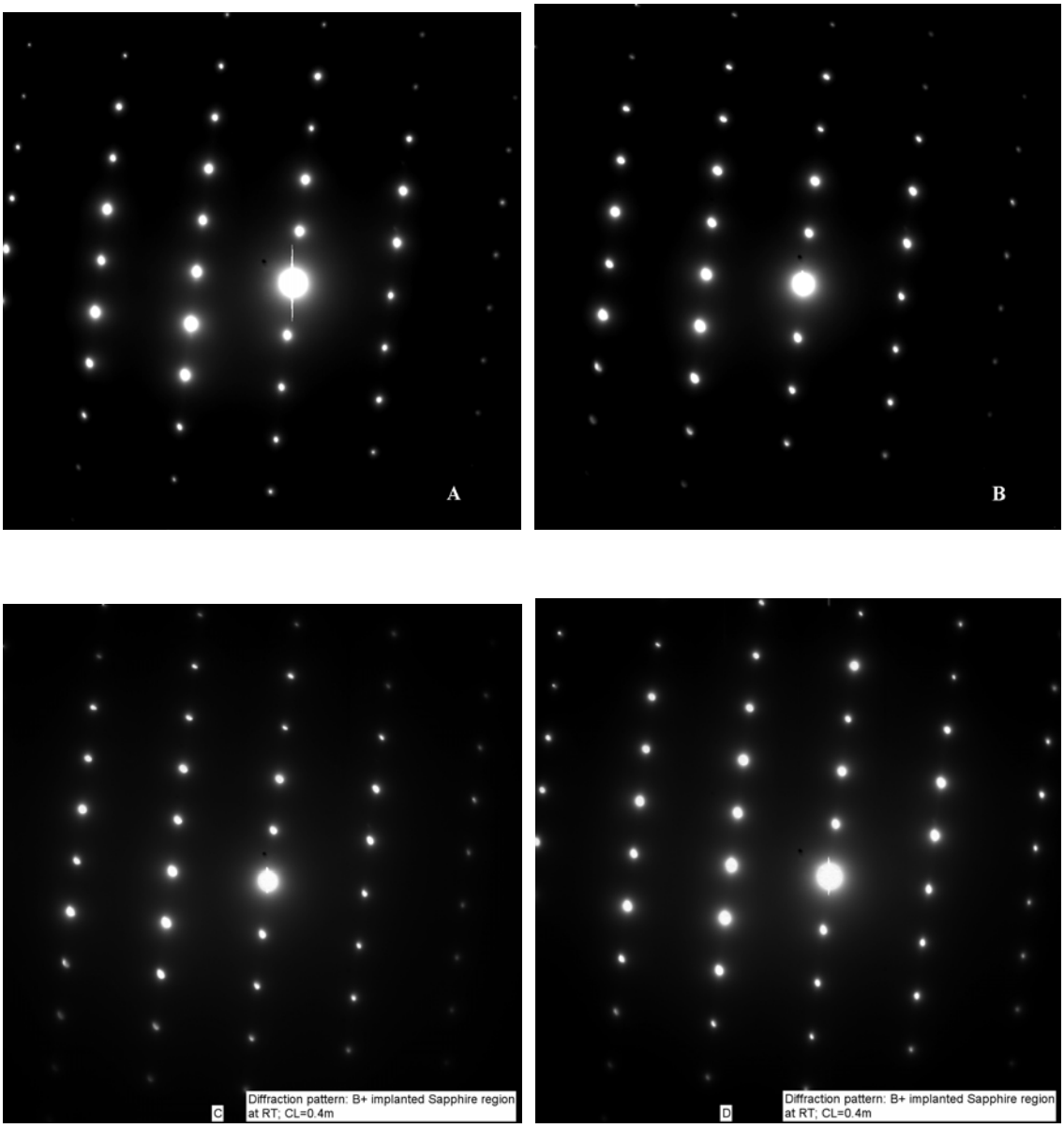


Figure 4.9: Selected area diffraction pattern of $\alpha-Al_2O_3$ specimen implanted with a fluence of 1×10^{17} B/cm^2 (150 keV) at room temperature. A, B, C and D are from regions A, B, C and D respectively of Figure 4.7 (a).

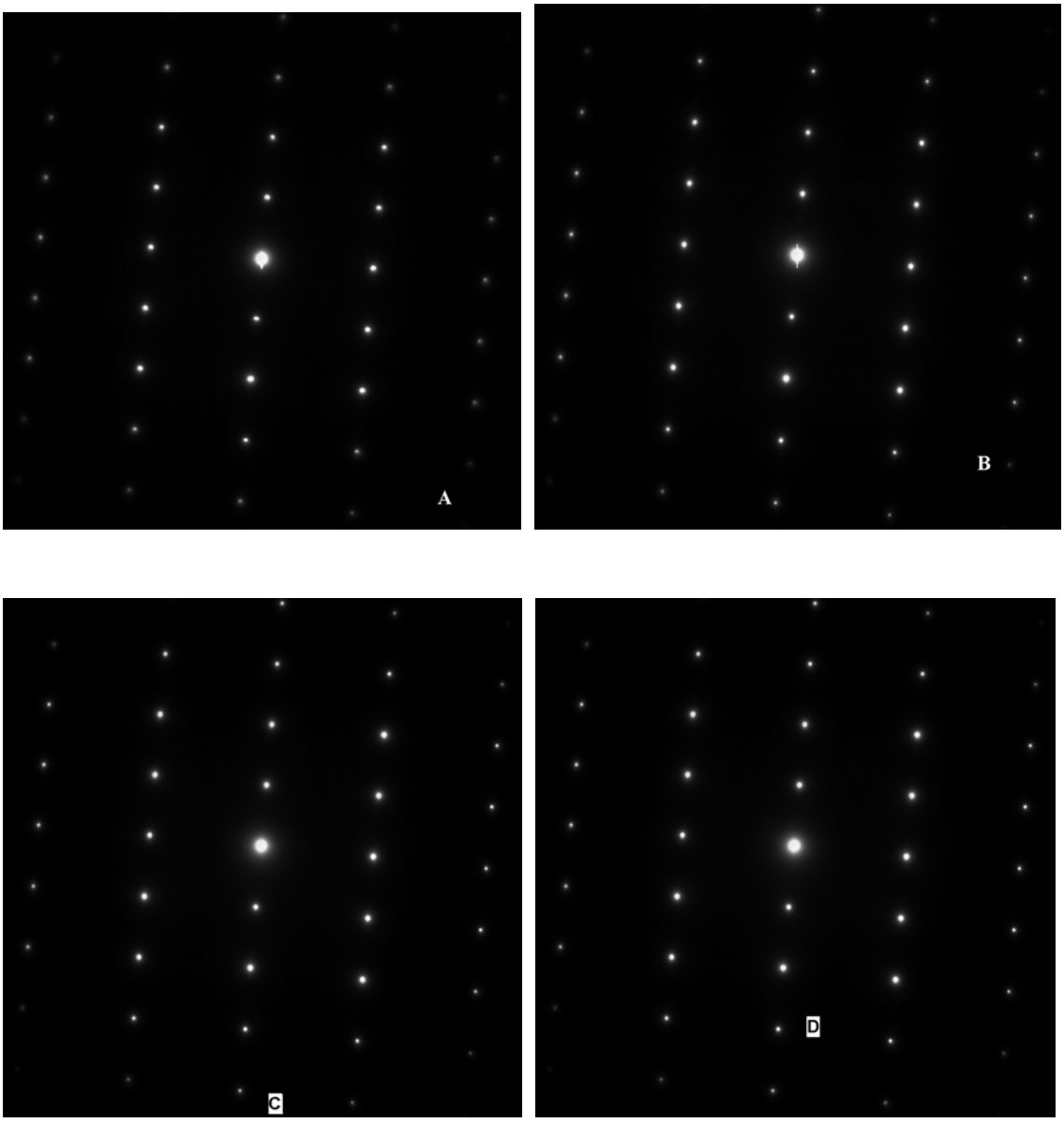


Figure 4.10: Selected area diffraction pattern of α–Al_2O_3 specimen implanted with a fluence of 1×10^{17} B/cm^2 (150 keV) at 1000^{o}C. A, B, C and D are from regions A, B, C and D respectively of Figure 4.8 (a).

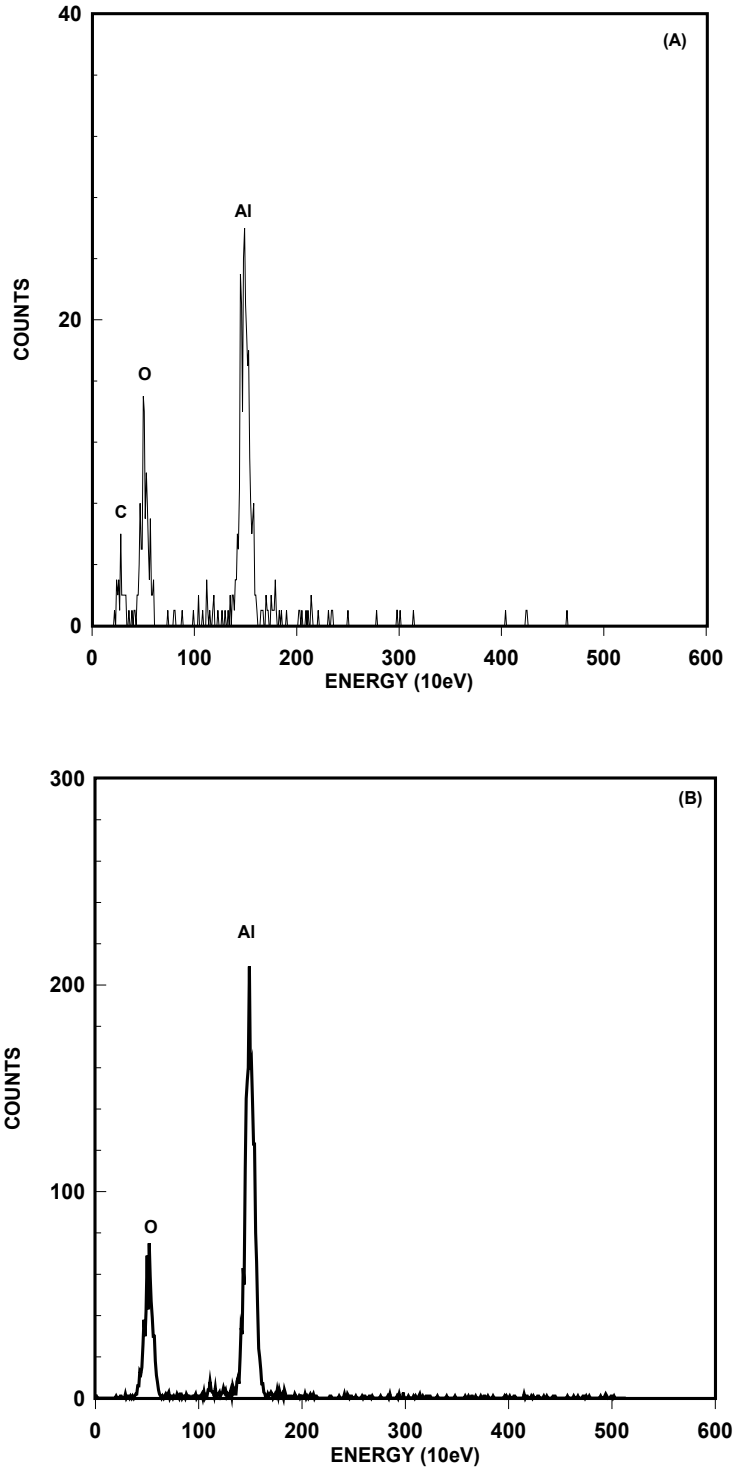


Figure 4.11: EDX spectra from a cross-section α–Al_2O_3 specimen implanted with boron at room temperature. A and B are from regions B and D respectively of Figure 4.7 (a).

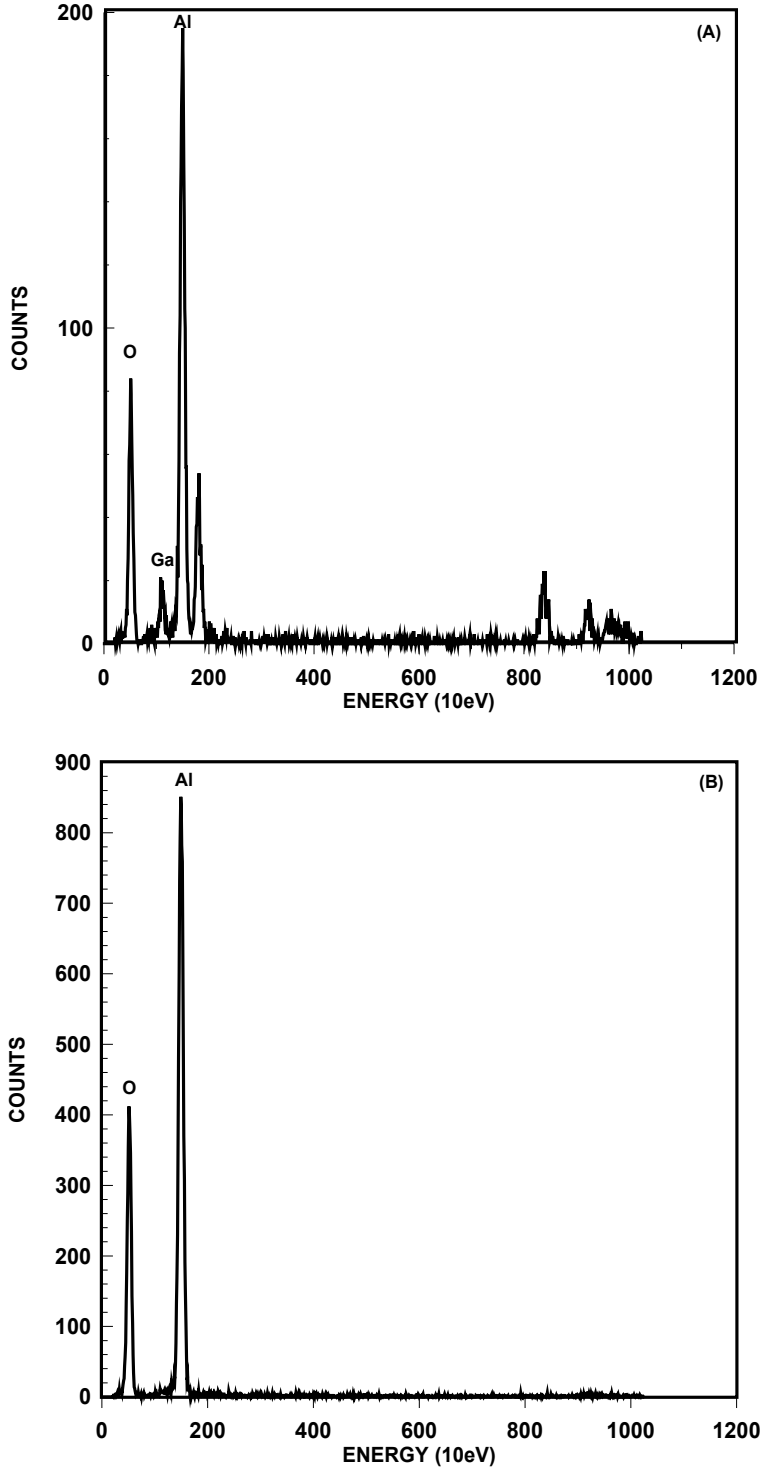


Figure 4.12: EDX spectra from a cross-section $\alpha-Al_2O_3$ specimen implanted with boron at 1000°C. A and B are from regions B and D respectively of Figure 4.8 (a).

(a)

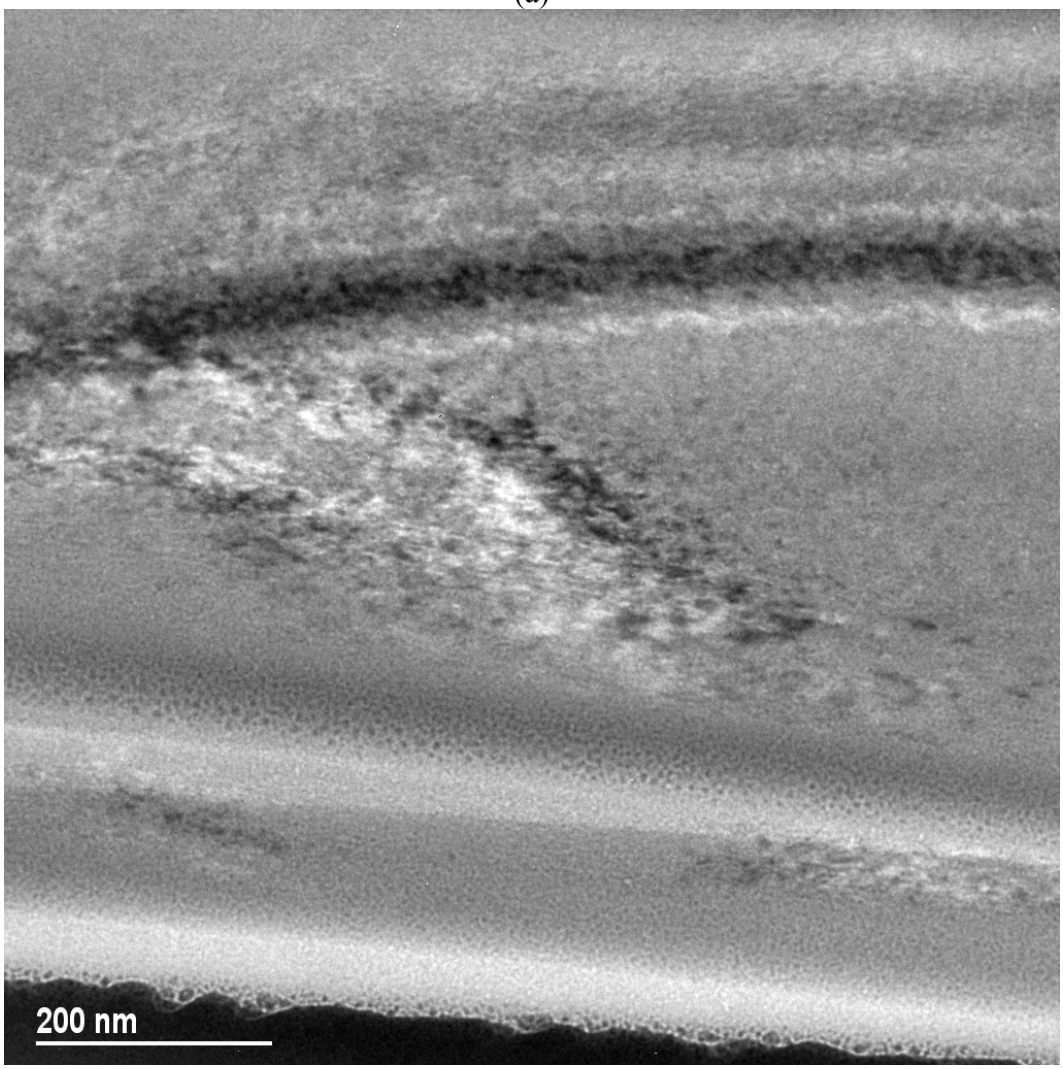


Figure 4.13: Cross-sectioned micrographs of α–Al_2O_3 specimen implanted with a fluence of 1×10^{17} B/cm^2 (150 keV) at room temperature and annealed in Ar-4% H_2 at 1000^{o}C for 1 hour. (a) x 20K (b) x 80K.

(b)

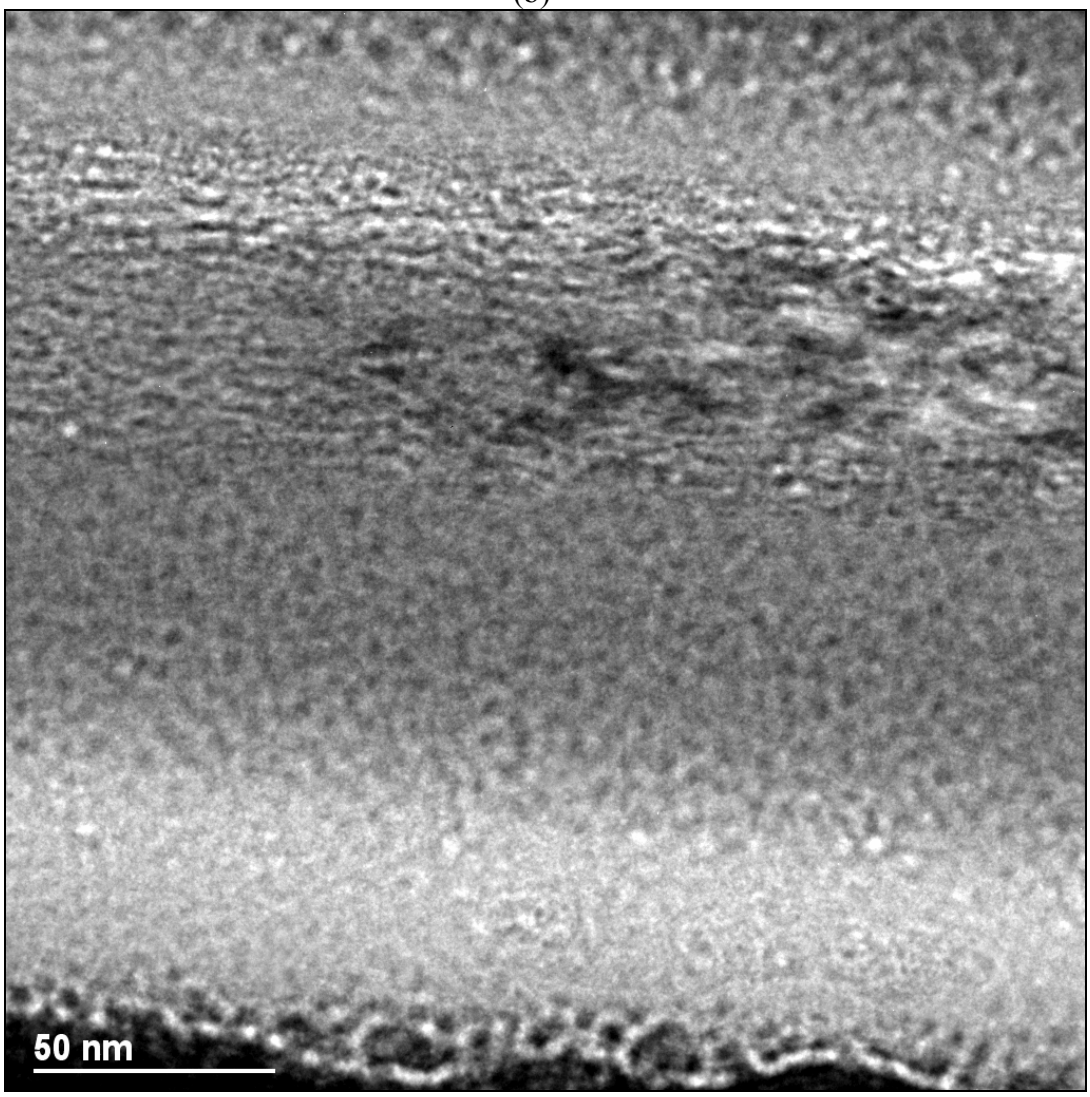


Figure 4.13 continued.

is resistant to annealing at this temperature.

4.1.3. *Rutherford Backscattering Spectroscopy*

Boron implanted sapphire at room temperature RBS-C spectra are shown in Figure 4.14 (a). Since the energy of the backscattered helium ions is proportional to the mass of the scattering atoms (ions), the spectrum for boron will be masked by the spectra of both aluminum and oxygen. Thus, the RBS-C spectra give no information on the amount of implanted boron nor on its distribution.

The backscattered energy from an element at the surface is given by

$$E_i = K_i E_o$$

where E_o is the incident energy and K_i is the kinematic factor. The kinematic factor (K) depends only on the ratio of the projectile to the target masses and on the scattering angle, θ. Tabulated values of K appropriate to the experimental arrangement [71] give values of E_i of 0.916 keV for Al, 0.593 keV for O, and 0.353 keV for B. The position at the surface for Al and O are marked on the figure (4.14).

The spectrum of Al shown in Figure 4.14 (a) show large dechanneling effects extending from about 150 nm with a peak near the peak position (Rp = 301 nm) of boron. The value of χ_{Al} is about 0.2 at 250nm, where χ is the ratio of channeled and random yields. A value of 0.02 for χ indicates a defect-free lattice and a value of 1 indicates a random structure. This dechanneling cannot be caused by the interference of boron signals. Possible causes could be (a) the presence of particles of an incoherent second phase, (b) clusters of interstitial impurities or defects that block the [0001] channels, and/or (c) extreme disorder in the Al sublattice due to some other cause. There is less disorder in the region from the surface to 100 nm. The value of χ_{Al} at 100 nm is 0.13 for the implanted region compared to 0.03 in the unimplanted region.

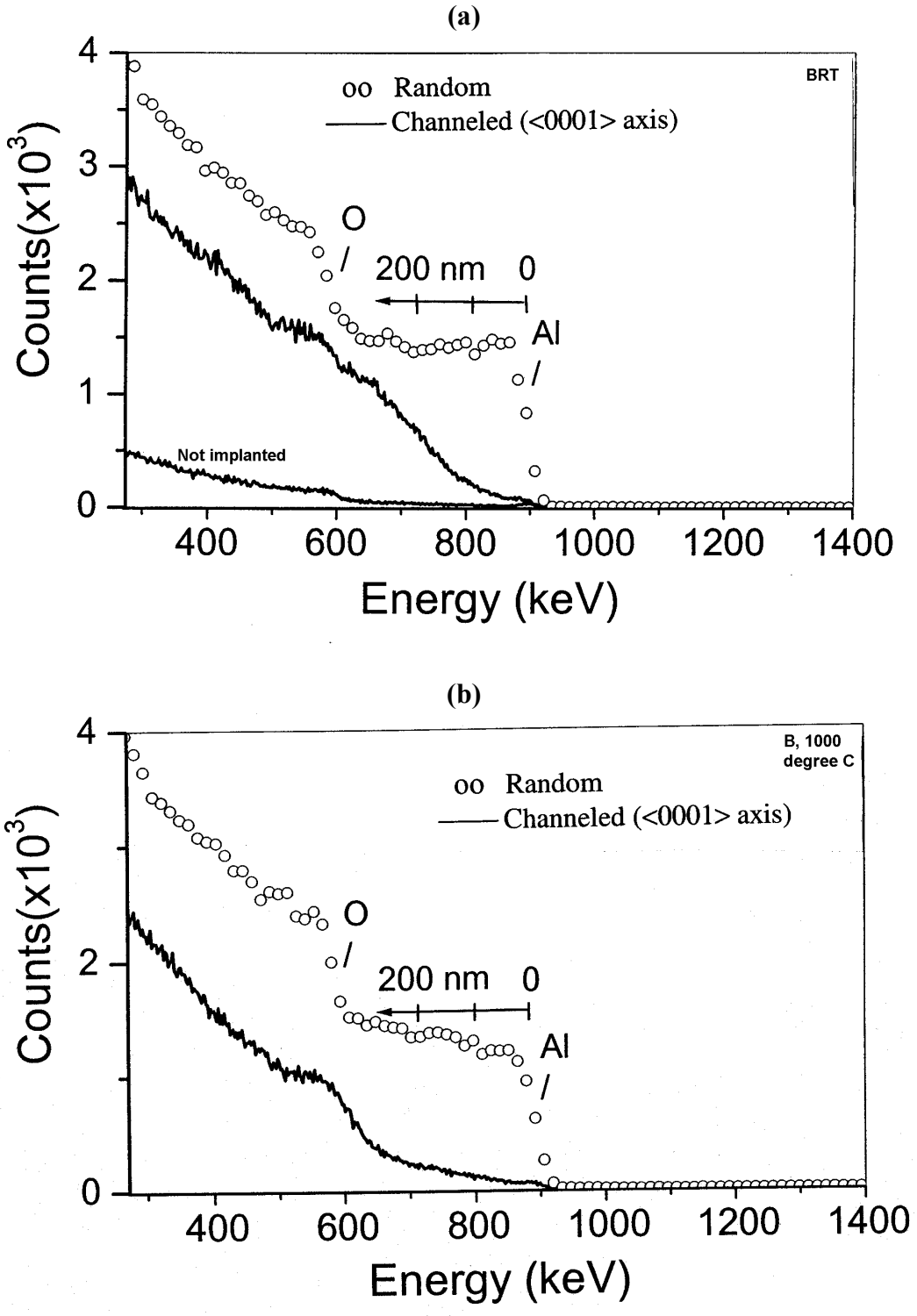


Figure 4.14: RBS spectra for α–Al_2O_3 specimens implanted with boron. (a) At room temperature and (b) at 1000°C.

A rough approximation of the disorder due to defects in a given sublattice is given by the slope of the aligned spectrum, after subtraction of the dechanneling in the aligned spectrum from a perfect (unimplanted) crystal [71]. The slope of the aligned Al-spectrum is approximately constant with a value of ~ 0.3 over a depth from just behind the surface peak (40 nm) to a depth of ~ 130 nm. There is a sharp increase in the slope to ~ 1.25 for the range of 130 to 260 nm. Examination of the TRIM plot for vacancy production as a function of depth (Figure 4.3) indicates that an increase in Al- vacancy production occurs at ~ 140 – 150 nm.

The RBS-C spectra for the crystal implanted with boron at 1000^{o}C are given in Figure 4.14(b). There is much less disorder (dechanneling) in the Al-sublattice (aligned spectrum) compared to the crystal implanted with boron to the same fluence at room temperature. The slope of the aligned spectrum is approximately constant at a value of ~ 0.13 for depths of 40 nm to ~ 250 nm. The slope increases as the depth approaches the position of maximum energy deposition (vacancy production) at 286 nm (see Figure 4.3: TRIM plot of vacancy production).

4.1.4. *Optical Absorption Measurements*

The optical absorption spectrum for sapphire implanted with 1×10^{17} B/cm^2 (150 keV) at room temperature is shown in Figure 4.15. It is characterized by a very strong, sharp absorption band centered at 206 nm and a weaker broad band at ~ 270 nm. Both F - and F^+ - centers have an absorption band near 200 nm: F at 205 nm; F^+ at 203 nm. The symmetry of the observed peak suggests that there is only one component and the lack of a band at 258 nm suggests that this band is due to a large concentration of F – centers. The observations of Dalal et al. [43] also suggest that F – centers are favored due to the low density cascades produced by B-implantation. The band at ~ 270 nm does not correspond to any defect listed in Table 2.2. It likely denotes a cluster of oxygen vacancies, possibly stabilized by the presence of one or more boron ions.

The optical absorption spectrum for the boron implanted at 1000^{o}C is also shown in Figure 4.15. The intensity of the absorption band near 200 nm is much reduced compared to the sample implanted at room temperature, consistent with the RBS-C

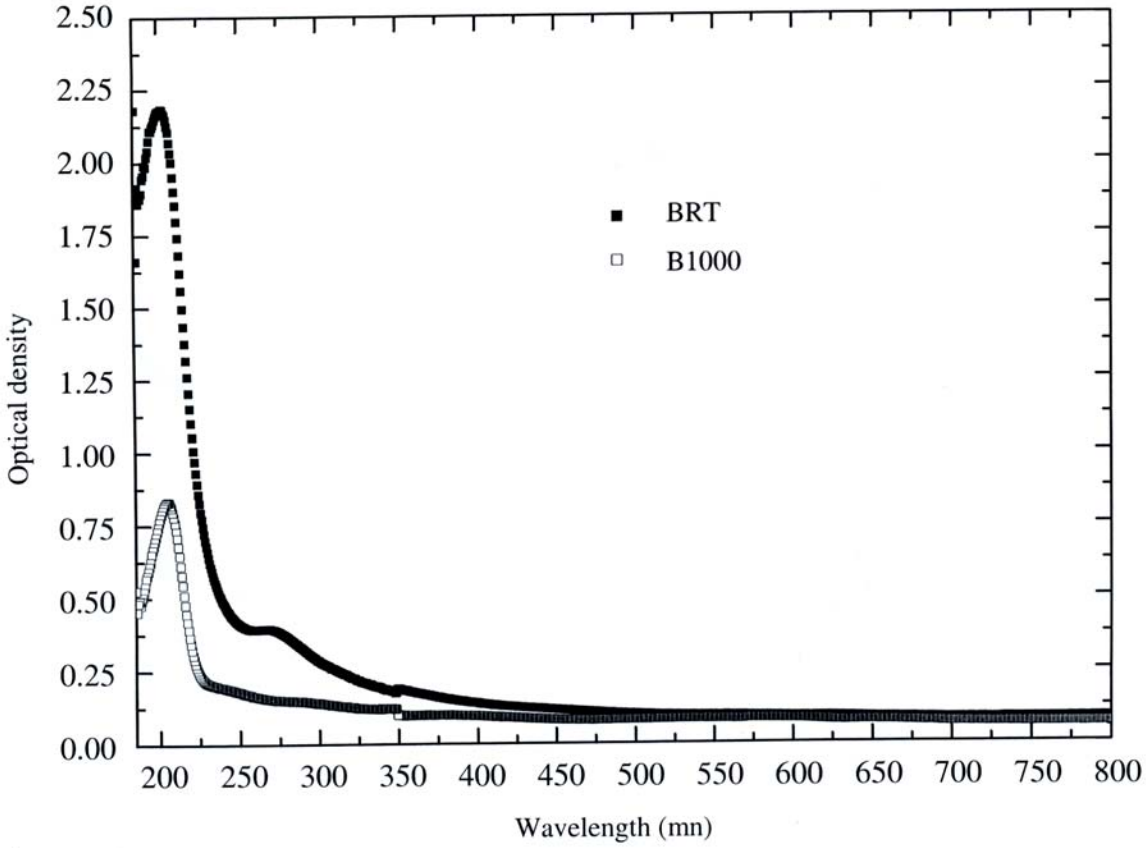


Figure 4.15: Optical absorption spectra for $\alpha-Al_2O_3$ specimen implanted with boron at room temperature and 1000^{o}C.

results that show much less retained disorder in this sample. The spectrum contains a hint of absorption bands at ~ 250 nm and near 300 nm. The band at 300 nm could arise from F_2 centers (clusters of 2 F center). The band at 250nm could be due to F^+-centers whose position is slightly shifted or to some other configuration involving oxygen vacancy clusters.

4.1.5. *X-ray Diffraction*

A further attempt to find boron and or identify a second phase in the boron-implanted specimen was carried out using x-ray diffraction technique. X-ray diffraction spectra for boron implanted sapphire at room temperature and at 1000^{o}C are shown in Figures 4.16 and 4.17 respectively. There is no boron peak observed.

4.1.6. *X-ray Photoelectron Spectroscopy*

Surface analysis by X-ray Photoelectron Spectroscopy (XPS) or Electron Spectroscopy for Chemical Analysis (ESCA) is accomplished by irradiating a sample with monoenergetic soft x-rays and analyzing the energy of the detected electrons. Mg Kα (1253.6 eV) x-ray was used. The photons have limited penetrating power in a solid on the other of 1-10 microns. They interact with atoms in the surface region causing electrons to be emitted by photoelectric effect. The emitted electrons have measured KE given by

$$KE = h\upsilon - BE$$

Where hυ is the energy of the photon and BE is the binding energy. The XPS spectrum obtained for boron implanted with sapphire at room temperature is shown in Figure 4.18; and no boron peak was detected.

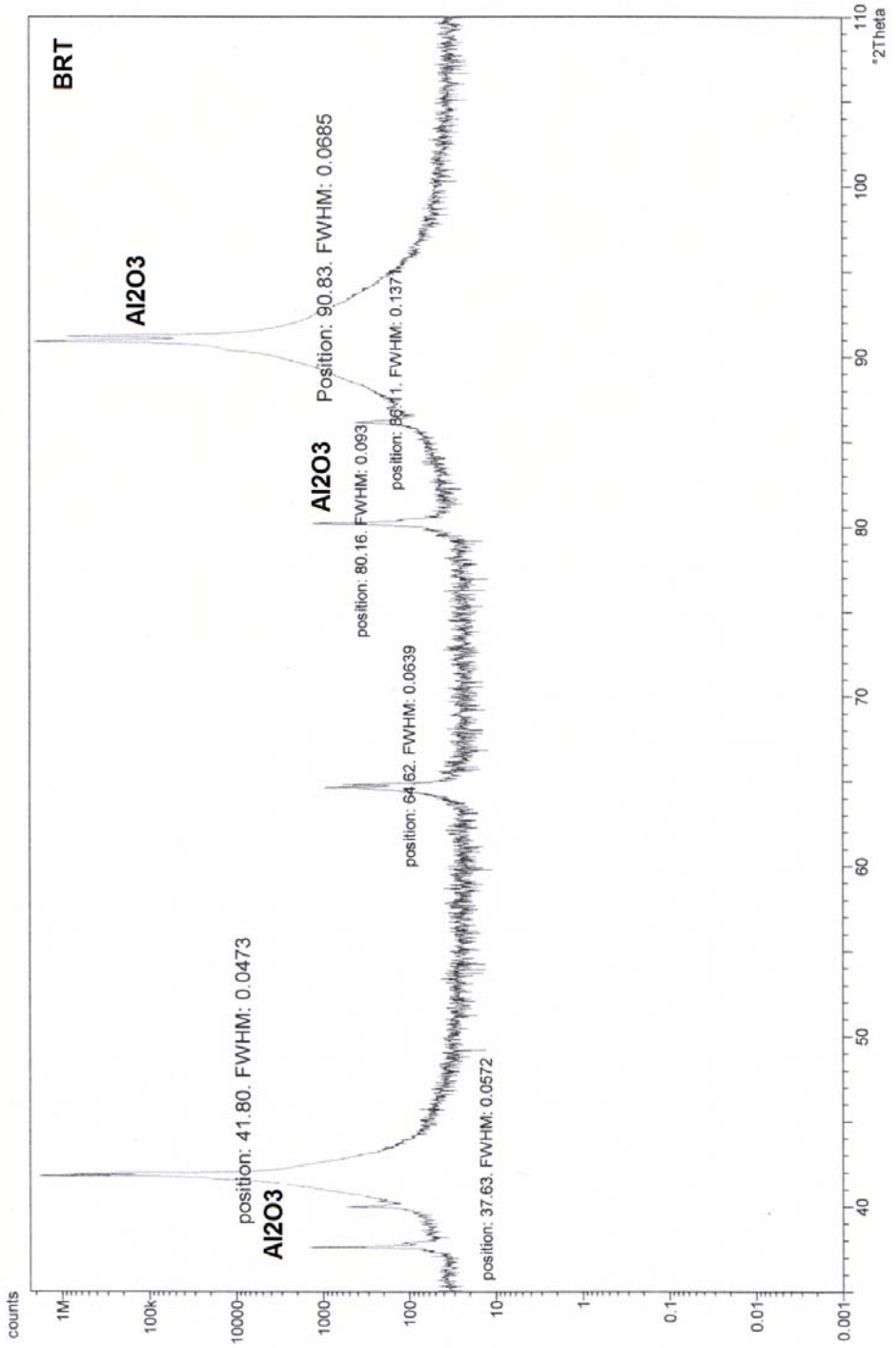


Figure 4.16: XRD spectrum for $\alpha-Al_2O_3$ specimen implanted with boron at room temperature.

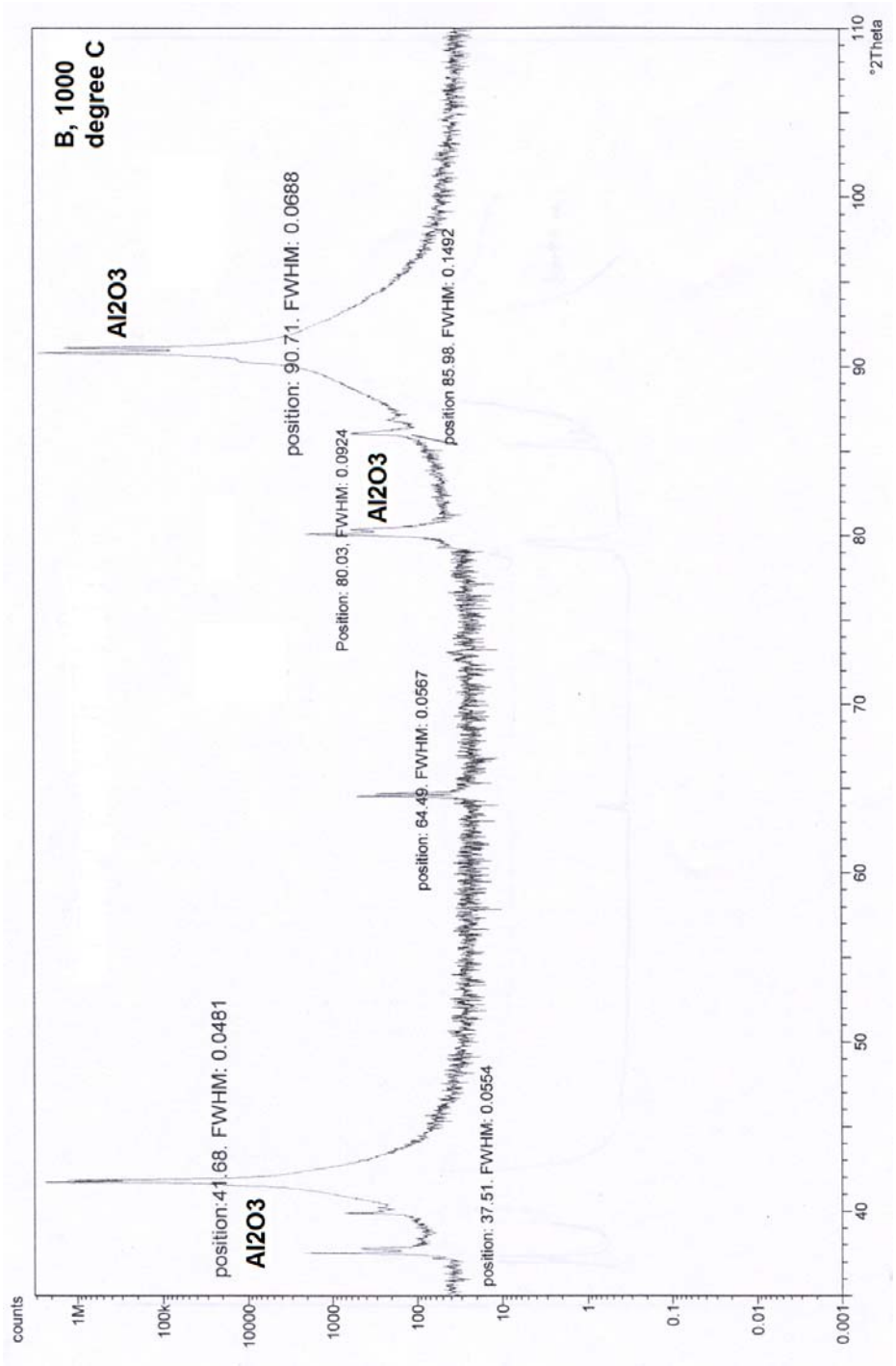


Figure 4.17: XRD spectrum for $\alpha-Al_2O_3$ specimen implanted with boron at 1000°C.

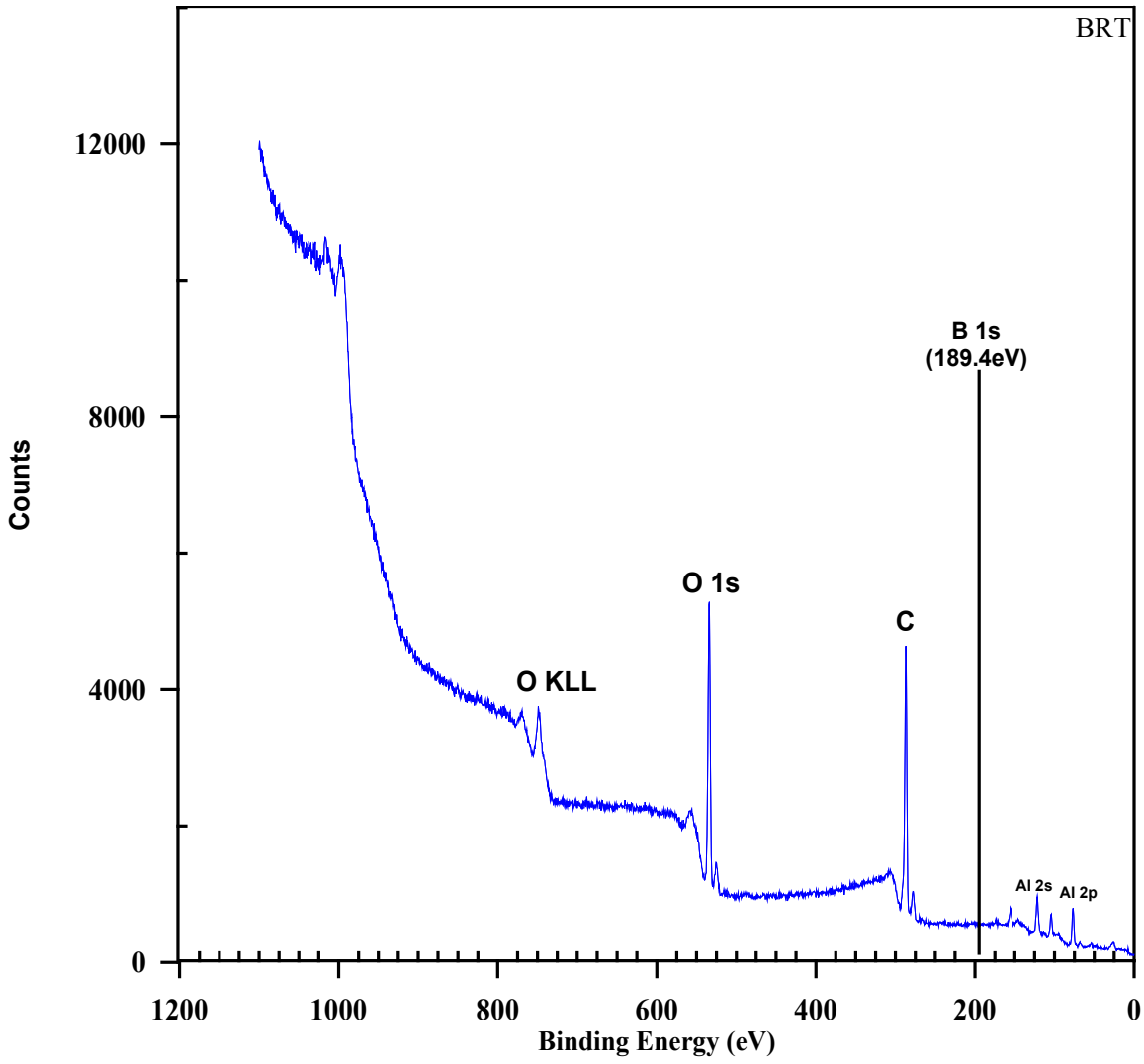


Figure 4.18: XPS spectrum for α–Al_2O_3 specimen implanted with boron at room temperature.

4.2. Nitrogen Implanted Sapphire (α-Al_2O_3)

4.2.1. *TRIM Calculations*

The range of ion (R_p), the range straggle and the number of vacancies per ion for 3×10^{16} N^+/cm^2 (150 keV) are 223.3 nm, 48.3 nm and 565 respectively, as calculated from TRIM program. The energy deposited (per ion) and vacancies produced per lattice ion are modeled with respect to position in the target as shown in Tables 4.3 and 4.4 respectively. The simulated nitrogen ions trajectories in sapphire are shown in Figure 4.19. The distribution of nitrogen ions, defects (the vacancies produced per lattice ion (dpa)) and deposited energy (electronic and nuclear) as a function of target depth are shown in Figures 4.20, 4.21, 4.22 and 4.23, and are based on 9999 incident ions per surface atom (ion). Since TRIM is a Monte Carlo calculation based on two-body interactions, the large number of incident ions is required to give satisfactory statistics to the calculated values. The areal density of ions for sapphire is 2.37×10^{15} ions/cm^2. For a fluence (dose) of 3×10^{16} N/cm^2 into sapphire, each surface ion is struck about 10 times compare to about 40 times for the boron implant at a fluence (dose) of 1×10^{17} B/cm^2. Because of lateral spreading, the ions located away from the surface will be struck to more ions as indicated in the figures.

The peak concentration of N using the data from Figure 4.20 and the fluence of 3×10^{16} N/cm^2 is calculated to be approximately 0.096 N per Al ion, which is about 10% in concentration. The data in Figures 4.21, 4.22 and 4.23 are shown per incident ion. The energy deposition (electronic and nuclear) per incident ion as a function of ion energy is also shown in Figures 4.24.

4.2.2. *Transmission Electron Microscopy*

Transmission electron micrographs of cross-sectioned samples of nitrogen implanted at room temperature are shown in Figures 4.25 (low and high magnification). The high magnification micrographs of Figure 4.25 (b & c) (bright and dark field images) reveal the presence of bubbles or voids in a band about 200nm wide, and centered about 200 nm from the surface; no other defects were visible. The

Table 4.3: Nitrogen energy deposited per incident N ion as a function of depth in the target material.

Target Position, x	**Inelastic (Ionizing or Electronic) (eV/Å)**			**Elastic (Displacement) (eV /Å)**	**Ratio (Inelastic/Elastic)**
	Ions	**Recoils**	**Total**		
Surface, x=0	60.0	3.2	63.2	8.0	7.9
Peak damage energy, x = 181nm	32.7	7.3	40.0	25.3	1.6
R_p, x = 223.3nm	20.0	6.0	26.0	18.0	1.4

Table 4.4: Vacancies produced per lattice ion (dpa) for a fluence of 3×10^{16} N^+/cm^2.

Target Position, x	**Al**	**O**
Surface, x=0	4.6	1.4
Peak damage energy, x = 181nm	15.0	4.8
R_p, x = 223.3nm	10.0	3.0

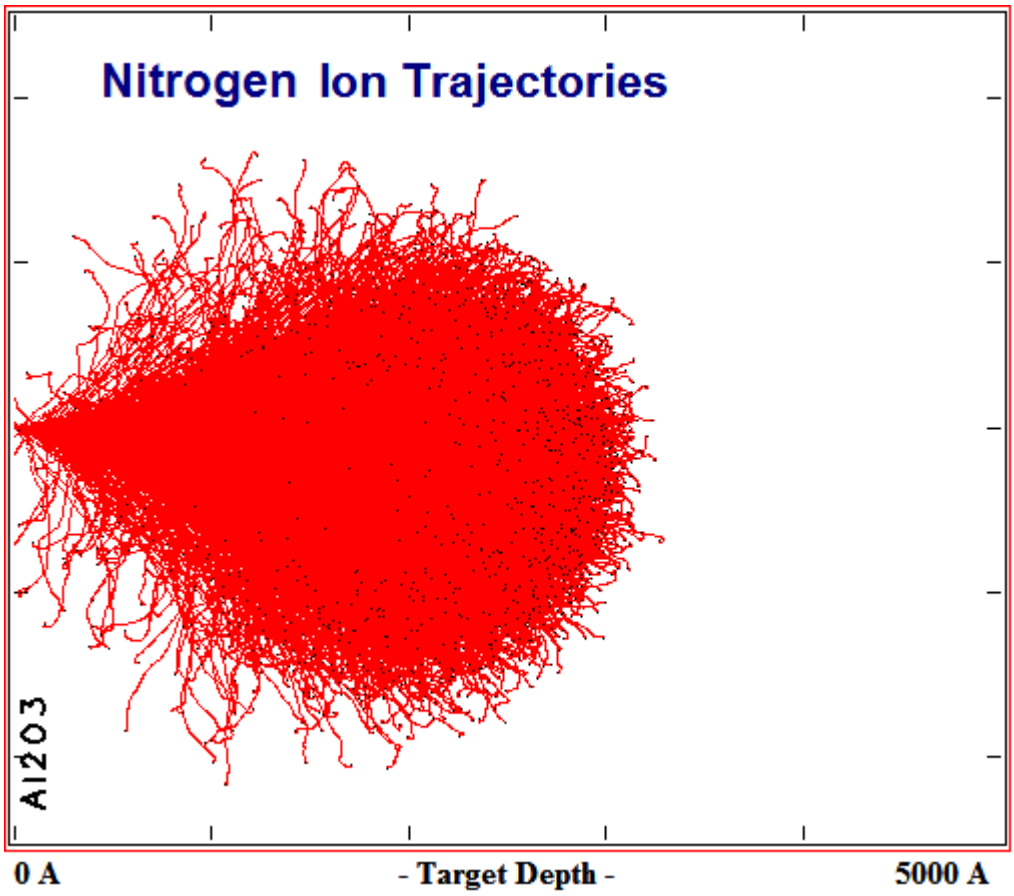


Figure 4.19: Nitrogen ion trajectories

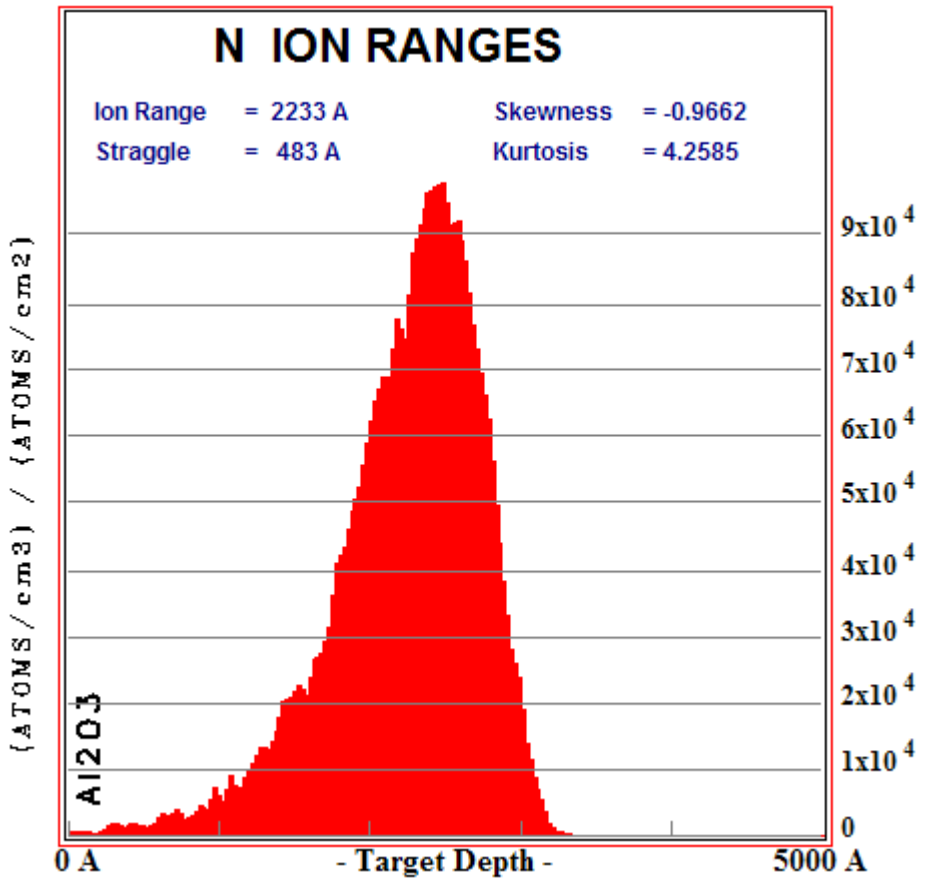


Figure 4.20: The range of nitrogen ion in sapphire as a function of depth.

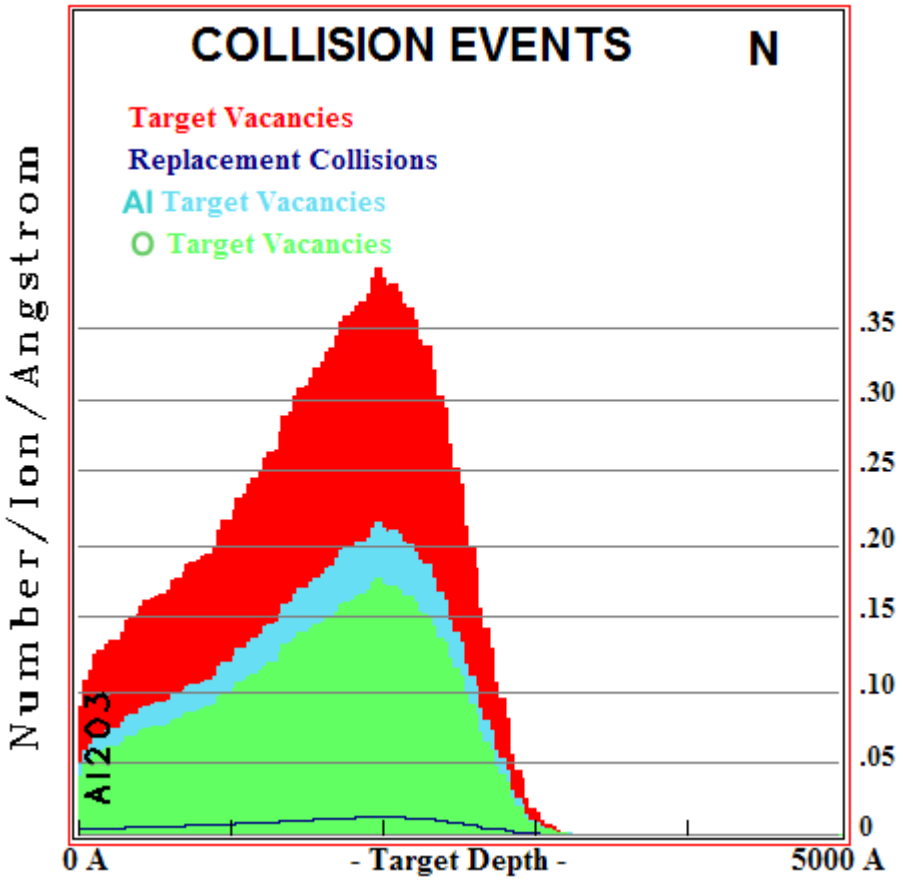


Figure 4.21: Nitrogen collision events showing the plots of the number of vacancies produced per lattice ion (dpa).

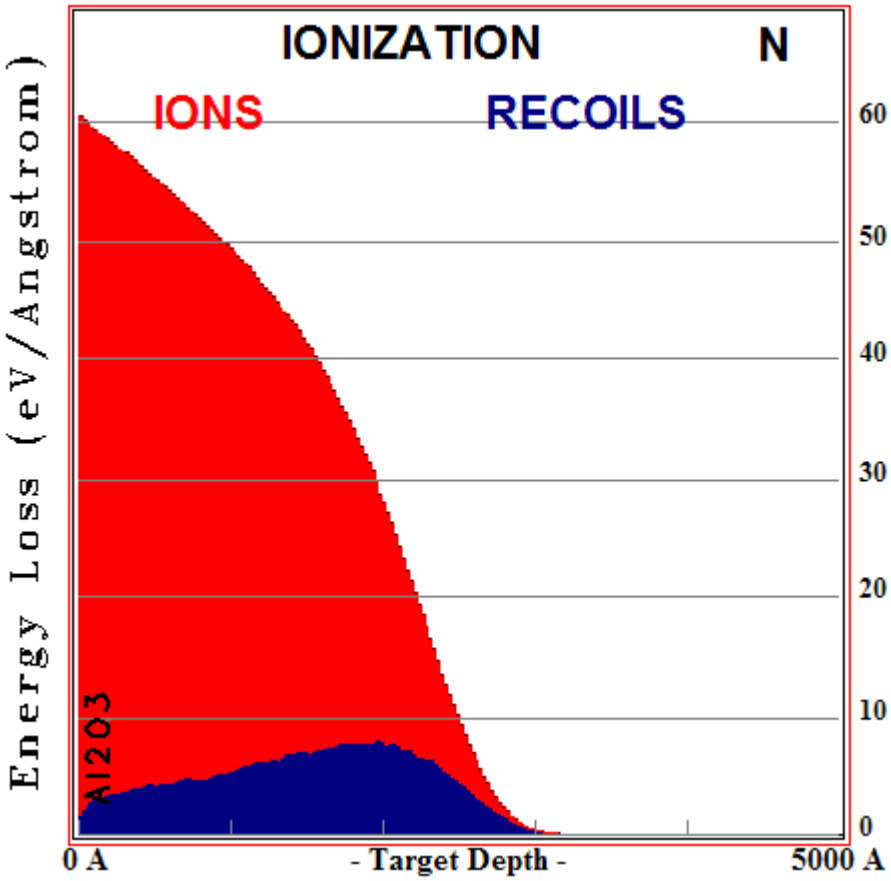


Figure 4.22: Plot of electronic (ionizing) energy loses with the target depth.

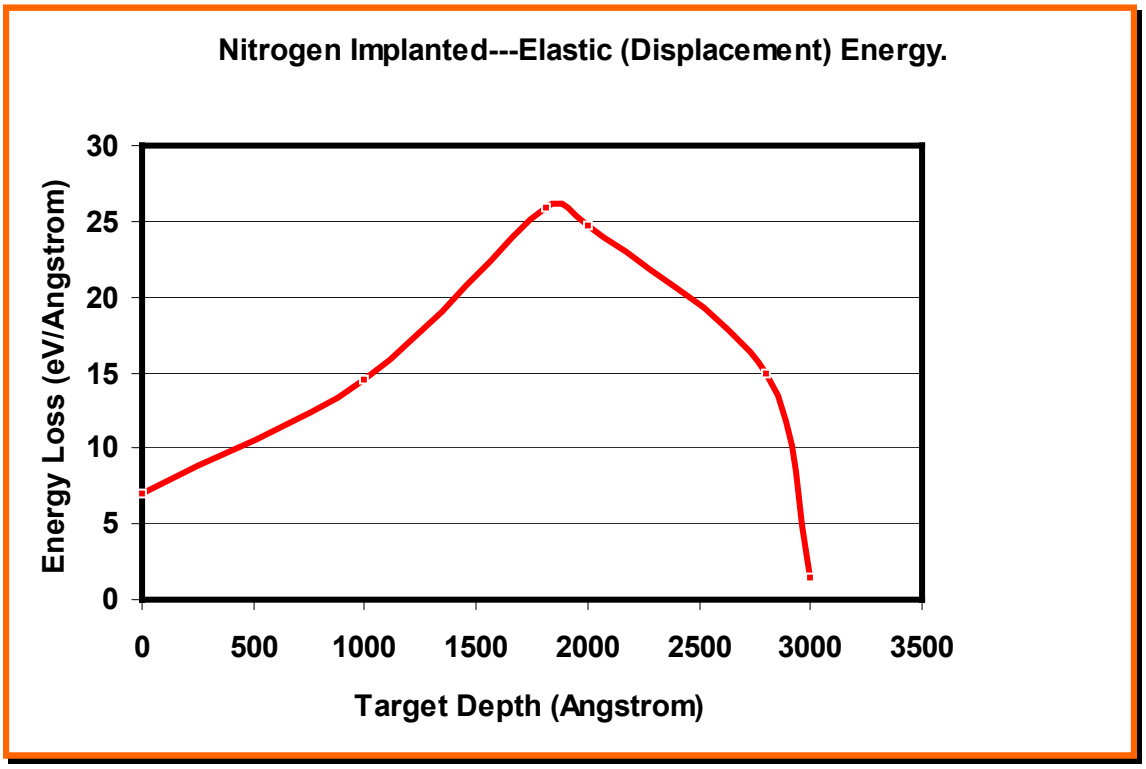


Figure 4.23: Plot of elastic (displacement) energy loses with the target depth.

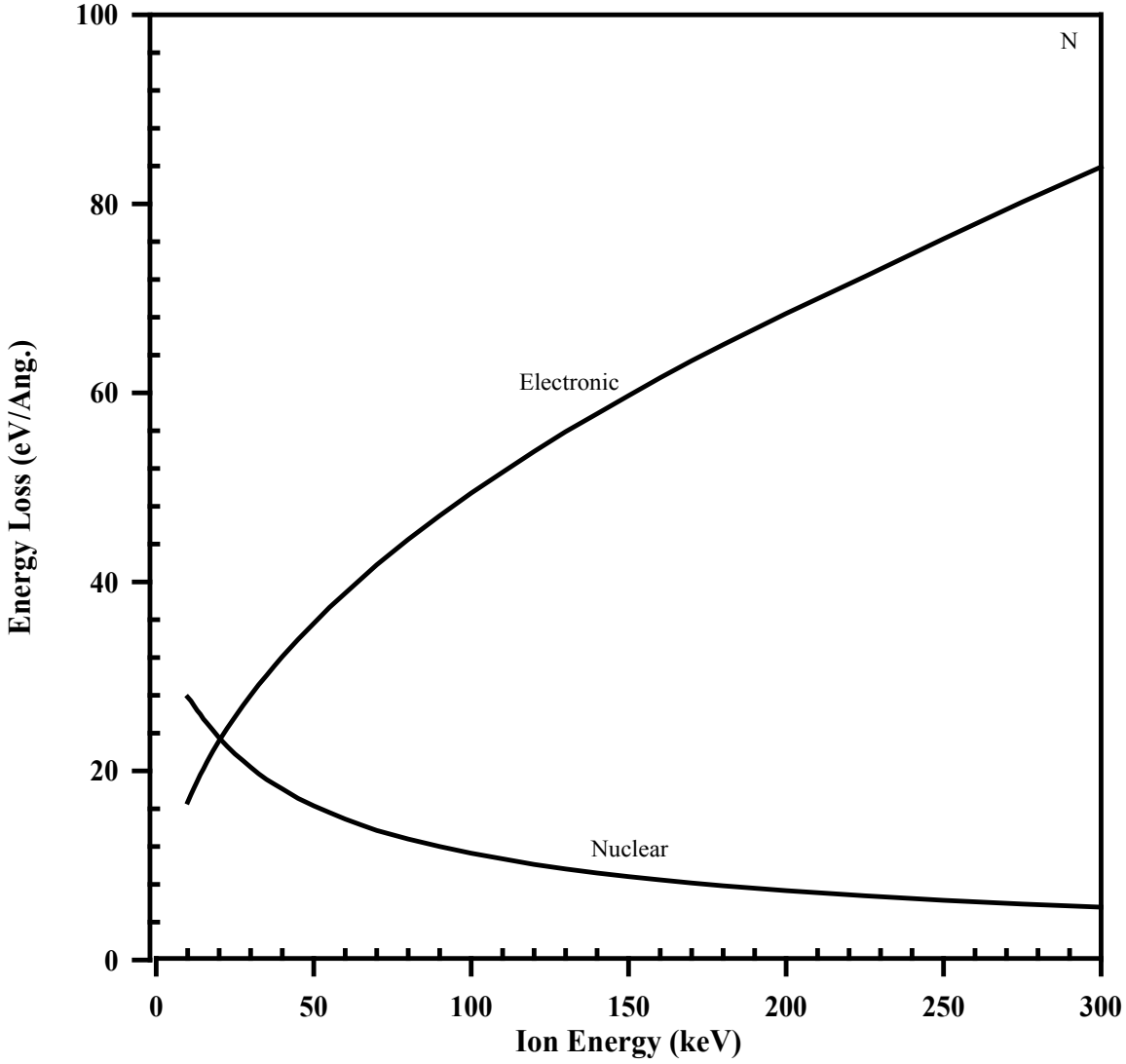


Figure 4.24: Plot of energy (electronic and nuclear) loses as a function of the nitrogen ion energy (the implant ion energy in this case is 150 keV).

(a)

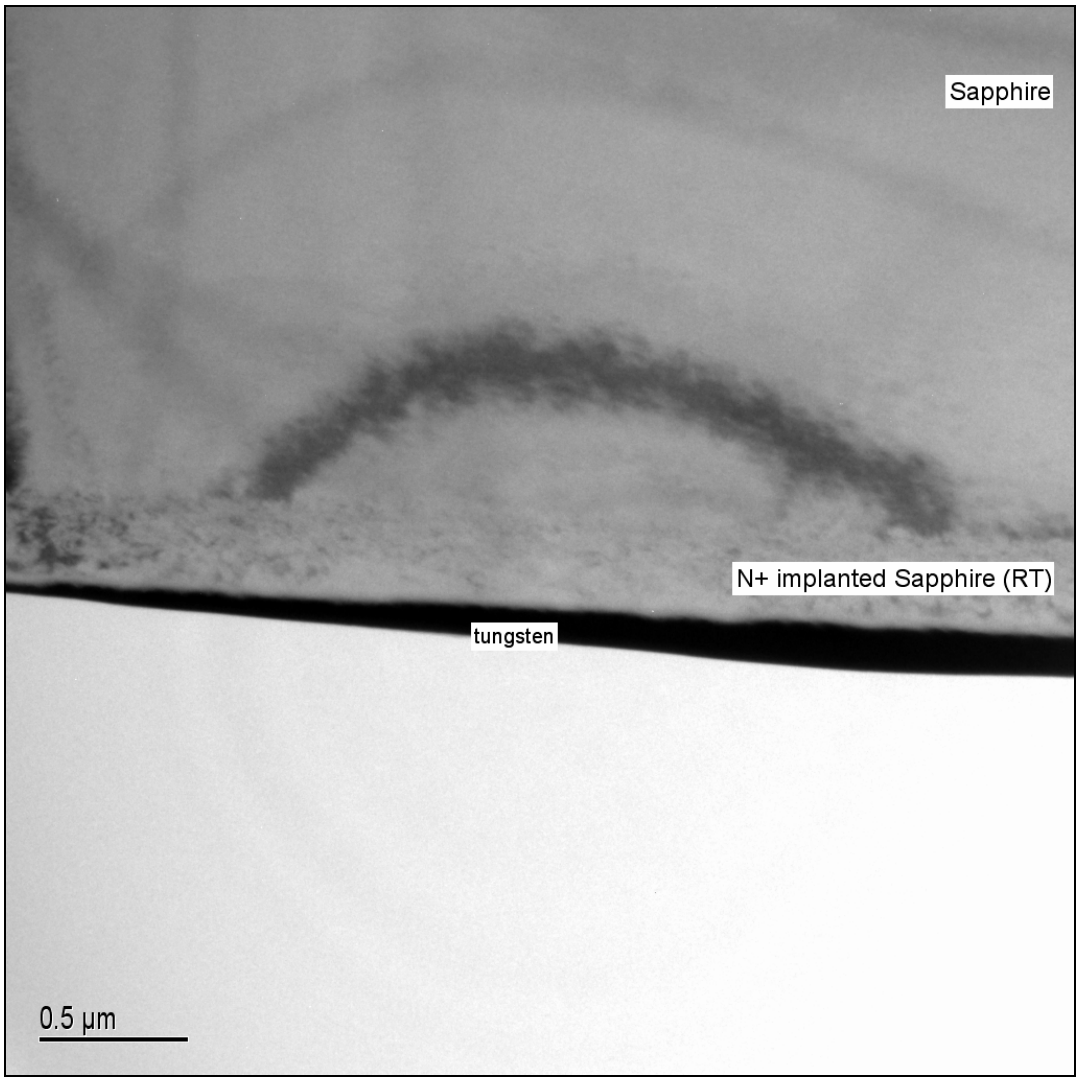


Figure 4.25: TEM cross-sectioned micrographs of α-Al_2O_3 specimen implanted with fluence of 3×10^{16} N/cm^2 (150 keV) at room temperature. (a) × 5K, (b) × 20K, (c) ×250K (Bright field image) and (d) ×250K (Dark field image).

(b)

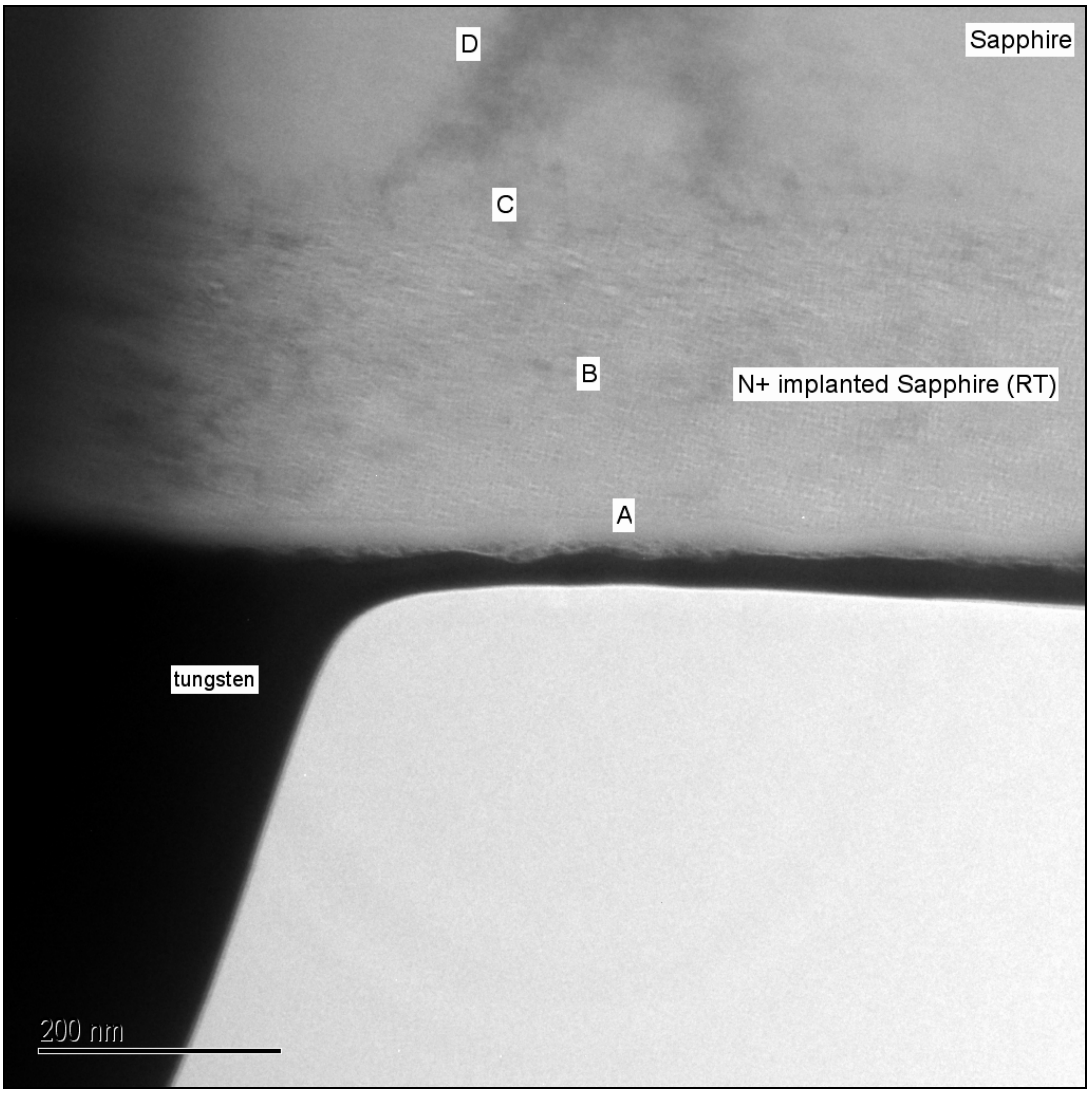


Figure 4.25 continued.

(c)



Figure 4.25 continued.

(d)

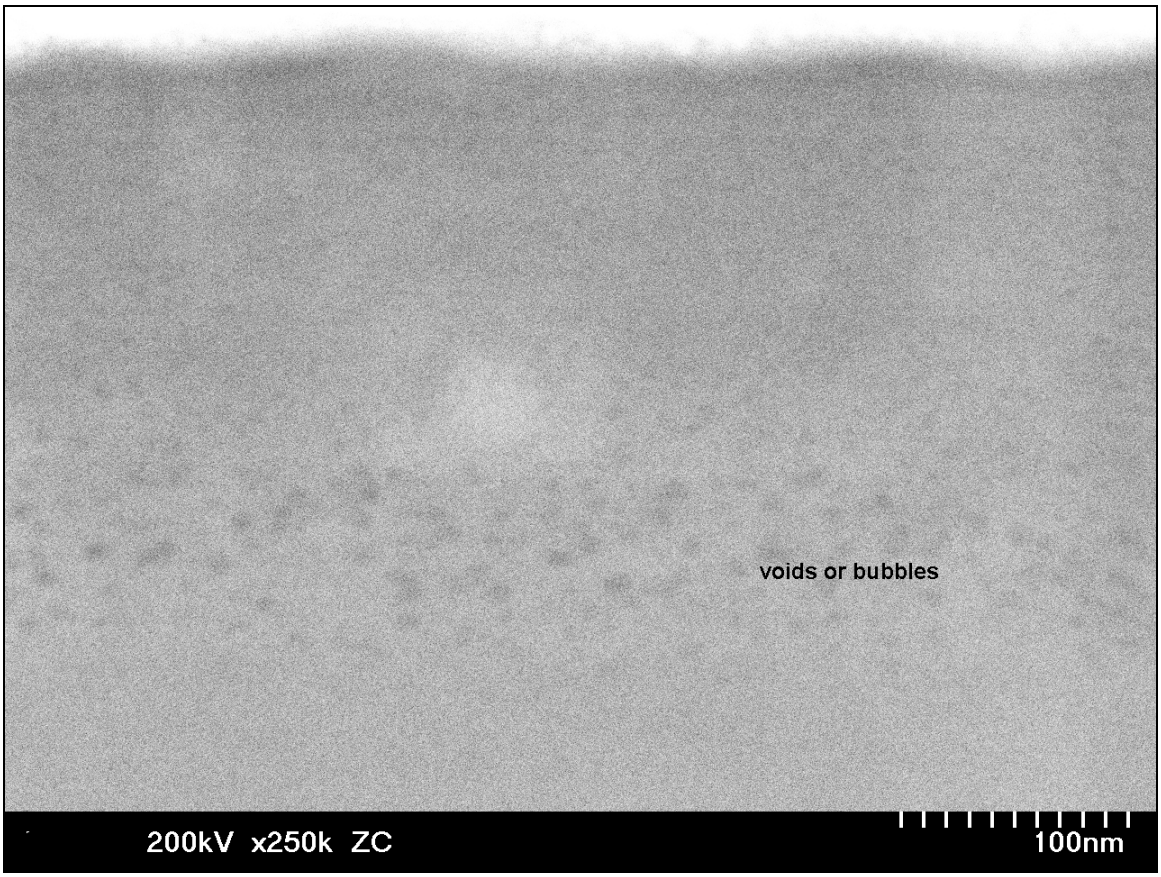


Figure 4.25 continued.

microstructures of nitrogen implanted α–Al_2O_3 at the fluence of 3×10^{16} N/cm^2 (150 keV) at 1000^{o}C are shown in Figure 4.26. These cross-sectional micrographs show a different type of "black spot" radiation damage. The exact nature of these clusters has not yet been determined. These features are generally ascribed to defect clusters. The selected area diffraction patterns for the room temperature and 1000^{o}C implants are shown in Figures 4.27 and 4.28 respectively. There are indications of a second phase observable by the presence of a few additional diffraction spots in the sample implanted at 1000^{o}C. The use of x-ray diffraction, electron micro-beam diffraction and convergent beam electron techniques to identify features were unsuccessful. The implanted regions remained crystalline as evidence from the selected area diffraction patterns.

The EDX spectra (Figure 4.29 and 4.30) showed only the presence of Al and O, and in the near surface region, gallium (Ga) retained from the ion milling and carbon contaminate.

The micrographs for room temperature implant cation followed by annealing in Ar-4% H_2 at 1000^{o}C for one hour micrographs are shown in Figure 4.31. The microstructural features reveal no "black spot" damage, but features that appear to be a second phase. The features differ from that implanted at room temperature and at 1000^{o}C. Attempts to identify these features by microbeam electron diffraction and convergent beam techniques were unsuccessful.

4.2.3. *Rutherford Backscattering Spectroscopy*

The RBS-C spectra for the sample implanted with 3×10^{16} N/cm^2 (150 keV) at room temperature are shown in Figure 4.32 (a). As for the boron implantation, the nitrogen spectra are hidden by the oxygen spectra. Scattering from the Al sublattice in the near-surface region (0 to 50 nm) differs only a little from that of the unimplanted crystal. Dechanneling increases rapidly at greater depth and χ_{Al} reaches a maximum value of only 0.16 at 265 nm. The low value of χ_{Al}, the shape of the aligned spectrum, and the depth in the random spectrum suggest that the dechanneling is not caused by disorder but by the presence of another scattering source. Since the implanted

(a)

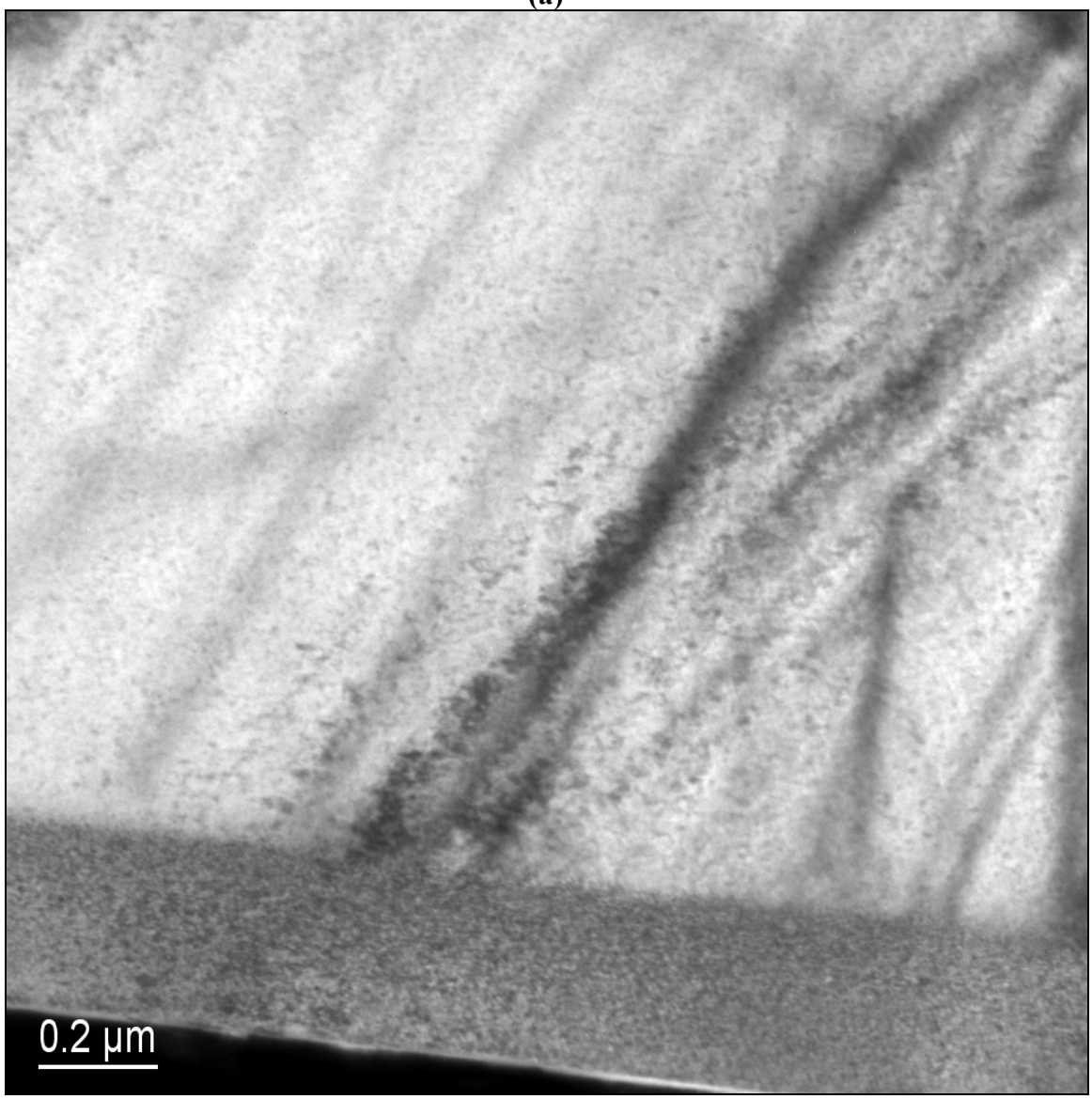


Figure 4.26: Cross-sectioned micrographs of α Al_2O_3 specimen implanted with fluence of 3×10^{16} N/cm^2 (150 keV) at 1000^{o}C. (a) x 10K, (b) x 20K and (c) 250 K.

(b)

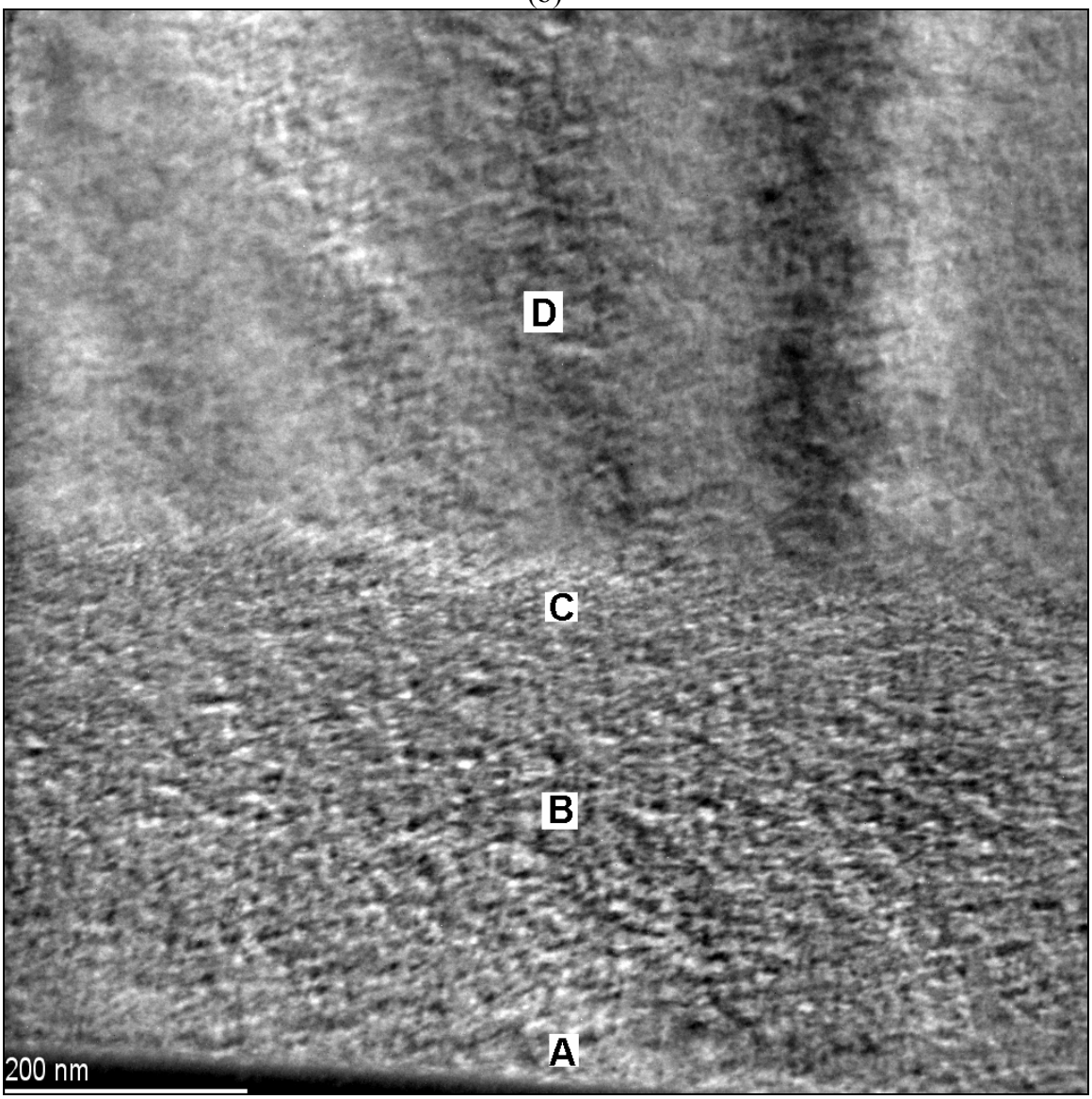


Figure 4.26 continued.

(c)

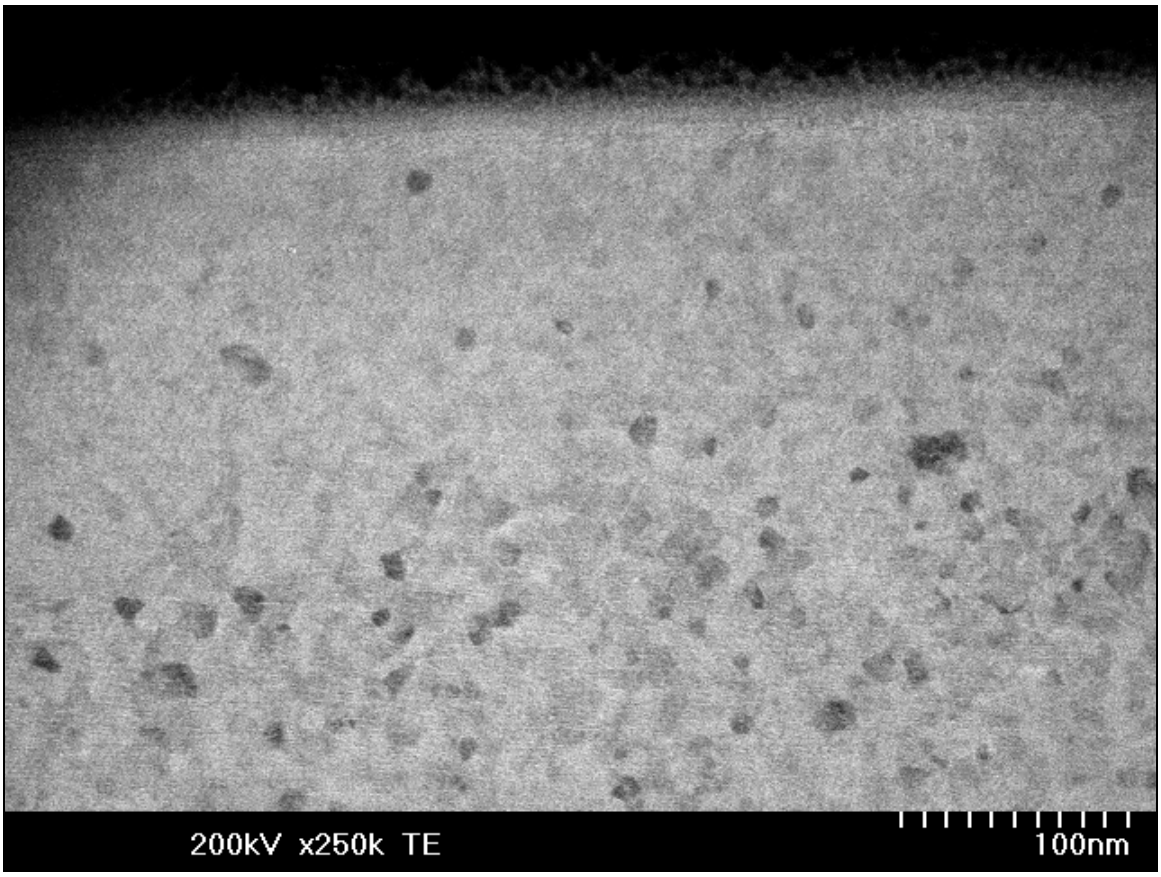


Figure 4.26 continued.

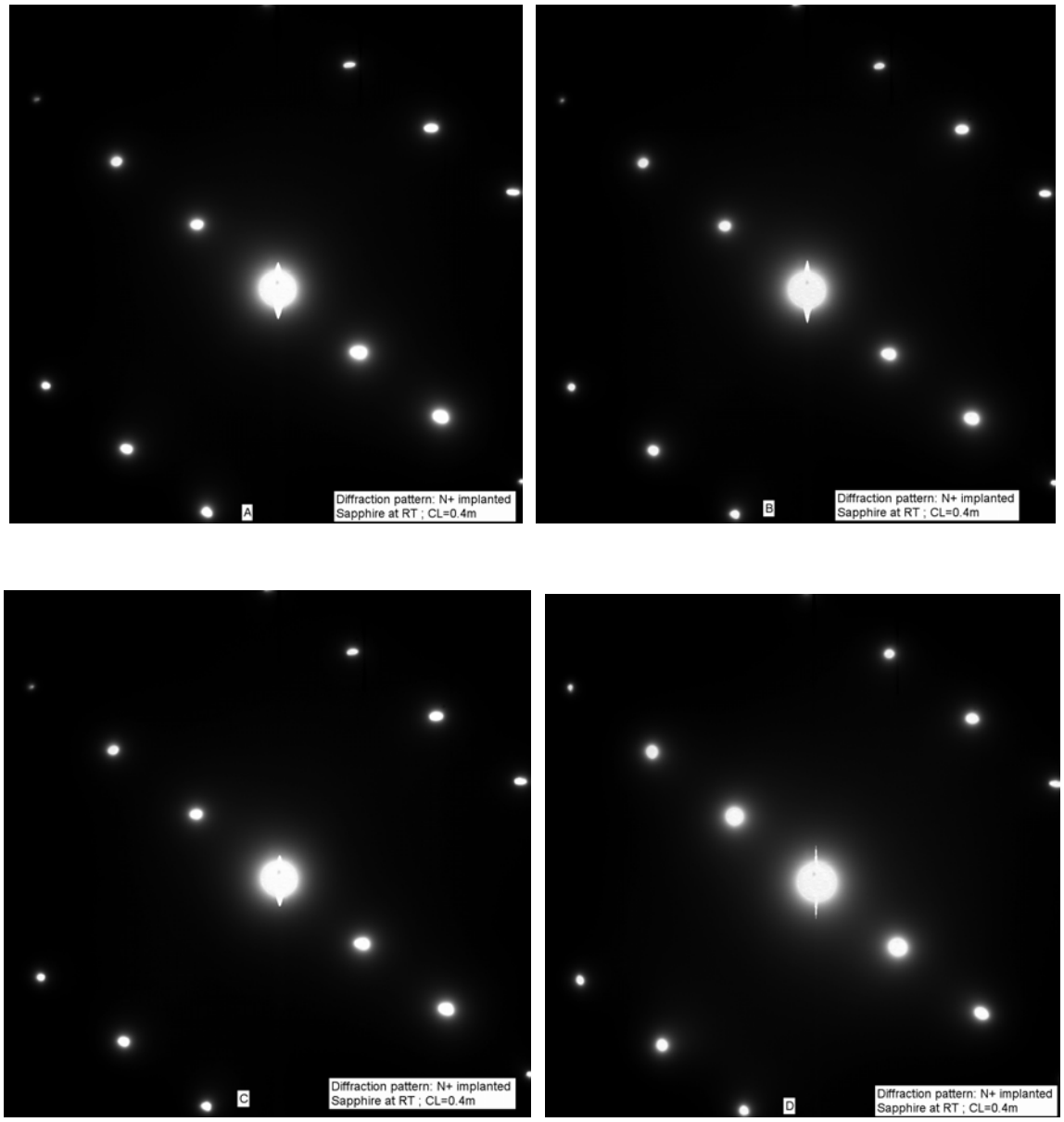


Figure 4.27: Selected area diffraction pattern of $\alpha-Al_2O_3$ specimen implanted with a fluence of 3×10^{16} N/cm^2 (150 keV) at room temperature. A, B, C and D are from regions A, B, C and D respectively of Figure 4.25(b).

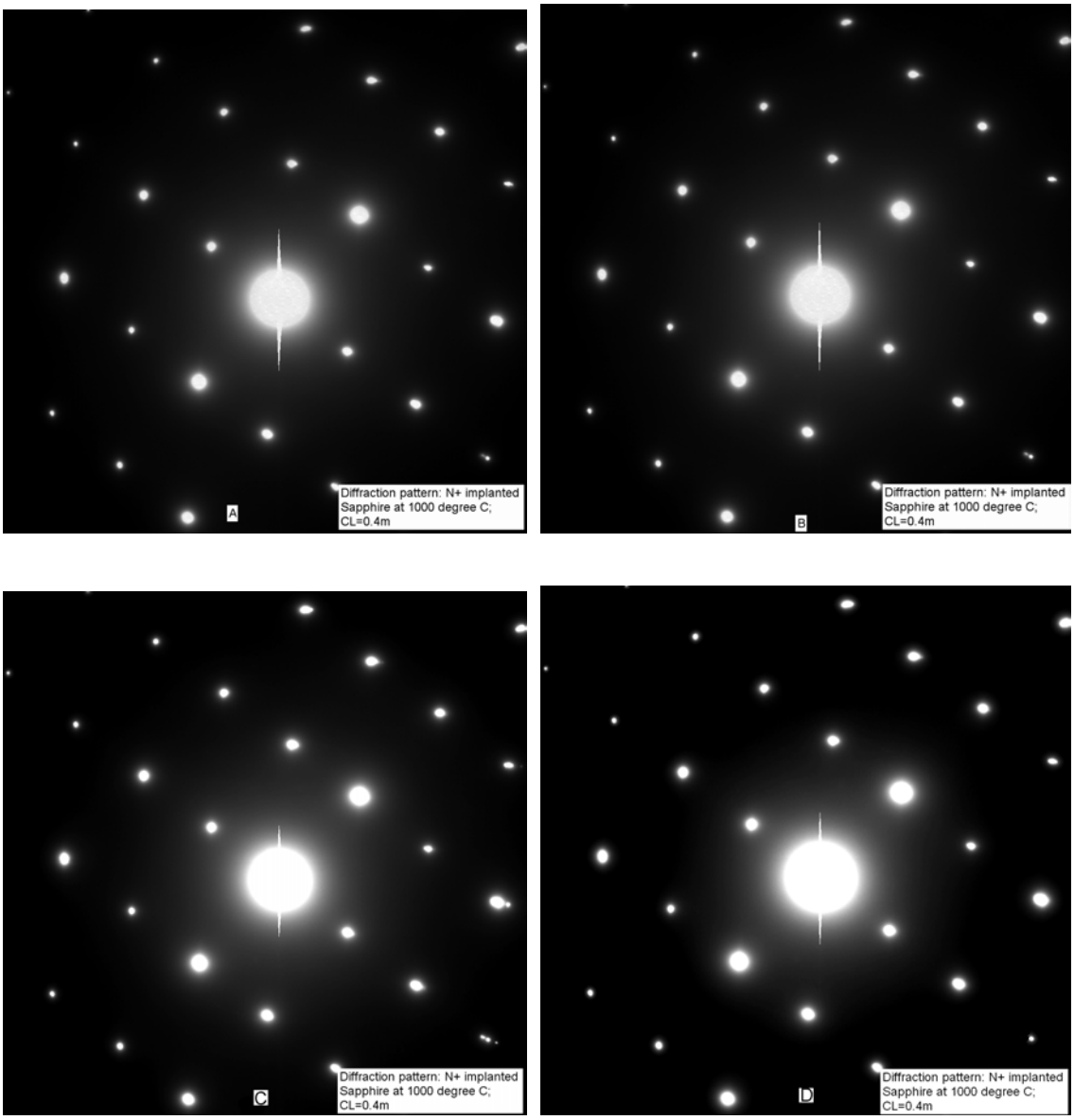


Figure 4.28: Selected area diffraction pattern of $\alpha-Al_2O_3$ specimen implanted with a fluence of 3×10^{16} N/cm^2 (150 keV) at 1000^{o}C. A, B, C and D are from regions A, B, C and D respectively of Figure 4.26 (b).

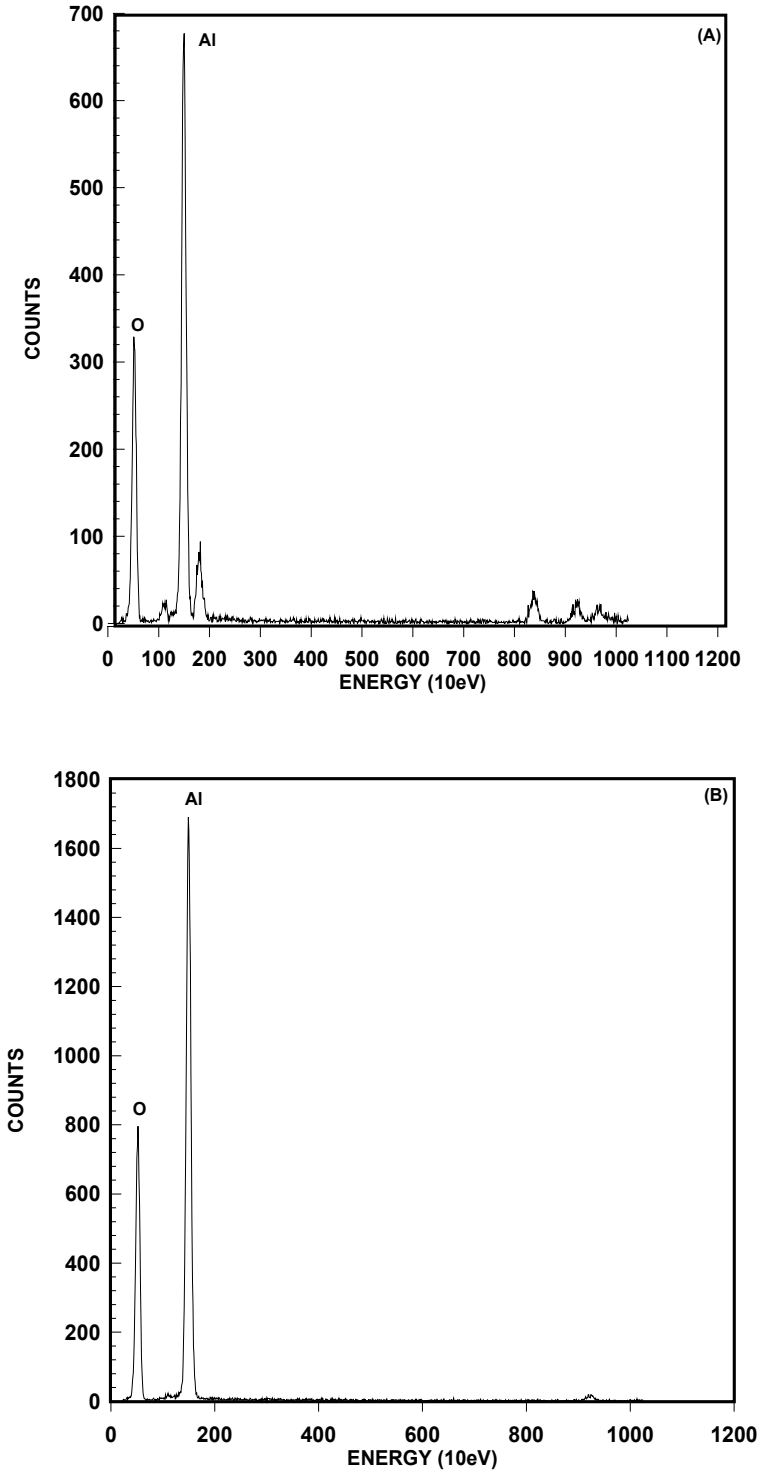


Figure 4.29: EDX spectra from a cross-sectioned $\alpha-Al_2O_3$ specimen implanted with nitrogen at room temperature. A and B are from B and D regions respectively of Figure 4.25 (b).

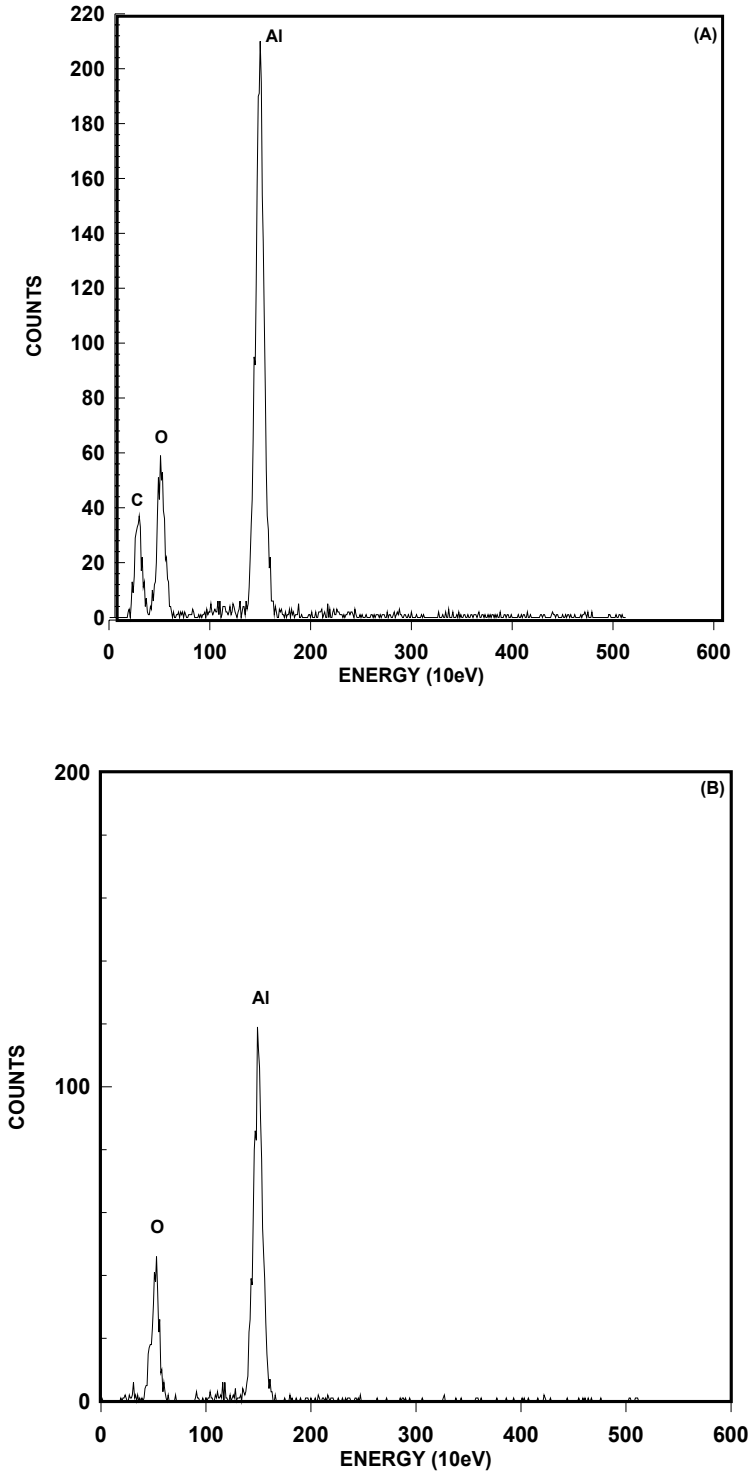


Figure 4.30: EDX spectra from a cross-sectioned $\alpha-Al_2O_3$ specimen implanted with nitrogen at 1000^{o}C. A and B are from B and D regions respectively of Figure 4.26 (b).

(a)

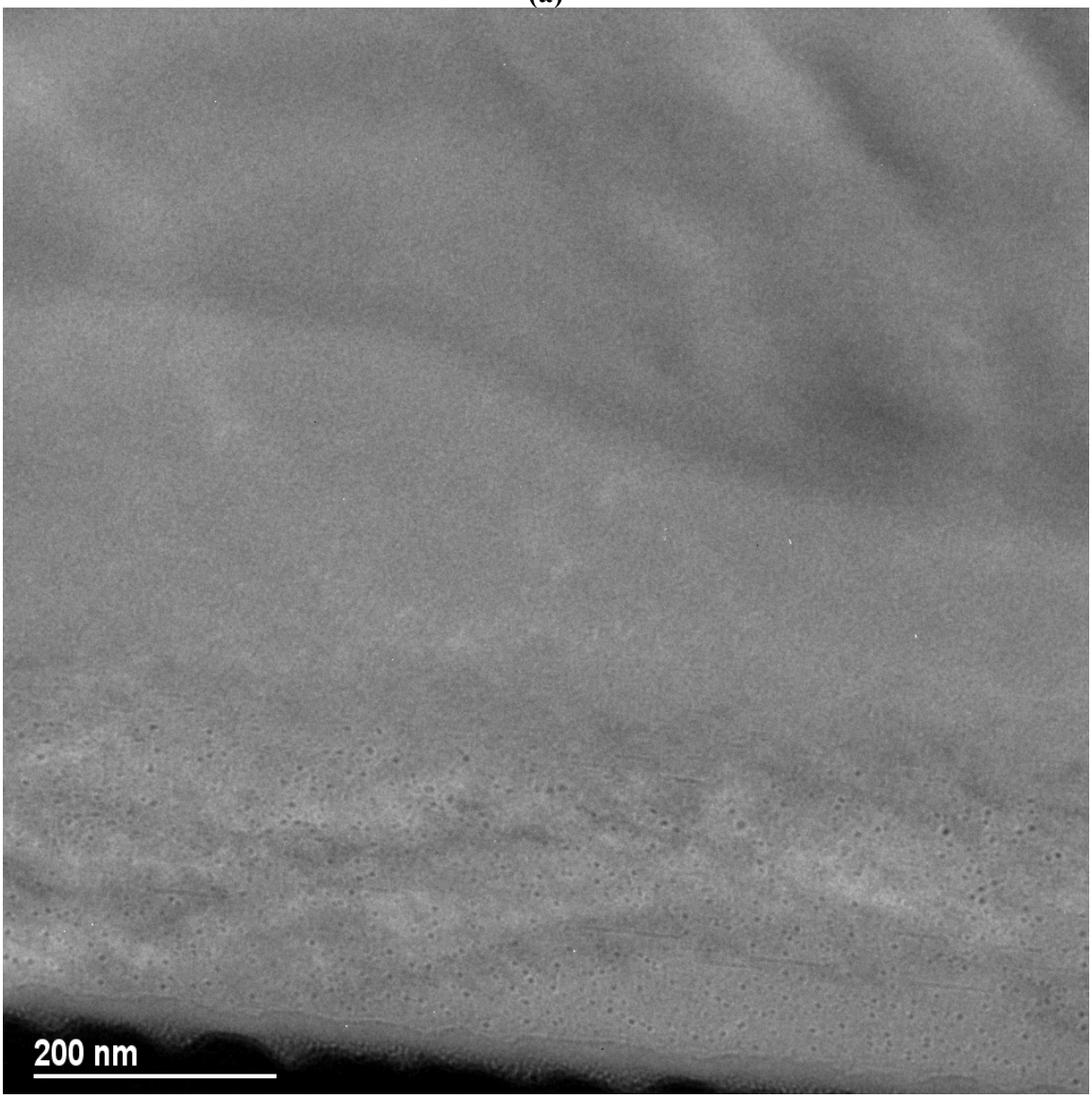


Figure 4.31: Cross-sectioned micrographs of α–Al_2O_3 specimen implanted with a fluence of 3×10^{16} N/cm^2 (150 keV) at room temperature and annealed in Ar-4% H_2 at 1000^{o}C for 1 hour. (a) x 20K, (b) x 40K and (c) x 80K.

(b)

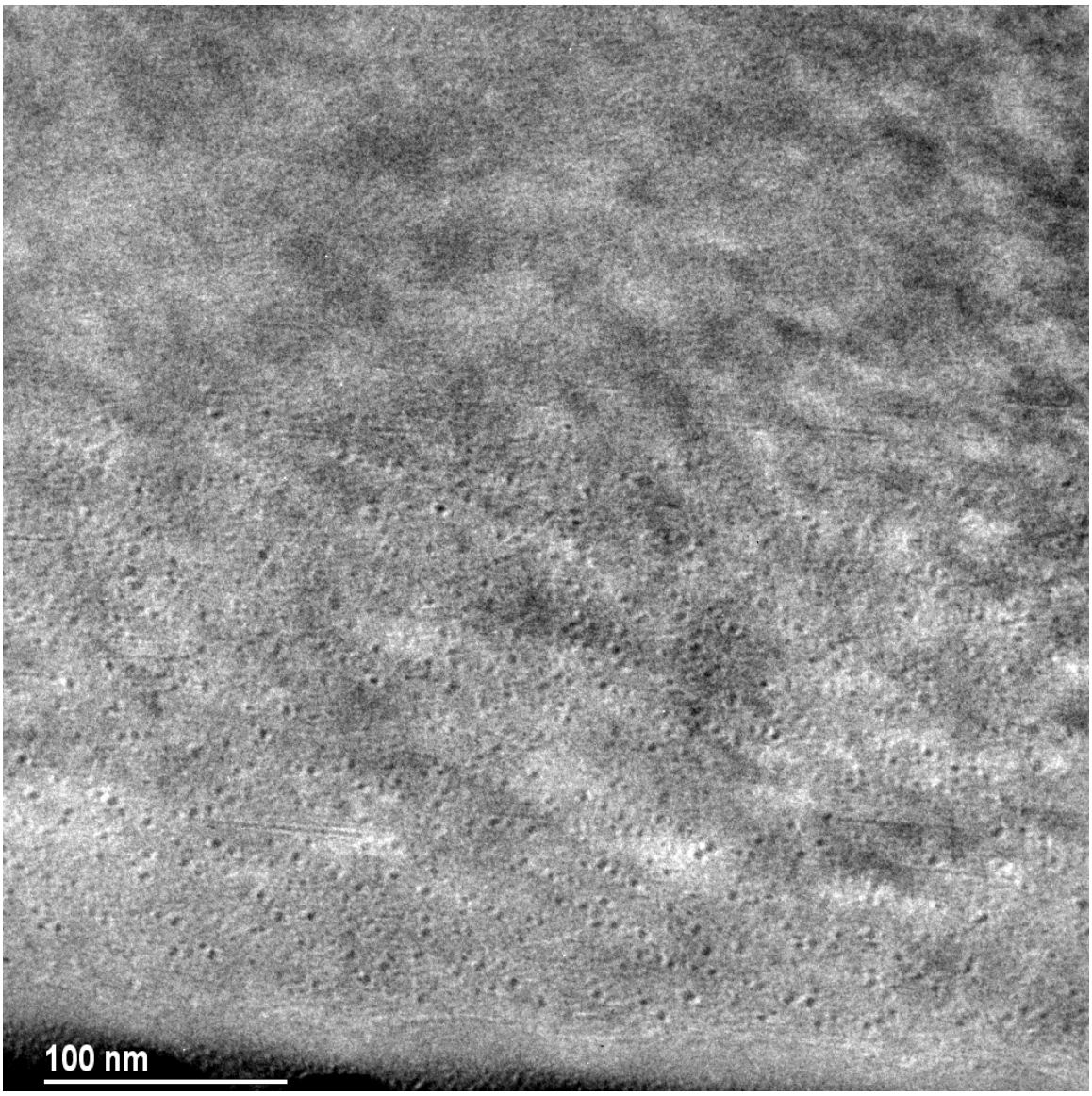


Figure 4.31 continued.

(c)

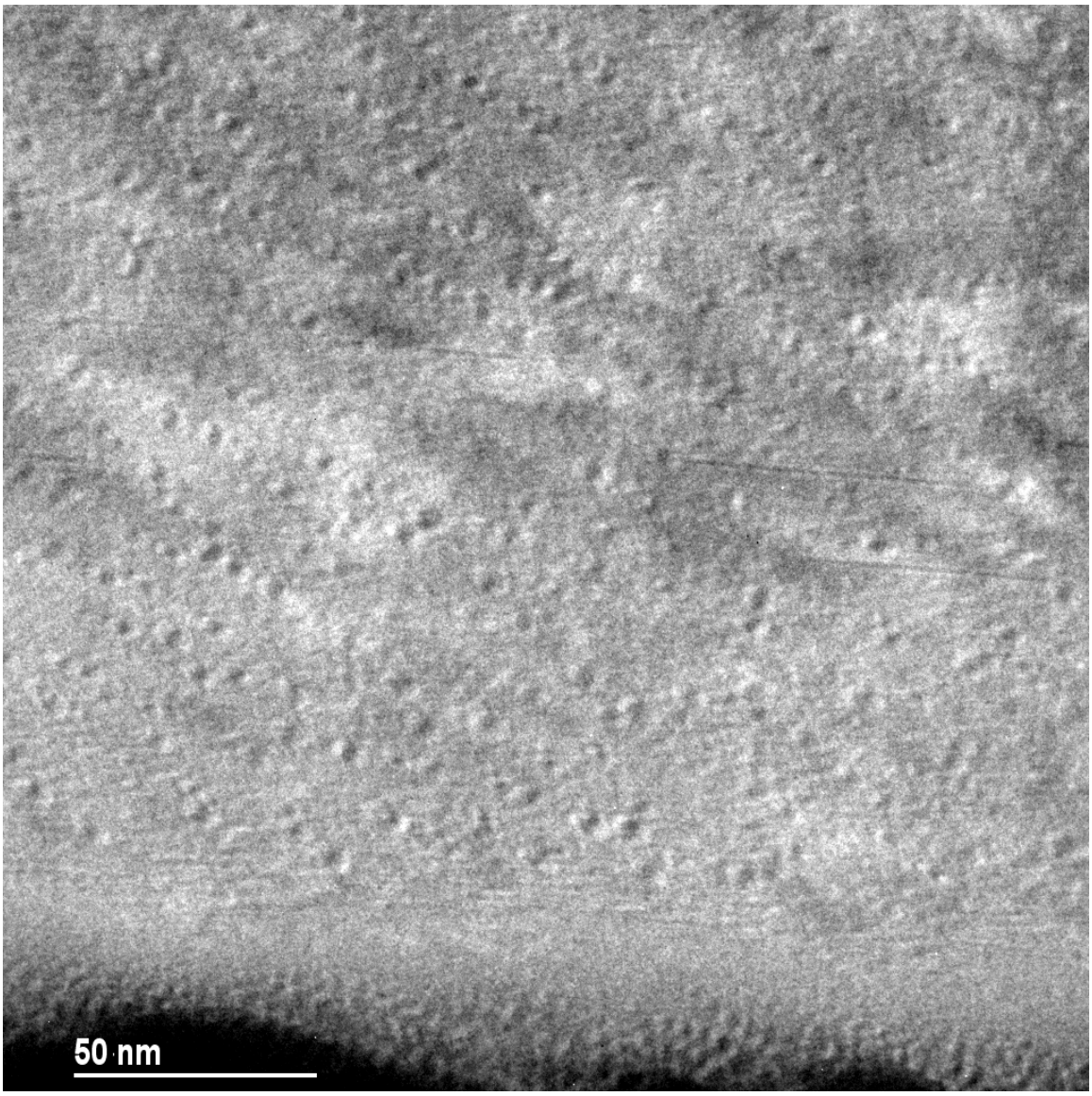


Figure 4.31 continued.

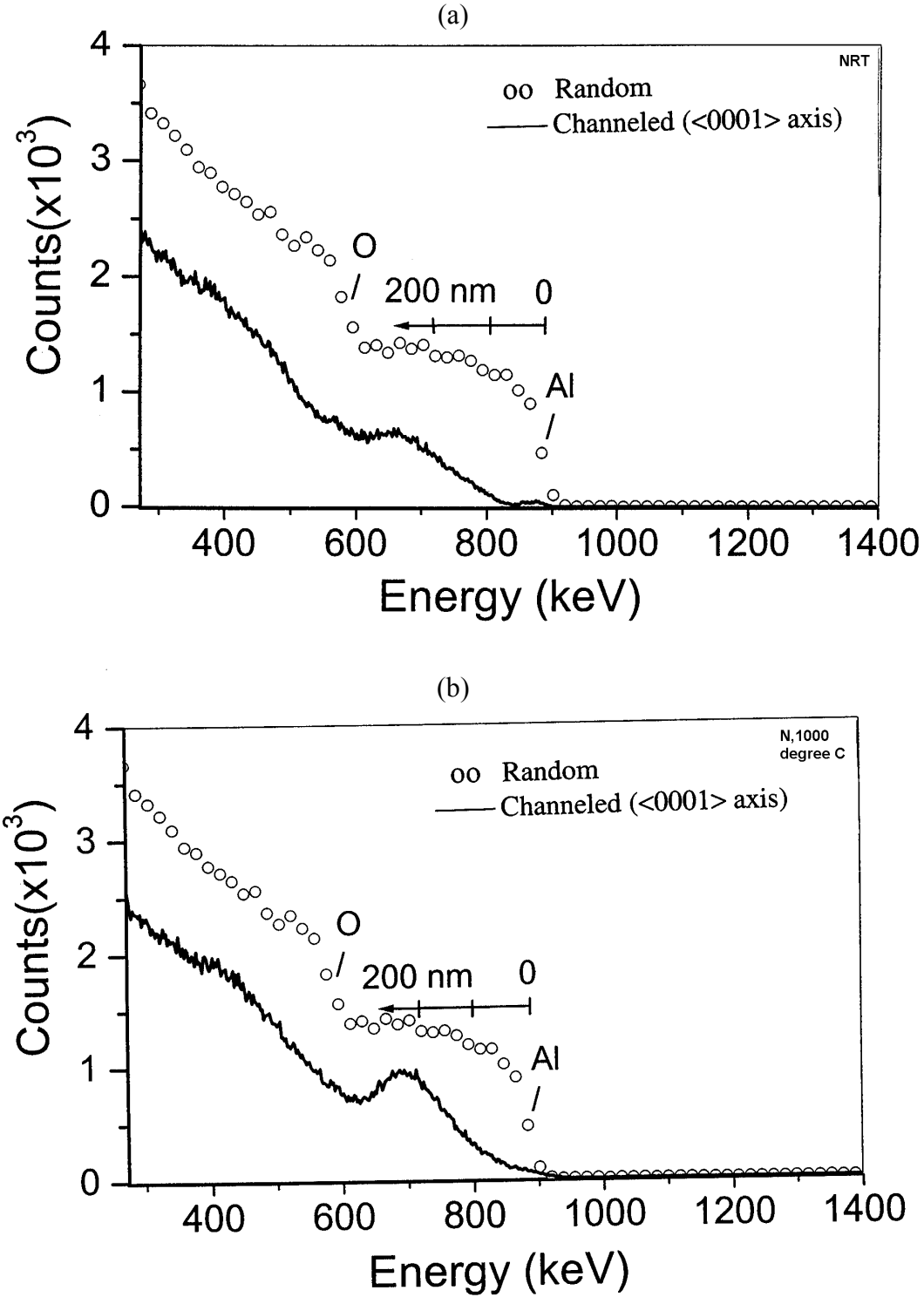


Figure 4.32: RBS spectrum α–Al_2O_3 specimen implanted with nitrogen. (a) At room temperature and (b) at 1000°C.

species (N) is a gas, the presence of gas bubbles is suspected. Such bubbles (or voids) are, in fact, observed in the TEM micrographs shown in Figure 4.26 (a and b). Figure 4.32 (b) shows that the RBS-C spectra for the Al- sublattice in the sample implanted at 1000^{o}C are quite different from those for the RT implanted specimen. There is more dechanneling for the entire depth with χ_{Al} increasing from 0.06 near the surface to 0.54 at 230 nm. There is a more pronounced peak in the aligned spectrum and the maximum dechanneling occurs closer to the surface.

4.2.4. *Optical Absorption Measurement*

The optical absorption spectra for the crystal implanted at room temperature and at 1000^{o}C are indistinguishable and are shown in Figures 4.33. There is one peak of relatively low intensity centered at ~ 203 nm. This peak is skewed to the lower wavelength, suggesting that both F- and F^{+} - centers may be present. The low intensity and lack of additional features indicate that relatively few oxygen vacancies may be present. The TRIM calculation also indicates that fewer vacancies are produced than for either the B or Fe implantation, due in part to the lower fluence.

4.2.5. *X-ray Diffraction*

A further attempt to find nitrogen or its compound in the implanted specimen was carried out using x-ray diffraction technique. X-ray diffraction spectrum for nitrogen implanted sapphire at room temperature is shown in Figures 4.34. There is also, no nitrogen peak observed.

4.2.6. *X-ray Photoelectron Spectroscopy*

Surface analysis by x-ray photoelectron spectroscopy (XPS) is accomplished by irradiating a sample with monoenergetic soft x-rays and analyzing the energy of the detected electrons. Mg Kα (1253.6 eV) x-ray was used. The photons have limited penetrating power in a solid on the order of 1-10 microns. They interact with atoms in the surface region causing electrons to be emitted by photoelectric effect. The emitted

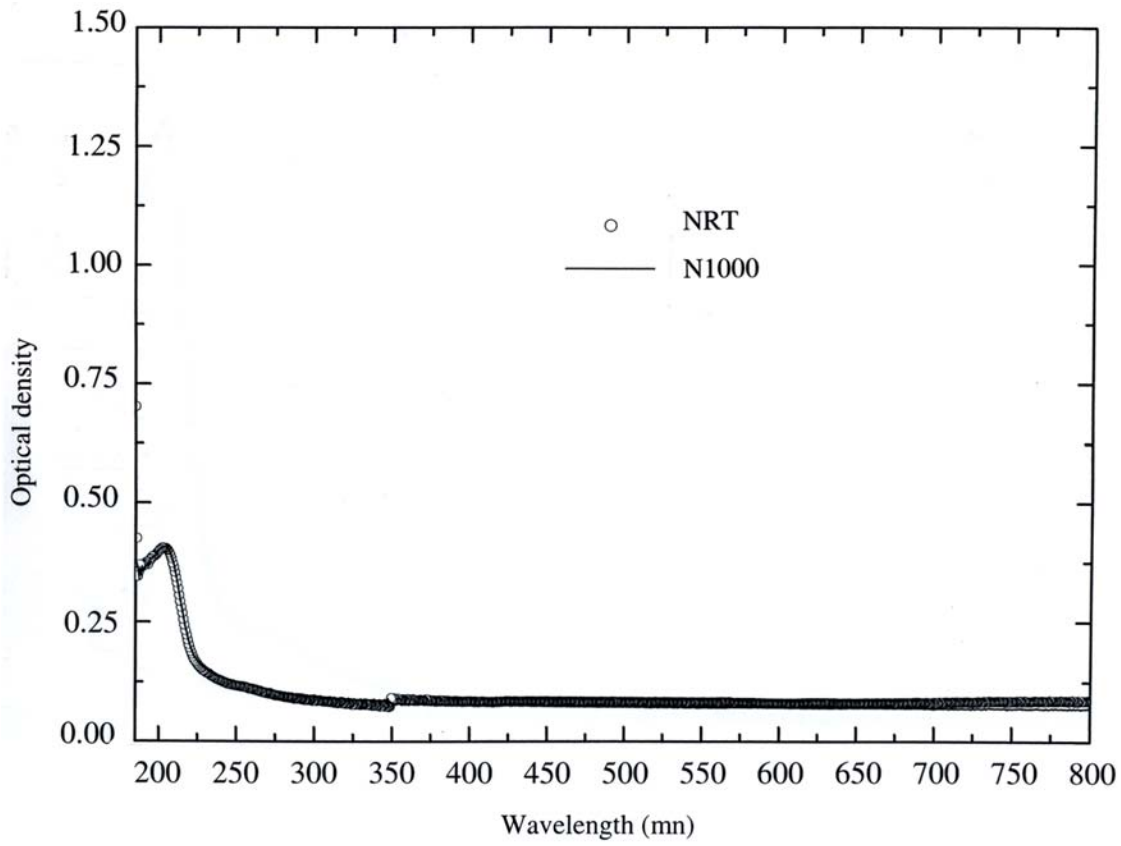


Figure 4.33: Optical absorption spectra for $\alpha-Al_2O_3$ specimen implanted with nitrogen at room temperature and 1000^{o}C.

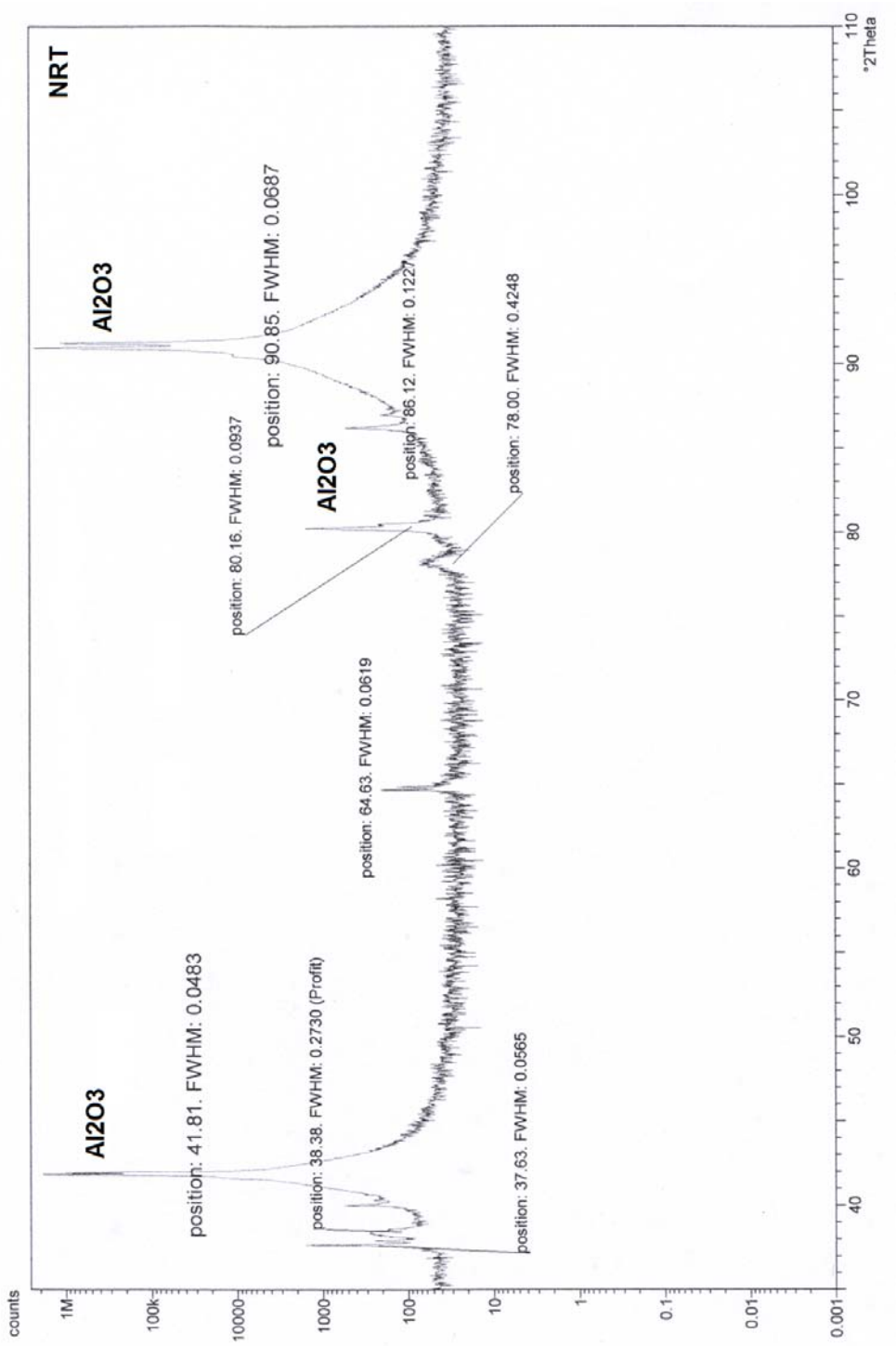


Figure 4.34: XRD spectrum for $\alpha-Al_2O_3$ specimen implanted with nitrogen at room temperature.

electrons have measured KE given by

$$KE = h\upsilon - BE$$

Where hυ is the energy of the photon and BE is the binding energy. The XPS spectrum obtained for nitrogen implanted with sapphire at 1000°C is shown in Figure 4.35; and no nitrogen peak was detected.

4.3. Iron Implanted Sapphire (α-Al_2O_3)

4.3.1. *TRIM Calculations*

The simulation of the implantation process and the model of the energy deposition (elastic and inelastic) as a function of depth from the surface, the range of implanted species, and the defect production were done using the TRIM program. From the TRIM calculation, the range of iron (R_p) in sapphire after implantation of 1×10^{17} Fe^+/cm^2 (150 keV) is = 67.4 nm, the range straggle = 20.7 nm and the number of vacancies per ion = 1326.7. The energy deposited (per ion) and vacancies produced per lattice ion as modeled with respect to position in the target are shown in tables 4.5 and 4.6 respectively. Figure 4.36 shows the simulated iron ions trajectories in sapphire. The range of iron ion and the vacancies produced per lattice ion (dpa) are shown in Figures 4.37 and 4.38 respectively. The energy deposition (electronic and nuclear) plotted as a function of target depth and ion energy is shown in Figures 4.39, 4.40 and 4.41. Note in Figure 4.39 that ionization from recoils makes a significant contribution to the deposited ionizing energy even at the surface. The contribution from recoils is equal to that from incident ions at a depth of 23.5 nm and is higher for greater depths. The ion implantation process simulated and the modeling thereafter are based on 9999 incident ions per surface atom (ion). The large number of incident ions is required to give satisfactory statistics to the calculated values because TRIM is a Monte Carlo calculation based on two-body interactions. The areal density of ions for sapphire is 2.37×10^{15} ions/cm^2. For a fluence (dose) of 1×10^{17} Fe/cm^2, each surface ion is struck about 40 times. Because of lateral spreading, the ions located away from the surface will be deposited to more ions as indicated in the figures. The peak concentration of Fe using the data from Figure 4.37

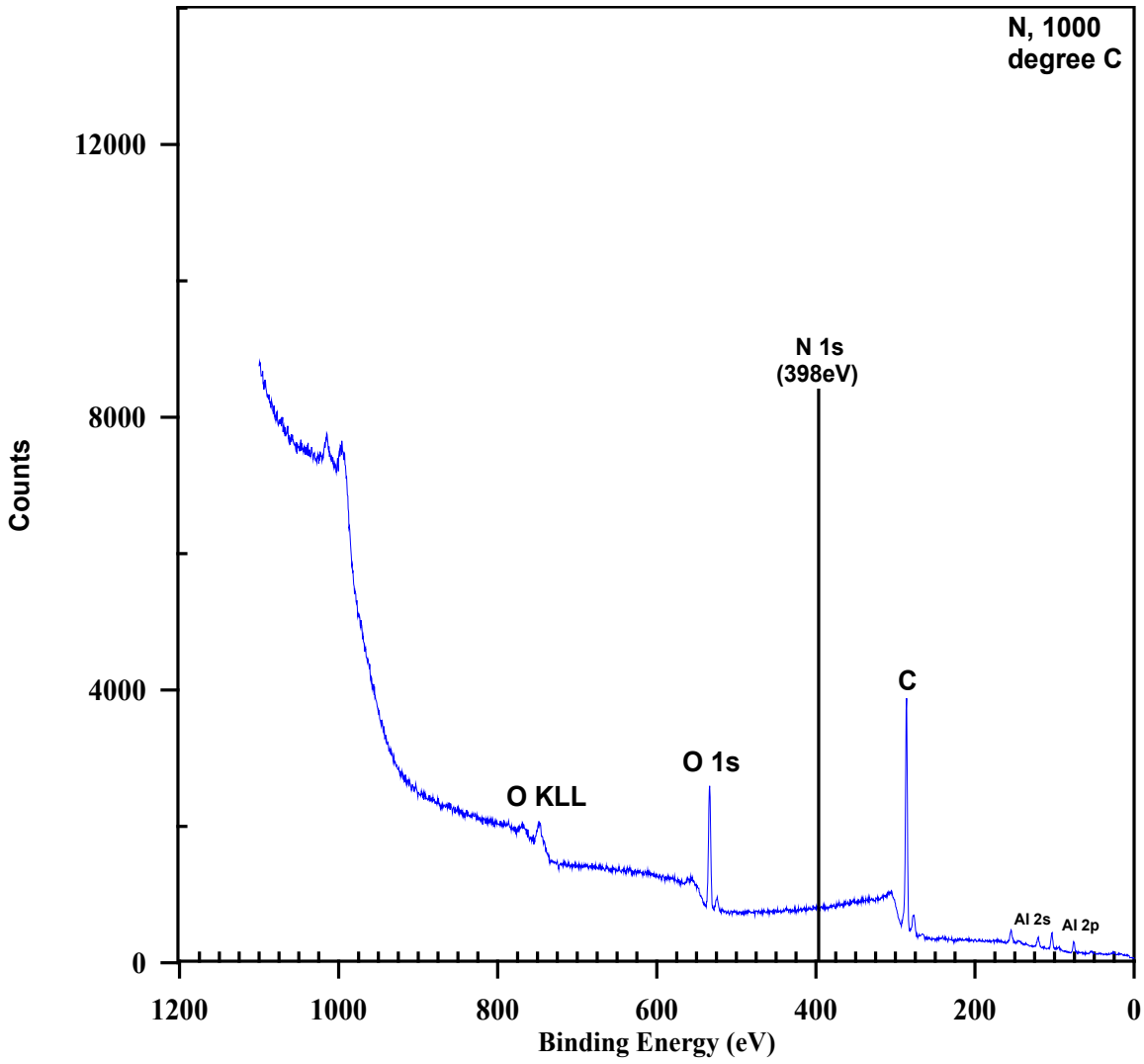


Figure 4.35: XPS spectrum for $\alpha-Al_2O_3$ specimen implanted with nitrogen at 1000^{o}C.

Table 4.5: Iron energy deposited per incident Fe ion as a function of depth in the target material.

Target Position, x	**Inelastic (Ionizing or Electronic) (eV/Å)**			**Elastic (Displacement) (eV/ Å)**	**Ratio (Inelastic/Elastic)**
	Ions	**Recoils**	**Total**		
Surface, x=0	58.0	37.0	95.0	91.0	1.04
Peak damage energy, x = 35.1nm	41.0	57.0	98.0	145.0	0.7
R_p, x = 67.9nm	10.0	25.7	35.7	85.0	0.4

Table 4.6: Vacancies produced per lattice ion (dpa) for a fluence of 1×10^{17} Fe^{+}/cm^{2}.

Target Position, x	**Al**	**O**
Surface, x=0	178.0	58.0
Peak damage energy, x = 35.1nm	274.0	96.0
R_p, x = 67.9nm	152.0	58.0

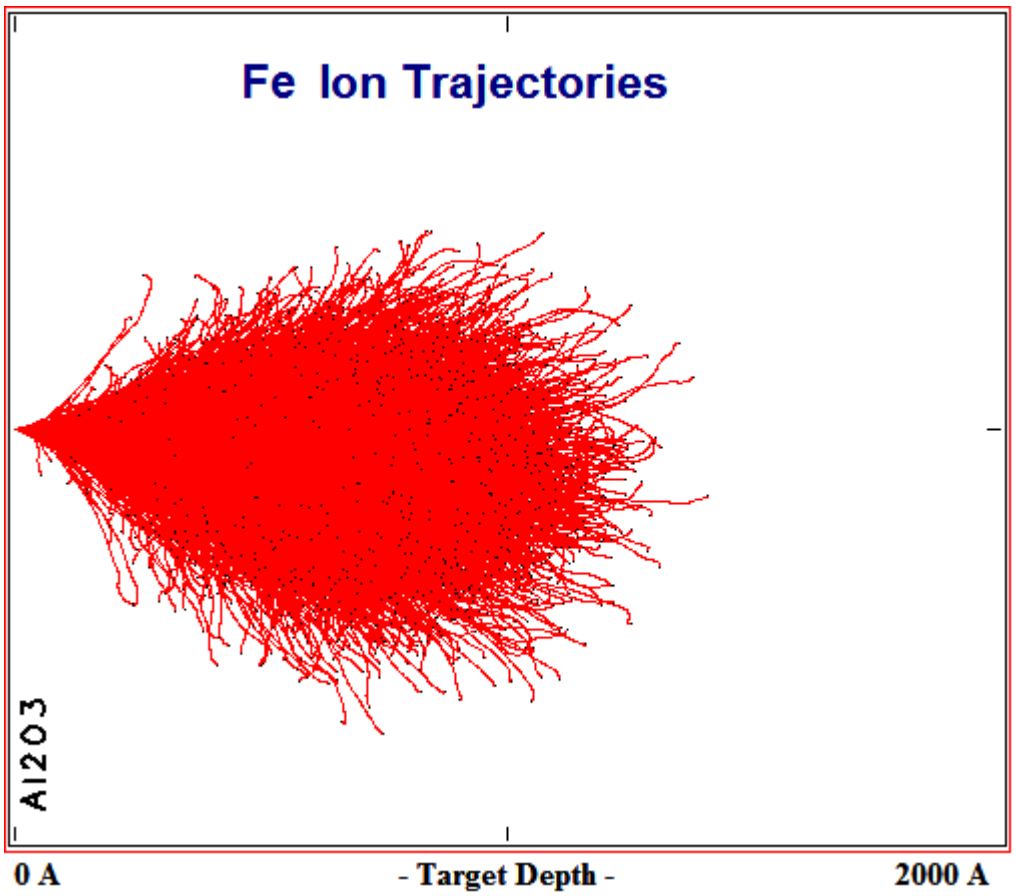


Figure 4.36: Iron ion trajectories.

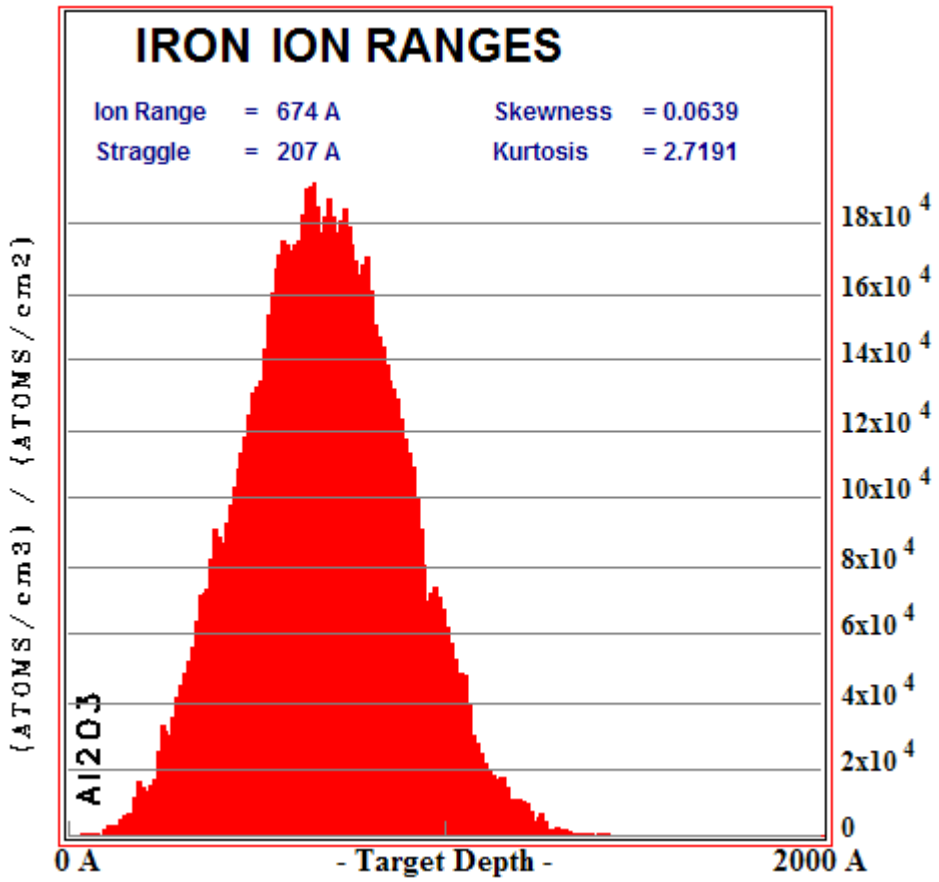


Figure 4.37: The range of iron ion in sapphire as a function of depth.

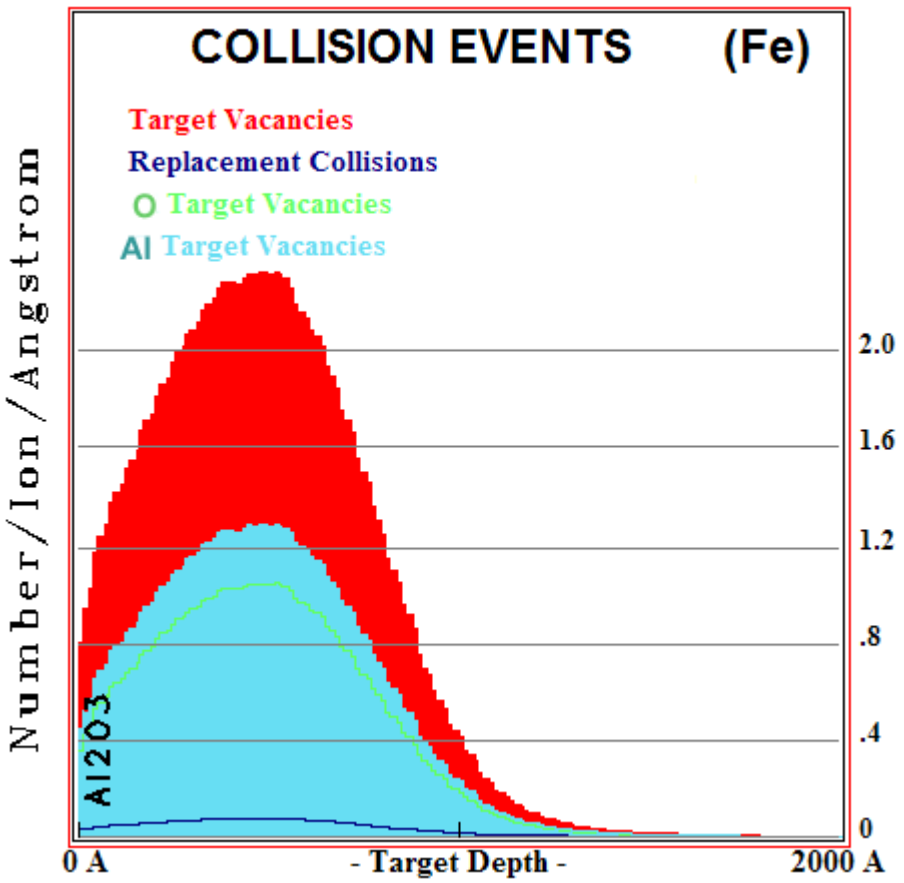


Figure 4.38: Iron collision events showing the plots of the number of vacancies produced per lattice ion (dpa).

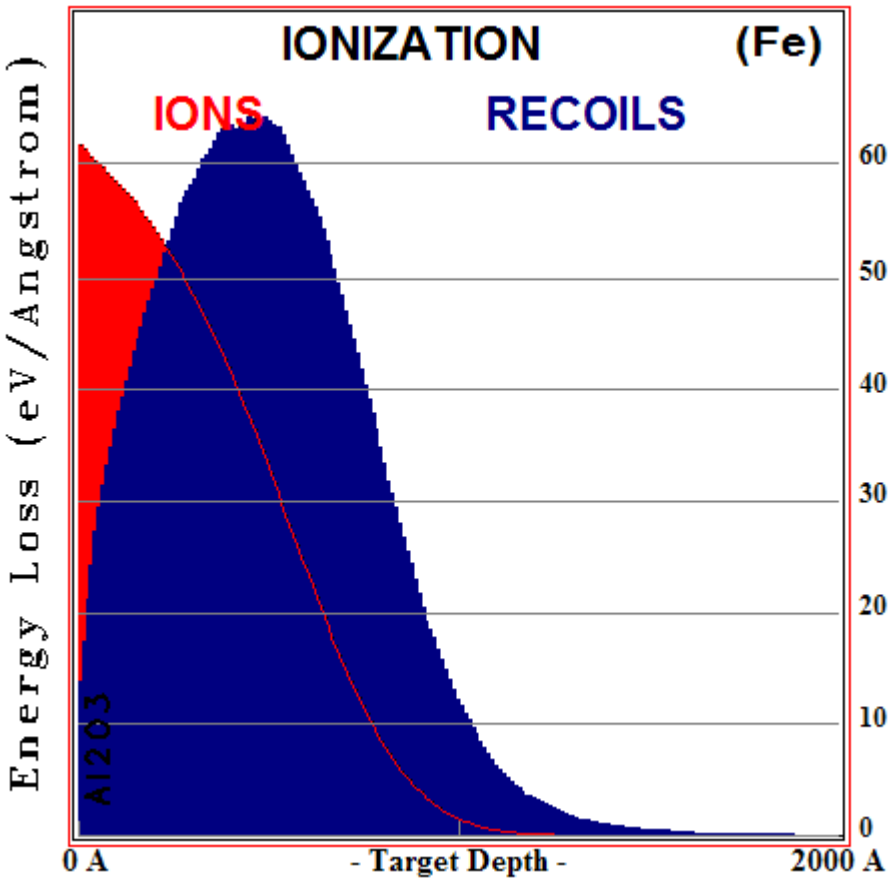


Figure 4.39: Plot of iron electronic (ionizing) energy loses with the target depth.

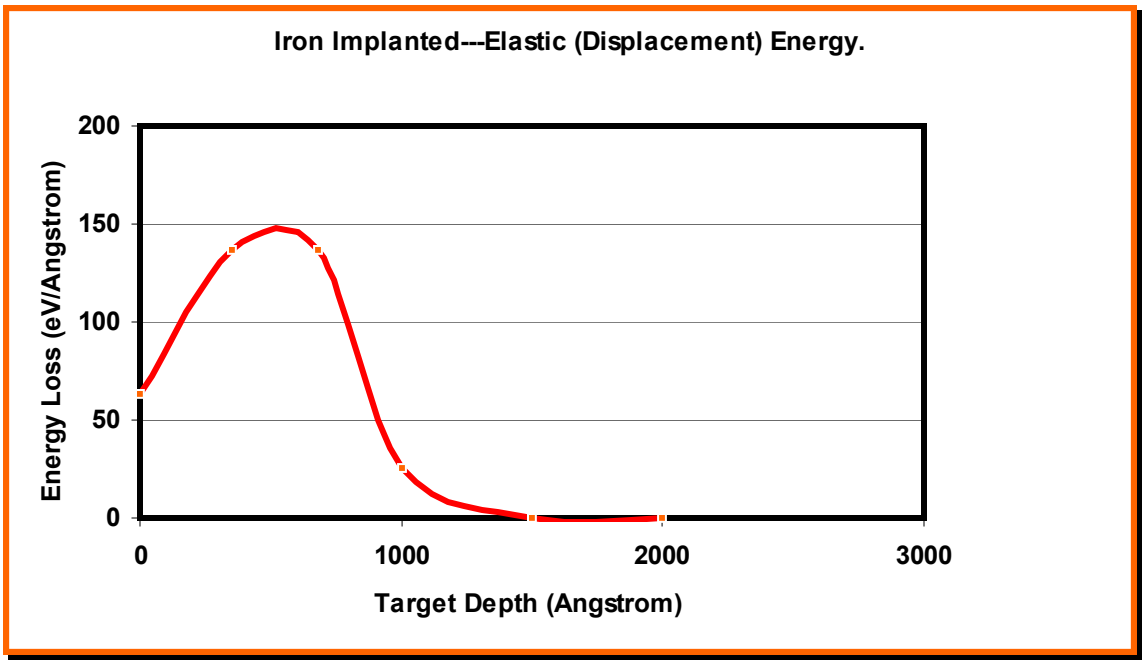


Figure 4.40: Plot of elastic (displacement) energy loses with the target depth.

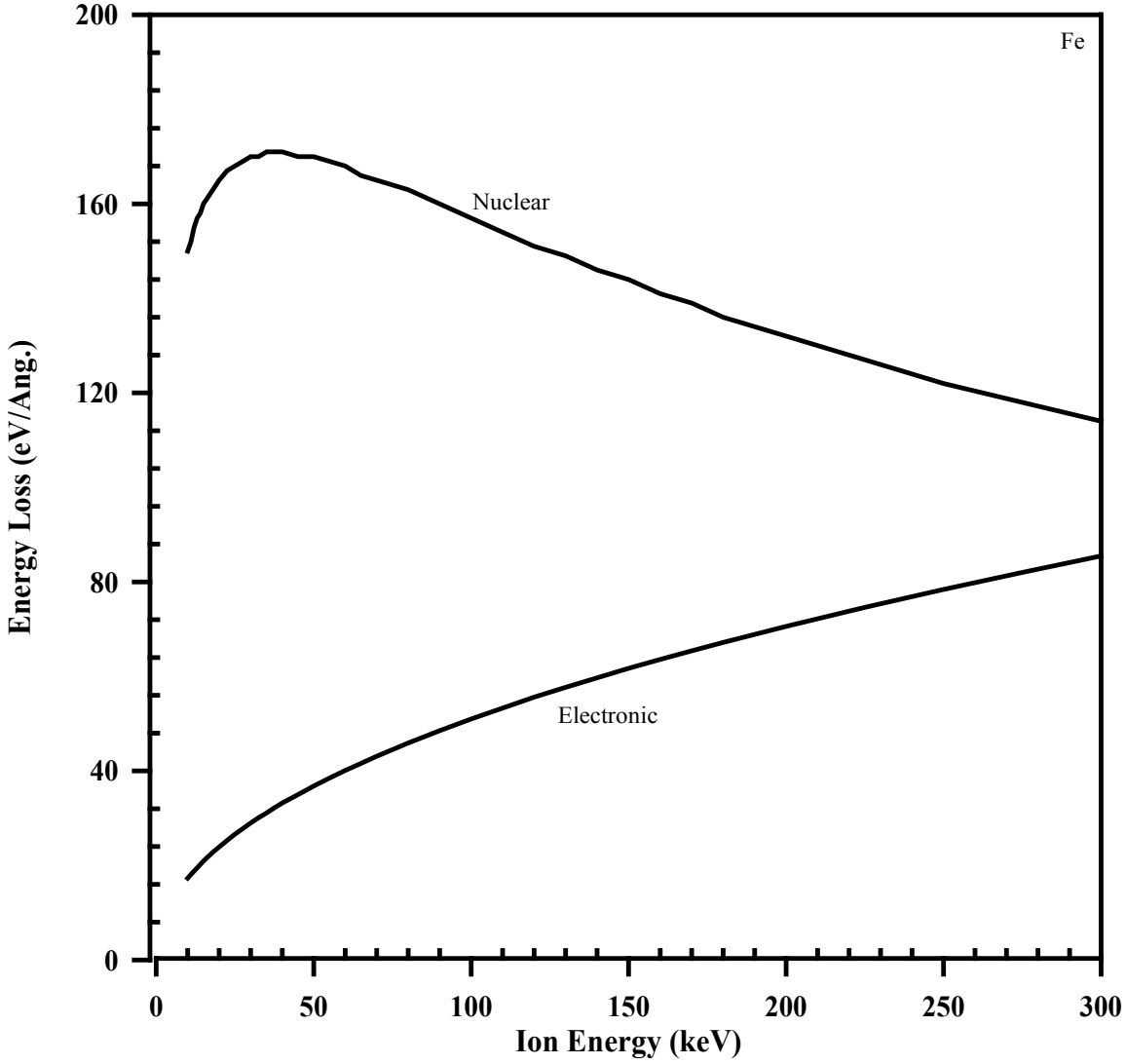


Figure 4.41: Plot of energy (electronic and nuclear) loses as a function of the iron ion energy (the implant ion energy in this case is 150 keV).

and the fluence of 1×10^{17} Fe/cm^2 is calculated to be approximately 0.46 Fe per Al ion, which is approximately 46% in concentration.

4.3.2. *Transmission Electron Microscopy*

The microstructures of iron implanted α–Al_2O_3 at room temperature and 1000^{o}C are shown in Figures 4.42 - 4.45. The influence of implantation temperature is obvious at the fluence of 1×10^{17} Fe/cm^2 (150 keV). The cross-section room temperature implant micrographs reveal small particles of iron concentrated at the depth between about 40 to 150 nm and dense array of cluster defects (Figure 4.42 (c and d)). In addition to the very small iron particles, the photographs show the typical "black spot" damage typical of radiation damage. The exact nature of these clusters has not yet been determined. EDX measurement (Figure 4.49) shows the region to be iron rich. The implanted regions remained crystalline as evidence from the selected area diffraction pattern (Figures 4.46). A careful examination of the SAD patterns from areas B and C of Figure 4.46 suggests that a second phase is present. However, these weak spots are near the entire diffraction spots from the sapphire and could not be uniquely identified.

Micrographs of cross-sectional and back-thinned specimens shown in Figures 4.44 and 4.45 for Fe implanted sapphire at 1000^{o}C reveal oriented precipitates of different shapes (faceted, elongated and round) and sizes ranging from about 1 to 100nm. The precipitates were found to be also rich in iron from EDX measurement (Figure 4.50). At this implantation temperature, the specimen also remained crystalline (Figure 4.47). Again, the SAD patterns from areas A and B, hint at the presence of a second phase. The patterns from the plan view (Figure 4.45 (a)) are given in Figure 4.48 and definitely show the presence of a second phase. The microstructures from the 1000^{o}C iron implant show no evidence for clusters. Some of the particles have voids attached to them. Ren [21] found body-centered iron precipitates in samples that had been implanted at room temperature and annealed in reducing atmospheres at 1100^{o}C. The x-ray diffraction results of section 4.3.5. confirmed the presence of α–Fe.

Post implantation annealing of the α-Al_2O_3 specimens irradiated at room temperature was conducted at 1000^{o}C in a reducing gas (Ar-4%H_2) for one hour and the

(a)

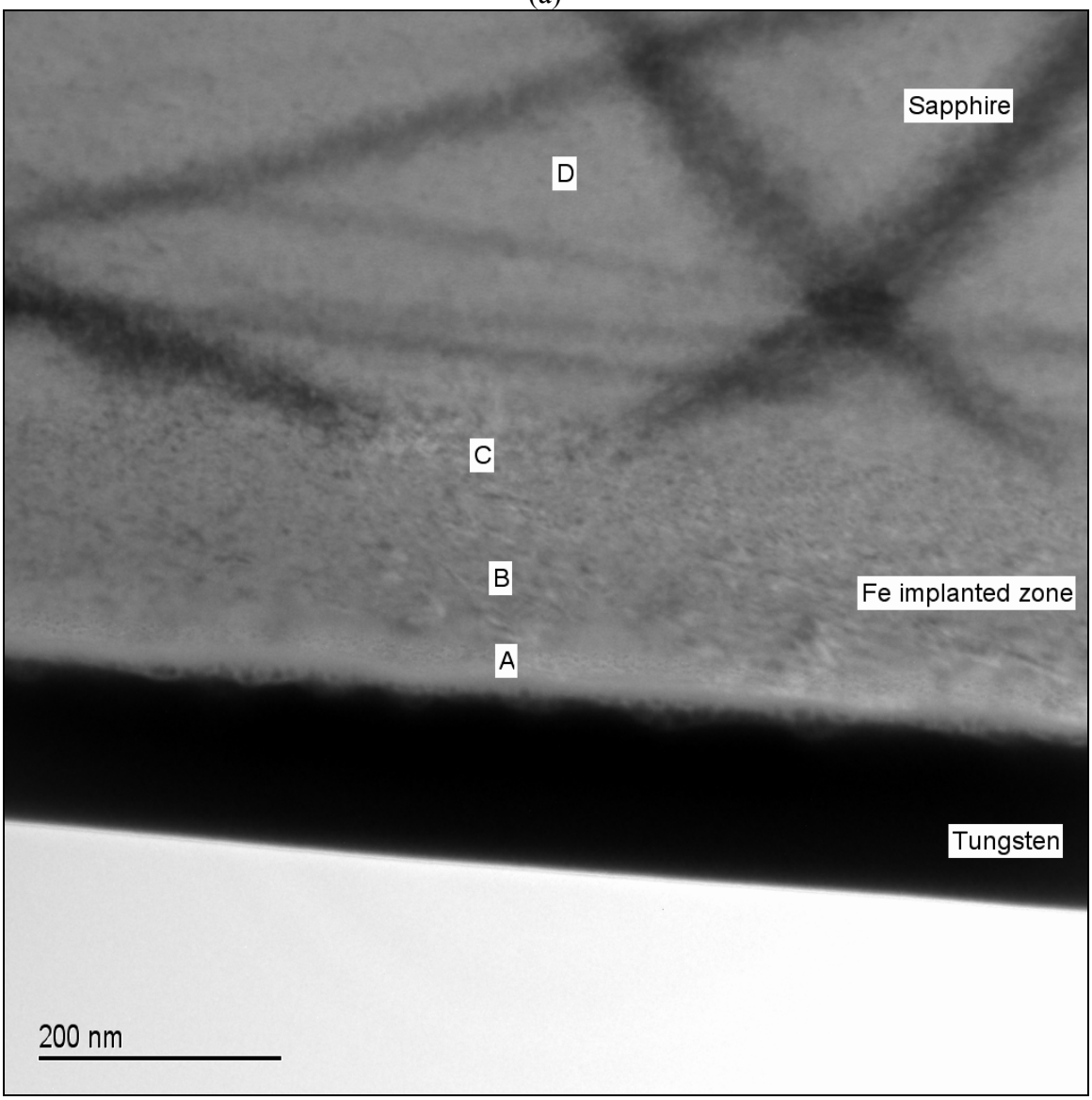


Figure 4.42: TEM cross-sectioned micrographs of $\alpha-Al_2O_3$ specimen implanted with a fluence of 1×10^{17} Fe/cm^2 (150 keV) at room temperature. (a) × 20K, (b) ×60K, (c) × 80K and (d) ×400K.

(b)



Figure 4.42 continued.

(c)

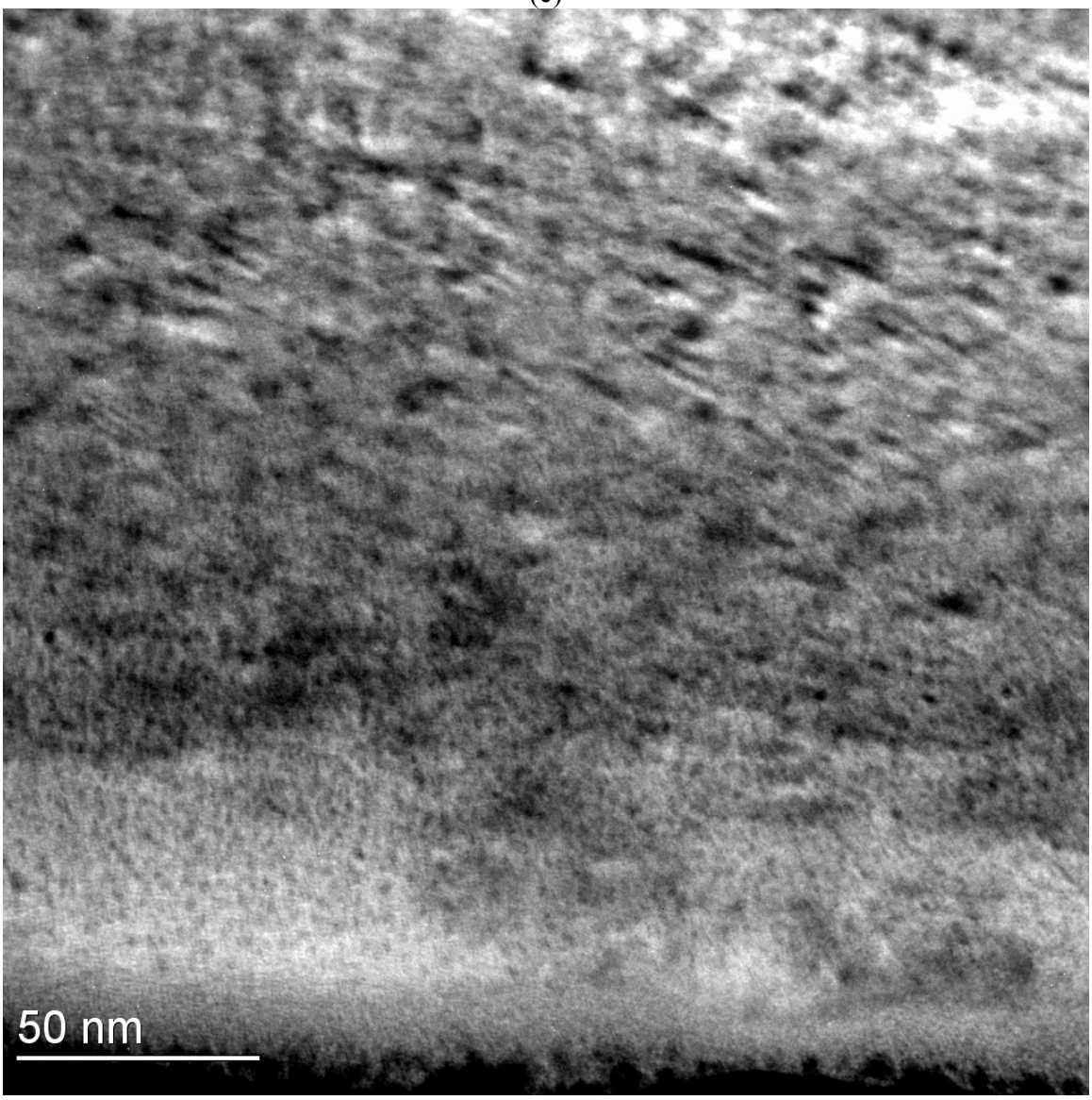


Figure 4.42 continued.

(d)

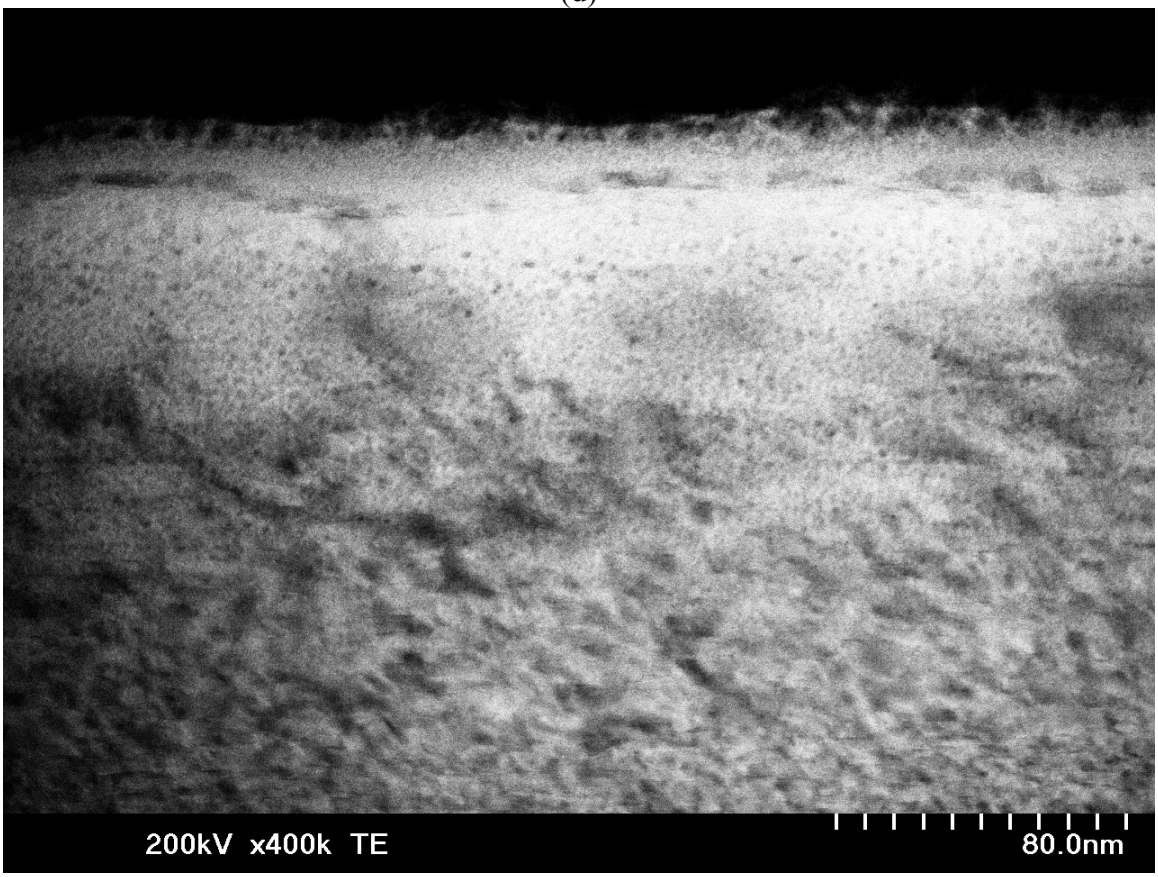


Figure 4.42 continued.

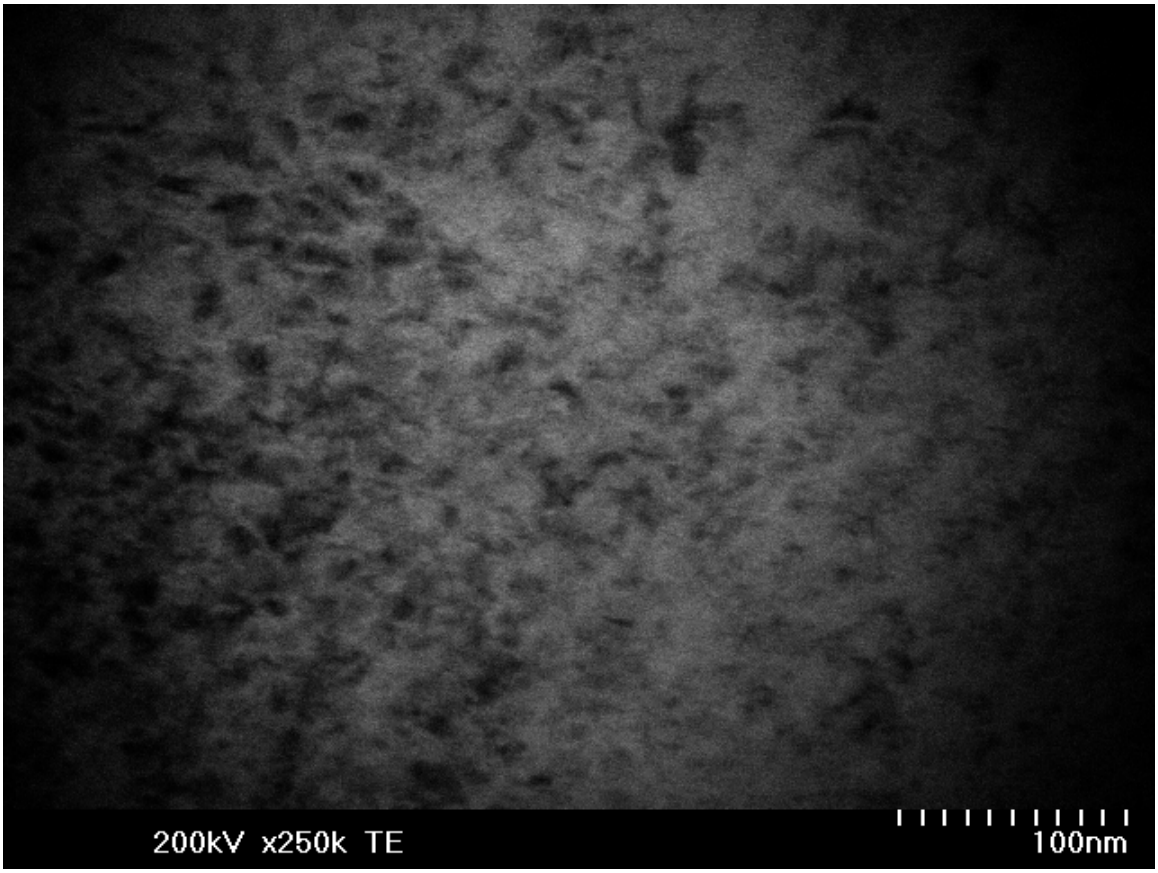


Figure 4.43: TEM plan view micrograph of $\alpha-Al_2O_3$ specimen implanted with a fluence of 1×10^{17} Fe/cm^2 (150 keV) at room temperature. (× 250K).

(a)

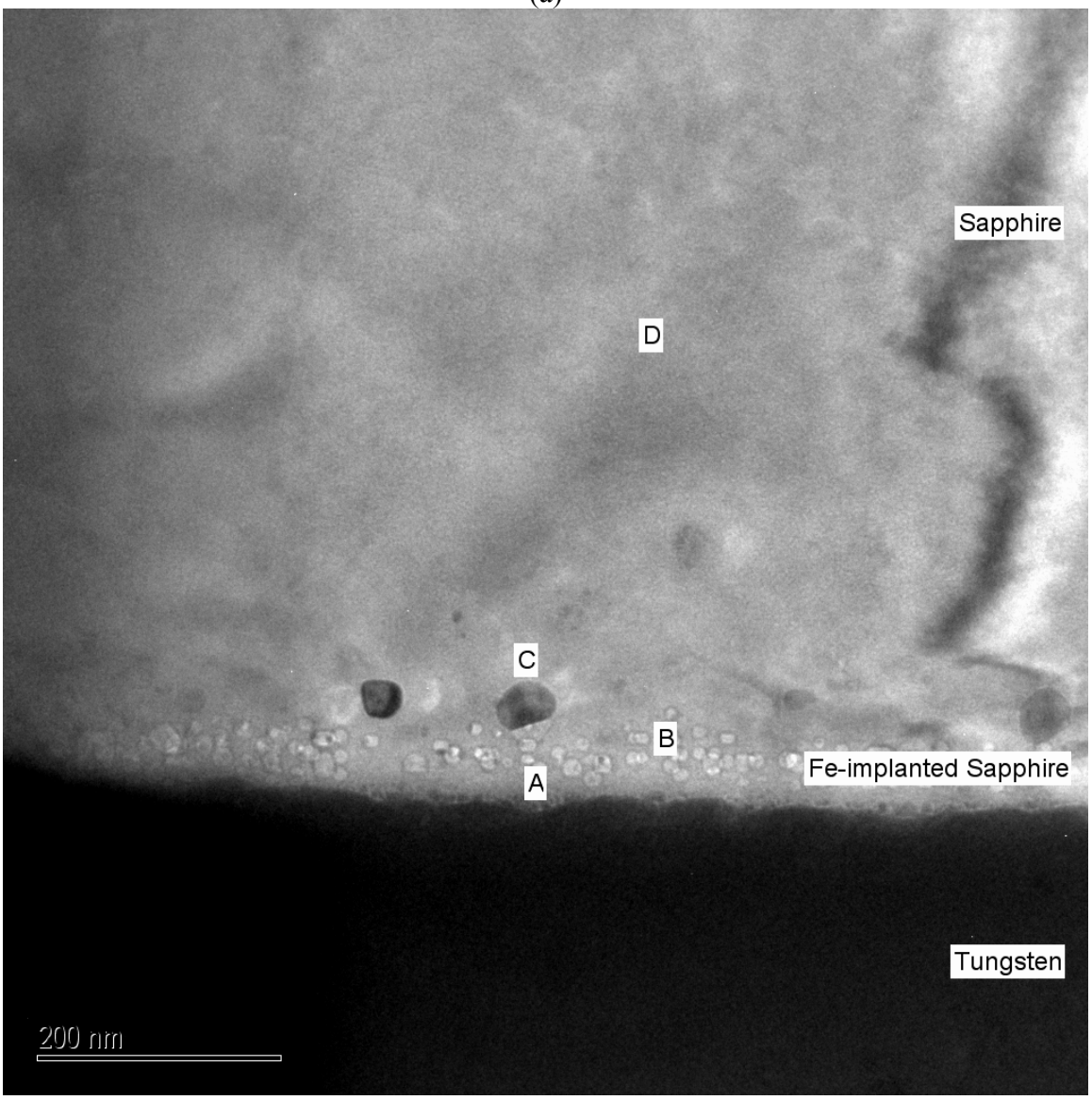


Figure 4.44: Cross-sectioned micrographs of $\alpha-Al_2O_3$ specimen implanted with a fluence of 1×10^{17} Fe/cm^2 (150 keV) at 1000^{o}C. (a) x 20K, (b) x 80K, and (c) 250 K.

(b)

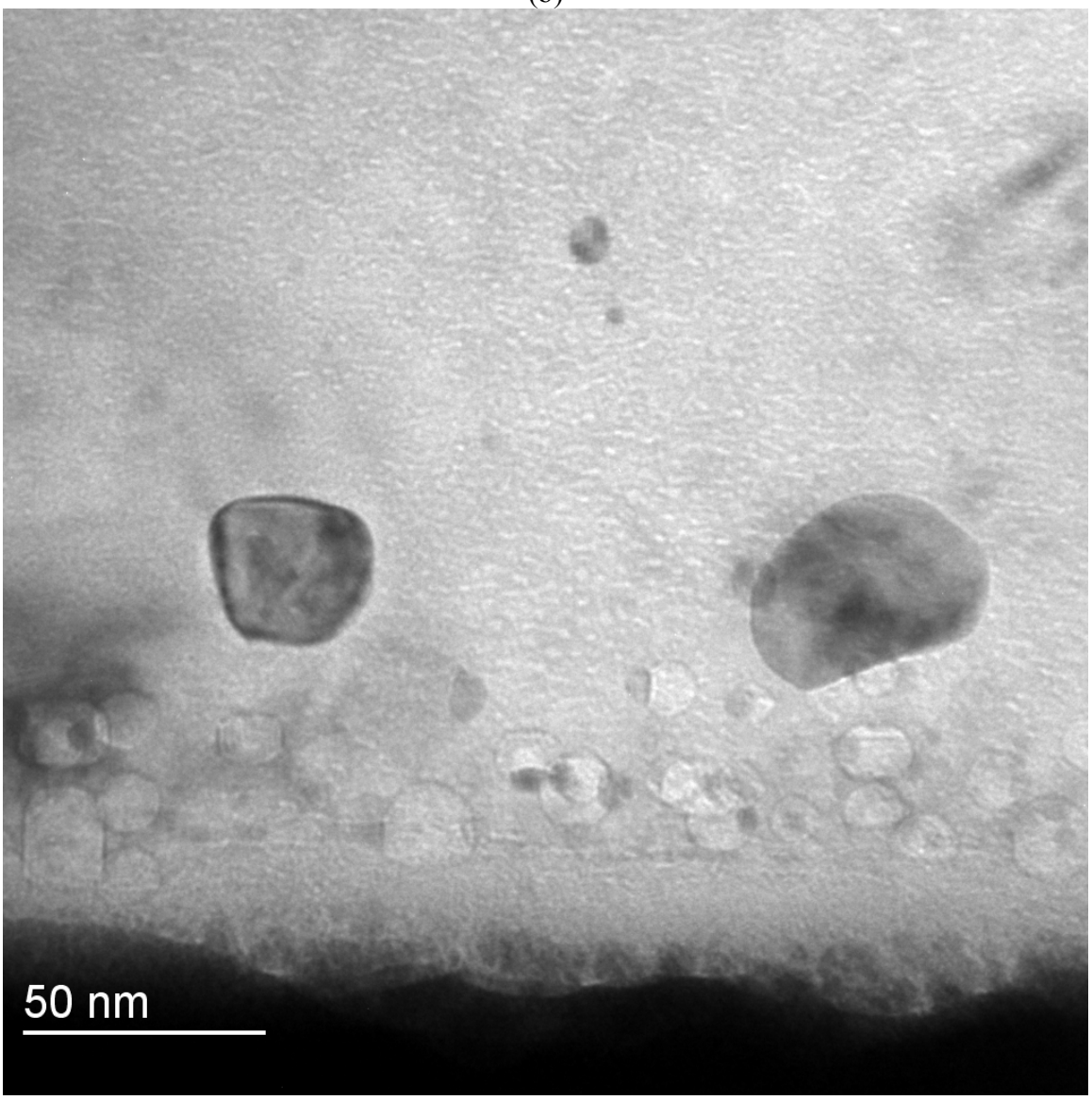


Figure 4.44 continued.

(c)



Figure 4.44 continued.

(a)

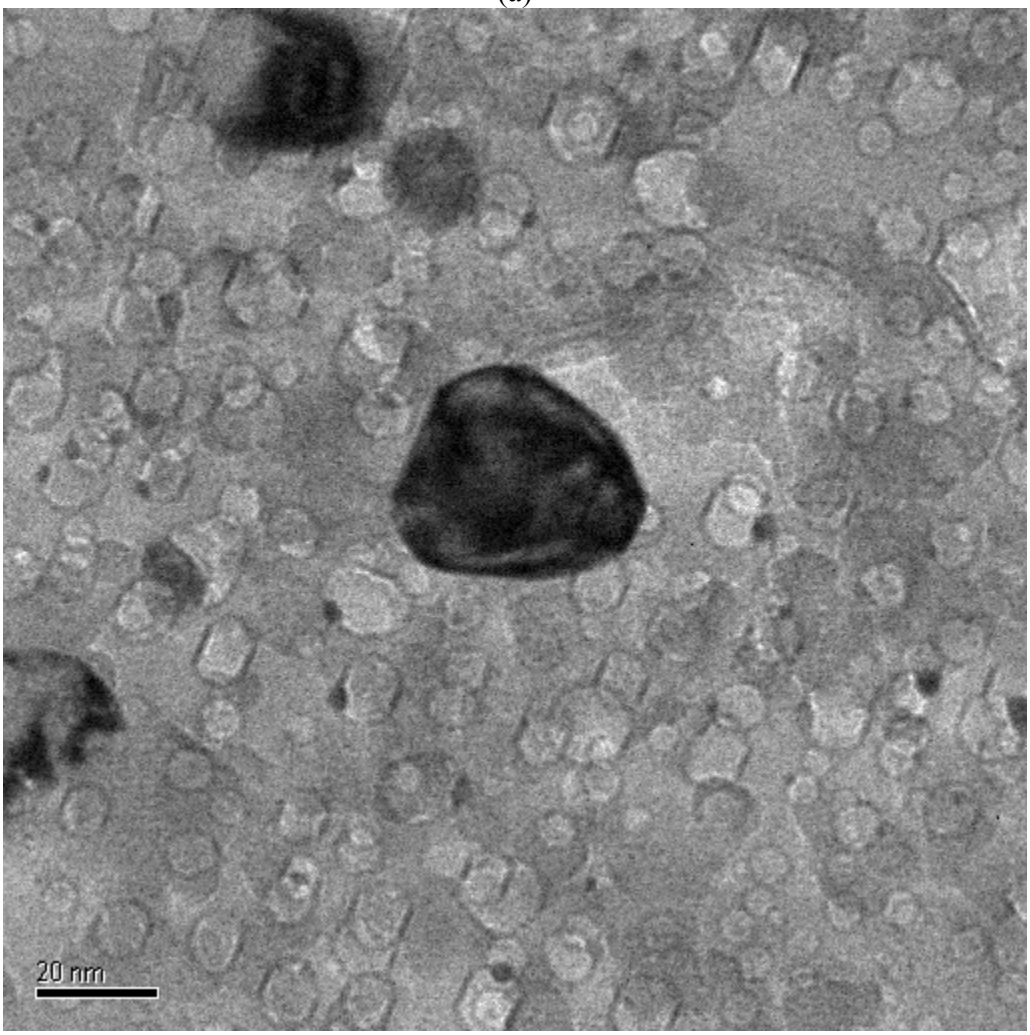
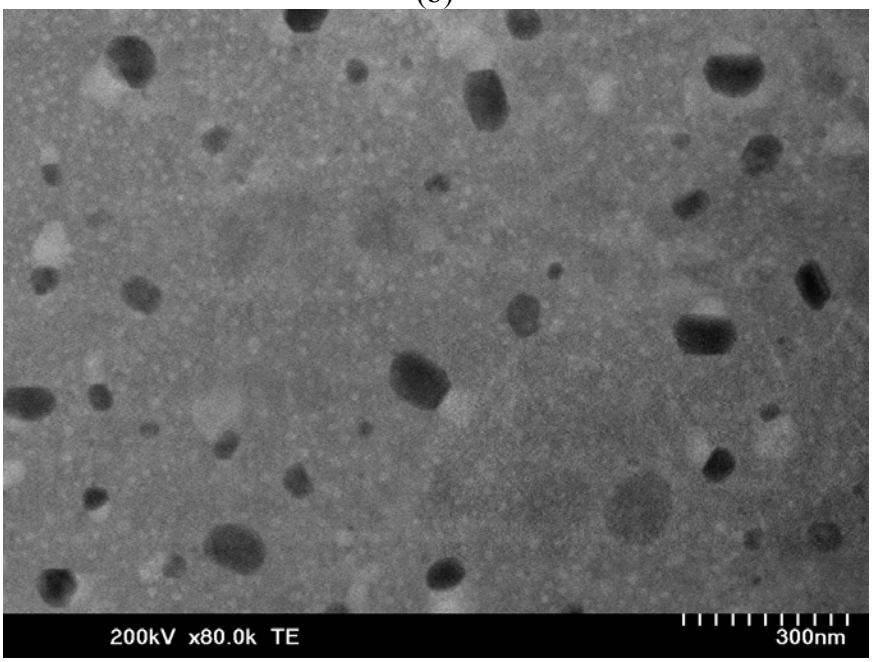


Figure 4.45: TEM plan view micrographs of α–Al_2O_3 specimen implanted with a fluence of 1×10^{17} Fe/cm^2 (150 keV) at 1000^{o}C. (a) 60 K, (b) x 80K (bright field image), (c) x 80K (dark field image), (d) × 250K (bright field image) and (e) × 250K (dark field image). .

(b)



(c)

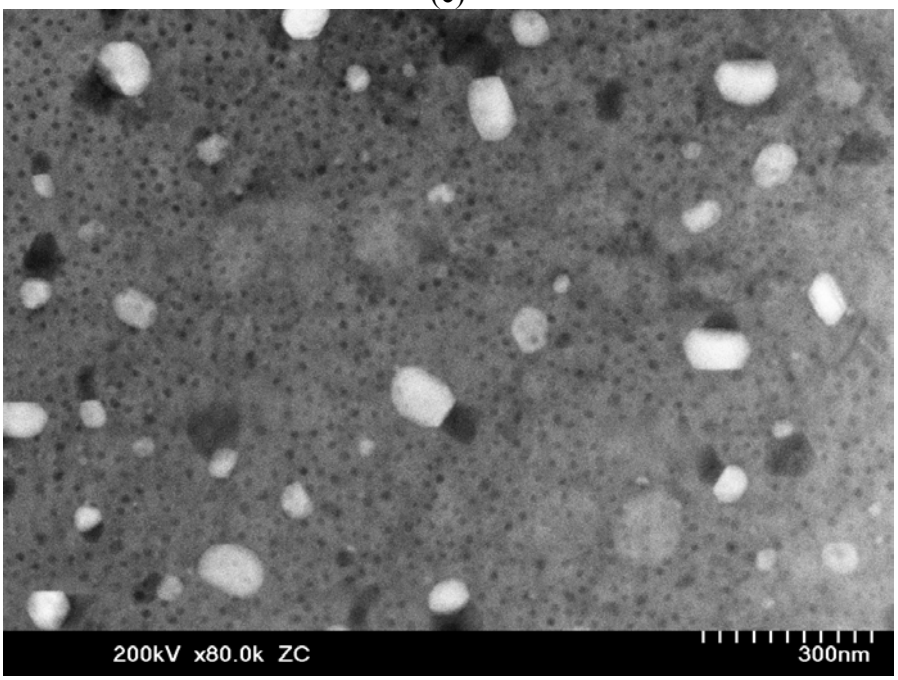
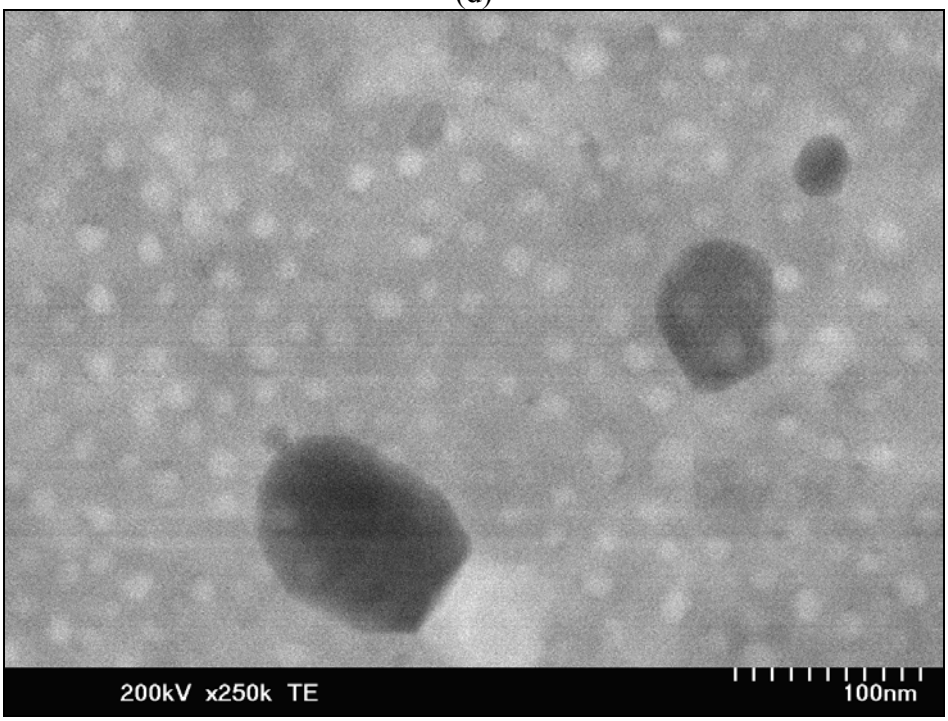


Figure 4.45 continued.

(d)



(e)

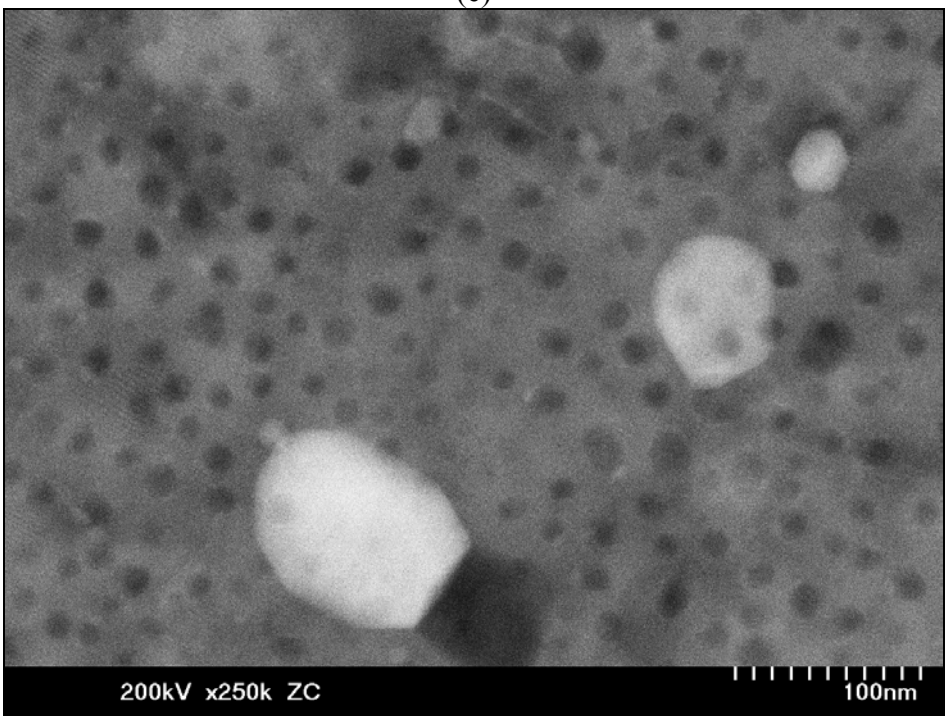


Figure 4.45 continued.

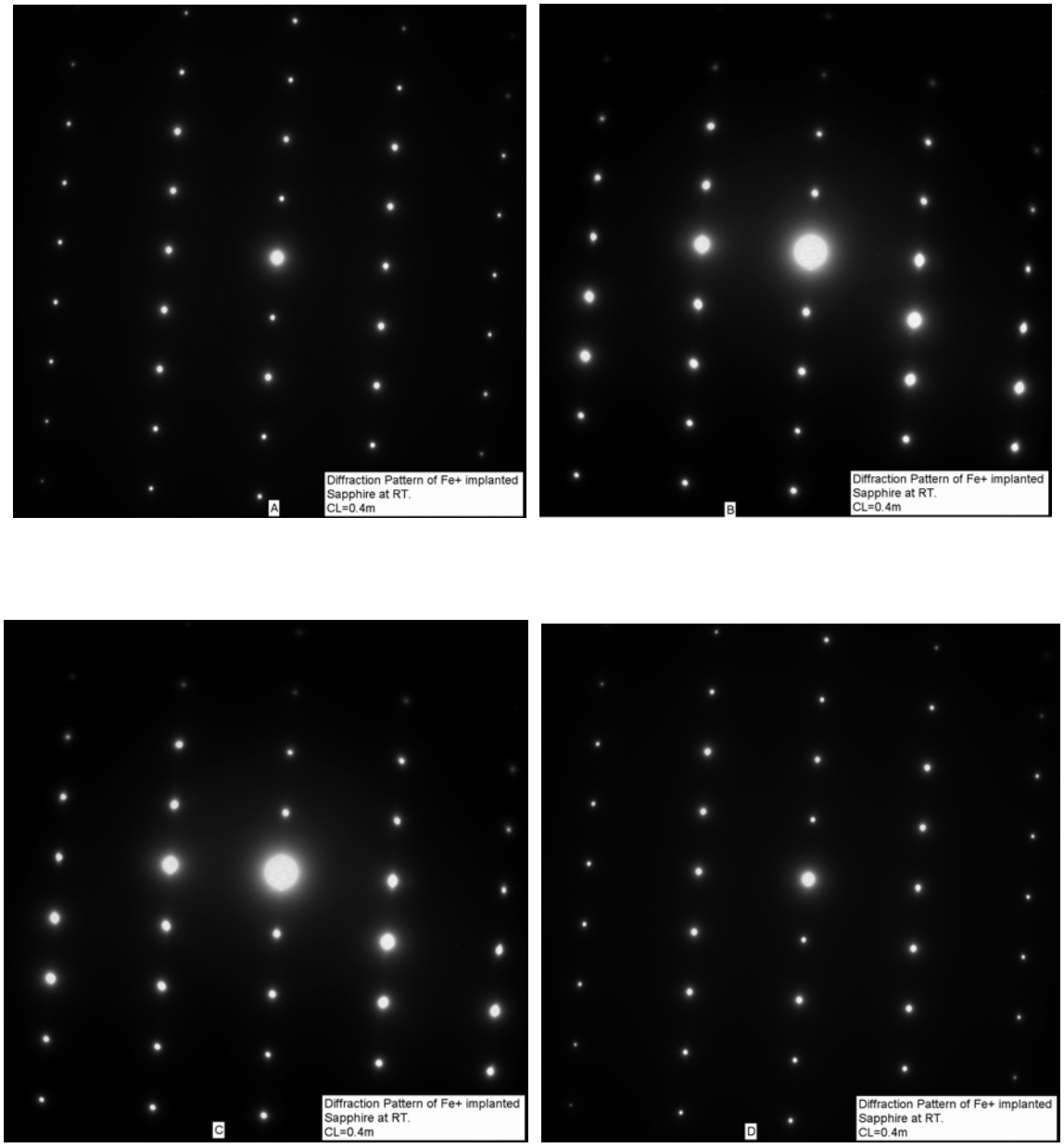


Figure 4.46: SAD taken from a cross-section $\alpha-Al_2O_3$ specimen implanted with iron at room temperature. A, B, C and D are from regions A, B, C and D respectively of Figure 4.42(a).

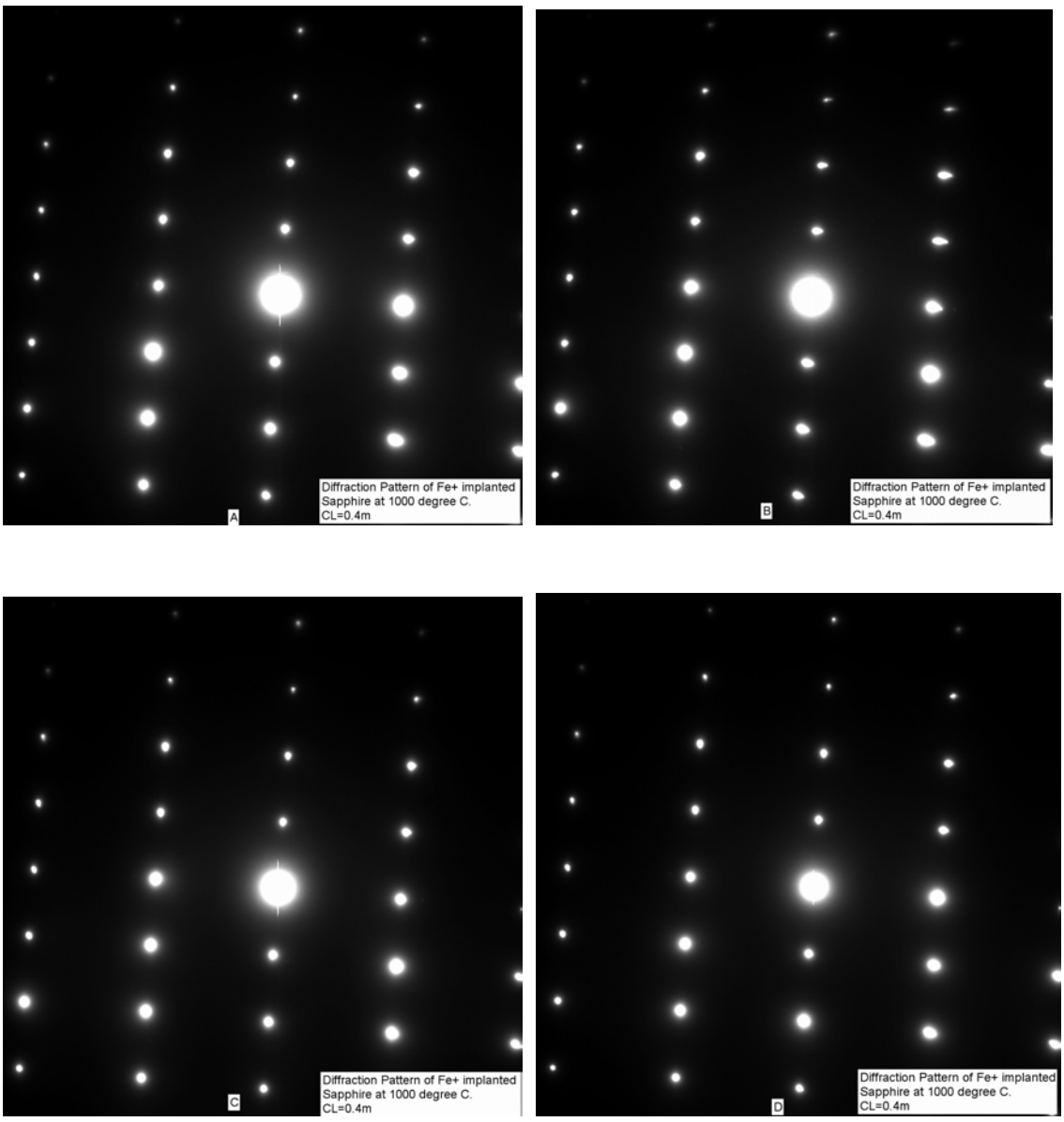
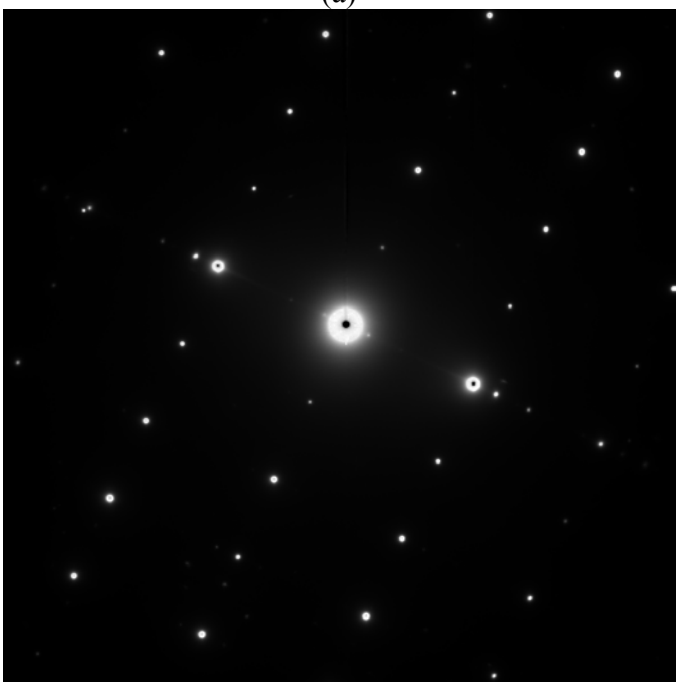


Figure 4.47: SAD taken from a cross-section α–Al_2O_3 specimen implanted with iron at 1000^{o}C. A, B, C and D are from regions A, B, C and D respectively of Figure 4.44 (a).

(a)

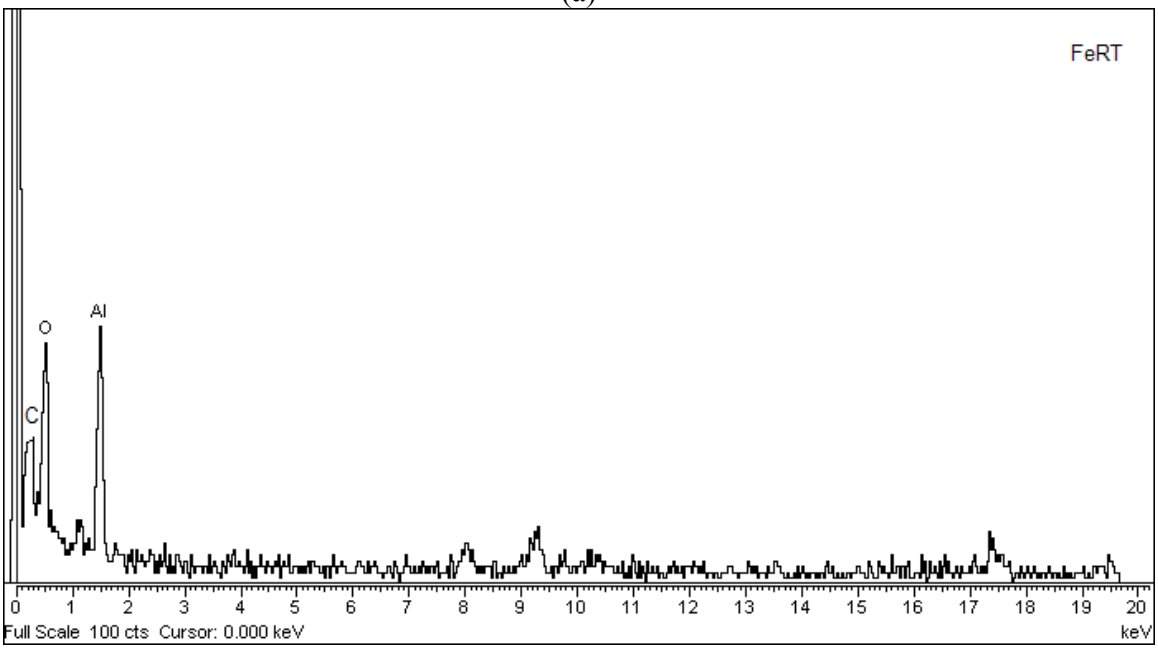


(b)



Figure 4.48: SAD taken from plan view $\alpha-Al_2O_3$ specimen implanted with iron at 1000^{o}C. (a) Is taken from the matrix region and (b) from the large particle of Figure 4.45(a).

(a)



(b)

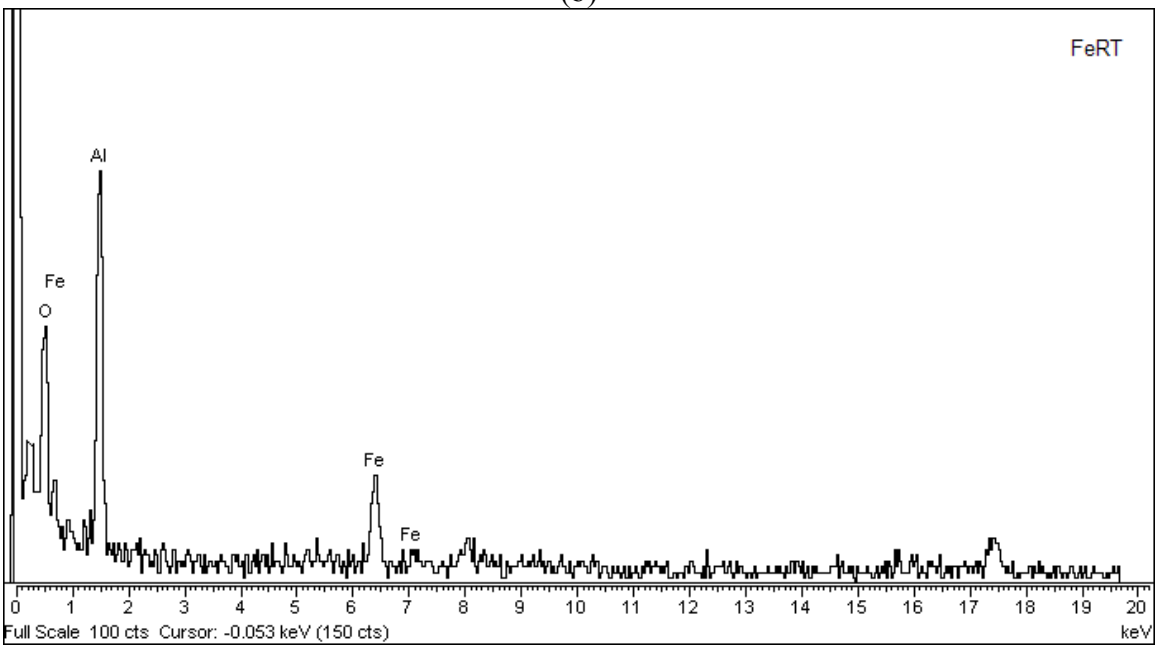


Figure 4.49: EDX spectra from a cross-section α–Al_2O_3 specimen implanted with iron at room temperature. (a), (b) and (c) are from regions A, B and D respectively of Figure 4.42 (a).

(c)

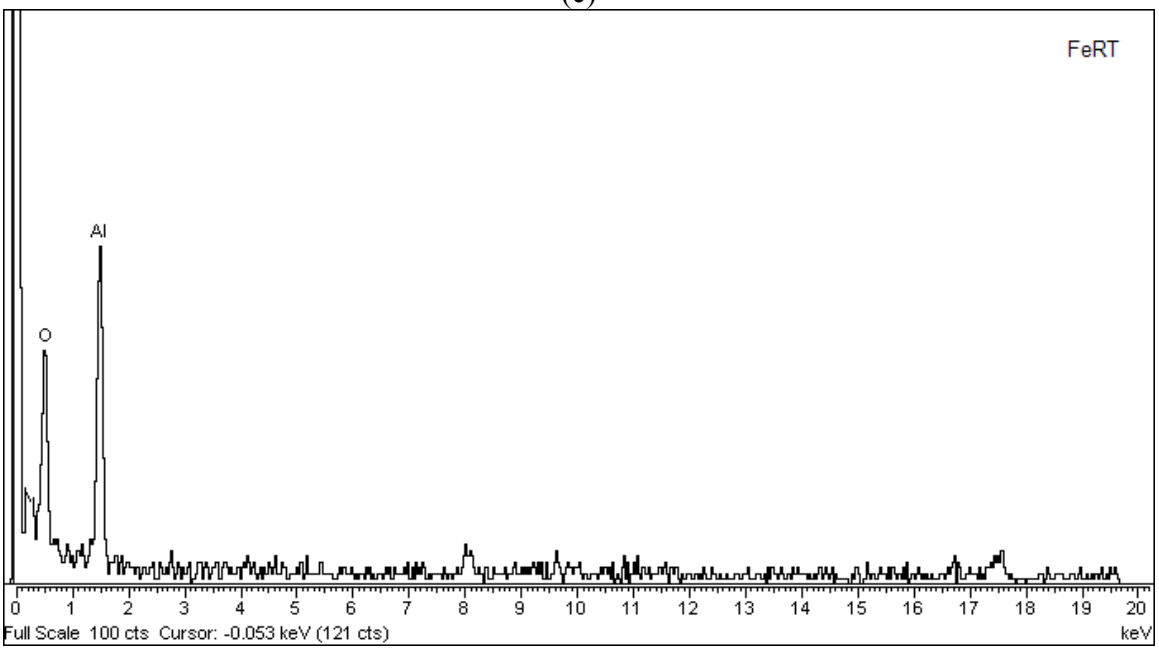
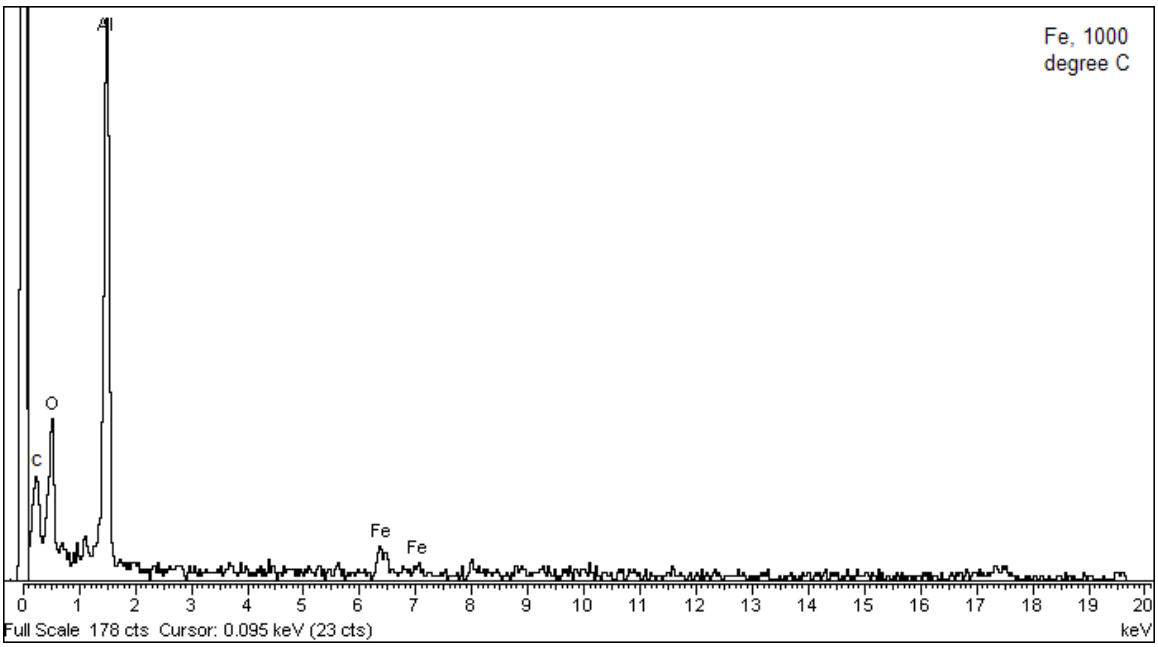


Figure 4.49 continued.

(a)



(b)

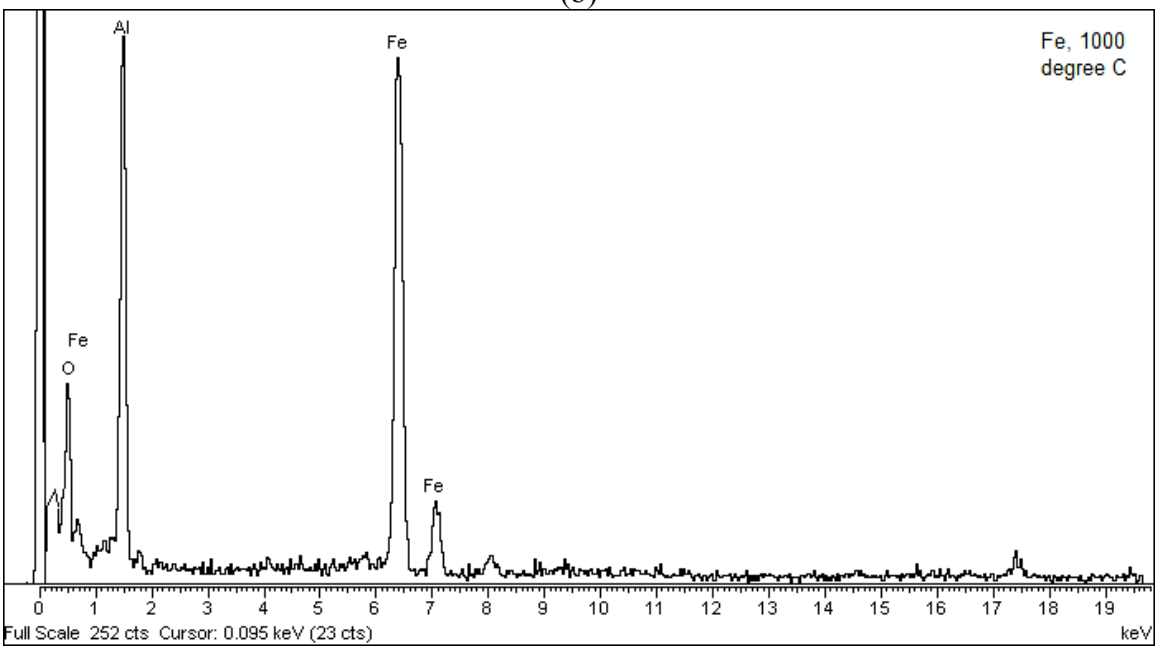


Figure 4.50: EDX spectra from a cross-section α–Al_2O_3 specimen implanted with iron at 1000^{o}C. (a), (b) and (c) are from B, C and D regions respectively of Figure 4.44(a).

(c)

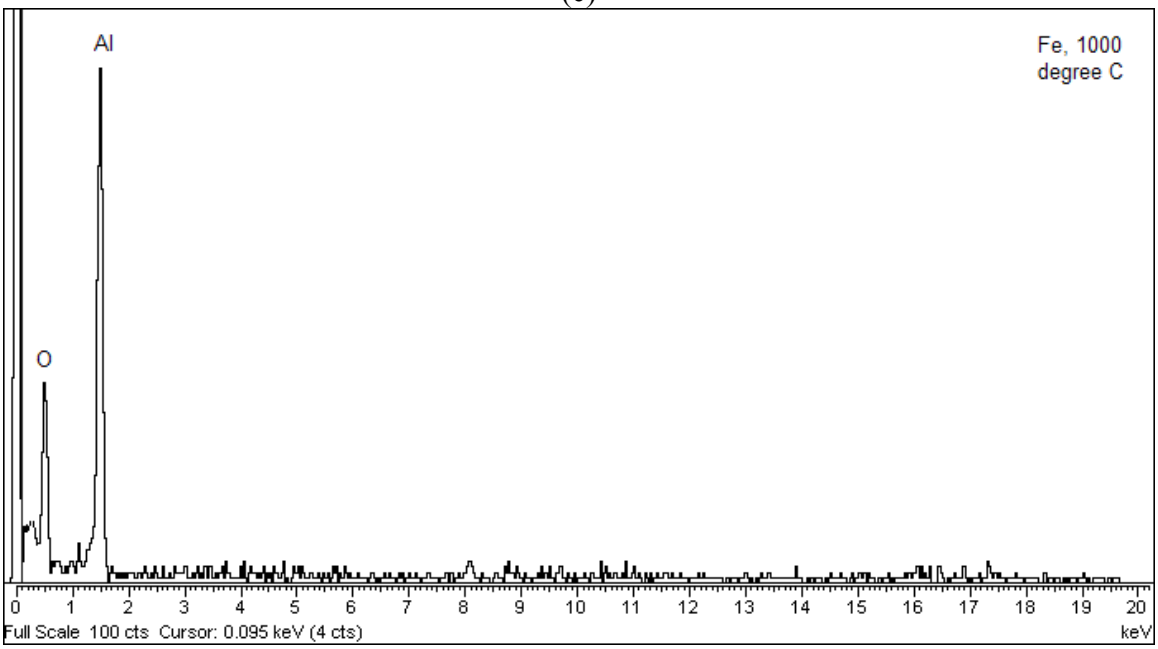


Figure 4.50 continued.

microstructure compared with that of α–Al_2O_3 specimen irradiated with Fe at 1000°C. The cross-section and back-thinned micrographs of these annealed specimens are shown in Figures 4.51 and 4.52 respectively. The micrographs show dense faceted iron precipitates ranging in size from about 1 to 60nm with fewer voids compared with the implanted specimens at 1000°C.

4.3.3. *Rutherfold Backscattering Spectroscopy*

Figure 4.53(a) contains the RBS-C spectra for sapphire sample implanted with 1×10^{17} Fe/cm^2 (150 keV) at room temperature. The random and aligned spectra for scattering from the implanted iron indicates a random distribution of the iron with respect to the sapphire as viewed along the c- axis; i.e., there are no coherent precipitates. The peak iron concentration occurs at 65–70 nm, in good agreement with the TRIM calculated value of 67.9 nm. There is a small surface peak in the aligned Al- spectrum and a region of low residual disorder extending to about 30 nm. The very low disorder in this region could be the result of heating by the ion beam during implantation that annealed the surface. There is a sharp rise in the damage beyond 30 nm, rising to a maximum value of 0.67 for χ_{Al} at 145 nm. Note that this disorder in the Al-sublattice extends well beyond the position of maximum energy deposition (35.1 nm) and the range plus straggling (89 nm) for the implanted iron. This is consistent with the often reported observation that damage extends to depths of 2 to 3 times the range of the implanted ions.

The RBS-C spectra for sapphire sample implanted with 1×10^{17} Fe/cm^2 (150 keV) at 1000°C are shown in Figure 4.53 (b) for the analyzing beam parallel to $< 0001 >$ and in Figure 4.53 (c) for the beam parallel to the $< 02\bar{2}1 >$. The channeling exhibited in the iron spectra of Figure 4.53 (b) indicates that some iron are present either in substitution sites (Al 3^+ - sites) or as precipitates coherent with the Al-sublattice as viewed along the $< 0001 >$ direction (c- axis). The value of χ_{Al} is 0.4. The lack of channeling in Figure 4.53 (c) indicates that the iron is not coherent when viewed along the $< 02\bar{2}1 >$ direction.

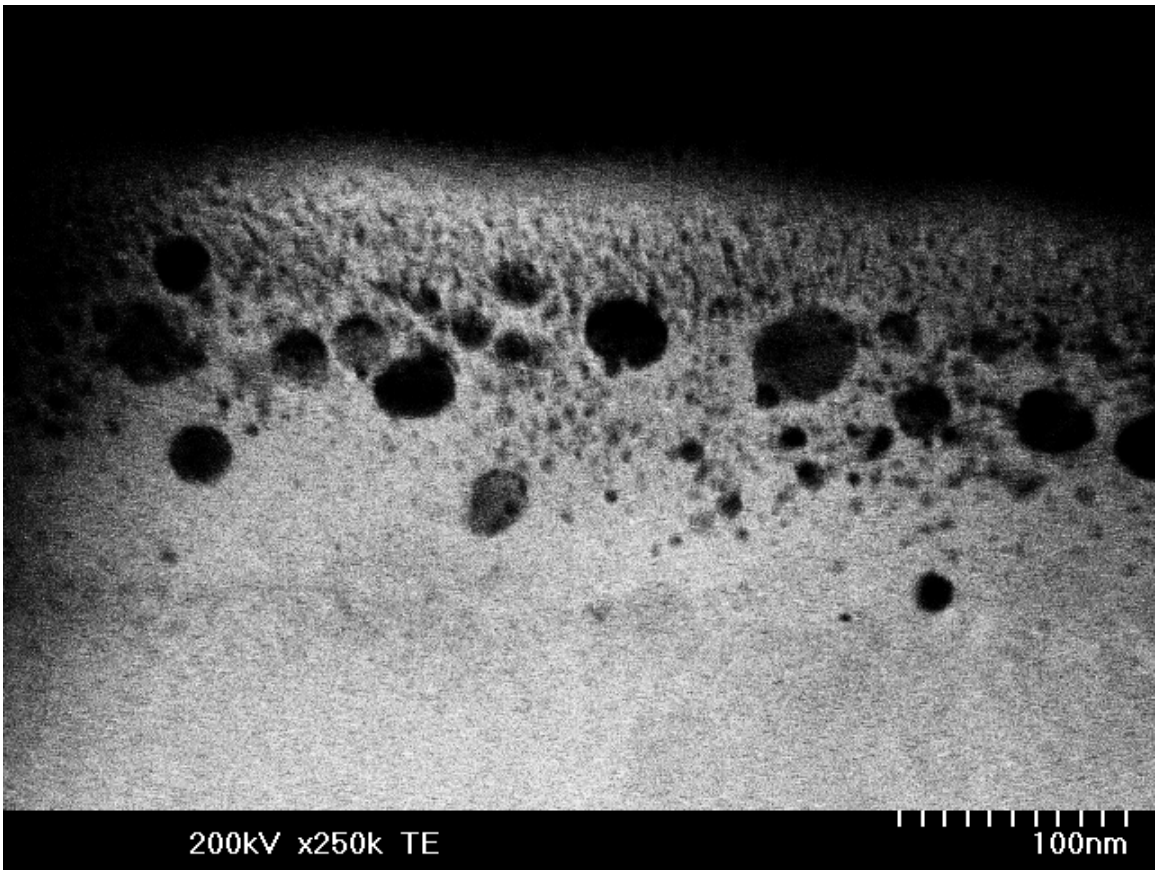
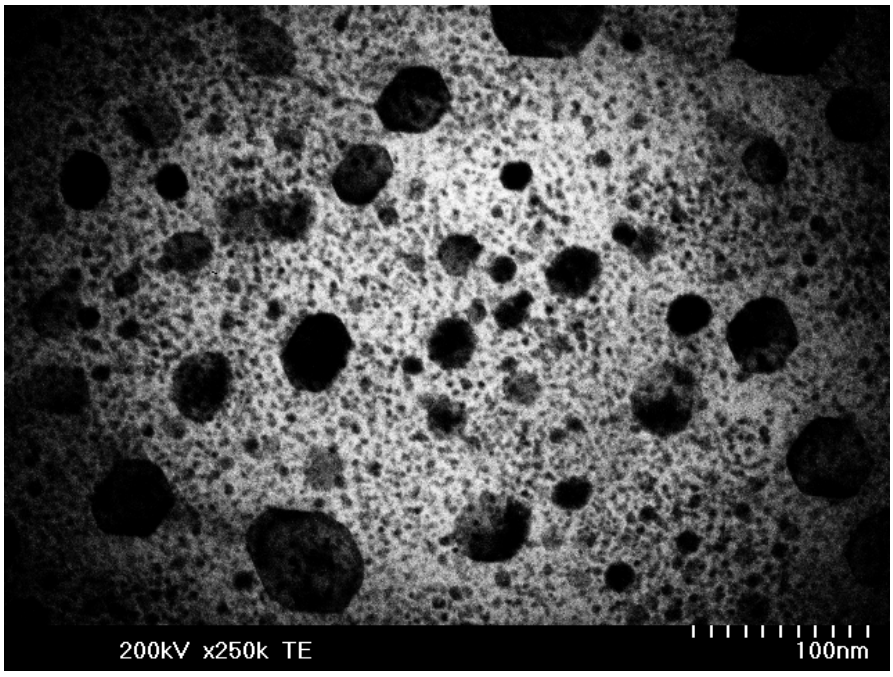


Figure 4.51: Cross-sectioned micrograph of $\alpha-Al_2O_3$ specimen implanted with a fluence of 1×10^{17} Fe/cm^2 (150 keV) at room temperature and annealed in Ar-4% H_2 at 1000^{o}C for 1 hour. (x 250K)

(a)



(b)

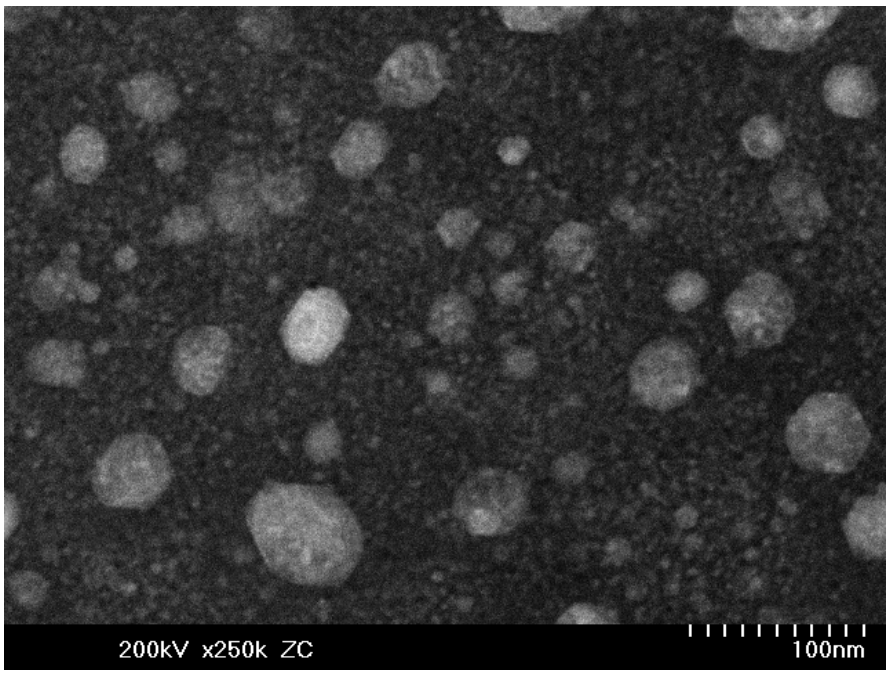
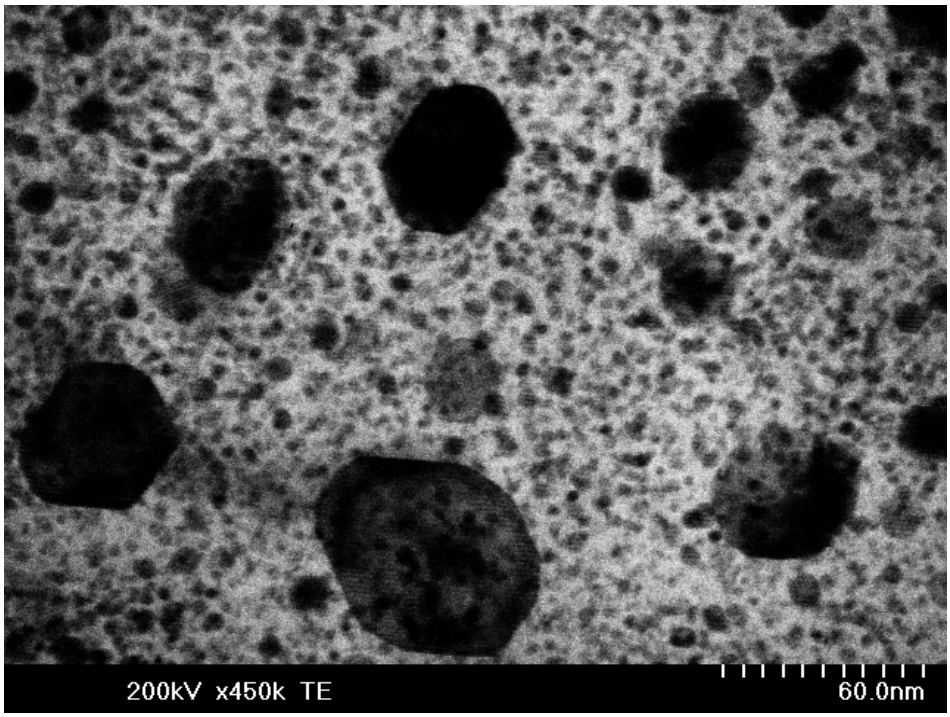


Figure 4.52: Plan view micrographs of α–Al_2O_3 specimen implanted with a fluence of 1×10^{17} Fe/cm^2 (150 keV) at room temperature and annealed in Ar-4% H_2 at 1000^{o}C for 1 hour. (a) x 250K-bright field image, (b) x 250K-dark field image, (c) x 450K-bright field image and (d) x 450K-dark field image.

(c)



(d)

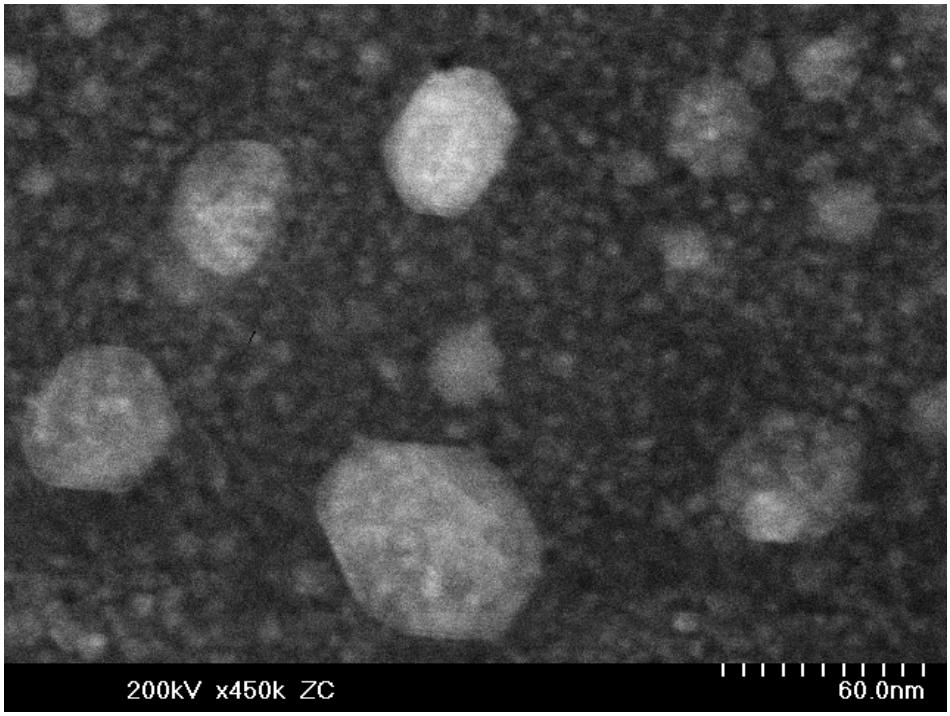
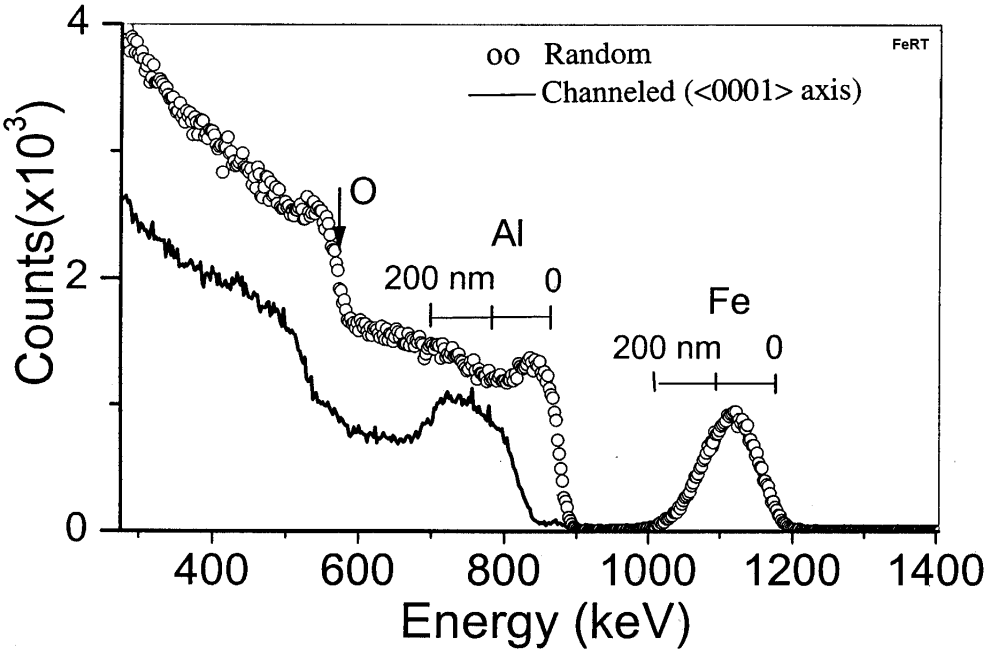


Figure 4.52 continued.

(a)



(b)

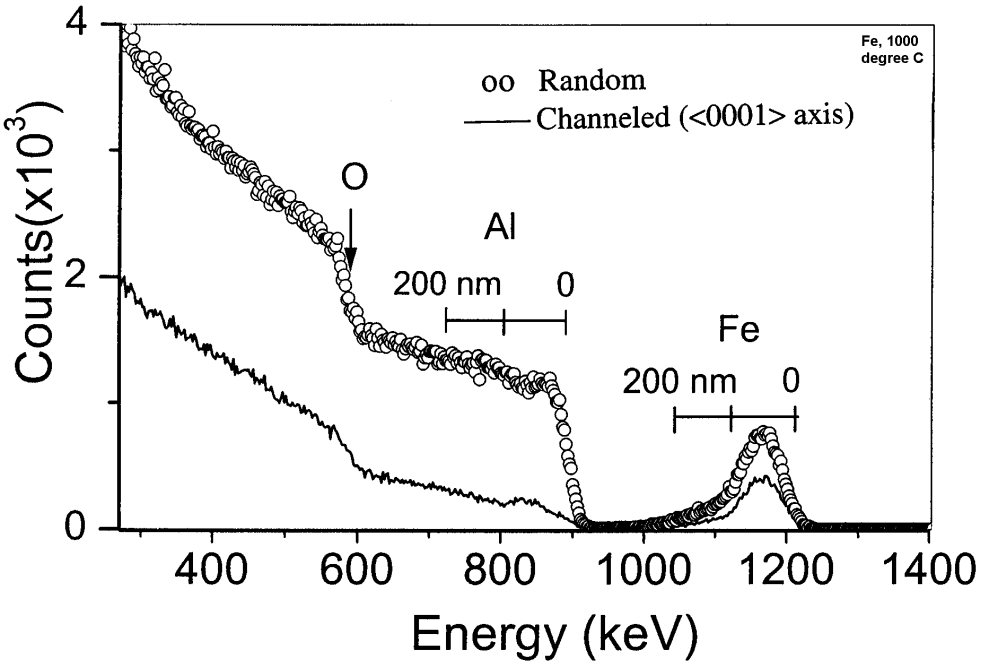


Figure 4.53: RBS spectra for $\alpha-Al_2O_3$ specimen implanted with iron. (a) At room temperature, (b) at 1000°C and (c) for the beam parallel to $< 02\bar{2}1 >$.

(c)

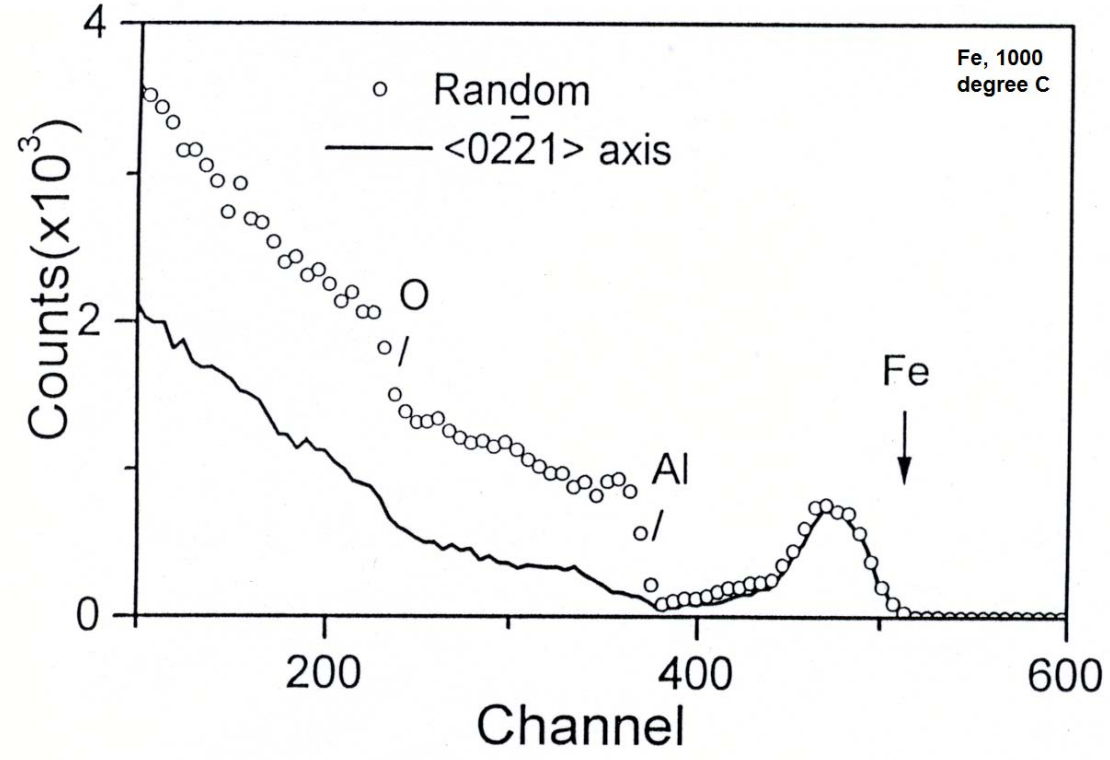


Figure 4.53 continued.

These observations suggest that the presence of iron-containing precipitates that are coherent with the basal plane but otherwise incoherent. Ren [21] found body centered iron precipitates in samples that had been implanted at room temperature and annealed in reducing atmospheres at 1100^{o}C. She determined the orientation relationships to be {011} Fe //{0001} sapphire; <111>Fe 10^{o} from <1010> i.e., the close packed planes were parallel but the close-packed directions were not.

The number of implanted atoms (ions) present in a given region can be obtained from the area under the backscattered peak. The iron peak in Figure 4.53 (b) is asymmetrical with a long tail extending into the crystal, indicating that some of the iron has diffused from the implanted zone into the crystal. About 52% of the implanted iron resides in the implanted zone, about 39% has diffused inwards, and about 10% has been lost from the surface. The peak of the iron distribution is located ~ 50 nm from the surface compared to 65 – 70 nm for the sample implanted at room temperature. There is little residual disorder in the Al–sublattice. The value of χ_{Al} is about 0.10 at the peak disorder position (65nm).

4.3.4. *Optical Absorption*

The sample implanted with 1×10^{17} Fe/cm^2 (150 keV) at room temperature exhibits a strong absorption band at 203 nm, and a weak band at ~ 290 nm (Figure 4.54). These bands are superimposed on a broad featureless scattering or absorption that extends to at ~ 500 nm. The peak at 203 nm could arise from either F or F^+ -centers. The peak at ~ 290 nm could come from F_2 – centers. The optical absorption pattern suggests the presence of several types of oxygen vacancy centers and their clusters (see Table 2.2). It is likely that some absorption arises from Fe^{2+} -oxygen vacancy cluster. Recall that the models for inserting divalent impurities into sapphire without adding oxygen postulate charge compensation is achieved by impurity – oxygen vacancy cluster of various types. The models also suggest that the oxygen vacancies tend to trap electron to form F- type centers adjacent to the divalent impurity. The Mossbauer studies of McHargue et al [20, 54] on sapphire implanted with the same fluence of iron under similar conditions

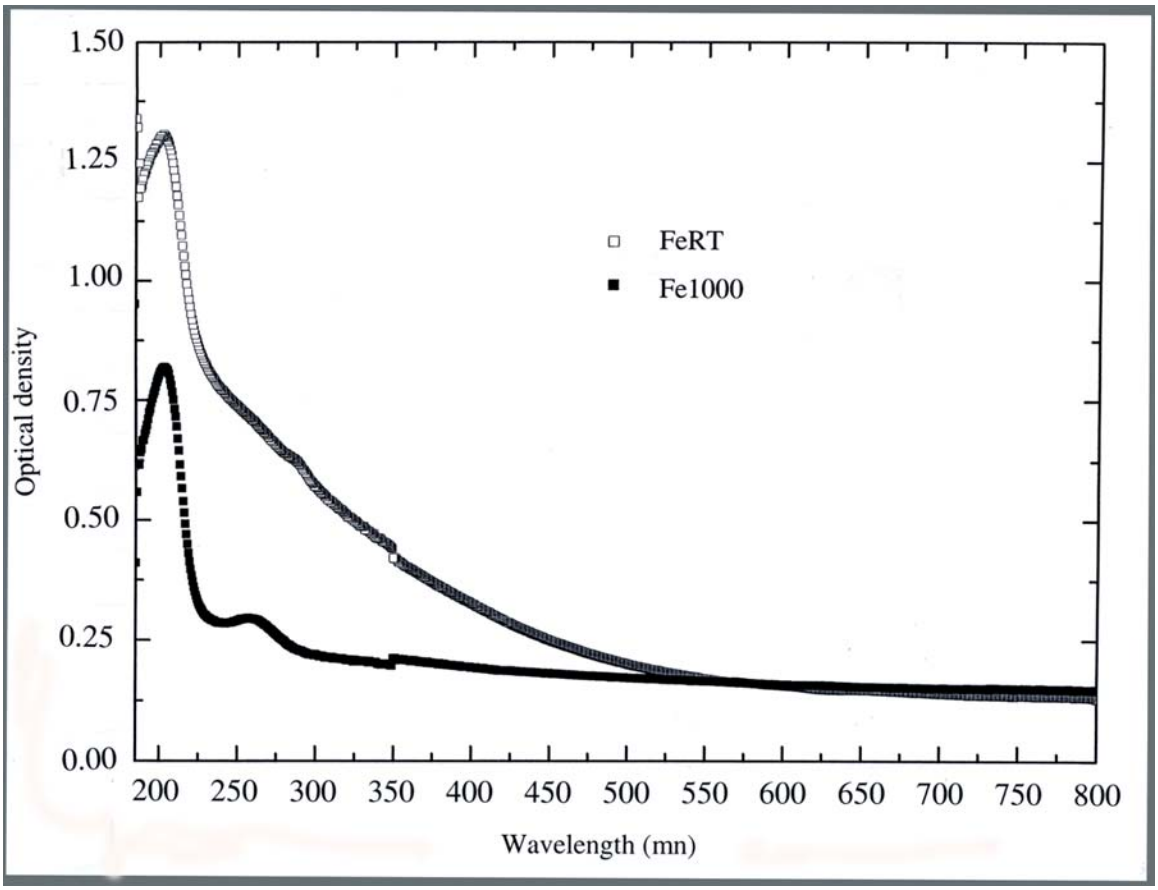


Figure 4.54: Optical absorption spectra for $\alpha-Al_2O_3$ specimen implanted with iron at room temperature and 1000^{o}C.

found that 40% of the iron was in the 2+ state, 40% in the metallic state (Fe^{o}) and 20% as Fe^{4+}. These investigations postulated that the Fe^{2+} was associated with oxygen vacancies. The intensity of the band at 203nm is reduced for the 1000°C implant compared to that for room temperature implantation but it is still the dominant feature (Figure 4.54). There is also a well-resolved band centered at 255 – 260 nm. These two bands correspond to those for F^{+} -centers. The broad background is absent signifying much less residual disorder in the oxygen sublattice.

4.3.5. *X-ray Diffraction*

X-ray diffraction results for iron-implanted sapphire at 1000°C are shown in Figures 4.55. The spectrum of Figure 4.55 (b), reveals the presence of BCC iron.

(a)

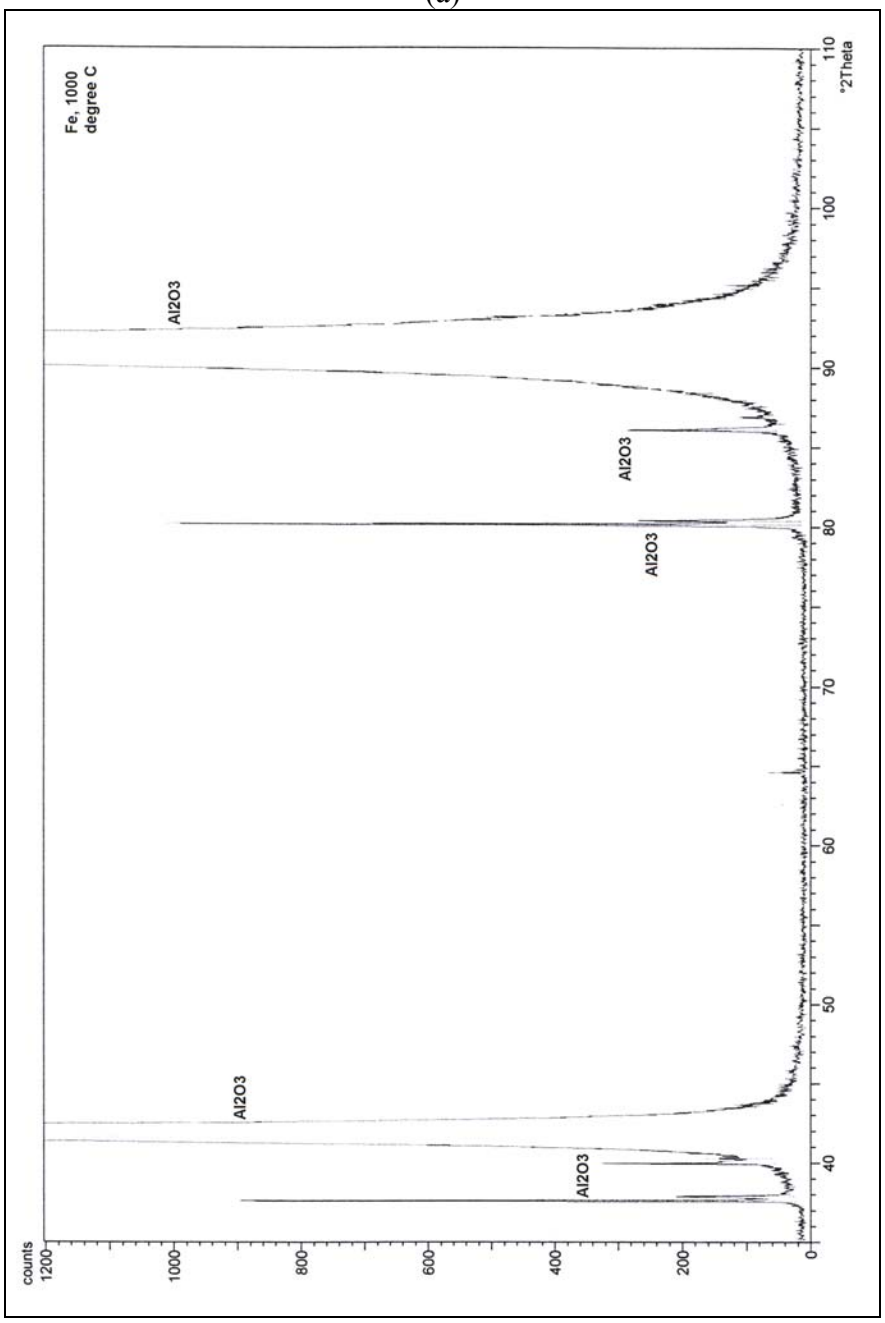


Figure 4.55: XRD spectra for $\alpha-Al_2O_3$ specimen implanted with iron at 1000°C. (a) Backside of the specimen (not implanted) and (b) Implanted surface.

(b)

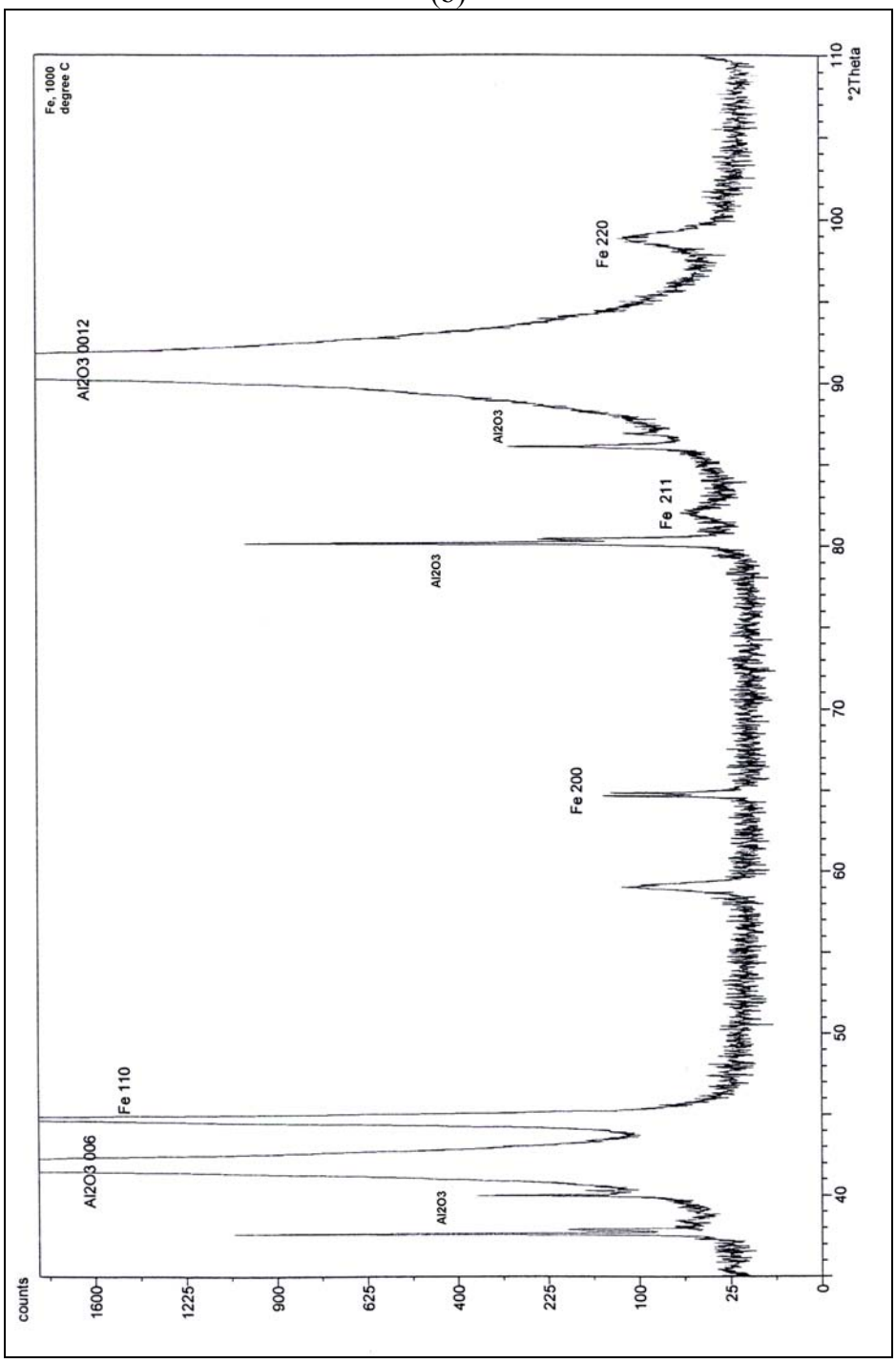


Figure 4.55 continued.

CHAPTER 5

DISCUSSION OF RESULTS

5.1. Role of Ionizing Energy to Displacement Energy Ratio

One objective of this study was to explore the effect of the ratio of ionizing energy deposition to elastic energy deposition on the microstructure under conditions usually used in ion implantation. Published tables of stopping power (dE/dx) indicate that the ratios of $(dE/dx)_e/(dE/dx)_n$ for boron, nitrogen and iron are 16, 8 and 0.3, respectively. [73]. It was thought that the factor of 53 between the value for B and Fe might be a factor in the microstructural development under the current experimental conditions. These tabulated values are based on the stopping of the bombarding ion at the surface of the target. However, simulations using the TRIM program show that the total deposited ionizing energy are heavily influenced by the contribution from the recoiling target ions. As shown in Tables 4.1, 4.3, and 4.5, the total ionizing energy deposited at the peak damage position differs only by a factor of two for B and Fe. Even at the surface of the target, about one third of the total deposited ionizing energy for iron implantation arises from the recoils of Al and O ions.

Because of the low nuclear stopping powers of B and N, little damage occurs in the near-surface region. The ratios $(dE/dx)_e/(dE/dx)_n$ are similar through the range where significant displacements occur that no effect on the microstructure should be expected.

5.2. Deposited Damage Energy Density and Nature of Cascades

Although Zinkle argues that Ionizing Radiation Induced Diffusion (RID) plays a major role for very high ratios of $(dE/dx)_e/(dE/dx)_n$, he acknowledges that details of the defect formation in the cascades and subcascades may significantly influence the resultant microstructures [14,32,57]. Other indications that such details may be important come from the observations of retained damage obtained from optical absorptions measurements by Agnew [44] and Dalal et al. [43]. Agnew reported that B-implanted

sapphire retained about twice the number of F-type centers as N-implanted samples for room temperature irradiation. Dalal et al. noted that dense cascades favor the formation of F^+ -centers relative to F-centers.

The TRIM simulations presented in Chapter 4 give information on the production of defects by the incident ions but no direct information regarding the defects that survive the "cool-down" period after the ion has stopped (~10^{-9} sec). Nevertheless, some reasonable assumptions about the nature of the residual disorder can be made.

The number of Al vacancies produced at all positions along the range are greater than the concentration of O vacancies by a factor of 1.8 to 2.0 for all three ion species. The specific value is determined by the ion masses, displacement energies and scattering cross-sections. The number of interstitials of each type will be in the same ratio. The stoichiometric ratio of Al to O is 0.667. If the surviving ratio is the same as the production ratio, there will be an excess number of Al interstitials even if all the oxygen interstitials combine with Al interstitials to form stoichiometric dislocation loops. One might expect that some portion of these excess Al interstitials would agglomerate into metallic Al colloids.

The density of vacancy (and interstitial) production is much higher for the Fe than for the B or N. This is a consequence of the greater mass of the incident ion that results in higher numbers of defects distributed over a shorter distance. The density of each type of vacancy is 5 to 10 times higher for Fe than for N and 6 to 28 times higher than for B. The ratio varies with the distance from the surface, being highest at the surface and lowest near end-of-range.

The concentration of implanted species at the same relative position from the surface also varies. The ratio of implanted ions to Al lattice ions at the peak concentration is given in Table 5.1. These calculations (Table 5.1) indicate that the relative numbers of each type of vacancy and interstitial and implanted ions available to form clusters or complexes at any given position varies in a complex manner.

TRIM simulations using only 5 or 10 impinging ions were used to examined the structure of damage along the ion path. The low number of incident ions allows the observation of individual collisions along the ions' paths. Figure 5.1 – 5.3 contain the

Table 5.1: The ratio of implanted ion to Al lattice ion at the peak concentration.

Implanted Ion Dose	**Peak Concentration Ratio: Implanted ion /Al lattice ion**
1×10^{17} B/cm^2	0.2 B/Al
3×10^{16} N/cm^2	0.065 N/Al
1×10^{17} Fe/cm^2	0.43 Fe/Al

results for (a) the ion trajectory and final position, (b) the ion paths and displacements projected onto the X-Y plane (where the x-axis is normal to the surface and y-axis is parallel to the surface); and (c) a lateral projection showing the spread around the projected path.

The maximum range of the Al and O ions displaced by an elastic collision at the surface of the sample can be estimated. The maximum energy transferred in an elastic collision is given by

$$E_{max} = 4\ M_1\ M_2\ E_0 / (M_1 + M_2)^2$$

Where M_1 is the atomic mass of the bombarding ion, M_2 is the mass of the target ion and E_0 is the incident energy. The "primary knock-on" ion is then treated as an ion striking the surface with that energy. The calculated energy transfers and projected ranges are given in Table 5.2. Note that these projected ranges are the maximum possible and the simulated ones will be affected by the stopping power or stopping for the incident ion. The first elastic collision for boron occurs at a distance of 45 nm from the surface of the sample whereas that for iron occurs much closer to the surface. Some of the incident energy for boron will have been lost by ionizing collisions and by phonon interactions, i.e., local heat deposition.

The pattern of simulated damage for B and N (Figs. 5.1 and 5.2) are similar. There is no damage (displacements) beyond the range of the stopped B or N ion. There are small subcascades, consisting of small clusters of Al or O ions near the end of range.

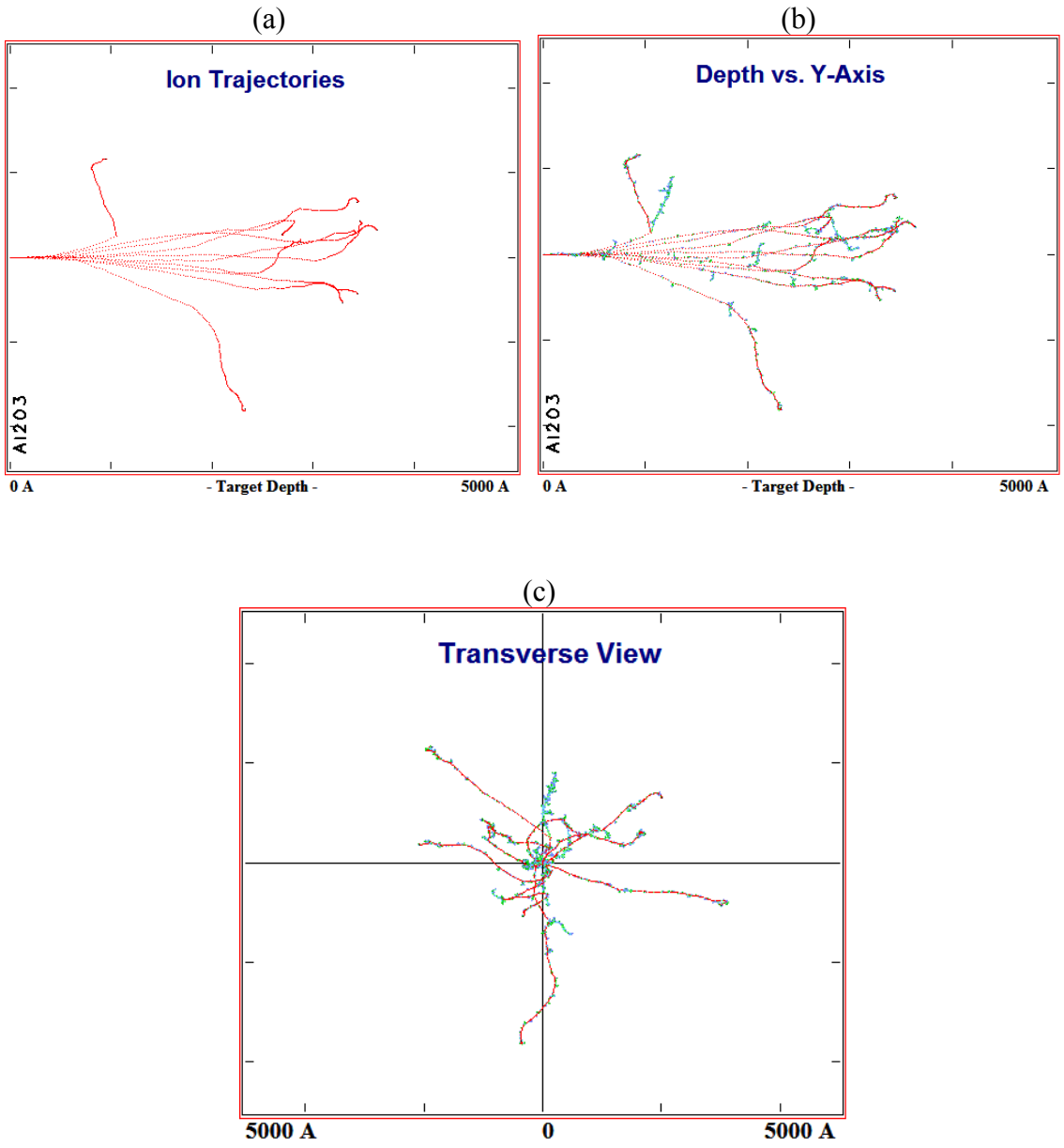


Figure 5.1: TRIM simulation of 10 B ions (150 keV) bombarding sapphire. The red lines indicate the path of the B ions, the black squares show the position of the stopped B ions, the dark blue points indicate stopped Al ions; and the dark green points indicate stopped O ions. (a) ion trajectories, (b) projection of ion paths and displaced ions onto the X-Y plane and (c) transverse projection showing the spreading of the ions and displacements.

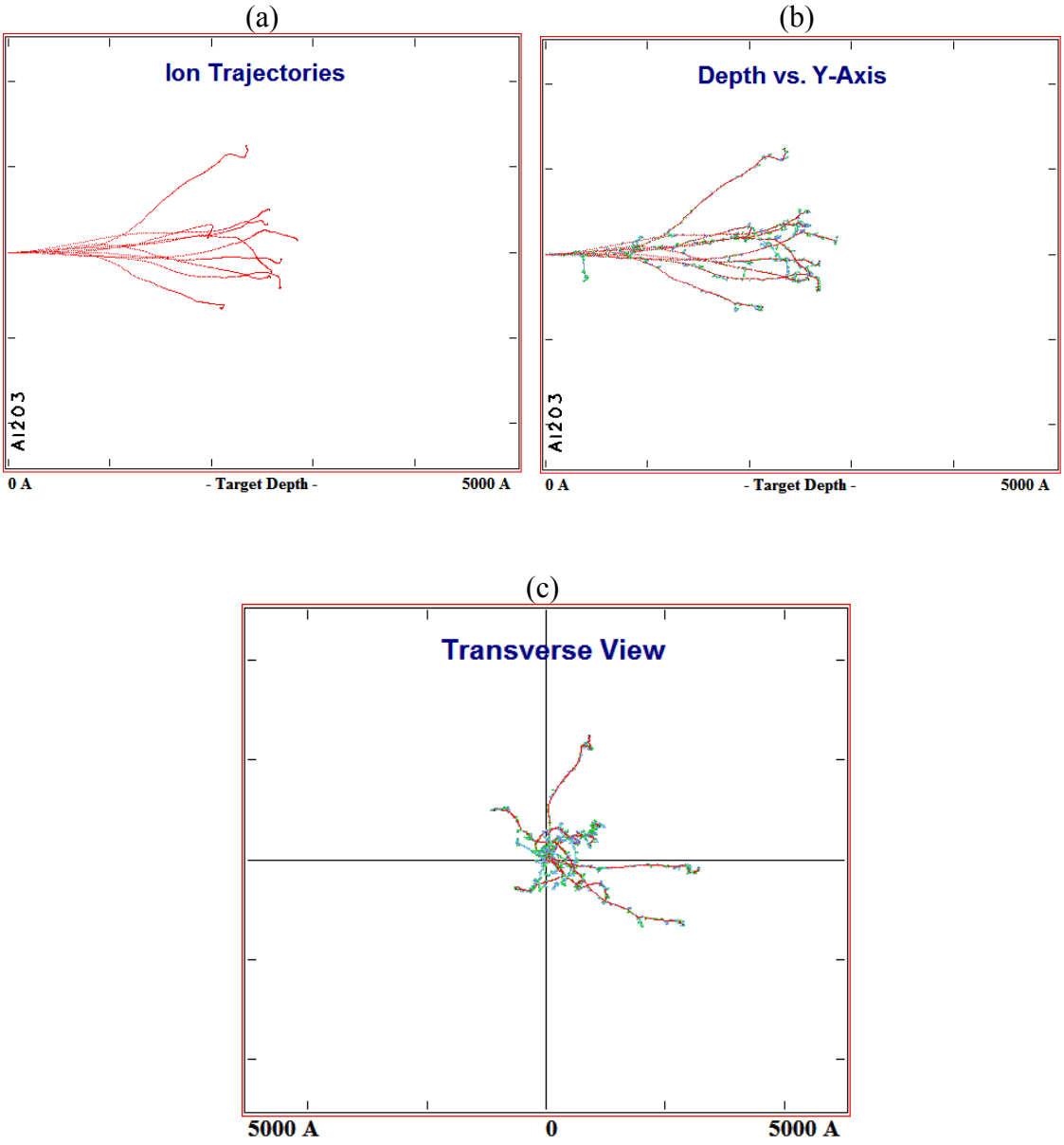


Figure 5.2: TRIM simulation of 10 N ions (150 keV) bombarding sapphire. The red lines indicate the path of the N ions, the black squares show the position of the stopped N ions, the dark blue points indicate stopped Al ions; and the dark green points indicate stopped O ions. (a) ion trajectories, (b) projection of ion paths and displaced ions onto the X-Y plane and (c) transverse projection showing the spreading of the ions and displacements.

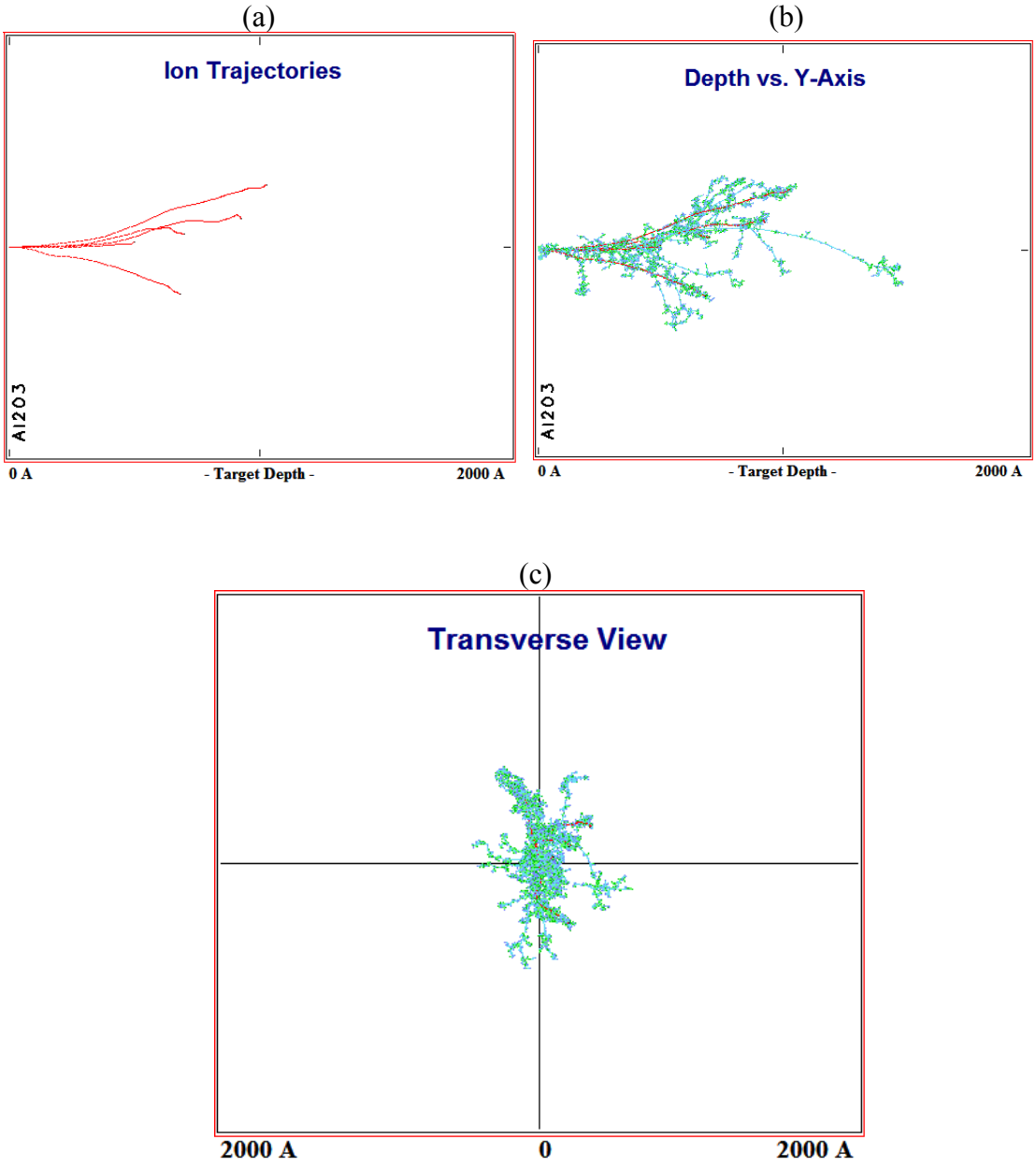


Figure 5.3: TRIM simulation of 5 Fe ions (150 keV) bombarding sapphire. The red lines indicate the path of the Fe ions, the black squares show the position of the stopped Fe ions, the dark blue points indicate stopped Al ions; and the dark green points indicate stopped O ions. (a) ion trajectories, (b) projection of ion paths and displaced ions onto the X-Y plane and (c) transverse projection showing the spreading of the ions and displacements.

Table 5.2: Energy transferred to "primary knock-ons" and projected ranges.

Incident Ion	**E_{max} to Al**	**E_{max} to O**	**R_p (Al)**	**R_p (O)**
B	123 keV	144 keV	123 nm	197 nm
N	135 keV	149 keV	141 nm	204 nm
Fe	132 keV	104 keV	136 nm	150 nm

Most of the displacements along the ion path consist of one or a few lattice ions. In both instances, the few dense subcascades appear to arise from the collision of "primary knock-ons", i.e., Al or O ions, with other lattice ions. The occurrence of subcascades is slightly higher for the N implantation than for the B, as would be expected from the higher mass. These observations suggest that the microstructure of B- and N-implanted specimens (room temperature) will be dominated by features characteristic of small defect clusters.

Figure 5.3 shows a very different damage pattern for the Fe-implantation. The projected range for displacements extends to about 140 nm, compared to a projected range of 67.9 nm for the iron. This extended damage is due to the displacements caused by the primary and secondary displaced Al and O ions. Many of the paths are characterized by the presence of single Al displaced ions (interstitials) with clusters of oxygen ions near the end-of-range. The subcascades produced by the primary displaced oxygen ions appear to be denser than those caused by the Al ions. The transverse projections show that the lateral spread for the Fe-implantation is much less than for the B- or N-implantation. As a result, the density of defects at any point is much higher for the Fe samples. The high density of defects would be expected to lead to recombination of many irradiation-produced defects and to agglomeration of the survivors into larger clusters or complexes.

5.3. Microstructures of Samples Implanted at Room Temperature

The microstructure, lattice disorder as revealed by ion channeling, and the optical

absorption spectra produced by implantation showed some similarities but some marked differences for the three ion species. The differences suggest again that the details of the cascades and subcascades and/or the thermochemistry of the ion-host are important factors in determining the response of sapphire to implantation.

As noted in Chapter 4, the microstructure of the sample implanted with boron at room temperature is characterized by "black spot damage" or defect clusters whose features could not be resolved due to the high strains fields associated with them. The size and density of such features increases toward the end of range. These features at a distance ~250 nm from the surface of the sample apparently are responsible for the large disorder observed in the RBS-channeling spectra. Note also that the optical absorption of the B-implanted samples was greater than for the N- or Fe-implanted ones.

It is suggested that the relatively small interstitial clusters observed in the TRIM simulations (Fig. 5.1) near the end-of-range are stabilized by the implanted boron ions. This stabilization would prevent the recombination of oxygen interstitials, for example, with oxygen vacancies. The increased oxygen concentration results in the observed high concentration of F-type centers.

Although the TRIM simulations suggest the damage distribution for boron and nitrogen implantation should be similar, the observed microstructures are different. The density of "black spot damage" is less for the N-implanted samples as is the optical absorption. Features identified as bubbles or voids were present in a band extending from ~150 to ~250 nm from the surface. These features are responsible for the dechanneling effects observed in the RBS-channeling spectra. The disorder in the spectrum for the Al-sublattice is less for the N-implantation than for the B-implantation, consistent with the lower density of defect clusters. The low optical absorption is also consistent with few F-type centers, i.e., oxygen vacancies.

The TRIM simulations represented by Figs. 5.1 and 5.2 suggest that the subcascades for the nitrogen implantation are slighter larger than for the boron. The larger defect clusters may be more effective in trapping nitrogen, leading to the formation of gas bubbles. The ionic radius of nitrogen ions is much larger than that of aluminum

and oxygen, whereas, the ionic radius of boron is much smaller. The relative sizes may explain why small cluster trap boron but larger ones are required to trap nitrogen.

Note that Agnew discounted any "chemical effect" to account for the variation in the amount of retained damage (F-type centers) although his measurements indicated more damage to be retained in B-implanted samples than in ones implanted with He, N, Ar or Kr [44]. He attributed the variation to errors in the values used for the stopping cross-sections used to calculate the number of defects produced during the implantation.

Dalal et al. [43] proposed that the distortions produced by neighboring defects in high-density cascades favor the retention of F^+ centers over F-centers. Since the F^+ defect contains only one trapped electron it is more tightly bound to its local site than is the "neutral" F-center.

The theoretical calculations of Catlow et al. [35] and Kotomin and co-workers [36,37,40] consider that the lattice relaxations near defects make an important contribution to the energy of the system. Thus, it is reasonable to expect that ions larger than the host ions will produce different effects from those that are smaller.

The microstructures of the Fe-implanted samples contain "black spot damage" clusters and small (1-2 nm) precipitates at depths greater than about 25 nm. These observations are consistent with previous studies [20 & 21]. The studies using conversion electron Mössbauer spectroscopy showed that about 45% of the implanted iron at this fluence was present in the metallic state. The TEM examinations showed that the metallic iron was body-centered cubic and present as 1-3 nm particles. The balance of the iron was present in charge states Fe^{2+} and Fe^{4+}. Both charge states are associated with oxygen vacancy clusters that are responsible for the features observed in the optical absorption spectra.

The electron diffraction patterns obtained in this study gave hints of additional spots but the patterns were to weak to be interpreted. The glancing angle x-ray diffraction study detected only signals from the sapphire. It was concluded that the precipitates are so small that the low intensity due to line-broadening prevented detection.

5.4. Effect of Implantation Temperature

Implantation at 1000° C produced very different microstructures than those produced at room temperature for all three-ion species. The TEM micrographs for the B-implantation contained discrete particles having sizes up to 5-7 nm and little evidence for "black spot" clusters. The particles appear to be aligned on planes running at an angle to the surface; that is, some plane other than (0001). The selected area diffraction patterns and the x-ray diffraction patterns gave no evidence for a second phase. In each case, the background from sapphire masked any weak signal from the very small precipitates. The optical absorption spectrum indicate F-type centers to be present but at a much reduced level than in the room temperature sample.

It is possible that the particles are colloidal aluminum. The mobility of displaced atoms (ions) at 1000°C may allow the interstitial clusters of aluminum to grow sufficiently large to precipitate as a second phase.

The database, TAPP2.2 [74] contains information for three Al-B compounds, AlB_2, AlB_{10} and AlB_{12} and shows no terminal solid solubility. Values of the free energies of formation indicate that boron will not reduce Al_2O_3 to form the compounds. However, if some of the particles are aluminum, there could be a reaction to form AlB_2. Further studies to identify this phase(s) are necessary.

The RBS-channeling spectra show significant retained disorder at positions near the end-of-range of the boron. The disorder in the Al-spectrum is much less than for the room temperature specimen. The micrographs suggest that there are more and possibly larger defect clusters in this region. This observation is consistent with the many reports of an uncharacterized end-of-range damage.

The micrographs of the N-implanted specimen also contain what appears to be nanometer sized particles. These particles appear to be aligned along a crystallographic plane parallel to (0001). The SAD patterns contain some spots from an as yet unidentified phase. There is one compound in the Al-N system, AlN. This compound has been reported to form in N-implanted aluminum at temperatures above 500°C and fluences of

$3x10^{17}$ N/cm^2 and higher [75]. The observed particles could be AlN or they could be aluminum.

There is also considerable "black spot damage", i.e., defect clusters, and the amount is higher than in the room temperature sample. The RBS-channeling spectra also indicate the dechanneling (damage) in the Al-sublattice is greater than for the room temperature implanted specimen. In contrast to the room temperature specimens, no bubbles or voids were detected. The reason for there being less disorder for the high temperature implantation than for room temperature is not clear. Since no bubbles or voids are observed for the higher temperature, one surmises that the nitrogen is mobile at this temperature and is able to diffuse from the specimen. It remains for further investigation to determine the role of nitrogen in relieving the "back spot damage" at the lower temperature.

The sample implanted with iron at 1000° C contains particles of iron as large as 50 nm. Both x-ray diffraction and electron diffraction (SAD) have identified these particles as α-Fe. There are smaller (2-10 nm) iron particles attached to faceted voids through the implanted region. Note in Fig. 4.42 (a) that there is a second phase (dark streaks) along two of the sides of many of the hexagonal shaped voids.

This figure and the dark field image of Fig. 4.42 (c) show the presence of a very large volume of voids. The question of the distribution of the displaced aluminum ion arises if we ascribe the voids to originating from either clusters of aluminum or oxygen vacancies. A recent paper by Meldrum et al. [76] reported similar features in silicon implanted with Zn or Cd at temperatures above the melting point of the implanted ion. They proposed that "liquid" clusters of the implanted species formed and the void was created due to their shrinkage upon solidification during cooling from the implantation temperature. The similarities between the present microstructure and those of Meldrum et al. suggest the possibility that the particles at the corners and sides of the voids are aluminum. Any aluminum colloid that formed as a result of the displacement damage would be liquid at 1000° C.

On the other hand, the precipitate-void configuration has been previously ascribed to the agglomeration of the Fe^{2+} -F-type center clusters proposed as the charge-neutral

complexes present after implantation [20]. If these clusters diffuse as a unit, the consequence of agglomeration would be an iron particle attached to (or near) a void (missing oxygen ions). Figures 4.41 and 4.42 are remarkable for the large numbers of voids (or bubbles). If these are due to condensation of oxygen vacancies or oxygen interstitials, there must be metallic aluminum either as a second phase of interstitial clusters at some location. Further studies will be necessary to definitively resolve the question of the location of the displaced aluminum.

5.4. Post-implantation Annealing

Samples implanted at room temperature were annealed for one hour at 1000°C in a reducing atmosphere of 4% H/Ar. Although the implantation was carried out in vacuum, the presence of the positively charged implanted ions provides a reducing environment. The microstructures were compared to those resulting from room temperature implantation and from implantation at 1000°C. The objective was to attempt to separate the effects of temperature from the effects of irradiation. A brief summary of the microstructural features from Chapter 4 is given in Table 5.3.

The microstructures for all three species contained no black-spot damage or interstitial clusters after annealing, but all contained a second phase. The second phase particles for B and N were in the range of 1 – 5 size. It was not possible to identify the nature of these phases with the equipment available for this study. The second phase in the B-implanted phase may be elemental boron, or metallic aluminum or a B-Al alloy phase. If it were an aluminum-boron oxide phase (e.g., $9Al_2O_3 \bullet 2B_2O_3$ or $2Al_2O_3 \bullet B_2O_3$), the oxygen to balance the B would come from the sapphire, leaving a large number of oxygen vacancies. Further optical absorption measurements should show if the number of F-type centers increases during this annealing treatment.

The discussion of the microstructures for N implantation at room temperature and at 1000°C given above appears likely that the precipitates are aluminum or AIN. The sample implanted with iron at room temperature and annealed at 1000°C contained a bimodal distribution of precipitate sizes, 1 – 10 nm and 50 – 100 nm. The earlier study [20] indicated that about one-half of the iron implanted to this fluence at room

Table 5.3: Summary of microstructures described in Chapter 4.

Ion	RT implant	1000°C implant	1000°C anneal
B	Back-spot damage precipitates?	Minor black-spot damage. Precipitates < 5nm.	Precipitates < 10 nm.
N	Some black-spot damage. Voids or bubbles.	Less black-spot damage. No voids or bubbles precipitates?	Precipitates < 6nm.
Fe	Black-spot damage. 1-2 nm precipitates.	No black-spot damage. Precipitate 1-3 nm and 20 –50 nm.	Precipitates 1-10nm and 50-100 nm.

temperature was in the metallic state (Fe^0) and the balance distributed between Fe^{2+} and Fe^{4+}. Annealing under similar conditions reduced all the iron to the metallic state. The larger precipitate may result from the growth of those observed in the RT sample and the smaller ones are those due to reduction during the annealing. The remarkable difference between the sample implanted at 1000°C and both the RT and RT plus annealed samples are the large number of voids in the former case that are absent in the other samples. It is also possible that some of the small precipitates are metallic aluminum, as discussed in Section 5.4.

CHAPTER 6

CONCLUSIONS AND SUGGESTIONS FOR FUTURE WORK

6.1. Conclusions

1. The microstructure of boron-implanted $\alpha-Al_2O_3$ at the fluence of 1×10^{17} B/cm^2 (150 KeV) was noticeably influenced by temperature. The room temperature implant microstructure consists of the typical "black spot" radiation damage. The features in the microstructure of the sample implanted at 1000^{o}C differ from the "black spots" of the room temperature implanted sample, and some may be due to precipitates of a second phase.

2. The microstructure of nitrogen implanted $\alpha-Al_2O_3$ at the fluence of 3×10^{16} N/cm^2 (150 KeV) was also influenced by temperature. The room temperature implanted microstructure reveals the presence of bubbles or voids in a band about 200nm wide, and extending from ~150 to ~250 nm from the surface and no any other evidence of defect. The 'black spot features of the 1000^{o}C implant have a different appearance. There were no observable voids or bubbles. There may be very small particles of a second phase.

3. The microstructure of the iron-implanted samples at the fluence of 1×10^{17} Fe/cm^2 (150 keV) was significantly influenced by the implantation temperature. The room temperature implant microstructure contains "black spot damage" clusters and small (1-2 nm) precipitates at depths greater than about 25 nm. The sample implanted with iron at 1000°C contains particles of iron as large as 50 nm. These iron particles were identified as α-Fe. The microstructural features of these 1000°C implant samples also consist of smaller (2-10 nm) iron particles attached to faceted voids through the implanted region and very large volume of voids. There is no evidence of "black spot" radiation damage.

4. The microstructures for all three species implanted into sapphire at room temperature followed by annealing in Ar-4% H_2 for one hour at 1000° C were quite

different from the as-implanted ones. None contained "black-spot damage" or interstitial defect clusters, but all contained evidence for small second phase particles. The annealing promoted the recombination of point defects and defect clusters and allowed the system to move toward the equilibrium phase compositions. Implantation at 1000° C involves complex interactions among defects and between the implanted ions and the defects. The specific microstructure was species dependent, indicating strong interaction between the implanted species and the defects. In instances where some "black-spot" damage was observed, defect production was faster than defect annihilation. The samples implanted with iron have large, easily observable defect configurations suggesting that the point defect condense rather than recombine to be eliminated. The microstructures suggest that the implanted iron stabilizes such configurations.

5. The lattice disorder as measured by Rutherford backscattering spectroscopy-ion channeling was greater for iron and boron implantation at room temperature than at 1000° C, but higher nitrogen implanted at 1000° C. The reason(s) for stabilization of the disorder by nitrogen at the higher temperature but the formation of gas bubbles at the lower temperature is not clear. The highest lattice disorder was produced by the iron implantation and is attributed to the higher density of displacements in the cascades.

6. With the exception of the large α-Fe particles in the specimens implanted at 1000° C, attempts to identify second phases were unsuccessful. A complete analysis of the effects of implantation upon the microstructure requires that these phases be fully characterized.

7. The optical absorption measurements indicate the presence of oxygen vacancies and defect clusters involving oxygen vacancies. The number of F-type centers was highest for boron implanted at 1000° C. Relatively few such centers were present after implantation of nitrogen at either temperature. The results are also consistent with the proposal that high density cascades (e.g., Fe) favor F^{+} -centers over F-centers.

8. The ionizing component of the irradiation did not noticeably affect the microstructures. The ENSP ratios $\{(dE/dx)_e/(dE/dx)_n\}$ obtained from the TRIM simulations did not differ significantly for the three species through the range where significant displacements occurred. The contribution to the total ionizing component from the recoils was equal to or greater than that from the incident ions for iron over most of the ion range.

9. The details of the damage cascades have a large effect on the resultant microstructures. The simulations using TRIM show that implantation of the lighter ions (B and N) produced small subcascades along the ion path, relatively few subcascades due to primary and secondary knock-ons, and no damage beyond R_p. The resultant disorder consists of small defect clusters that are well separated for a given incident ion. The heavier ion (Fe) produced dense cascades along the entire ion path. Much of the disorder arises from subcascades caused by the primary and secondary knock-ons, and defect production extends to distances as much as two times R_p. The defect clusters are larger and more densely spaced than for the lighter ions. Many of the microstructural features involve the interaction of the implanted ions with these defect clusters.

10. The thermochemical properties of the implanted species and the host play an important role in microstructure development. In order to understand this role, a complete determination of the composition and structure of the second phases is required.

6.2. Suggestions for Future Work

1. It is essential to obtain a complete characterization of the second phases in order to understand the interactions among defects, implanted species, and the matrix (sapphire). In particular, the existence or absence of colloidal aluminum needs to be established. Detection of light elements such as B and N and detection of Al in a matrix of Al_2O_3 are difficult. It may be possible to successfully apply some of the techniques

used in this study by carefully optimizing specimen preparation and selection of specimen geometry.

2. Studies to determine the origin of the extensive void formation observed after the elevated temperature implantation of iron are suggested. Studies to determine if this void structure can be used as a template to produce other nanoparticles by implantation of another ion species in samples having this void microstructure may lead to applications in the field of catalysis or nanotechnology.

3. Implantation of other light ions may assist in understanding the boron and nitrogen results. The role of implant species and defects in second phase formation might be studied by implantation of carbon in order to compare with the boron results. The details of damage cascades for B and C should be the same. There is one compound, Al_4C_3, which is somewhat analogous to AlB_2. The reactivity of Al with B and C should be similar; [AlB_2 - ΔG_f = -149 kJ/mol at 298.15 K; Al4C3 - ΔG_f = -196 kJ/mol].
Implantation of a different gaseous species may help understand the microstructures produced by the N-implantation, Fluorine might be considered for this purpose. . Since the mass of F (18.99) is similar to N (14), the damage cascades should be similar. There is one compound, AlF_3 in this system. The fluorine should be more reactive with any aluminum (as clusters or colloids); [AlN - ΔG_f = -287 kJ/mol at 298.15 K; AlF_3 = -1431 kJ/mol].

4. A more complete characterization of the samples annealed after room temperature implantation; e.g., analysis of precipitates, optical absorption, RBS-C. These studies will aid in separating the effects of annealing from those of annealing in the presence of displacing irradiation.

5. There have been reports that implantation of microstructures that contain a second phase may cause the size of the second phase particles to shrink due to a “sputtering” effect or due to displacements. In some instances, re-precipitation near the original

particle has been observed in a so-called inverse Ostwald effect. Implantation of samples from this study that have second phases with other ions may produce a method for controlling the size of the nanoparticles and perhaps produce even smaller particles.

LIST OF REFERENCES

[1] P. J. Burnett and T. F. Page, Radiation Effects, Vol. 97 (1986) 283-296.

[2] C. J. McHargue, Structure –Property Relationships in Surface Modified Ceramics, C. J. McHargue, R. Kossowsky, and W. O. Hofer, eds. Kluwer Academic Publishers, Dordrescht, (1989) 253.

[3] C. W. White, C. J. McHargue, P. S. Sklad, L. A. Boatner and G. C. Farlow,"Ion Implantation and Annealing of Crystalline Oxides", Mater. Sci. Rep. 4, No. 2,3, (1989) 41-146.

[4] A. Alghamdi and P. D. Townsend, Rad. Eff. Def. Solids, 115 (1990) 73-8.

[5] J. C. Bourgoin and J. W. Corbett, Rad. Eff., 36 (1978) 157-88.

[6] R. Bullough and J. J. Gilman, J Appl. Phys., 37, 6 (1996) 2283-7.

[7] I. P. Chernov, et al., Rad. Eff., 97 (1986) 155-60.

[8] A. Dunlop, D. Lesueur, G. Jaskierowicz and J. Schildknecht, Nucl. Instr. Meth. Phys. Res. B 36 (1989) 412-9.

[9] E. P. EerNisse, J. Appl. Phys., 45, 1 (1975) 167-74.

[10] C. P. Flynn and R. S. Averback, Phys. Rev. B 38 (1988) 7118-20.

[11] N. Itoh, Rad. Eff. Def. Solids, 110 (1989) 19-26.

[12] H. J. Pabst, Rad. Eff., 25 (1975) 279-81.

[13] A. M. Stoneham, Nucl. Instr. Meth., Phys. Res. B 48 (1990) 389-98.

[14] S. J. Zinkle, in Microstructural Evolution During Irradiation, T. Diaz de la Rubia, L. W. Hobbs, I. M. Robertson and G. S. Was (eds.), MRS Symp. Proc. Vol. 439 (Materials Research Society, Pittsburgh, 1997) p. 667.

[15] http://www.crystalsystems.com.

[16] C. J. McHargue and W. B. Snyder, Jr., "Surface Modification of Sapphire for IR Window Application", Proceedings SPIE, 2018, (1993) 135-142.

[17] E. D. Specht, C. J. Sparks and C. J. McHargue, "Determination of Residual Stress in Cr-implanted Al_2O_3 by Glancing Angle X-ray Diffraction, "Appl. Phys. Ltrs., 60 (1992) 2216-1118.

[18] C. J. McHargue, M. E. O'Hern, C. W. White and M. B. Lewis, "Ion Implantation in Ceramics – Residual Stresses and Properties", Mater. Sci. Eng., A115 (1989) 361-367.

[19] A. Kirkpatrick, Report to the Task Force on Sapphire Window Reliability, Huntsville, AL, March 10, 1997.

[20] C. J. McHargue, P. S. Sklad, C. W. White, G. C. Farlow, A. Perez and G. Marest, "Microstructural and Chemical Effects in Al_2O_3 Implanted with Ion at Room Temperature and Annealed in Oxidizing or Reducing Atmospheres", J. Mater. Res., 6 (1991) 2145-2159.

[21] S. Ren, Ph. D. Dissertation, University of Tennessee, 1995.

[22] N. Cue, "Compositional Studies" in Method of Experimental Physics, Vol. 21 (Academic Press, New York), 222 &258.

[23] E. Rauhala , "Energy Loss" in Handbook of Modern Ion Beam Materials Analysis, Editors Joseph R. Tesmer, Micheal Nastasi, Materials Research Society, Pittsburgh, Pennsylvania, (1995) 3.

[24] P. D. Townsend, P. J. Chandler and L. Zang, Optical Effects of Ion Implantation (Cambridge University Press, New York, 1994).

[25] N. Bohr, Philosophical Magazine 25 (1913) 10.

[26] P. Sigmund, Nuclear Instrument Methods B12 (1986) 1.

[27] J. F. Ziegler, J. P. Biersak and U. Littmark, The Stopping and Range of Ions in Solids (Pergamon Press, New York, 1985).

[28] J. W. Mayer, L. Eriksson, and J. A. Davis (1970) Ion Implantation in Semiconductors (Academic Press, New York).

[29] W. Eckstein (1991), Computer Simulation of Ion-Solid Interactions, (Springer-Verlag, Berlin).

[30] J. Lindhard, Scharff, and H. E. Schiott, (1963), Mat. Fys. Medd. Dan.Vid. Selsk. 33 (14).

[31] R. Simonton and A. F. Tasch (1992) Channeling Effects in Ion Implantation, in Handbook of Ion Implantation Technology, J. F. Ziegler, ed. (North-Holland, New York) p. 119.

[32] S.J. Zinkle and C. Kinoshita, Defect Production in Ceramics, Journal of Nuclear Materials 251 (1997) 200-217.

[33] C. Moty, in Defects in Solids, A. V. Chadwick and M. Terezi, eds. (Plenum, New York, 1986) P.377.

[34] Y. Chiang, D. Birnie III and W. D. Kingery, "Physical Ceramics", (John Wiley & Sons, Inc., New York)

[35] C. R. A. Catlow, R. James, W. C. Mackrodt and R. F. Stewart, Defect energetics in α-Al_2O_3 and rutile TiO_2, Phys. Rev. B, 25 (1982) 1006-1026.

[36] P. W. M. Jocobs and E. A. Kotomin, Defect Energies for pure corundum and for corundum doped with transition metal ions, Phil. Mag. A, 68 (1993) 695-709.

[37] E. A. Kotomon, A. Stashans, L. N. Kantorvich, A. I. Lifshitz, A. I. Popov, I A. Tale and J. L. Calais, Calculations of the Geometry and Optical Properties of F_{Mg} Centers and dimer (F_2-type) centers in corundum crystals, Phys. Rev. B, 51 (1995) 8770-8778.

[38] M. Hirai and A. B. Scott, J. Chem. Phys., 44 (1966) 1753.

[39] J. H. Crawford, Defects and Defect Processes in Ionic Oxides: Where Do We Stand Today?, Nucl. Instr. Methods Phys. Res., B1 (1984) 159-165.

[40] E. A. Kotomon, A. I. Popov and A. Stashans, A Novel Model for F+ $\rightarrow$ F Photoconversion in Corundum Crystals, J. Phys.: Condense Matter, 6 (1994) L569 – L573.

[41] B. D. Evans and M. Stapelbroek, Phys. Rev., B18 (1978) 7089.

[42] Y. Chen and M. M. Abraham, Nucl. Instr. Methods in Phys. Res., B59/60 (1991) 1163-1166.

[43] M. L. Dalal, M. Rahmani and P. D. Townsend, UV Absorption of Ion Implanted Sapphire, Nucl. Instr. Methods in Phys. Res., B32 (1988) 61 – 65.

[44] P. Agnew, Displacement Damage Efficiency in Sapphire, Nucl. Instr. Methods in Phys. Res., B65 (1992) 305- 310.

[45] G. P. Pells, AERE Report, AERE R- 9359 (1979).

[46] G. P. Pells and D. C. Philips, J. of Nucl. Matr., 80 (1979) 207.

[47] G. P. Pells and D. C. Philips, J. of Nucl. Matr., 80 (1979) 215.

[48] A. Y. Stathopoulous and G. P. Pells, Radiation Damage in the Cation Sublattice of α-Al_2O_3, Phil. Mag., 47 (1983) 381.

[49] E. M. Hunt and J. M. Hampikian, Formation and Thermal Stability of Aluminum nanoparticles synthesized via yttrium ion implantation into sapphire, J. Materials Sci., 32 (1997) 3393 – 3399.

[50] G. C. Farlow, C. W. White, C. J. McHargue and B. R. Appleton, "Annealing Studies of Al_2O_3 implanted with Bromine", Radiation Effects, 97 (1986) 257-264.

[51] C. J. McHargue, J. M. Williams, G. C. Farlow, and M. B. Lewis, "Implantation of Gases into Sapphire", Nucl. Instr. Methods in Phys. Res., B19/20 (1987) 809-812.

[52] T. Hioki, A. Itoh, S. Noda, H. Doi, J. Kawamoto and O. Kamigaito, "Effects of Ion Implantation on Fracture Stress of Al_2O_3", Nucl. Instr. Methods in Phys. Res., B7/9 (1985) 521-525.

[53] C. Soumoy, F. Bodart and J. Chevallier, "study of Damage Accumulation in Sapphire during Nitrogen Implantation", Nucl. Instr. Methods in Phys. Res., B85 (1994) 516-519.

[54] C. J. McHargue, P. S. Sklad, C. W. White, G. C. Farlow, A. Perez and G. Marest, "Microstructural and Chemical Effects in Al_2O_3 Implanted with Ion at 77 K and Annealed in Oxidizing or Reducing Atmospheres", J. Mater. Res., 6 (1991) 2160-2177.

[55] R. L. Fleischer, P. B. Price and R. M. Walker, Nuclear Tracks in Solids, Principles and Applications (University of California Press Berkeley, 1975).

[56] M. Toulemonde, S. Bouffard and F. Studer, Nucl. Inst. Meth. In Phys. Res., B91 (1994) 108-123.

[57] S. J. Zinkle, V. A. Skuratov and D. T. Hoelzer, "On the Conflicting Roles of Ionizing Radiation in Ceramics", Nucl. Inst. Meth. In Phys. Res., B119 (2000) 758-766.

[58] G. W. Arnold, G. B. Kreft and C. B. Norris, Appl. Phys. Lett., 25 (1974) 540.

[59] G. B. Krefft. J. Vac. Sci. Technol. 14 (1977) 533.

[60] G. B. Kreft, W. Beezhokd and E. P. EerNise, IEEE Trans. In Nucl. Sci., NS-32 (1975) 2247.

[61] G. B. Kreft and E. P. EerNise, J. Appl. Phys., 49 (1978) 2725.

[62] S. J. Zinkle, J. Nucl. Mater. 219 (1995) 113.

[63] S. J. Zinkle, Nucl. Instr. Meth. in Pys. Res. B91 (1994) 234.

[64] S. J. Zinkle and L. L. Snead, Nucl. Instr. Meth. in Pys. Res. B116 (1996) 92.

[65] R. Brenier et al., Nucl. Instr. Meth. B 80/81 (1993) 1210.

[66] J. C. Bourgoin, Radiat. Eff. Def. Solids 111 and 112 (1989) 29.

[67] J. C. Bourgoin and J. W. Corbett, J. Chem, Phys. 59 (1973) 4042.

[68] Y. Chen, R. Gonzalez and K. L. Tsang, Phys. Rev. Lett. 53 (1984) 1077.

[69] J. W. Corbett and J. C. Bourgoin, IEEE Trans. Nucl. Sci. Ns-18 (1971)11.

[70] I. Jencic and I. M. Robertson, J Mater. Res. 11 (1996) 2152.

[71] W. K. Chu, J. W. Mayer, and M. A. Nicolet, Backscattering Spectrometry, Academic Press, New York, 1978.

[72] D. L. Joslin, Ph. D. dissertation, University of Tennessee, 1993.

[73] J. P. Biersack, Appendix in Ion Beam Modification of Insulators, P. Mazzoldi and G. W. Arnold, eds., Elsevier, Amsterdam, 1987

[74] TAPP2.2, Thermochemical and Physical Properties, ESM Microware, Inc., Hamilton, OH.

[75] S. Lucas, G. Terwane, M. Piette and F. Bodart, "Study of Nitrogen Implanted at High Temperature into Aluminum," Nucl. Instr. Methods Phys. Res., B59/60 (1991) 925-929].

[76] A. Meldrum, S. Honda, C. W. White, R. A. Zuhr and L. A. Boatner, "Nanocrystals in Crystalline Silicon: Void Formation and Hollow Particles," J. Mater. Res., 19 (2001) 2670-2679.

VITA

Lawretta Chineze Leaticia Ononye was born in Lagos, Nigeria. She attended Queen Elizabeth School, Ilorin where she obtained General Certificate of Education (GCE) (high school diploma) in 1983. Lawretta continued her education, and obtained a Bachelor of Science degree in Physics in January of 1990 from Edo State (former Bendel State) University, Ekpoma, Nigeria. She did National Service for one year (1990-1991) at Army Day Secondary School, Ibadan, Nigeria, where she taught Physics. She came to USA in 1992 and continued her education. In 1994, she obtained another Bachelor of Science degree in Computer Science, from Knoxville College, Knoxville, Tennessee. Lawretta enrolled at The University of Tennessee in August of 1996, where she obtained Master of Science degree in Metallurgical Engineering in August of 1998, and will earn a Ph.D. in Materials Science and Engineering in December 2002. While at the University of Tennessee, she worked as a Graduate Teaching Assistant (1996–1998) and a Research Assistant (1998-2002).